UNIVERSITY OF SOUTHAMPTON

FACULTY OF PHYSICAL AND APPLIED SCIENCES

Electronics and Computer Science

End-to-End Solutions for a Droplet Microfluidic Autonomous Experimentation System

by

Gareth Lyle Jones

A thesis submitted in partial fulfillment for the degree of Doctor of Philosophy

November 2012

UNIVERSITY OF SOUTHAMPTON

ABSTRACT

FACULTY OF PHYSICAL AND APPLIED SCIENCES
Electronics and Computer Science

Doctor of Philosophy

END-TO-END SOLUTIONS FOR A DROPLET MICROFLUIDIC AUTONOMOUS EXPERIMENTATION SYSTEM

by Gareth Lyle Jones

Scientific discovery is limited by finite experimental resources. Therefore, careful strategic planning is required when committing resources to an experiment. Often the decision to commit resources is based upon observations made from previous experiments. However real-world data is inherently noisy and often follows an underlying nonlinear trend. In such circumstances the decision to commit resources is unclear. Autonomous experimentation, where machine learning algorithms control an experimentation platform, is one approach that has the potential to deal with these issues and consequently could help drive scientific discoveries. In the context of applying autonomous experimentation to identify new behaviours from chemical or biological systems, the machine learning algorithms are limited by the capability of the hardware technology to generate on-demand, complex mixtures from a wide range of chemicals. This limitation forms the basis for the work described in this thesis. Specifically this thesis documents the development of a hardware system which is designed to support scalability, is capable of automating processes, and is built from technology readily accessible to other researchers. The hardware system is derived from droplet microfluidic technology and allows for microscale biochemical samples of varying composition to be automatically created. During the development of the hardware system, technical challenges in fabrication, sensor system development, microfluidic design and mixing were encountered. Solutions to address these challenges were found and are presented as, fabrication techniques that enable integrated valve microfluidic devices to be created in a standard chemistry laboratory environment without need for sophisticated equipment, a compact UV photometer system built using optical semiconductor components, and a novel mixing strategy that increased the mixing efficiency of large droplets. Having addressed these technical challenges and in fulfilling the aims set out above, the work in this thesis has sufficiently improved hardware technology to free the machine learning algorithms from the constraint of working with just a few experimental variables.

Contents

List of Figures

List of Tables

Nomenclature

AAF	Anti Alias Filter
AChE	Acetylcholine Esterase
αCT	α-chymotrypsin
Ca	Capillary number
Cat	Catalase
CCD	Charge Coupled Device
ChOx	Choline Oxidase
DAC	Digital-to-Analogue Converter
DAQ	Data Acquisition
DFR	Dry Film Resist
ES	Enzyme-Substrate
FDH	Formaldehyde Dehydrogenase
FG	Fox Group
GDH	Glucose Dehydrogenase
GOx	Glucose Oxidase
HF	Hydrogen Fluoride
HRP	Horseradish Peroxidase
LED	Light Emitting Diode
LOD	Limit of Detection
LPF	Low Pass Filter
MDH	Malate Dehydrogenase
mLSI	Microfluidic Large Scale Integration
MP-11	Microperoxidase-11
NADH	Nicotinamide Adenine Dinucleotide (reduced form)
NAD^+	Nicotinamide Adenine Dinucleotide (oxidised form)
NC	Normally-Closed
NO	Normally-Open
NS	Nitride Semiconductor
PCB	Printed Circuit Board

PD	Photodiode
PDMS	Polydimethylsiloxane
Pe	Péclet number
PEB	Post Exposure Bake
PET	Poly(ethylene terephthalate)
PFD	Perfluorodecaline
PFO	Perfluorooctanol
PMMA	Poly(methyl methacrylate)
PSD	Phase Sensitive Detector
PSU	Power Supply Unit
Re	Reynolds number
RMS	Root Mean Square
SDS	Sodium Dodecyl Sulfate
SHM	Staggered Herringbone Mixer
USB	Universal Serial Bus
UV	Ultraviolet
UV-Vis	Ultraviolet-Visible
WAVE	Water Alignment Vacuum Extraction

Declaration of Authorship

I, Gareth Lyle Jones, declare that the thesis entitled *End-to-End Solutions for a Droplet Microfluidic Autonomous Experimentation System* and the work presented in the thesis are both my own, and have been generated by me as the result of my own original research. I confirm that:

- this work was done wholly or mainly while in candidature for a research degree at this University;
- where any part of this thesis has previously been submitted for a degree or any other qualification at this University or any other institution, this has been clearly stated;
- where I have consulted the published work of others, this is always clearly attributed;
- where I have quoted from the work of others, the source is always given. With the exception of such quotations, this thesis is entirely my own work;
- I have acknowledged all main sources of help;
- where the thesis is based on work done by myself jointly with others, I have made clear exactly what was done by others and what I have contributed myself;
- parts of this work have been published as: (Jones et al., 2012), (Jones et al., 2011), (Jones et al., 2010), (Lovell et al., 2010) and (Lovell et al., 2011)

Signed:.....

Date:.....

Acknowledgements

I would like to thank Klaus-Peter Zauner for introducing me to the fascinating world of unconventional computing. I am grateful for his advice, feedback and patience. I would like to thank Hywel Morgan for generously allowing me use of his labs.

A special thank you is extended to the following people without whom this project would never have been accomplished: Prameen Chacko for staying around after hours and on weekends so that I could work in the lab; Barry Bailey for continually loaning equipment despite often short notice; Lee Onslow and David Kemmish, who handled my numerous purchase orders; Cedric Floquet for use of his measurement equipment; and Tim Forcer for advice on circuit design.

I would like to thank Lianne Niehaus for tolerating my late nights and long working hours. I would like to thank my parents, Andrew and Deneen Jones, and my family for all of their support throughout my University studies. I would like to thank Chris 'Chirs' Lovell for his friendship and for sharing the wrath of our supervisor during our respective PhDs. I would like to thank my friends at home and in the Hybrid Biodevices Group for their encouragement.

I gratefully acknowledge the support from Microsoft Research European in funding this project.

For my late grandfather

Vernon Houston

a man of truly inspirational work ethic and character

Chapter 1

Introduction

Scientific discovery, whether it be in the chemistry laboratory or on the surface of Mars, is ultimately constrained by the availability of experimental resources. Given finite resources there is a requirement for experimental strategies to consider the most effective use of resources; are resources committed to a wide survey or invested in fully characterising one small region of interest? Making a decision from previously collected data is often difficult, particularly when dealing with data that contains nonlinear behaviours that are not easily appreciated. One means by which these issues can be addressed is to utilise an autonomous experimentation approach.

Autonomous experimentation (Plouvier et al., 1992; Du and Lindsey, 2002; Matsumaru et al., 2004) is an approach that uses a system that automatically plans and conducts experiments. An autonomous experimentation system consists of machine learning algorithms that drive experimenting apparatus. Autonomous experimentation can be considered to belong to the field of computational scientific discovery, which is in itself is a branch of artificial intelligence. Early work in computational scientific discovery focused on model scenarios where historic discoveries from several disciplines including biology, chemistry, physics, and mathematics were at first replicated using a variety of computer algorithms (these are reviewed by Langley et al. 1987). The field progressed towards using algorithms to support discovery of new scientific knowledge, mostly through finding patterns in data (Langley, 2000). A recent trend has been towards using the machine learning algorithms to both analyse data and drive the experimentation process (Matsumaru et al., 2002; King et al., 2004; Whelan and King, 2004) in an effort to conduct more effective experiments.

However a major limiting factor to autonomous experimentation systems, particularly in biological and chemistry disciplines, is the experimental apparatus. Taking for example the exploration of the response of a biological system to predetermined chemical environments, the scope for the composition of the chemical environment is large in terms of the number of individual chemicals that could be used and in the potential combinations of chemicals. To achieve the production of complex chemical environments requires that the experimental apparatus be capable of handling numerous chemical inputs. Often researchers are reliant upon existing technology offerings such as the robotic laboratory systems employed by King et al. (2004). Existing systems are unlikely to be a feasible approach for many researches as existing systems are not necessarily, efficient at handling resources, easily integrated, or scalable due to component costs. One technology that has the potential to address these issues specifically in the biological and chemical disciplines is microfluidic technology.

Microfluidic technology enables fluid manipulation at the microscale. Consequently typical fluid volumes can be as low as atto-litres (10^{-18}) (Whitesides, 2006) therefore offering substantial chemical resource savings over conventional macroscale equipment. Multiple laboratory processes can be incorporated into a single microfluidic device no larger than a few centimetres square. The term *lab-on-chip* is used as a general description of such devices. Automated microfluidic devices can be created through utilising microvalves (see Oh and Ahn 2006 for a review) making possible the creation of complex devices such as that shown in Figure 1.1.

The aim of the work documented in this thesis is to investigate microfluidic technology for autonomous experimentation in an effort to address the issues highlighted above. Specifically the objectives of the work are to demonstrate a system that, supports scalability in its design, is capable of automating processes, and is built from technology readily accessible to other researchers.

As a starting point for the work, the problem of investigating the computational properties of enzymes was selected as it is an example of where autonomous experimentation is thought to be particularly useful. The complex functionality of an enzyme can be explored by monitoring the often nonlinear response of an enzyme to chemical signals, such as the addition of ions (Zauner and Conrad, 2001; Matsumaru et al., 2002). From the review on basic enzyme theory in chapter 2, it can be seen that the functions of creating dilutions, mixing, and performing measurements are required to be integrated into the microfluidic device design. It

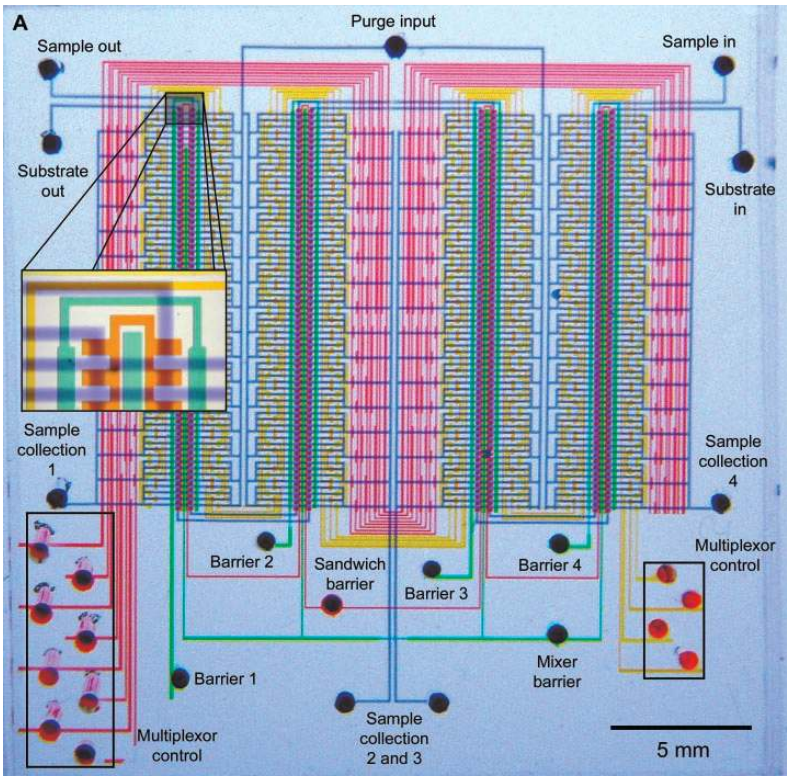

Figure 1.1: A microfluidic comparator used to test bacteria protein expression. Experiments are conducted in parallel. There are 256 reaction chambers and 2056 integrated microvalves. Image modified from (Thorsen et al., 2002)

should be noted that these functions are also common to many other biological and chemical experiments.

Adopting microfluidic technology for autonomous experimentation is challenging with no standardised approach to solving issues such as mixing, dilution, automation, and sensor interfacing, in existence. Consequently as highlighted in Figure 1.2 many different aspects of microfluidic research were covered during this work. While the author had developed a new electrohydraulic interface (appendix E) as well as a new out-of-plane detection channel (appendix F), this thesis concentrates on where the author had advanced the state-of-the-art the most, specifically in fabrication, sensing, automation and design.

Following the conceptual device design in Figure 1.3, integrating the functions of mixing and diluting, as well as providing automated sample handling required the inclusion of on-chip membrane valves (see section 3.4) in the device design. While there are common processes to the fabricating devices containing membrane valves (section 3.5), two issues were encountered. Current fabrication methods reported

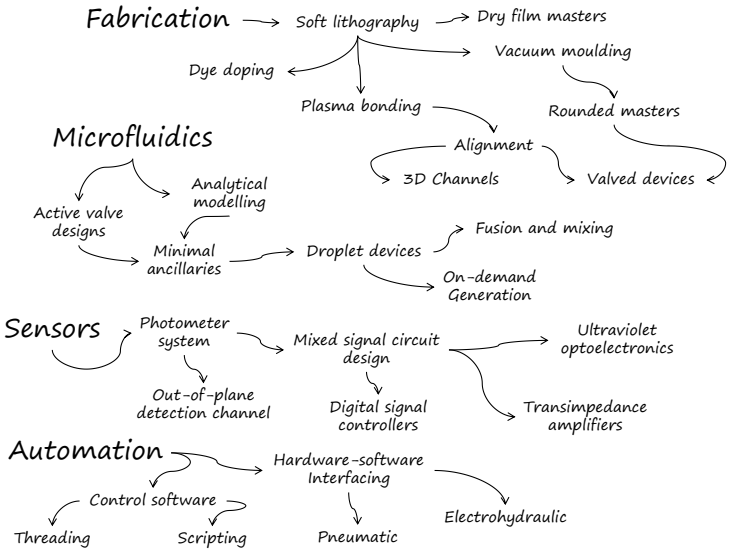

Figure 1.2: A research map summary of the work reported in this thesis.

in the literature tend to rely upon cleanroom environments, sophisticated equipment and costly materials. In chapter 4 it is demonstrated that valved technology can be implemented using alternate materials and fabrication techniques suitable for a standard chemistry laboratory, thus improving the accessibility to valved technology. Second the bonding and alignment of multiple device layers to create three-dimensional microfluidic devices is problematic. Although there are many potential solutions in the literature, not one solution is sufficiently reliable to become the standard approach. Using water as a lubricant as a potential solution to alignment and bonding is explored in detail in chapter 5, and it is found that by appropriate modification of the alignment and bonding process, reliable bonding and accurate alignment can be achieved, which is crucial in the production of valved devices.

Before designing and implementing a particular microfluidic design, consideration has to be given to the physics of fluids at the microscale. In chapter 3 it will be seen that fluid behaviour at the microscale is easily more predictable and linear in nature than what is normally experienced at the macroscale. This allows for microfluidic networks to be treated in analogous fashion to electrically resistive networks thus simplifying the design of device functionality, and it is the same approach that was used to ensure scalability in the device design in chapter 7.

The linear nature of microscale flow however, poses a significant problem to the mixing of fluids. Chaotic flow, which is largely missing from microscale flow, is required for rapid mixing. There is no general solution to improve mixing

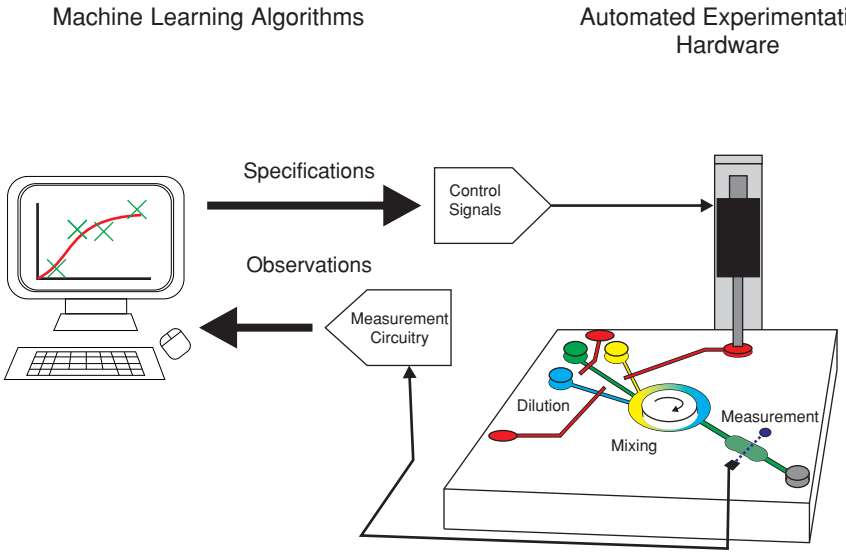

Figure 1.3: Conceptual design of the autonomous experimentation system. Machine learning algorithms drive the automated experimentation platform based on observations made from past experiments. In the context of enzyme assays the functions, dilution, mixing and measurement are required on a microfluidic chip.

times in microfluidic devices and as such there exist numerous passive and active methods in the literature, several of which are reviewed in section 3.2. Particularly interesting are the mixing methods available in the droplet microfluidics approach (section 3.3), where discrete aqueous samples are suspended as droplets in a bulk organic flow. Rapid mixing can be achieved far more simply with droplets than in microfluidic devices that manipulate solely aqueous flows.

A droplet microfluidics approach to the design of the microfluidic device was chosen as it was also the most appropriate means to obtaining dilution functionality. However mixing in droplets was actually found to be particularly difficult, particularly when sample volumes were increased to obtain a wider range of dilutions. Both passive (appendix D.3) and active mixer designs were trialled in this work, with the mixing problem overcome by using the novel active mixing solution presented in chapter 7.

In the context of the autonomous experimentation system (Figure 1.3), the UV photometer provides the machine learning algorithms the necessary capability to observe experiments in order to drive the automated hardware. Chapter 6 documents the development of a photometer system suitable for spectroscopic monitoring (c.f. chapter 2) of enzyme reactions. The photometer system features ultraviolet optical semiconductor components, that are low-cost yet offer

sufficient performance to enable the system to be comparable to a commercial spectrophotometer.

As shown in the conclusions (chapter 8), the aims of demonstrating a system that, supports scalability in its design, is capable of automating processes, and is built from technology readily accessible to other researchers, has been achieved. Consequently the previous limits of the experimental apparatus specifically for chemical and biological studies, have now been overcome. Machine learning algorithms for autonomous experimentation are no longer constrained to working with just a few experimental variables.

Chapter 2

Theory: Enzymes

This chapter describes basic enzyme theory and forms part of the background to this thesis. The topics covered include, enzyme structure, function, kinetics, factors affecting enzyme catalysis, and the absorption spectroscopy method to monitoring enzymatic catalysed reactions. It will be seen that enzymes are complex molecules with a functionality that is capable of being modulated by many factors.

2.1 Enzyme structure

The building blocks of enzymes are amino acid molecules. There are twenty different types of amino acid common to all enzymes. As seen from Figure 2.1a, amino acids have a general structure that consists of an amine group (NH_2) covalently bonded to a carbon atom (α carbon), which in turn is covalently bonded to a carboxyl group (COOH). Side chain groups covalently bond to the α carbon and it is from the composition of the side chain groups of an amino acid (denoted R), distinctions between amino acids are made. The side chains vary both physically (e.g. mass and length) and chemically. The side chains can be polar either exhibiting either positive, negative or neutral charge, or they can be non-polar. Amino acids covalently bond together via a condensation reaction between the carboxyl group of amino acid and amine group of another amino acid. The bond between amino acids is referred to as a peptide bond. Ribosomes synthesize the peptide bonds between amino acids allowing for polymer chains to be constructed. The polymer chains of amino acids are referred to as polypeptides. Each polypeptide chain contains a free amine group and a free carboxyl group,

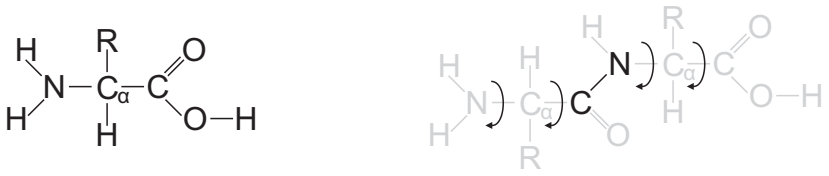

(a) (b)

Figure 2.1: The building blocks of an enzyme are the amino acids. The general structure of an α amino acid molecule (a). The central carbon atom, conventionally known as the α carbon, is covalently bonded to an amine group (left) and a carboxyl group (right). The R represents a side chain. Two amino acids form a peptide bond (C-N) through a condensation reaction (b). The peptide bond provides structural rigidity, while the N-C_α and C_α-N bonds are free to rotate.

referred to as the N-terminus and C-terminus respectively. The sequence of amino acids within a polypeptide chain is specific, which gives an enzyme its unique properties. The sequence of amino acids within a polypeptide chain is referred to as the primary structure of an enzyme. Enzymes can contain one or more polypeptide chains in their structure. A enzyme containing only one chain is referred to as monomeric, while an enzyme containing multiple polypeptide chains is referred to as oligomeric (Nelson and Cox, 2005).

The peptide bond between amino acids has partial double bond character, which restricts rotation between the amino acids. However the N-C_α and C_α-N bonds are free to rotate. This allows for the amide (N-H) and carboxyl (C=O) groups between different amino acids to interact and form hydrogen bonds. Given favourable structural (steric) arrangements and environmental conditions, the hydrogen bonding causes a polypeptide chain to distort and fold yielding characteristic three-dimensional structures. These folded structures are referred to as the secondary structures of an enzyme and can be further stabilised by disulphide bonds forming between Cysteine amino acids. Common forms of secondary structure are α helices, β conformations and β turns, two examples are shown in Figure 2.2.

α helices resemble a spring with the amino acid sidegroups oriented outwards from the centre of the structure. They are rigid and insoluble compared to β conformations, which are soft and flexible. β conformations take on a planar form, from which they too orient their amino acid sidegroups outwards away from the plane on both sides. The planar form can resemble a pleated sheet or instead take

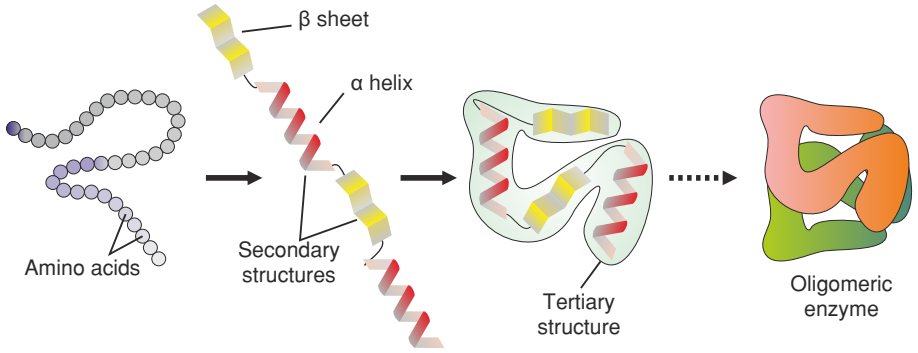

Figure 2.2: Structural elements of an enzyme. The primary structure (left) is formed by the sequence of amino acids, which bond yielding polypeptide chains. With interactions between the individual amino acids, a chain folds into characteristic three-dimensional secondary structures. The secondary structures continue to fold and stack into a functional tertiary structure. An enzyme may consist of multiple subunits that are not necessarily alike.

on the form of loops or turns. The loops and turns allow for a folded polypeptide chain to be stacked resulting in an overall compact three-dimensional shape or subunit referred to as the tertiary structure of an enzyme (Nelson and Cox, 2005).

Within the tertiary structure hydrophobic amino acid side chains orient themselves towards the interior of the structure forming a distinctive cleft or pocket. The cleft or pocket is called the active site and is where reactions are catalysed. The arrangement of the amino acid sidegroups within the active site provides the enzyme with the feature of specificity. Enzymes are capable of discriminating between molecules based on a the combination of shape, charge, and hydrophobic/hydrophilic characteristics. The specificity of an enzyme can be absolute, therefore only catalysing the reaction of one particular substrate molecule. Or the specificity of an enzyme can be group specific, where several different but closely related substrate molecules can be catalysed by the same enzyme. Multiple folded polypeptide chains (or subunits) can link together through non-covalent interactions forming an overall quarternary structure. Linked subunits can be identical or different, and can provide either regulatory or catalytic functions. Next the enzyme catalytic process is discussed.

2.2 Enzyme catalysis

Consider a reactant (or substrate) S that proceeds in a spontaneous (δG $<$ 0) chemical reaction to transform into a product P, represented graphically in Figure 2.3. Energy is required in the transformation of the reactant to product. The energy requirement increases and peaks as the reaction progresses. At the peak, which is known as the transition state, the substrate exists in a different unstable chemical form that is equally likely to yield a product or return back towards its original form. The energy required to reach the transition state of a molecule is known as the activation energy (G‡). By exceeding the activation energy product molecules are formed (Palmer, 1981).

Large activation energy peaks indicate a greater energy requirement to obtain a product molecule, and therefore a slower reaction. The rate of a reaction can be increased by either supplying more energy to the reactant molecules (e.g. through heating) or by using catalysts. A catalyst lowers the activation energy of a reaction. Therefore at an equivalent temperature, a catalysed reaction proceeds more quickly than the same uncatalysed reaction. In an enzyme-catalysed reaction, catalysis takes place when the enzyme and substrate molecule bind and form an enzyme-substrate (ES) complex. Within the ES complex a number of catalytic mechanisms can take effect. The catalytic mechanism include: general acid-base catalysis, covalent catalysis, metal ion catalysis and non-covalent interactions such as proximity and orientation effects (Nelson and Cox, 2005).

In general acid-base catalysis protons are removed and supplied to a substrate, which allows for the transition state to be stabilised and thus increasing the likelihood of product formation. Amino acids in the active site with sidegroups that act as proton donors or acceptors participate in general acid-base catalysis. Example amino acids that participate in general-acid base catalysis include: Arginine, Tyrosine and Cysteine.

In covalent catalysis, an amino acid within the active site containing a nucleophilic group donates an electron pair to an electrophilic chemical species in the substrate. This results in a covalent bond forming between amino acid residue and substrate. The covalent bond acts to stabilise the transition state and therefore increase the likelihood of product formation. Amino acids that participate in covalent catalysis include: Lysine, Serine and Aspartic acid. Before a product is released from the enzyme, the covalent bond is broken returning the enzyme to its original form.

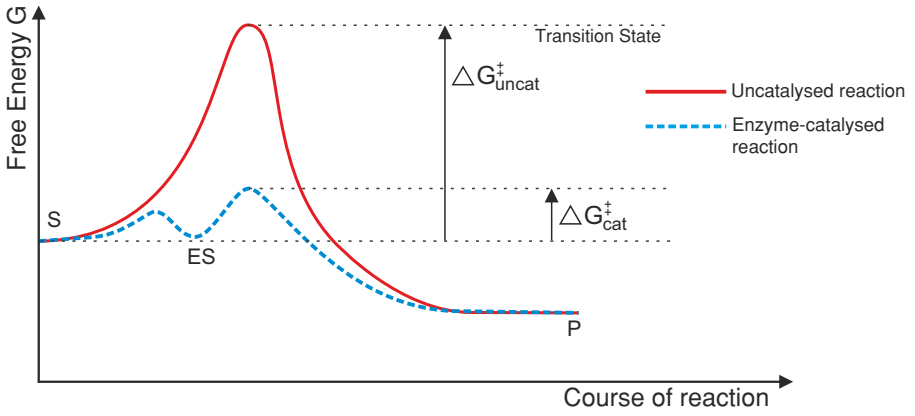

Figure 2.3: Reaction coordinate example of an uncatalysed (upper curve) and an enzyme-catalysed (lower curve) reaction. The reaction begins at the substrate (S) and progresses towards the product (P). In the uncatalysed case there is a large energy barrier known as the transition state that requires a certain amount of activation energy $G^{\ddagger}$. Using a catalyst such as enzyme lowers the activation energy required and speeds up the reaction. The enzyme is not used up in catalysis and may in some cases catalyse the reverse reaction from P to S.

Metal ion cofactors can either be tightly bound to an enzyme or taken up from solution. Metal ions can participate either in a catalytic role or structural role. Those that participate in catalysis tend to be tightly bound to an enzyme, examples include: Fe_2^+, Fe_3^+, Cu_2^+, Mn_2^+ and Co_2^+. In catalysis, metal ions can form ionic bonds with, and therefore stabilise, a negatively charged intermediate molecule. Metal ions that have a structural role such as, Na_2^+, K^+ and Ca_2^+, can activate an enzyme by modifying its structure. Similarly metal ions can also reduce enzymatic activity as will be discussed later. Ions such as Mg_2^+ and Zn_2^+ can be found participating in both catalytic and structural roles.

Additional molecules other than the metal ion cofactors are required by some enzymes for catalysis. These can exist in the form of complex organic or metalloorganic molecules known as a coenzymes, which as in the case of pyridoxal phosphate act as transient carriers of specific functional groups.

Non-covalent interactions include electrostatic interactions (i.e. forces between ions) and van der Waals interactions (i.e. forces between dipoles). These are relatively weak when compared individually to covalent interactions (Berg et al., 2002). In combination the non-covalent interactions assist with stabilising the transition state and therefore lower activation energy. The enzyme is capable of arranging itself around a substrate therefore promoting interactions between it and

the substrate. This is known as induced fit and can either involve small movements near the active site or the movement of entire domains (Nelson and Cox, 2005).

Both covalent and non-covalent interactions can be found working in concert during catalysis hence why enzymes are such effective catalysts. There are however a number of factors that can interrupt these mechanisms and slow down catalysis. Investigating the effect of these factors is achieved through kinetic studies.

2.3 Enzyme kinetics

Enzyme concentration, substrate concentration, the presence of inhibitor and activator molecules, temperature, pressure and pH all have an effect on enzyme catalysis. The rate constant (or turnover number) of an enzyme is used as a measure of the rate (velocity) of a reaction. The discussion starts with the Michaelis-Menten model.

2.3.1 The Michaelis-Menten model

A frequently used model to describe the kinetics of an enzymatic reaction with change in substrate concentration is the Michaelis-Menten model (Tipton, 2002). This model assumes simple kinetics with the following to be taken into account in its use,

- The reaction has only one substrate
- The molar concentration of the substrate is much higher than that of the enzyme
- The initial reaction rate is considered when the product concentration is so low that the reverse reaction is negligible

The Michaelis-Menten model is described mathematically:

$$V_o = \frac{V_{max}[S]}{K_m + [S]} \tag{2.1}$$

where K_m is the Michaelis constant specific to the enzyme, $[12S]$ the substrate concentration in Moles, V_o the velocity of the reaction and V_{max} the maximum

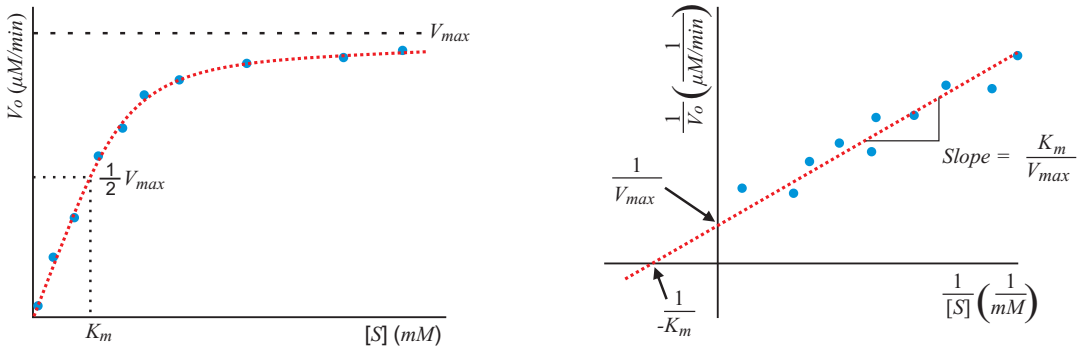

(a) (b)

Figure 2.4: Typical enzyme kinetic plots. A Michaelis-Menten plot is shown in (a) and a Lineweaver-Burke plot is shown in (b).

velocity of the reaction. The Michaelis-Menten equation yields a hyperbolic plot (see Figure 2.4a) of initial velocity vs substrate concentration. K_m is equal to one-half the theoretical maximum velocity V_{max}. A small value of K_m therefore indicates an enzyme that only requires a small concentration of substrate to achieve maximum velocity. Likewise a large value of K_m indicates an enzyme that requires a large concentration of substrate to achieve maximum velocity. V_{max} and hence K_m are difficult to determine from the Michaelis-Menten plot. By inverting the Michaelis-Menten equation, a double-reciprocal, Lineweaver-Burk plot (see Figure 2.4b) can be constructed from which K_m and V_{max} can be determined graphically. Knowing V_{max} the rate constant of the enzymatic reaction, k_{cat} can be found by dividing V_{max} by the enzyme concentration. The constants k_{cat} and K_m by themselves provide little information when comparing different enzymes. For example two enzymes that catalyse different reactions may have the same values of k_{cat} but not K_m. To compare the efficiency of enzymes the specificity constant (the ratio of k_{cat} to K_m) is often used (Tipton, 2002).

The Michaelis-Menten model does not describe the behaviour of all enzymes. However the parameters V_{max} and K_m are still used in their comparison. Deviations from Michaelis-Menten behaviour are considered next beginning with allosteric enzymes.

2.3.2 Allosteric enzymes

Allosteric enzymes do not follow Michaelis-Menten kinetics. Plotting the reaction velocity against substrate concentration for an allosteric enzyme generally yields a

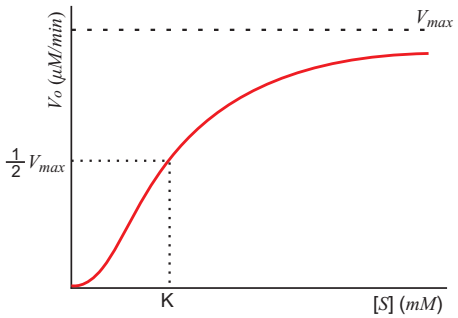

Figure 2.5: A typical response of an allosteric enzyme to increasing substrate concentration.

sigmoidal curve (Figure 2.5) rather than the Michaelis-Menten hyperbolic curve. The quarternary structure of allosteric enzymes tend to consist of several subunits with multiple active sites (allosteric sites) in addition to a main active site. Small molecules (effectors) bind to the allosteric sites altering the quarternary structure of an enzyme and therefore causing it to become either more or less catalytically active. The effectors may be the substrate itself in which case they are called homotropic effectors, or some other small molecules in which case they are called heterotropic effectors. Homotropic effectors tend to interact cooperatively with the binding of one molecule enhancing the binding of additional molecules. Heterotropic effectors are often end products from a metabolic pathway that tend to inhibit enzyme activity thus providing a means of feedback inhibition or regulation (Nelson and Cox, 2005).

2.3.3 Inhibition

Enzyme catalysis can be slowed or halted by molecules known as inhibitors. There are two broad categories of enzyme inhibitors: (1) irreversible where the enzyme is completely inactivated, and (2) reversible where the enzyme activity is slowed. Reversible inhibitors can act in one of four different ways: (i) competitive, (ii) uncompetitive, (iii) mixed, and (iv) non-competitive (Nelson and Cox, 2005).

Competitive inhibitors compete with the substrate for the enzyme active site. Structurally competitive inhibitors are similar to the substrates with which they are competing. Competitive inhibition results in a lower K_m value while V_{max} remains unaffected. This type of inhibition can be overcome through increasing substrate concentration. Uncompetitive inhibitors bind only to an enzyme-substrate complex at a site distinct to the active site. Uncompetitive inhibitors

reduce the speed at which products are released from an enzyme therefore resulting in lower K_m and V_{max} values. In mixed inhibition an inhibitor binds either to an enzyme or enzyme-substrate complex. As in uncompetitive inhibition, the inhibitors bind at a site distinct to the active site. The effect of mixed inhibition is to lower both K_m and V_{max} values. Non-competitive inhibition is a form of mixed inhibition, but instead only K_m is affected (Nelson and Cox, 2005).

Example inhibitors include, the products of an enzymatic reaction which gives rise to negative feedback control. This is known as product inhibition and is usually competitive with respect to one of the substrates of the reaction. Another example is substrate inhibition where the velocity of the reaction decreases at high substrate concentrations. Substrate inhibition may indicate the existence of two substrate binding sites on the enzyme. This again allows for negative feedback control. In addition to inhibitor molecules there are also physical and chemical factors that are capable of affecting enzymatic activity (Nelson and Cox, 2005).

2.3.4 Physical and other chemical factors that affect structure

Enzyme activity is affected by physical factors such as pressure, temperature and chemical factors such as, pH and ionic strength. Pressure affects the overall volume of an enzyme and when increased brings subunits closer together. This has been found to have both activating and inhibitory effects (Ohmae et al., 2007).

A typical response of an enzyme to increasing temperature is shown in Figure 2.6a. The effect of raising temperature will speed up reactions as the increased thermal energy drives collisions between molecules. However given a sufficient increase in temperature, hydrogen bonds are sufficiently agitated to become disrupted leading to denaturing of an enzyme. Once denatured enzyme catalytic activity is lost (Nelson and Cox, 2005).

The ionic composition of the solution in which an enzyme resides affects the conformation of the enzyme. Specifically pH changes ionise the amino acid residues of an enzyme and can lead to the disruption of hydrogen bonds. As a result the enzyme structure becomes destabilised and eventually denatures if pH is adjusted beyond the optimal range for an enzyme (Figure 2.6b). Salt ionises amino acids and affects the solubility of an enzyme. The solubility of enzyme can be enhanced (salting-in) by adding salt, in which case the salt acts to increase the interactions

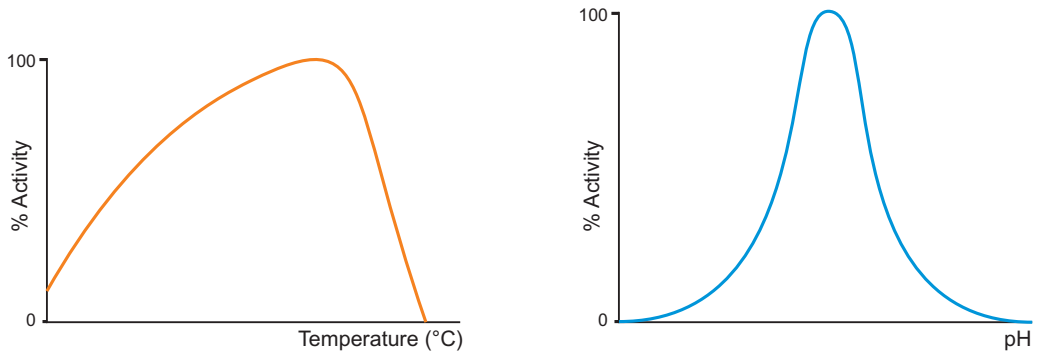

(a) (b)

Figure 2.6: The effects of temperature and pH on catalytic activity. The rate of the reaction increases with increasing temperature as more energy is provided to the system. Given sufficient heating, the enzyme succumbs to thermal agitation and denatures (a). Adjusting the pH to either side of an optimal pH range will ionise amino acid sidegroups, resulting in increases or decreases in enzyme catalytic activity (b).

between water and enzymes. Sufficiently high salt concentrations added to the solution will interfere with the interactions between water and enzyme, resulting in the enzyme being precipitated from solution (salting-out) (Stevens, 1989).

2.4 Absorption spectroscopy

Measuring the rate of product formation from an enzymatic assay can either be performed directly or indirectly. Direct measurements are obtained by measuring the concentration of a molecule that participates in the enzyme catalysed reaction. Indirect measurements are obtained by measuring the concentration of another chemical species that forms on reacting with a product of the enzyme catalysed reaction. Measuring the concentration can be achieved using absorption spectroscopy. The underlying principle is that molecules absorb light at distinct wavelengths. Increasing concentrations of a light absorbing molecule will result in increased light absorbance. This is described by the Beer-Lambert law (Jaffé and Orchin, 1962; Pavia et al., 2001):

$$A = \varepsilon \cdot c \cdot l \tag{2.2}$$

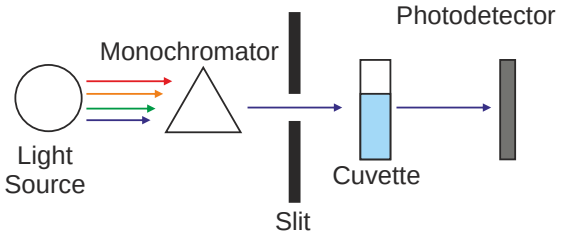

Figure 2.7: Basic components used in a spectrophotometer

where A is the absorbance in dimensionless units, ε is the molar extinction coefficient ($l\ mol^{-1}\ cm^{-1}$) of the absorbing species, c is the concentration of that species and l is the path length of the sample. The molar extinction coefficient varies from species to species and is a function of wavelength. Absorbance is defined as:

$$A = -log_{10}\left(\frac{I}{I_0}\right) \tag{2.3}$$

where I_0 is the light transmitted by solution in absence of the absorbing species (i.e. before the reaction) and I is the light transmitted by solution in presence of the absorbing species (i.e. during the reaction). Through rearrangement of equations 2.2 and 2.3, setting the path length to 1 cm, the concentration of the absorbing species can be obtained:

$$c = \frac{A}{\varepsilon} \tag{2.4}$$

Recording these measurements is achieved by using an instrument known as a spectrophotometer. Four essential components comprise a spectrophotometer (Figure 2.7), a light source, a monochromator, the absorption cell assembly, and the photometer.

Summarised in Table 2.1 are data from enzymatic computing studies reported in the literature. The data collated from studies that used absorption spectroscopy as the measurement method. The study reported by Zauner and Conrad (2001) (first line of the table) serves as a starting point for development of the autonomous experimentation system described in this thesis.

Table 2.1: Enzymatic computers

Enzyme	E.C. Number	Substrate	Input Signals	Measurement Species	Measurement Wavelength	Measurement Time	Functions	Reference
MDH	1.1.1.37	L-malate	Ca_2^+, Mg_2^+	NADH	339 nm	5 min. 10 s	AND OR NOR NAND NXOR XOR	Zauner and Conrad (2001)
GDH coupled to HRP	1.1.1.47 1.11.1.7	Glucose H_2O_2	Glucose H_2O_2	NADH Hydroxamate– Fe(III)	340 nm 500 nm	20 min. 5 min.	inhibAND AND	Baron et al. (2006c)
All in series AChE ChOx MP-11 coupled to GDH	 3.1.1.7 1.1.3.17 1.1.1.47	 Acetylcholine Butyrylcholine Choline H_2O_2 Glucose	 Acetylcholine Butyrylcholine O_2 Glucose	 - - - NADH	 - - - - 340 nm	 - - - 20 min.	 OR AND XOR	Niazov et al. (2006)
GDH coupled to HRP	1.1.1.47 1.11.1.7	Glucose H_2O_2	Glucose H_2O_2	NADH	340 nm	20 min.	Inhibit A Inhibit B XOR	Baron et al. (2006b,a)
GOx coupled to Cat	1.1.3.4 1.11.1.6	Glucose H_2O_2	Glucose H_2O_2	Hydroxamate– Fe(III)	500 nm	20 min.	AND	
GOx coupled to HRP	1.1.3.4 1.11.1.7	Glucose H_2O_2	Glucose H_2O_2	NADH	340 nm	20 min.	OR	
GOx coupled to FDH	1.1.3.4 1.2.1.46	Glucose Formaldehyde	Glucose H_2O_2	NADH	340 nm	20 min.	NOR	
FDH	1.2.1.46	Formaldehyde	H_2O_2	NADH	340 nm	20 min.	NOT	
GOx	1.1.3.4	Glucose	Glucose	Hydroxamate– Fe(III)	500 nm	20 min.	Identity	
GDH coupled to HRP in parallel GOx coupled to Cat	1.1.1.47 1.11.1.7 1.1.3.4 1.11.1.6	Glucose H_2O_2 Gluconic Acid H_2O_2	Glucose H_2O_2	NADH Hydroxamate– Fe(III)	340 nm 500 nm	10 min. 5 min.	Half Adder (XOR in parallel to AND)	Baron et al. (2006a)

Chapter 3

Theory: Microfluidics

This chapter discusses basic microfluidic theory and reviews the microfluidic literature. Topics covered include, microfluidic flow, mixing, droplets, automation, and fabrication. The information contained within this chapter serves as background to the work reported in chapters 4, 5 and 7.

3.1 Laminar flow

The behaviour of fluids flowing in microscale channels is markedly different to the familiar behaviour of fluids at the macroscale. At the macroscale, fluids tend to flow turbulently and mix readily whereas microscale flows do not. This difference arises from a shift in the competition between the inertial and viscous forces that act on a flowing fluid. This competition is represented by the dimensionless Reynolds number (Re):

$$Re = \frac{Inertial\ Forces}{Viscous\ Forces} = \frac{\rho U D_H}{\eta} = \frac{U D_H}{\nu} = \frac{Q D_H}{\nu A} \tag{3.1}$$

where ρ is the fluid density, U the mean flow velocity, η the absolute (or dynamic) viscosity, D_H the characteristic length scale of the system (sometimes hydraulic diameter is used (Stone et al., 2004); equal to 4 $\times$ cross-sectional area divided by wetted perimeter), ν the kinematic viscosity, Q the volumetric flow rate and A the cross-sectional area. As Equation 3.1 indicates, decreasing channel dimensions or reducing the average flow velocity will result in a lower Reynolds number.

Typically systems exhibiting Re less than 2300 are considered to be laminar (Beebe et al., 2002) despite non-linearities in the flow present from $Re \geq 1$.

Because of the linear and predictable nature of laminar flow, under particular conditions it has been possible in the design process to treat microfluidic networks as analogous to electrical resistive networks. This in turn has allowed for the creation of microfluidic devices containing passive fluidic networks capable of producing chemical concentration gradients (Jeon et al., 2000), linear (Walker et al., 2007) and/or logarithmic (Kim et al., 2006b, 2008) dilutions. The conditions necessary to obtaining electrically equivalent models of microfluidic channels begin with the Navier-Stokes equations.

3.1.1 Electrical equivalence model

The nonlinear partial differential Navier-Stokes equations describe the motion of fluids. In the case of an incompressible fluid driven through a microchannel by an externally applied pressure with characteristic laminar flow, the Navier-Stokes equations can be solved to relate the pressure-drop along the channel to the velocity field of the fluid. By integrating the velocity field of the fluid over a cross-section of the channel, the volumetric flow rate Q can be determined. If the flow is laminar, the Hagen-Poisseuille law can then be applied and thus the volumetric flow rate Q can be related to the pressure drop ΔP by way of a fluidic resistance term R. Thus an electrically equivalent model can be obtained. As an example of this process, first consider the Navier-Stokes equations:

$$\underbrace{\rho\left[\frac{\partial \mathbf{u}}{\partial t} + (\mathbf{u}\cdot\nabla)\mathbf{u}\right]}_{\textbf{inertia}} = -\nabla p + \underbrace{\eta\nabla^2\mathbf{u}}_{\textbf{viscosity}} + \mathbf{f} \tag{3.2}$$

with ρ the density of the fluid, $\mathbf{u}$ the velocity field of the fluid, $\mathbf{f}$ the body force and ∇p representing the pressure drop along the channel. From the left-hand side of Equation 3.2 there are two acceleration terms. The first temporal acceleration term, $\frac{\partial \mathbf{u}}{\partial t}$, arises from time-varying flow. The second nonlinear convective acceleration term, $(\mathbf{u}\cdot\nabla)\mathbf{u}$, arises from changes in velocity with position such as experienced in diffusers or nozzles. On the right-hand side of Equation 3.2 the three terms represent stresses arising from application of external pressure, viscosity (friction) and body force (gravity or electric forces).

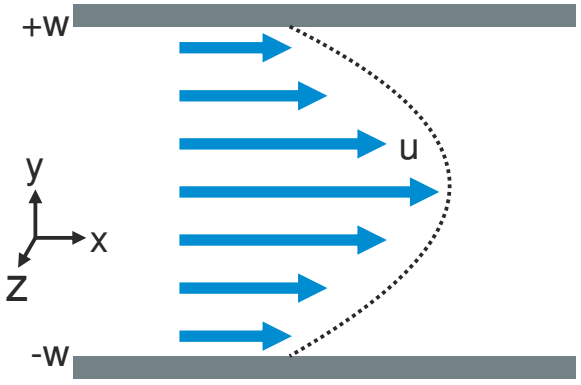

Figure 3.1: Parabolic fluid velocity profile across the y-axis of a microchannel arising from the flow in the x-direction.

Given a flow with a low Reynolds number, viscosity dominates and the inertial terms above can be considered negligible. Assuming an insignificant effect from body forces, Equation 3.2 simplifies to the Stokes equations:

$$\nabla p = \eta \nabla^2 \mathbf{u} \tag{3.3}$$

yielding the relationship between pressure and viscosity. If the fluid is treated as flowing along the channel length (x-axis) only and velocity varying in one-dimension across the channel (y-axis) as depicted in Figure 3.1, Equation 3.3 becomes:

$$\frac{\partial^2 u_x}{\partial y^2} = \frac{-\Delta p}{\eta L} \tag{3.4}$$

with Δp the pressure drop along the channel and L the length of the channel. The velocity profile can then be derived through integration and application of the no-slip boundary condition, i.e. the fluid velocity is zero at the channel walls (when y = $\pm$w):

$$u_x = \frac{\Delta p}{2\eta L}(w^2 - y^2) \tag{3.5}$$

which gives the parabolic flow profile depicted in Figure 3.1. The volumetric flow rate (Q) can then obtained by integrating the velocity over the cross-section (between +w and -w),

$$Q = \int_{-w}^{+w} u_x dy = \frac{2d^3}{3\eta L}\Delta p \tag{3.6}$$

From the Hagen–Poiseuille law the reciprocal of $\frac{2d^3}{3\eta L}$ is called the fluidic resistance R, which makes Equation 3.6 analogous to Ohm's law. It must be noted that the Hagen–Poiseuille law holds true when the flow is laminar, deviations can be expected if the flow is turbulent and non-linear.

The one-dimension example described here is a simple illustration. A more realistic scenario is to consider the flow velocity varying in two-dimensions along both the y and z-axes. The fluidic resistance for two-dimensional flow can be obtained from the analytical solution reported by Kovacs (1998) for channels of width w, height h and length L:

$$R = \frac{12\eta L}{wh^3}\left[1 - \frac{h}{w}\Big(\frac{192}{\pi^5}\sum_{n\,=\,1,3,5}^{\infty}\frac{1}{n^5}\tanh(\frac{n\pi w}{2h})\Big)\right]^{-1} \tag{3.7}$$

which for square cross-sections of side a approximates to:

$$R = \frac{28.545\eta L}{a^4} \tag{3.8}$$

or rectangular cross-sections with high-aspect ratios ($w \gg h$) approximates to:

$$R = \frac{12\eta L}{wh^3} \tag{3.9}$$

By fixing the channel width and height, it is then possible to create channels of lengths proportional to their fluidic resistances. Therefore as illustrated in Figure 3.2 networks of varying resistances can be created that divide fluid flow accordingly to allow for in this case, gradient generation devices.

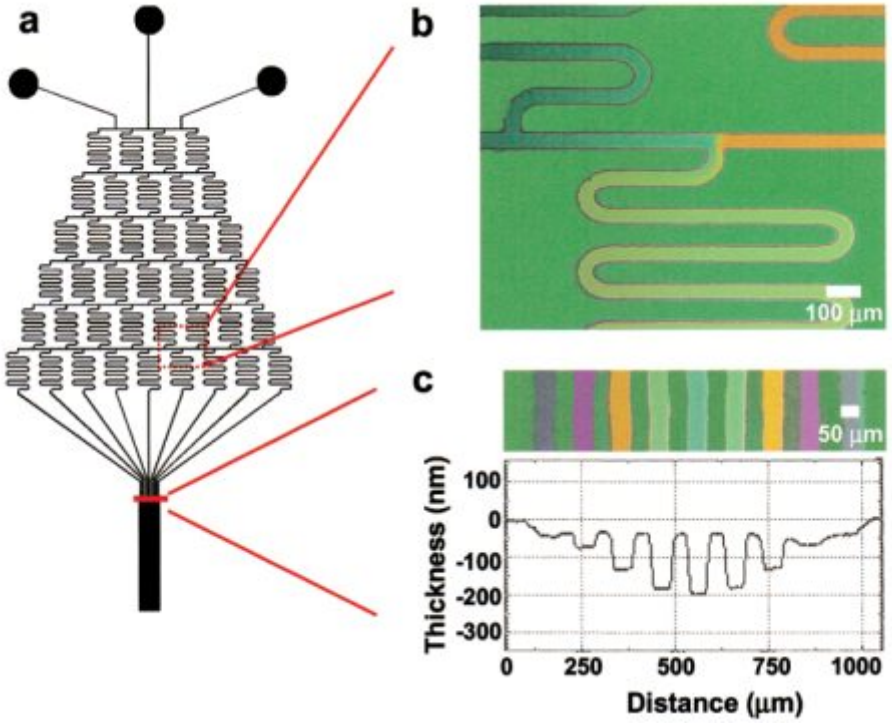

Figure 3.2: Chemical gradient generator. The gradient generator device design (left) is obtained from an electrical equivalence model. The microfluidic device sits on top of a SiO_2 coated silicon wafer. Hydrogen fluoride (HF) 5% in water is flowed through one input of the gradient generator, and water through the other. The different concentrations of HF in the microfluidic device result in the oxide film being etched at different depths. The colour of the oxide film changes with etch depth and therefore indicates the concentration of HF (right). Image reproduced from (Jeon et al., 2000).

3.2 Mixing

3.2.1 Diffusion and convection

Mixing on both the macro and microscale ultimately relies upon molecular diffusion, but the time required for complete mixing can be significantly longer at the microscale. An explanation for this begins with considering Fick's first law of diffusion, where the diffusion flux J is a product of the diffusion coefficient D of a molecule and concentration gradient over a distance $\frac{\partial \phi}{\partial x}$:

$$J = -D\frac{\partial \phi}{\partial x} \tag{3.10}$$

The change in the concentration of molecules in time (t) is described by Fick's second law, which in one dimension (x) is (Geschke et al. 2004):

$$\frac{\partial \phi}{\partial x} = D\frac{\partial^2 \phi}{\partial x^2} \tag{3.11}$$

Solving Equation 3.11 yields the average diffusion time (t) for a molecule over distance (x) as (Beebe et al. 2002):

$$t = \frac{x^2}{2D} \tag{3.12}$$

It can be seen that the time taken for a molecule to diffuse is approximately dependent on the square power of distance to be travelled. On the macroscale the diffusion distances are reduced as the distribution of molecules is subjected to varying pressure and velocity fields, which are more extreme when the flow is turbulent. In microfluidic devices the flow is laminar, which yields relatively fixed diffusion distances and thus mixing is time-consuming. For example the enzyme malate dehydrogenase (MDH) has a diffusion coefficient of 6.45×10^{-7} cm^2/s (Englard and Siegel, 1969) or 64.5 μm^2/s. From Equation 3.12 to diffuse across a microchannel of width 200 μm starting from oneside would take the enzyme approximately 310 s.

Above the fluid was considered as motionless. If the fluid is flowing, the molecules within the fluid will also experience transport (convection) along the direction of the flow in addition to diffusion (see Figure 3.3). The convection has little impact

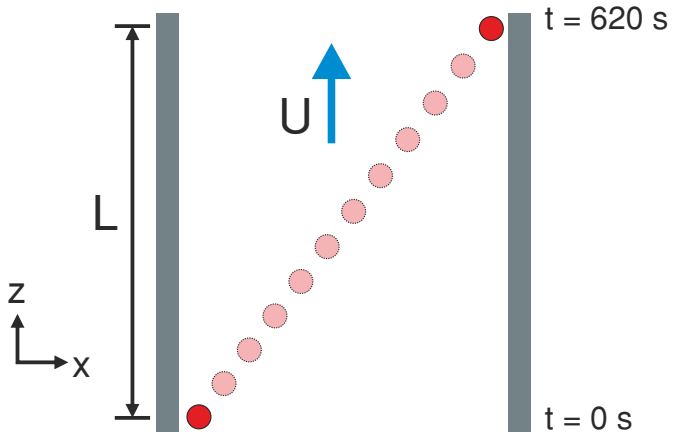

Figure 3.3: Molecules in a channel are subjected to a flow (U) in the z-axis direction. Complete mixing occurs further downstream at distance L.

on the mixing time but a certain channel length L is then required to obtain complete mixing. This is calculated from:

$$L \approx \frac{Uw^2}{D} \tag{3.13}$$

where U is the mean flow velocity. Given the same enzyme and channel width parameters used above, and a mean flow velocity U of 100 μm/s, from Equation 3.13 the required channel length is approximated to be 6.2 cm. An alternate method to estimating the channel length can be found in using the dimensionless Péclet number (Pe), which relates the rate of convection of a flow to its rate of diffusion (Squires and Quake, 2005). The Péclet number is defined as:

$$Pe = \frac{Uw}{D} \tag{3.14}$$

with Pe = 310 for the same values used previously. Taking the Pe and multiplying it by the channel width, here 200 μm, an estimate of the channel length can be obtained, 6.2 cm as before. Reflecting on Equations and 3.6–3.9 it is important to remember that the channel length is proportional to the fluidic resistance. Consequently the channel length required to achieve complete mixing in some cases may impose pressure requirements too large to practically implement. In addition to estimating the channel length required for complete mixing, the Péclet number can also provide an indication of whether the phenomena known as Taylor dispersion may be observed.

3.2.2 Taylor Dispersion

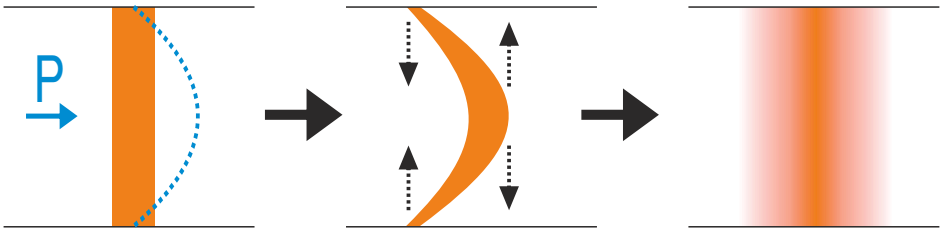

Figure 3.4: Taylor dispersion. A homogeneous plug of molecules is stretched axially due to the pressure driven flow. Because the flow is pressure driven, the plug takes on a parabolic profile that through diffusion becomes smeared into a wider plug.

Following Figure 3.4 a microchannel contains a fluid with a plug of molecules homogeneously distributed across the width of the channel (i.e. completely mixed). The fluid is pressurised and flows with a parabolic flow profile. The parabolic flow profile causes the convective stretching of the molecules in the direction of the flow, which results in concentration gradients at both the front and rear of the stretched plug. Diffusion set-up by the concentration gradient acts to smear the parabolic plug into a plug wider than before. Thus the plug cannot stretch indefinitely. This process is repeated continually resulting in a plug with a longitudinal concentration profile following a Gaussian distribution. This process of molecules diffusing axially in the direction of the flow is known as Taylor dispersion and is described by an associated diffusivity: D_z (Squires and Quake, 2005):

$$D_z \approx \frac{U^2 w^2}{D} \approx Pe^2 \cdot D \tag{3.15}$$

where U is the flow velocity, w the channel width and D the diffusion coefficient of the molecular species. Taylor dispersion occurs only when molecules have completely mixed across the width of a microchannel. This corresponds to a time scale $t \gg \frac{w^2}{D}$ or a downstream distance of $L \gg Pe{\cdot}w$ - from the previous examples above, 620 s and 6.2 cm respectively. The effect of Taylor dispersion can be problematic when measuring the concentration of a chemical species due to the Gaussian spreading of molecules axially. Taylor dispersion can be prevented by either adopting an oil phase in the flow or by switching from pressure-driven flow to electroosmotic flow, i.e. flow that arises from the movement of ions due to an applied electric field.

3.2.3 Mixer designs

To improve mixing between two co-flowing fluids the distance over which molecules have to diffuse has to be reduced. This can be achieved by introducing additional flows, time-variations in the overall flow, or by increasing interfacial area between the flows (Ottino and Wiggins, 2004). Here three passive mixers from the literature are described that implement one of the aforementioned approaches to improve mixing.

The F-mixer shown in Figure 3.5 acts to reduce the diffusion distance through increasing interfacial area. It takes two parallel flowing fluids, splits them into multiple smaller segments and then laminates the segments on top of one other (Kim et al., 2004). The SLM was able to achieve complete mixing of fluids in a distance 20× shorter than a T-junction mixer of similar dimensions, and at low Reynolds numbers (0.44–12.28).

The mixer in Figure 3.6 introduces additional flows by splitting off a part of the flowing fluid. The split part is then reintroduced into the bulk flow further downstream. The split flow is arranged to meet the bulk flow at an angle, thus providing additional transverse flows (Hong et al., 2004a). This type of mixer was found to operate consistently over a wider range of flow rates when compared to a T-junction, which had experienced a decline in performance with increasing flow rate.

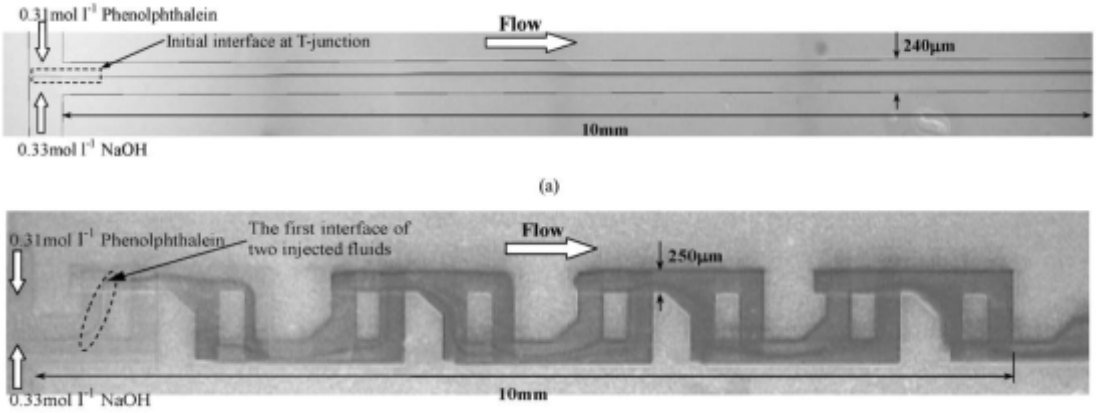

Figure 3.5: Mixing in a T-junction versus mixing in a serpentine lamination mixer. The mixing of phenolphthalein and NaOH results in a dark coloured fluid. The T-junction (top) mixes poorly with only a thin mixed region visible. Over the same distance the serpentine lamination mixer (bottom) exhibits far more efficient mixing. Image adapted from Kim et al. (2004).

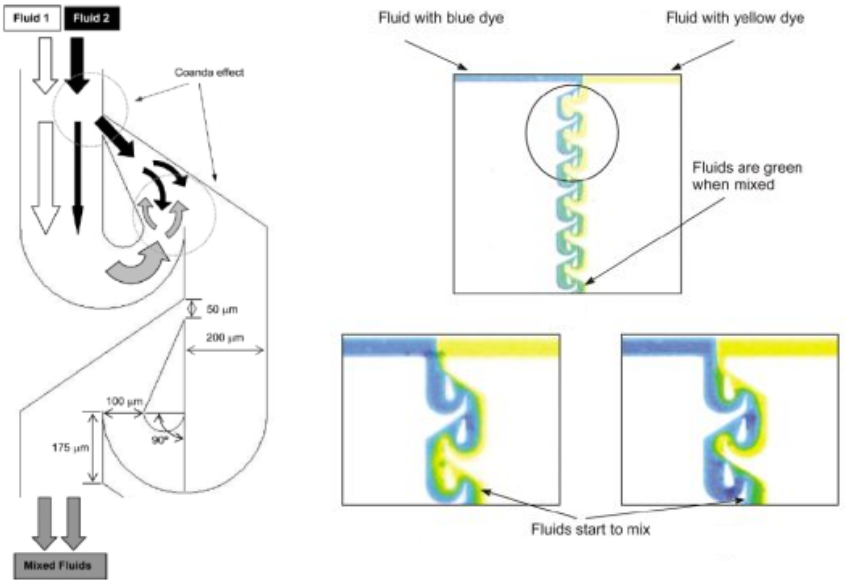

Figure 3.6: A mixer that splits and recombines flow to reduce mixing time. The principle of the mixer is shown on the left. On the right two streams of food dye can be seen to flow through the mixer. Images adapted from Hong et al. (2004a)

The staggered herringbone mixer (SHM) in Figure 3.7 creates time-varying flow by using a series of asymmetric grooves patterned in a channel. The grooves cause two co-flowing fluids to be stirred axially as they progress longitudinally through the channel (Stroock et al., 2002). It was found that for $Pe = 10^4$, the SHM would be capable of mixing a protein molecule within 1 cm. A significant improvement over the 100 cm required for a simple channel relying on only diffusion for mixing. This last strategy to mixing is particularly effective as diffusion distances are reduced exponentially with time. This exponential decrease in diffusion distance is known as *chaotic mixing* and can also be observed to occur in water droplets flowing within an oil stream (Bringer et al., 2004).

The mixer examples described above are all passive requiring no moving elements. Integrated microvalves can be used to create a rotary mixer to enable active mixing of solutions (Chou et al., 2001). In the operation of a rotary mixer solutions are confined to a circular channel. The circular channel contains three valves that are activated in a peristaltic pumping sequence during mixing. The pumping sequence drives the confined solutions around the circular channel causing their mixing. Mixing by this approach is not as rapid as chaotic mixing, but this approach does allow for mixing of discrete segments of fluid whereas the other require continuous flows.

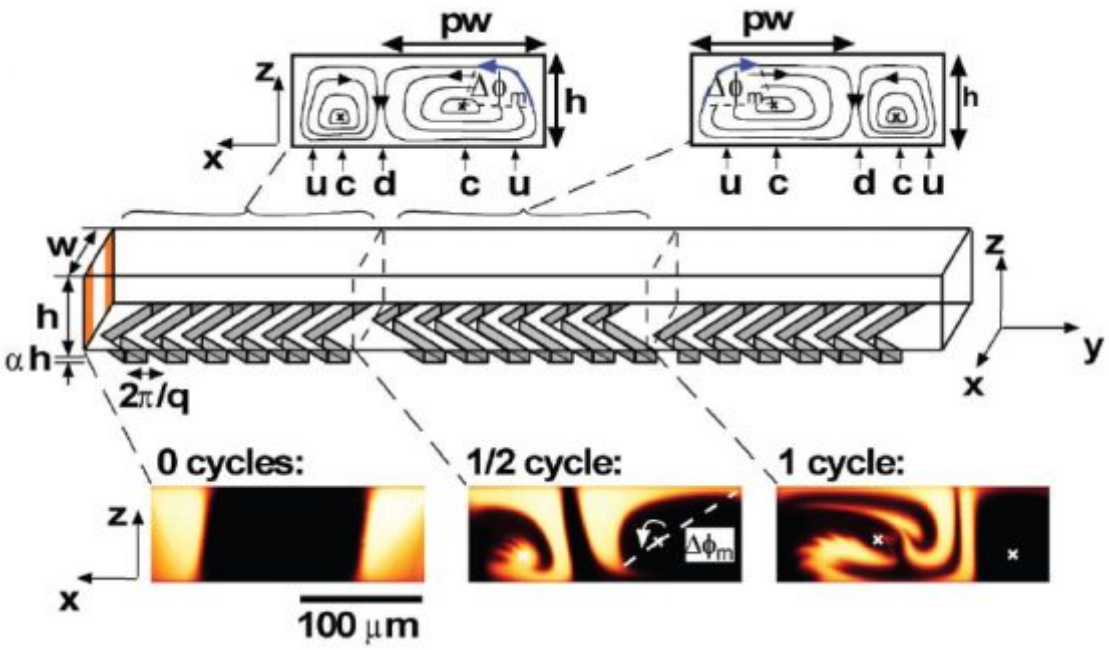

Figure 3.7: Chaotic mixing with a staggered herringbone mixer. Two fluorescent streams are injected either side of a stream of clear fluid. Cross-section images obtained by confocal microscopy show stirring of the streams as they progress downstream. Images adapted from Stroock et al. (2002).

3.3 Droplet-based microfluidics

Droplet-based microfluidics involves the formation and manipulation of individual droplets inside a microchannels. To obtain the droplets, two immiscible fluids (or phases) are used. For example water droplets can be created in air (Burns et al., 1998) or in oil (Thorsen et al., 2001). Manipulation of droplets can be achieved through exploiting the Marangoni effect induced by localised laser heating (Kotz et al., 2004), by optical trapping (Lorenz et al., 2007), through utilizing electric fields (Pollack et al., 2002; Srinivasan et al., 2004) or by viscous flow (Tice et al., 2003).

Droplet-based microfluidics holds several advantages over single-phase microfluidics. Through employing droplets, it is possible to reduce reagent volumes further without resorting to nanoscale channels. Because of reagent confinement to within a droplet, the effect of Taylor dispersion is eliminated (Song et al., 2003b). Rapid (chaotic) mixing can be achieved in droplets through simple channel design (Song et al., 2003a). Multiple droplets can be formed in a single channel, thus reactions can be performed in parallel without the need for complex devices. Dilutions too can be performed without requiring complex microchannel networks (Song and Ismagilov, 2003).

Thus droplet-based microfluidic technology has been adopted in a range of applications that include, nanoparticle synthesis (Shestopalov et al., 2004), directed evolution experiments on proteins (Agresti et al., 2010) and enzymatic assays (Song and Ismagilov, 2003). To realise devices for these and other example applications, functions that include sorting (Agresti et al., 2010), fision (Link et al., 2004), fusion (Tan et al., 2007), mixing (Song et al., 2003a) and encapsulation of droplets (double emulsions) (Nisisako et al., 2005) have had to be implemented. With the application of enzymatic assays in mind, the discussion here will be limited to aspects of droplet generation, mixing and fusion. More complete reviews on droplet microfluidics can be found by Song et al. (2006); Chiu et al. (2009); Baroud et al. (2010); Huebner et al. (2008); Theberge et al. (2010); Teh et al. (2008). Before discussing the different strategies to implement the functions of droplet generation, mixing, and fusion, the basic theory underlying droplet microfluidics first requires consideration. For clarity in the forthcoming discussion, the term continuous phase refers to the stream in which droplets are generated, and the term disperse phase refers to the stream from which droplets are created.

3.3.1 Interfacial tension

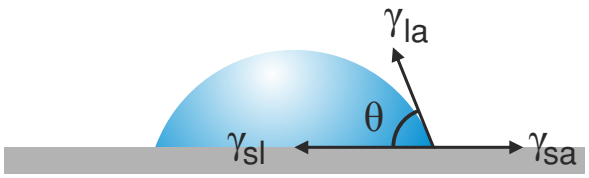

Figure 3.8: The sessile-drop technique. A drop of water is placed on the surface of a material. Due to the balance between adhesive and cohesive forces, the drop takes on a characteristic shape. Measuring the angle (θ) at the periphery of the drop provides an indication of whether the material surface is hydrophilic ($\theta < 90^o$) or hydrophobic ($\theta > 90^o$).

When two immiscible fluids are brought into contact the cohesion of like molecules in each fluid gives rise to forces that pull at the interface between the two fluids. These competing forces act in a way as to minimise the interfacial area of contact between the two fluids, thus resulting in droplets being formed. Quantification of the cohesive forces between two liquids is achieved through the property of surface or interfacial tension γ [N/m]. Acquiring a value for surface tension between two liquids is possible through the sessile-drop technique illustrated in Figure 3.8 with the relationship between the different surface tensions given by the Young equation:

$$\gamma_{sl} = \gamma_{sa} - \gamma_{la}\cos\theta \tag{3.16}$$

where γ_{sa} represents the surface tension between the solid and air, γ_{la} the surface tension between the liquid and air, (θ) the contact angle and γ_{sl} the surface tension between the solid and liquid. The successful implementation of a microfluidic droplet device requires knowing the surface tensions between fluids and the material from which device has been constructed.

To create droplets in an immiscible flow within a microfluidic channel requires several criteria be satisfied. Consider the production of water droplets in a continuous oil stream. Adhesion of the water droplets to the microfluidic channel has to be prevented in order to form well defined water droplets within the oil. This is achieved by ensuring the following two criteria are satisfied. First the oil must preferentially wet the microfluidic channel, i.e. the oil-solid interfacial tension

must be lower than the aqueous-solid interfacial tension. Second, the aqueous-oil interfacial tension must be lower than the aqueous-solid interfacial tension (Tice et al., 2003). With these two criteria fulfilled, even large droplets will be separated from channel walls by a thin layer of oil. There are circumstances where these criteria may not be met, but remedial actions can be taken. For example if hexadecane is used as carrier fluid in a PDMS microchannel, following the values summarised in Table 3.1 a drop of hexadecane exhibits a 40^o contact angle when placed on PDMS (Chaudhury and Whitesides, 1991). This indicates that in comparison to water, hexadecane will preferentially wet a PDMS microchannel. However the interfacial tension between hexadecane and water is 53.3 mN/m which is higher than the intefacial tension between PDMS and water. But by adding the surfactant Span 80 to hexadecane, the interfacial tension can be lowered sufficiently to meet the criteria set above, and thus prevent the adhesion of water droplets to channel walls.

Table 3.1: Interfacial tension and contact angle data. The interfacial tensions and contact angles are listed for interactions between water and immiscible fluids or solid materials

	Interfacial Tension [mN/m]	Contact Angle [Degrees]	Viscosity [mPa.s]	Reference
Air	72.8	-	-	(Reiter et al., 2000)
Water	-	-	0.894	(Tice et al., 2003)
Cured PDMS	≈38	104	-	(Reiter et al., 2000)
Plasma-treated PDMS	-	<5	-	(Bhattacharya et al., 2005)
Glass	-	20	-	(Bhattacharya et al., 2005)
PMMA	-	67.8	-	(Ma et al., 2007)
Teflon®	-	114	-	(Sandison et al., 2007)
Hexadecane	53.3	-	8	(Aveyard and Haydon, 1965; Lin and Su, 2008)
Hexadecane/Span 80	5	-	-	(Link et al., 2004)
Mineral Oil	38	-	30	(Malloggi et al., 2008)
Mineral Oil/Span 80	5	-	-	(Malloggi et al., 2008)
Mineral Oil/Triton X-100	3.1	-	-	(Malloggi et al., 2008)
PFD	≈55	-	5.1	(Tice et al., 2003)
PFO/PFD	12–14	-	-	(Tice et al., 2003)
Oleic Acid	15.6	-	27.64	(Tan et al., 2007)
Silicone Oil	38	-	-	(Binks and Clint, 2002)
Silicone Oil/SDS	4	-	-	(Utada et al., 2007)
Silicone Oil/Span 80	3.4	-	10	(Jiao et al., 2007)

PDMS - polydimethylsiloxane; PMMA - poly(methyl methacrylate); SDS - sodium dodecyl sulfate; PFD - Perfluorodecaline; PFO/PFD - 1H,1H,2H,2H-perfluorooctanol/PFD mixture

3.3.2 The Capillary number

Earlier the concept of the dimensionless Reynolds number was introduced that serves as an indication of the degree of nonlinear behaviour of a flow. In two phase flows, distinct behaviours arise from the competition between viscous forces and interfacial tension. Similarly the competition is associated with a dimensionless number, the Capillary number (Ca):

$$Ca = \frac{\eta U}{\gamma} \tag{3.17}$$

where η is the dynamic viscosity of the continuous oil phase, U the velocity of the oil phase and γ the interfacial tension between the oil and aqueous phases. The Capillary number is used in descriptions of both droplet fission (e.g. Link et al. 2004) and generation (e.g. Thorsen et al. 2001).

3.3.3 Generating droplets

Droplets can be generated in microfluidic devices through designs that utilise flow focusing (Anna et al., 2003), coflowing streams (Umbanhowar et al., 2000; Utada et al., 2007) or T-junction (Thorsen et al., 2001) configurations. Typically in coflowing designs (Figure 3.9), a channel (or capillary) is positioned coaxially within another channel (or capillary). The continuous and disperse phases are flowed through the outer and inner channels respectively. Droplet formation in coflowing fluids has been characterised as either dripping or jetting. In the former, droplets develop close to the orifice of the inner channel. In the latter, a liquid jet extends downstream where it then breaks up in droplets. The mechanisms underlying the different flow patterns are described by Cramer et al. (2004).

Following Figure 3.9, flow focussing designs see the continuous phase flow through the two opposing channels meeting at a point that intersects with the disperse phase. The continuous phase acts to squeeze the disperse phase through the orifice where it then breaks into droplets. As in coflowing stream designs, flow focusing is capable of exhibiting different droplet formation patterns that include dripping, jetting, squeezing and threading by adjusting the continuous phase flow rate relative to the disperse phase. The role of geometry and fluid properties on these patterns are discussed in (Lee et al., 2009).

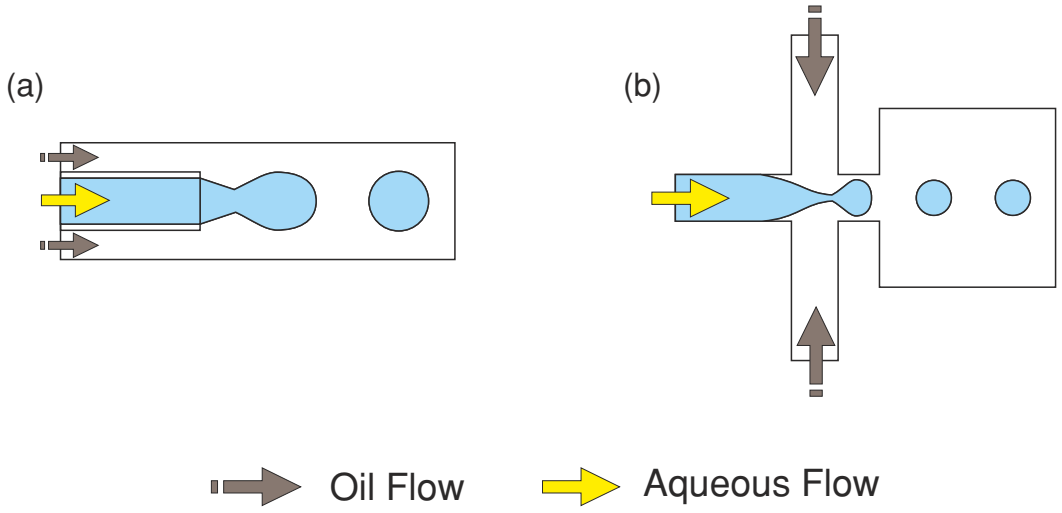

Figure 3.9: Droplet production by coflowing and flow-focusing. Droplets are produced from a channel containing aqueous solution that is positioned coaxially within a larger channel containing oil (a). An oil stream is focused to pinch off an aqueous stream to create droplets (b).

Both coflowing and flow focusing configurations allow for the continuous generation of monodisperse (equal-sized) droplets at a rate of several kilohertz (Cramer et al., 2004; Ahn et al., 2006b). A capability very much desirable for high throughput screening (Abate et al., 2009). In applications where throughput is less critical but rather the control of individual drop sizes and their fusion is essential, designs that allow for the generation of droplets on demand are more interesting.

Drop on demand systems are based on the popular T-junction channel configuration first introduced by Thorsen et al. (2001). Following Figure 3.10 the T-junction configuration consists of a main channel and up to several perpendicularly intersecting side channels. The continuous phase is flowed through the main channel while the disperse phase is introduced through a side channel. Some designs use branched side channels as depicted in Figure 3.10 allowing for multiple reagents to be introduced as a single droplet in the main channel (Zheng et al., 2003). The advantage of using a branched T-junction design is that dilutions are possible through balancing the relative flow rate of the different reagents. T-junction configurations have largely been operated with droplets generated continuously. Once more as for coflowing and flow focusing designs, there exist different droplet formation regimes for T-junctions. These are treated in-depth by de Menech et al. (2008). The inclusion of active valves in T-junction designs as depicted in Figure 3.11 have been show capable of producing different sized

droplets on demand (Willaime et al., 2006; Zeng et al., 2009). This is particularly interesting in the context of this work as dilutions of reagents could conceivably be achieved by creating different sized droplets and then mixing them into one larger droplet.

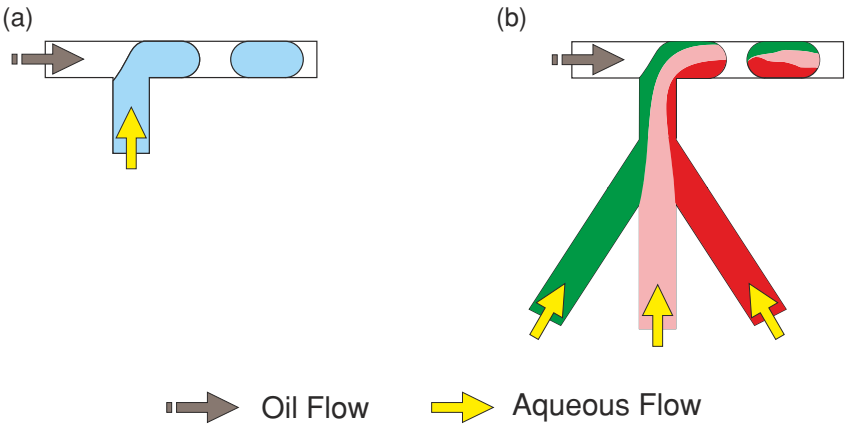

Figure 3.10: Droplet production using T-junctions. A single T-junction is used to generate aqueous droplets in an oil stream (a). Multiple aqueous streams are combined in a branched T-junction to generate droplets containing multiple chemicals (b).

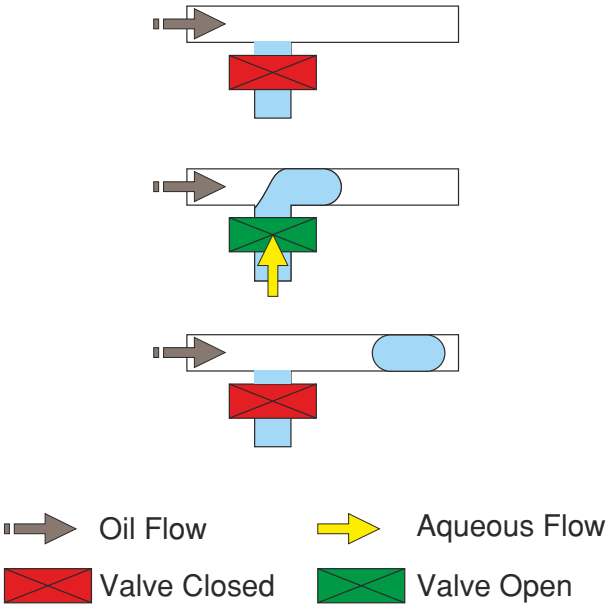

Figure 3.11: A valved T-junction allows for on-demand droplet generation. Pulsing the valve between open and closed allows a predefined amount of aqueous solution to be injected into the oil stream.

3.3.4 Mixing within droplets

Mixing within droplets is normally achieved passively, by relying on the recirculation flows internal to a droplet travelling downstream to stir the contents of a droplet (Hosokawa et al., 1999; Handique and Burns, 2001; Kinoshita et al., 2007). However droplets do require some amount of reorientation once generated to support mixing. For example Tice et al. (2003) found that droplets generated with contents localised in each half of the droplet as depicted in Figure 3.12 would not easily mix. But through the use of winding microchannels alternating asymmetric time-periodic flow patterns could be created within droplets (Song et al., 2003a), which induced exponential thinning of the mixing distance within a droplet (Bringer et al., 2004). In particular the winding serpentine channel design illustrated in Figure 3.13 was found capable of mixing dilute solutions within milliseconds (Song et al., 2003b; Sarrazin et al., 2007).

However winding channels are not always capable of inducing rapid mixing in droplets. For example in the case of mixing highly viscous solutions containing high concentrations of macromolecules, the serpentine design was found to be ineffective. The winding channel design had to be modified to include protrusions along the channel walls (see Figure 3.14), which enhanced internal circulation within droplets sufficiently to enable rapid mixing of concentrated protein solutions (Liau et al., 2005). Rapid mixing in droplets can therefore be achieved using fairly simply channel designs. The mixing or fusion of different droplets however requires potentially far more elaborate schemes.

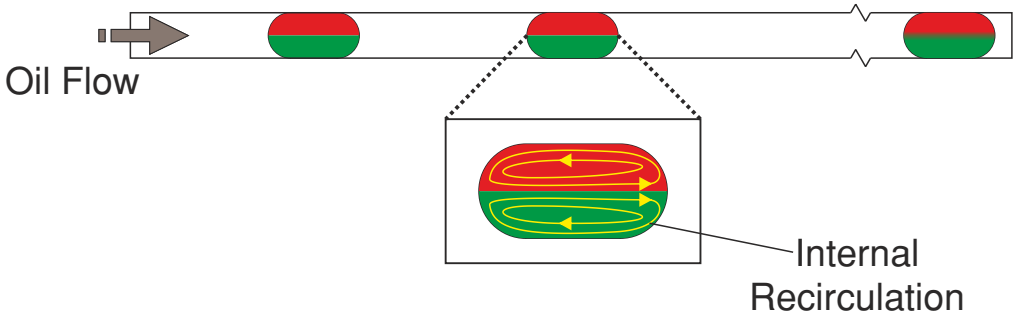

Figure 3.12: A generated droplet composed of two halves. Internal recirculation flows occur as the droplet moves downstream through a channel. The flows do not cross and therefore the contents of the droplet do not easily mix.

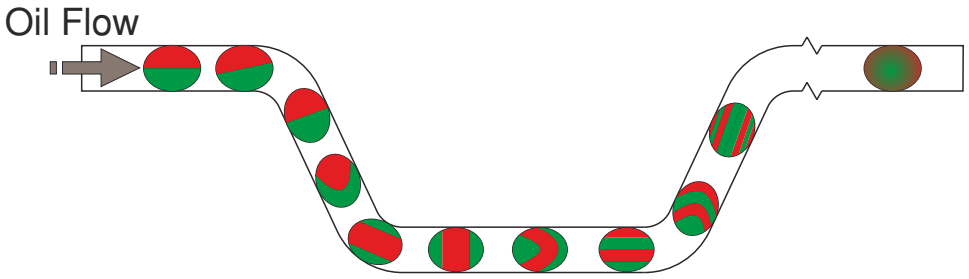

Figure 3.13: A serpentine channel to induce rapid mixing within droplets. The drop contents are reoriented as the drop passes through the corners. The recirculation flows are then able to mix the drop contents.

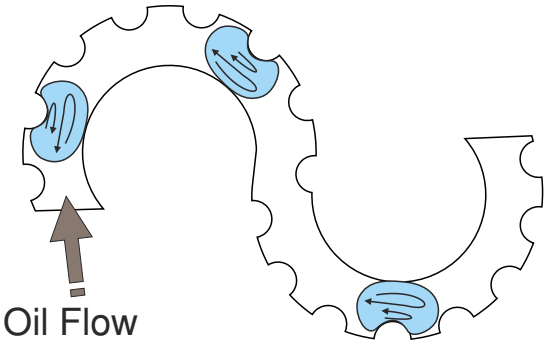

Figure 3.14: A bumpy serpentine channel to induce rapid mixing of viscous solutions contained within droplets. The bumps induce stress concentrations within the droplet that induce circulations that facilitate mixing.

3.3.5 Droplet Fusion

The fusion of droplets faces several challenges. First the distance between droplets to be fused has to be reduced and sufficient time allowed for droplets to coalesce. This can be achieved by for example creating a hydrophilic patch within a hydrophobic microchannel. As described by Fidalgo et al. (2007) the patch acts to trap aqueous droplets bringing them into close proximity and providing sufficient drainage time necessary for fusion.

An alternate method to bringing droplets into close proximity can be achieved through exploiting the mismatch in velocities between different sized droplets within the same flow. For example Song et al. (2003b) introduced small droplets into a channel in front of large droplets. The large droplets travelled more quickly catching up with the small droplets. Contact was made between the droplets and eventually they fused. In the case of equal-sized droplets, the difference in velocity is negligible and therefore can no longer be exploited to obtain fusion. Here designs such as tapered expansions (or diffusers) (Hung et al., 2006), trifurcating channels (Tan et al., 2004, 2007) and diffuser-nozzle chambers (Bremond et al., 2008) can be used to obtain fusion between equal-sized droplets. Such designs slow the droplet at the front allowing the droplet at the rear to catch up and make contact, then fuse.

Surfactants present in the oil stream to prevent droplets sticking to channel walls, also act to stabilise droplets against coalescence. The use of surfactants can lead to droplets even in close proximity remaining completely separate. To overcome the effect of the surfactants and in doing so induce fusion, the local concentration of surfactants at the interface between droplets must be depleted. This can be achieved by using the design reported by Bremond et al. (2008). As depicted in Figure 3.15 the design consists of a rectangular chamber sandwiched between a diverging inlet (or diffuser) and a converging outlet (or nozzle). Two droplets would enter the chamber, collide and then settle side-by-side without coalescing. Then as the front droplet approached the nozzle it would compress and separate slightly from the rear droplet. This induces two small local points on each droplet, which were interpreted as being regions depleted of surfactant molecules (Bremond et al., 2008). After the formation of the two points on each droplet, fusion would occur.

The methods to droplet fusion discussed so far do not address the challenge of periodicity. For example if droplets to be fused are generated too far apart,

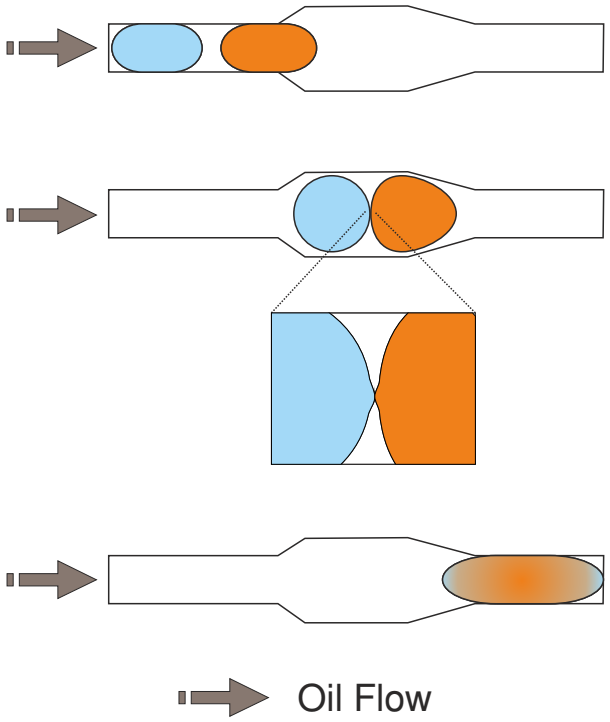

Figure 3.15: Droplet fusion within an expansion channel. Two droplets separated by oil enter the expansion chamber. The front droplet slows allowing the rear droplet to catch up. The two droplets collide then relax. After relaxing the two droplets separate slightly, which causes two points to appear on each droplet (inset). The points are regions of depleted surfactant that lead to the droplets to fusing.

coalescence will not be achieved. Rather the more elaborate design depicted in Figure 3.16 is required to fuse droplets independently of periodicity. The design was introduced by Niu et al. (2008) and consists of a large tapered chamber containing a series of pillars arranged in pairs of varying size. The pillars acted to trap droplets within a specific size range while still allowing the oil to continue flowing. Droplets could be trapped and effectively made to wait for another to arrive. The arrival of another droplet would see it collide with the trapped droplet. Fusion would initiate and provided the fused droplet volume was large enough (related to chamber volume) it would be released from the trap. This design is more complicated and due to the dependence of trapping on the geometric configuration of the pillars, likely to be sensitive to variations arising from fabrication. Here active fusion designs may provide an advantage as the channel designs typically used are simpler.

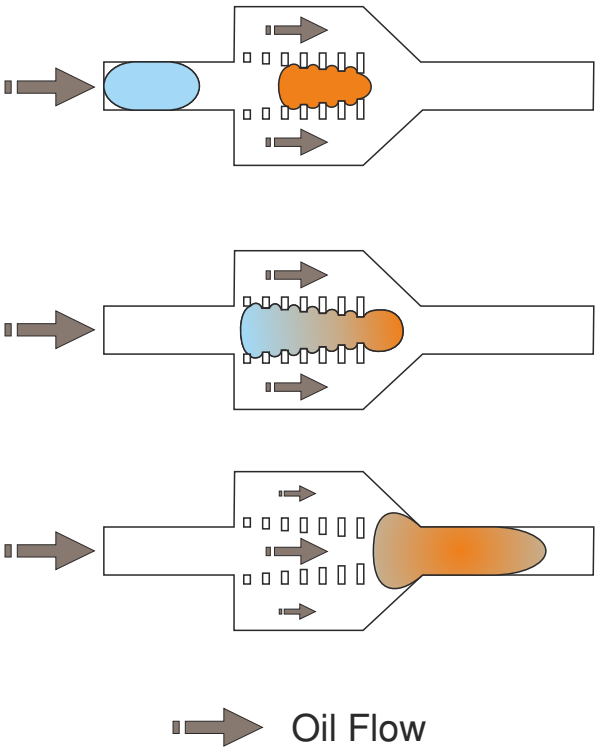

Figure 3.16: Droplet fusion within a pillar trap. The pillar trap is designed to capture droplets of specific size. A droplet is trapped and waits for a second droplet to arrive. The second droplet arrives and fuses with the first droplet. Their combined size causes the fused droplet to be released from the trap.

The active fusion of droplets in continuous flows has been performed electrostatically or through using on-chip valves. In electrostatic approaches, an electric field is applied to droplets which has the effects of redistributing surfactant molecules at the droplet interface as well as charging the droplets. These effects have been harnessed to fuse pairs of unequally sized droplets (Ahn et al., 2006a) as well as trains of equally sized droplets (Priest et al., 2006; Zagnoni et al., 2009). Link et al. (2006) used an electric field to both dispense and fuse two oppositely charged droplets. The voltages required to set up electric fields capable of fusing droplets range from a few tens (Priest et al., 2006; Zagnoni et al., 2009) to hundreds (Link et al., 2006; Ahn et al., 2006a) of volts depending on the distance between electrodes. All of the channel designs in these examples consisted of simple straight channels. However all of the designs appear to be incapable of dealing with periodicity. Certainly the designs could fuse droplets generated out of phase but once again if the phase is too large, droplets would not be in close enough proximity for fusion. The best active approach to fusion may therefore be

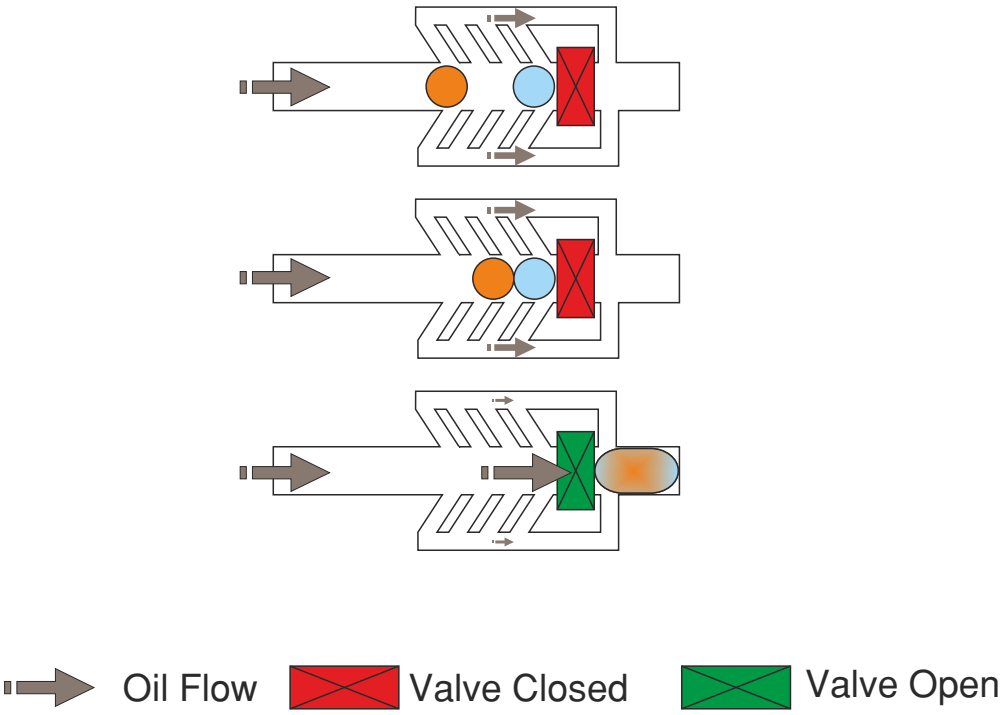

Figure 3.17: Droplet fusion within a valved trap. With the valve closed a droplet is trapped and waits for a second droplet to arrive. The bypass channels either side of the trap ensure that the oil continues flowing during trapping. A second droplet arrives and comes into contact with the first droplet. Fusion proceeds when the valve opens.

the integrated valve trap. Following Figure 3.17, the design reported by Lin and Su (2008) consisted of a channel that was blocked by the actuation of a single on-chip valve. Smaller bypass channels connecting both upstream and downstream from the valve ensured that oil could continually flow when the valve was actuated. On actuation of the valve, droplets are trapped and the bypass channels allow the oil between droplets to drain bringing them into close proximity. On release of the valve the droplets separate slightly before fusing as described above. Droplet fusion by using an integrated valve design has advantages over other techniques that include, the ability to fuse independently of periodicity, and no apparent restriction in droplet sizes that can be fused.

3.4 Automating microfluidic devices

In recent years, the field of microfluidics has moved beyond designing and testing individual components towards the design and application of integrated systems, capable of automating entire laboratory processes (Whitesides, 2006; Haeberle and Zengerle, 2007). Key to automation of microfludic devices was the development of the pneumatically actuated integrated microvalve components, in particular membrane or in-line valves in normally-closed (Hosokawa and Maeda, 2000; Lagally et al., 2000) and normally-open (Unger et al., 2000) configurations. The reason why these particular valve types have made automation more amenable is because multiple microvalves can be packed in close proximity. For example within 50 μm of each other as reported in (Thorsen et al., 2002). This packing density has been achieved by moving the relatively bulky valve driving component (e.g. the pressure or vacuum source) away from the microvalve. Instead *control* microchannels are created that link the on-chip microvalve to the driving component at the periphery of the chip. By contrast other active microvalves have the external work source directly acting on a fluidic channel (Weibel et al., 2005).

Following Figure 3.18, both normally-open and normally-closed membrane valves are formed by sandwiching a membrane between two patterned device layers. The one layer contains microfluidic channels and is known as the fluidic layer, while the other layer contains the control channels. Where the fluidic and control channels intersect constitutes a valve. By supplying external pressure or vacuum to control channels, the membrane between intersecting fluidic and control channels is either deflected into or pulled away from the fluidic channels. Typically in the case of a normally-closed valve, a seat is included in the design onto which the membrane rests thereby restricting flow. On application of a vacuum to the control channel the membrane is deflected away from the seat allowing fluid to flow.

Pressurising normally-open valves causes the membranes to be deflected into the fluidic channel thereby restricting flow. There are two configurations of normally-open valve determined by orientation between fluidic and control channels. Fluidic channels can be assembled on top of control channels therefore the membrane is pushed upwards on actuation. Similarly control channels can be assembled on top of fluidic channels and the membrane is then pushed downwards on actuation. These two arrangements have different pressure requirements in closing a valve, the push up type is reported to require less pressure (Studer et al., 2004).

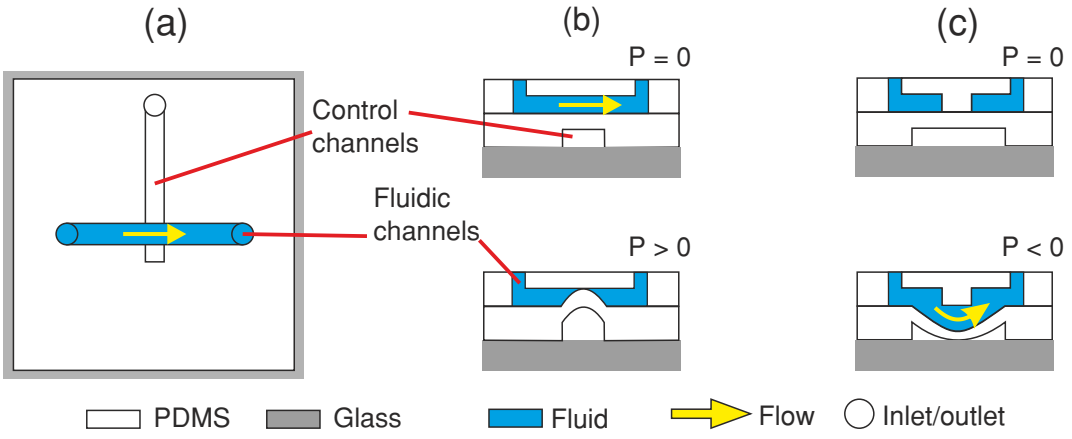

Figure 3.18: The concept of normally-open and normally-closed integrated valves. A normally-open valve when pressurised restricts flow as the membrane is deflected into the fluidic channel (a). A vacuum applied to a normally-closed valve pulls the membrane away from a seat allowing flow in the fluidic channel (b).

Summarised for comparison in Table 3.2 are data from normally-open and normally-closed valves reported in the literature. The fabrication of normally-open valves is easier than normally-closed valves, particularly where irreversible sealing is required between control and fluidic device layers. Normally-open valves have been shown to enable construction of on-chip components such as peristaltic pumps and rotary mixers (Chou et al., 2001). Normally-open valves have also been multiplexed so that large numbers of fluidic channels can be controlled with fewer control channels; one example demonstrated 20 control channels addressing 1024 fluidic channels (Thorsen et al., 2002). Such microfluidic large-scale integrated (mLSI) schemes in combination with pumping and mixing components have allowed for complex devices to be created capable of performing parallel operations on a single chip (Hong et al., 2004b; Jambovane et al., 2009). The device complexity that can be achieved and the rapid prototyping techniques available (soft lithography; discussed next) to the creation of normally-open valves, makes attractive their use in the design of the autonomous experimentation system.

Table 3.2: Summarised membrane valve data

Reference	Valve Type	Valve Action	Fluidic Channel Dimensions (w x d μm)	Valve Dimensions (w x d μm)	Membrane Thickness (μm)	Actuation Pressure (kPa)	Flow Pressure (kPa)	Dead Volume	Valve Time (on/off)	Actuation Method	Material	Bonding Method
Hosokawa and Maeda (2000)	NC	Pull Up	100 x 25	450(l) x 200 x 70	25	-60	-30	6.3 nl	-	Pneumatic	PDMS	Reversible
Unger et al. (2000)	NO	Push Down	100 x 10	100 / 50 x 10	30	40–50	-	0–100 pl	13 ms	Pneumatic	PDMS	Part-ratio
Studer et al. (2004)	NO	Push Up	300 x 54	300 x 50	$\approx$ 3–16	$\approx$ 5–15	-	-	-	Pneumatic	PDMS	Part-ratio
	NO	Push Up	300 x 54	100–600 x 10	-	15–5	-	-	-	Pneumatic	PDMS	Part-ratio
Hong et al. (2004b)	NO	Push Up	100 x 50	100 x 50	5	$\approx$35	55–104	-	-	Pneumatic	PDMS	Part-ratio
	NO	Push Down	100 x 10	200 x 15	-	-	3.4–13.8	-	-	Pneumatic	PDMS	Part-ratio
Grover et al. (2006)	NC	Pull Down	50 (d)	50 (d)	254	-85 / 40	17	10 nl	120 ms	Pneumatic	Glass/PDMS	O_2 Plasma
Go and Shoji (2004)	NO	Push Up	200 x 55	2.5 mm dia x 247	30	10	1	0	500 ms	Pneumatic	PDMS	Part-cure
Urbanski et al. (2006)	NO	Push Up	60 x 20	150 / 100 x 20	-	82–104	41–62	-	14 ms	Pneumatic	PDMS	Part-ratio
van Noort and Zhang (2005)	NO	Push Down	300 x 10	100 x 10	40	104 / 207	-	-	-	Pneumatic	PDMS	Part-ratio
Wang et al. (2004)	NO	Push Down	150 x 12	300 x 50	58	551	413	0.1 nl	-	Pneumatic	PDMS	O_2 Plasma
Gu et al. (2007)	NO	Push Down	100 x 9	100 x 16	-	$\approx$217	-	-	300 ms	Piezoelectric	PDMS	O_2 Plasma

NO – normally-open; NC – normally-closed

3.5 Microfluidic device fabrication

Microfluidic channels can be patterned in substrate materials that include glass (Lin et al., 2001), silicon (Harris et al., 2003) and polymeric materials in the forms of elastomers and thermoplastics (Becker and Gärtner, 2008). There are many fabrication techniques associated with the different substrate materials. Some examples include, injection moulding (Kim et al., 2006a) and hot embossing (Becker and Heim, 2000) of plastics, chemical (wet) etching of glass (Stjernström and Roeraade, 1998), plasma (dry) etching of silicon (Losey et al., 2002) and laser machining of plastics (Klank et al., 2002). But out of the available substrate materials and associated fabrication techniques, soft lithography with the silicone elastomer polydimethyl(siloxane), or PDMS, is arguably the most widely employed method to prototype microfluidic device creation.

Reasons for the widespread adoption of soft lithography with PDMS are two-fold. First the technique of soft lithography (Duffy et al., 1998) is in itself relatively quick and simple. Second, PDMS has several attractive properties that include the ability to support the creation of high density integrated valved devices (Thorsen et al., 2002), little optical absorbance in the range of wavelengths between 230 nm and 700 nm (Fujii, 2002), tunable optical properties through dye-doping (Hofmann et al., 2006), biocompatibility (Folch and Toner, 1998), modifiable surface wettability (Bhattacharya et al., 2005) and reasonable solvent compatibility (Lee et al., 2003).

Prototyping microfluidic devices in PDMS involves three major steps, the fabrication of a replication master, the processing of PDMS, and finally alignment and bonding. These three steps are discussed in more detail next.

3.5.1 Replication master fabrication

Prototyping with PDMS first requires the creation of a master that is patterned with the desired microchannel design. The fidelity of resulting microstructures in PDMS is dependent on the replication master. Therefore replication master fabrication tends to be the most time-consuming and expensive step in prototyping. Typically silicon wafers are used to create replication masters and thus many of the techniques used for replication master fabrication have been borrowed from the integrated circuit industry. Similarly replication master fabrication is often

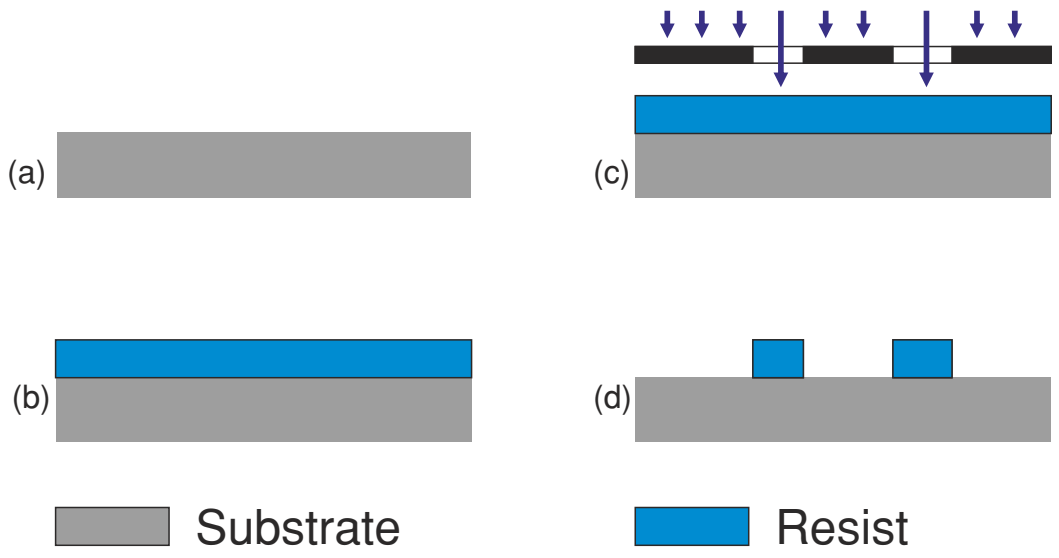

Figure 3.19: Summary of the master fabrication process. A silicon wafer is cleaned and dehydrated before photoresist is applied (a). The clean silicon wafer is coated with photoresist of uniform thickness (b). The photoresist is selectively exposed to UV light through a photomask (c). The photoresist is developed leaving behind features that constitute the pattern to be replicated in PDMS (d).

performed in specialist cleanroom environments using sophisticated equipment (e.g. Standford Microfluidic Foundry and Southampton Nanofabrication Centre).

Creating patterns on a silicon substrate can be achieved either through bulk or surface micromachining. Bulk micromachining involves the selective removal of material from the substrate, while surface micromachining involves the selective deposition of materials on to the substrate. In microfluidics, one of the most popular methods to patterning silicon wafers is photolithography, which is a surface micromachining technique.

Following Figure 3.19, typically liquid photoresists are deposited on to a silicon wafer by spin coating. In spin coating the substrate is loaded on to a vacuum chuck that is in turn coupled to an electric motor. An excess amount of photoresist is dispensed on to the substrate. The substrate is then spun to obtain a predefined thickness of photoresist. Both positive (e.g. AZ series, MicroChemicals GmbH, Germany) and negative (e.g. SU-8 series, MicroChem Corp., USA) tone photoresists are used in microfluidic master fabrication. After deposition, the photoresist is patterned by selective exposure to ultraviolet (UV) light through

a photomask. The UV exposure is typically performed within a mask-aligner containing a collimated UV light source. The exposure to UV light causes negative tone resists to become insoluble to developer solution, while in positive tone resists UV exposure causes the resist to become more soluble to developer solution. Thus during development excess material can be removed leaving behind a pattern. After development, the patterned silicon wafer is normally subjected to a surface treatment (silanization) to render it non-stick to PDMS, which aids separation of cured PDMS from the wafer without causing damage to the master or PDMS.

3.5.2 Processing PDMS

Two commercially available types of PDMS are used in microfluidics, Sylgard 184 made by Dow Corning, and RTV 615 made by GE Bayer. Both types of PDMS are supplied as two components, a base polymer and a curing agent. The two components are mixed together normally at the manufacturers' specified ratio of 10:1 (w/w) base to curing agent. The mix is then degassed and deposited on to a replication master. The method of deposition depends on the desired thickness of the PDMS layer. For thick layers, as depicted in Figure 3.20, PDMS is simply poured on to the replication master and then degassed to remove any air bubbles that are introduced during pouring.

To obtain thin ($\ll$ 1 mm) device layers, the approaches of either spin coating or sandwich moulding can be used. Spin coating allows for the deposition of material (PDMS) of uniform thickness, which is determined by the spin coating speed (see for example (Zhang et al., 2004)). In the sandwich mould approach (Jo et al., 2000) PDMS is first poured on to a master. The PDMS-covered master is placed on top of a rubber sheet that has already been put on of an aluminium plate. A transparency film is then placed on top of the PDMS-covered naster. A Pyrex wafer is put on top of the transparency film, and a rubber sheet is placed on top of the Pyrex wafer. Finally a second aluminium plate is put on top of the upper rubber sheet to complete the sandwich. A C-clamp is used to apply pressure to the sandwich and the entire assembly is then baked. After baking the sandwich is disassembled to reveal a thin PDMS film. The thickness of the film is altered by adjusting the clamp pressure prior to baking. Hard stops can be incorporated into the replication master to provide further control over PDMS thickness during clamping.

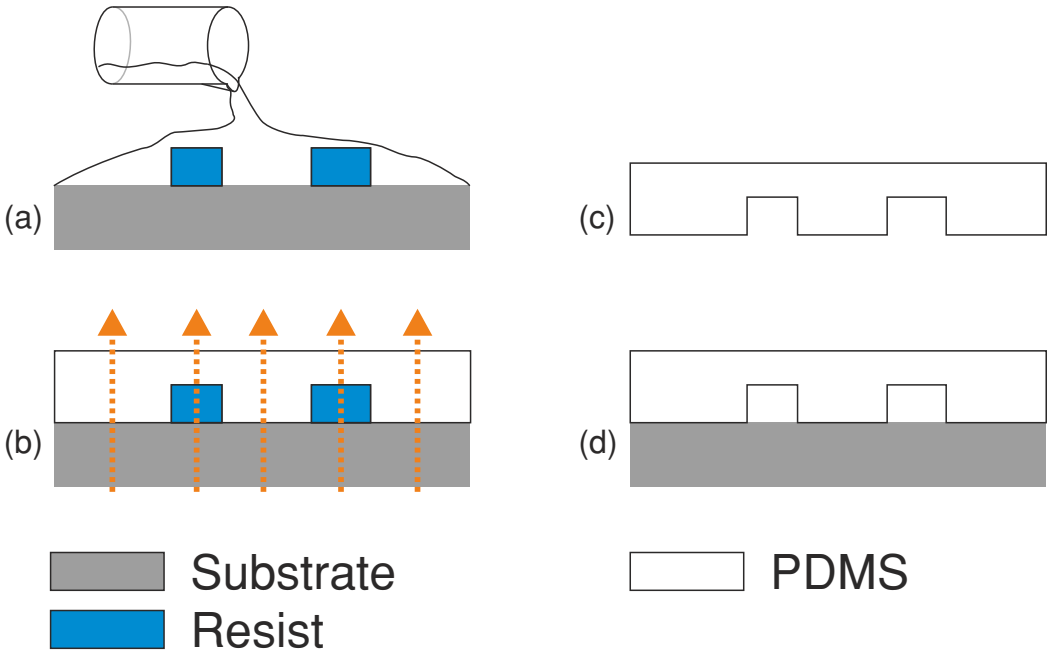

Figure 3.20: Processing PDMS. First PDMS is poured on to a replication master (a). The PDMS is cured in place (b) and afterwards released from the replication master (c). The microchannels contained with the cured PDMS layer are then sealed by bonding to another substrate (d).

Once deposited PDMS is cured in place over the replication master. This can take as long as 48 hours at room temperature. Curing can be accelerated through baking, however PDMS does experience temperature-dependent shrinkage during curing (Lee and Lee, 2008). The shrinkage can be accounted for by scaling photomask designs so that the resulting replication master features are slightly larger (Marcus et al., 2006). A selection of photomask scale values used to offset the baking induced shrinkage of PDMS is summarised from Lee and Lee (2008) in Table 3.3.

Once cured, the PDMS is released from the replication master. Fluid access holes are then made in the cured PDMS using a coring tool, biopsy punch, drill or by punching with a needle. The PDMS is then ready to be bonded.

Table 3.3: Photomask feature scale values to account for PDMS shrinkage during curing

Temperature (^{o}C)	Cure Time (hours)	Scale Value (%)
65	4	+1.07
80	2	+1.54
100	1	+1.98

3.5.3 Bonding

PDMS can bond reversibly by simply bringing it into conformal contact with a substrate such as glass, silicon or another piece of PDMS, provided all mating surfaces are clean. For applications that involve higher operating pressures, such as valved devices, irreversible bonding of PDMS is required. Irreversible bonding techniques in general either involve surface treatments (Haubert et al., 2006), adhesives in the form of uncured PDMS or curing agent (Satyanarayana et al., 2005; Samel et al., 2007) or variation of the PDMS processing parameters, for example temperature or ratio of curing agent (Unger et al., 2000; Go and Shoji, 2004). A particularly popular and effective method of bonding involves treating PDMS with an O_2 plasma generated by a plasma cleaning machine. Plasma treatment can be used to irreversibly bond pieces of PDMS to one another and glass provided that both the PDMS and glass are exposed to the O_2 plasma.

Chapter 4

Accessible prototyping of integrated valve microfluidic devices

4.1 Introduction

A bespoke microfluidic design containing integrated valves is required for enzymatic computing studies with an autonomous experimentation system. Potentially many prototyping cycles are required to obtain a suitable microfluidic design for the autonomous experimentation system. In soft lithography (Duffy et al., 1998), associated with each prototyping cycle is the fabrication of replication masters from which devices are constructed. Creating replication masters can be costly, particularly when specialist processing environments and sophisticated equipment are used (e.g. the Stanford Microfluidic Foundry and Southampton Nanofabrication Centre). One means by which the cost of prototyping can be reduced is to switch photoresist material used in creating microfluidic replication masters, from a liquid to a dry film type.

Dry film resists are supplied as thin polymer sheets of pre-defined thickness, which are then laminated onto a substrate. A liquid photoresist is instead spin coated onto a substrate, where the spin speed and repeated coatings determine photoresist thickness. There are several advantages to using dry film resists (DFRs) over liquid resists. These include: easier handling and processing of coated substrates, no edge beading, good uniformity and a requirement for simpler processing equipment. Moreover DFRs are substantially cheaper than liquid photoresists (e.g. order of

magnitude between AM150 and SU8). Dry film resists can be either fabricated in-house from SU-8 liquid photoresist (Abgrall et al., 2008) or obtained commercially. Some commercially available DFRs include: Ordyl (Elga Europe S.r.l., Italy), Riston/MX (DuPont, USA), Etertec (Eternal Chemical Co. Ltd., Taiwan) and TMMF (Tokyo Ohka Kogyo Co. Ltd., Japan).

Dry film photoresists were originally intended for patterning printed circuit boards, but have been used in microdevice fabrication since the mid 1990s (Lorenz et al., 1996). Vulto and co-workers demonstrated dry film resists used as part of the structural elements of microfluidic devices (Vulto et al., 2005). Other examples of devices made in a similar manner include: an electrowetting immunoassay device (Nashida et al., 2007), a capillary electrophoresis device to separate and detect dopamine and catechol (Tsai et al., 2006), a device for dielectrophoretic separation of colloidal particles (Yunus and Green, 2010) and a normally closed microvalve actuator (Lemke et al., 2011). Dry film resists can also be used to create hot embossing masters. For example Sandison and Morgan used dry film resist laminated on to glass slides to hot emboss patterns into the thermoplastics poly(methylmethacrylate) (PMMA) and poly(ethylene terephthalate) (PET) (Sandison and Morgan, 2005). More recently it has been shown that PDMS replication masters can be created from dry film resists laminated on to silicon and glass substrates (Stephan et al., 2007; Thomas et al., 2010).

Dry film replication masters are not fully capable of supporting the creation of normally-open integrated valve microfluidic devices such as the so-called Quake variety (Unger et al., 2000). For normally-open integrated valves to close fully, channels with rounded cross-sections are required. Fabricating replication masters containing rounded features is in theory far simpler to achieve with liquid resists than with dry film resists. An additional bake cycle causes some liquid resists to reflow resulting in a rounded profile as described by Unger et al. (2000). Dry film resists do not reflow and rounded channels can only be obtained by mechanical modification. Methods for obtaining rounded replication masters without using liquid resists do exist. Examples include, aluminium foil shaped over wire (Graf and Bowser, 2008), and vacuum moulds constructed in PDMS which are used to shape UV curable glue (Kang et al., 2010). Conceivably by combining an alternate method of obtaining rounded masters with dry film resist masters, the cost of prototyping could be significantly reduced and therefore the accessibility to integrated valve microfluidic technology could be greatly improved.

Presented in this chapter are fabrication methods that enable the construction of integrated valved microfluidic device within a standard chemistry laboratory and without the need for sophisticated processing equipment. Replication masters are obtained by laminating dry film photoresists onto glass microscope slides. To create patterns within laminated dry film resists, a hand-held UV lamp is used. With this set-up, features smaller than 100 μm can be obtained. Vacuum moulds are used to create replication masters containing rounded features. Previously replication masters had been fabricated with liquid resists and silicon wafers were used to obtain vacuum moulds (Jeong et al., 2006; Kang et al., 2010). Instead DFR replication masters are used here to create vacuum moulds in PDMS. Hot glue is deposited on to the vacuum mould and a glass microscope slide placed on top of the hot glue, thereby yielding a rounded master. The rounded master can be used immediately after cooling. The applicability of the fabrication methods reported here for creating integrated valve devices, is demonstrated by the implementation of a peristaltic pump device.

4.2 Experimental methods

4.2.1 Replication masters with rectangular features

4.2.1.1 Photomasks

Photomasks were designed using AutoCAD software (Autodesk, USA) and sent for printing at a resolution of 20,000 dpi to Micro Lithography Services Ltd. (Chelmsford, UK).

4.2.1.2 Glass slide preparation

Standard borosilicate glass microscope slides were used as replication master substrates on to which dry films were laminated. The glass microscope slides (76 mm by 38 mm by 1.2 mm) were obtained from Fisher Scientific (Loughborough, UK). Before lamination, the slides were washed with dishwashing liquid and water, and rinsed under acetone, methanol and isopropyl alcohol. Afterwards the slides were dried with nitrogen gas and baked for 10 minutes on a hot plate set to 110 ^{o}C. The slides were left on the hot plate until required for lamination.

4.2.1.3 Dry film lamination

Rolls of 50 and 75 μm thick negative dry film resist (Ordyl AM150 and AM175) were purchased from Elga Europe (Daventry, UK). An A3 hot roll laminator (GMP Photonex 325) was used to laminate the dry film resist on to glass slides. A sheet of 200 gsm card was cut into pieces of width 60 mm and length 220 mm. Each piece of card was folded in half across its length. Ordyl dry film resist was cut into several pieces with dimensions slightly less than the card pieces (typically 100 mm long by 50 mm wide).

For lamination, the hot roll laminator was set to a temperature of 110 ^{o}C and speed 2. The folded pieces of card were fed through the laminator. Following Figure 4.1, lamination of the dry film resist (DFR) onto glass proceeded as follows: (1) the protective film covering the bottom of the DFR was peeled back by approximately 10 mm from one of the short edges. The unprotected laminate edge was pressed against a short edge of the card. The laminate and card were then fed through the laminator by approximately 8 mm before reversing the feed. (2) The remainder

of the DFR bottom protective film was then peeled off completely. A heated glass slide was removed from the hot plate and placed onto the partially laminated card. The slide and partially laminated card were fed through the laminator. During lamination the DFR was kept taut and angled at approximately 20 to 30 degrees above the surface of the glass slide. At the same time pressure was applied to the glass slide to prevent slipping during the initial feed into the laminator. (3) After lamination the glass slide was cut free from the card with a scalpel and left to cool to room temperature for 10 minutes. Exposure of the laminated slide to ultraviolet light could then be performed.

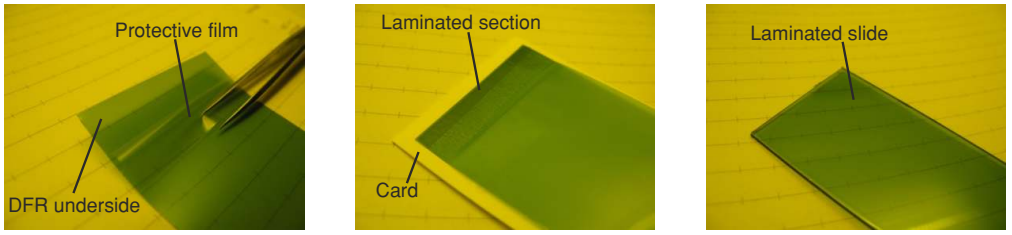

(a) (b) (c)

Figure 4.1: Dry film resist lamination. The protective film is removed from the underside of the dry film before lamination (a). The dry film is partially laminated on to card to ease handling during lamination (b). A laminated microscope slide (c).

4.2.1.4 UV exposure

Laminated slides were exposed to ultraviolet (UV) light within a custom exposure box that had been fabricated in-house (Figure 4.2). Integrated into the box was a sliding metal screen that provided exposure control, and a movable shelf that provided intensity control. The UV light source used was a high intensity UV lamp (100 W, 365 nm, Black-Ray B-100AP).

For exposure, the UV lamp was turned on for at least 10 minutes to warm up. The following steps were performed: (1) a laminated slide was placed laminate side up on top of a piece of black card, which had been put on the exposure box shelf. (2) A photomask was put on top of the laminated slide. (3) A cleaned non-laminated microscope slide was then put on top of the photomask. (4) Two small 20 gram masses were placed at opposite ends on top of the cleaned non-laminated slide. (5) The shelf was then loaded into the light box at the uppermost level (70 mm from the lamp). (6) The metal screen was then moved to expose the laminated slide to UV light. After 10 seconds ($\approx$ 115 mJ dose - see appendix A.1) the metal

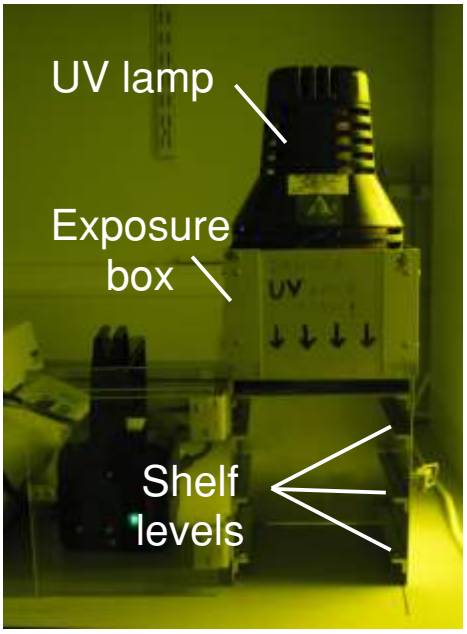

Figure 4.2: Handheld UV lamp and exposure box. The box has three shelf levels allowing for different intensities of exposure.

screen was moved to block the UV light. (7) After exposure, the laminated slide was put on a hot plate set to 65 ^{o}C and baked for a duration of 10 minutes. (8) The slide was removed from the hot plate and left to cool to room temperature.

4.2.1.5 Developing

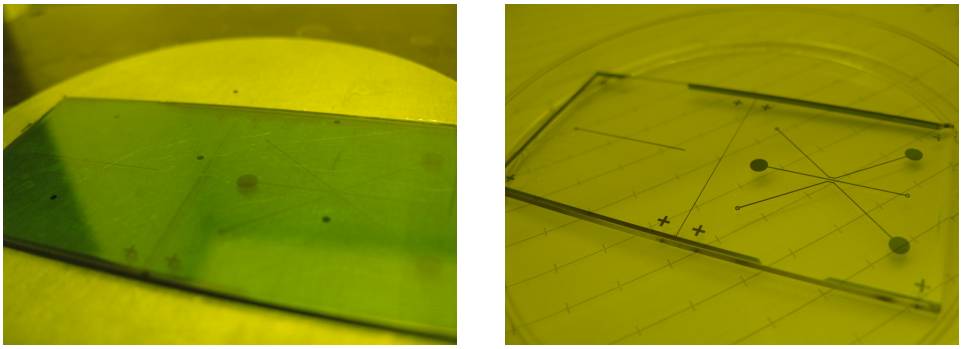

(a) (b)

Figure 4.3: Laminated slides before and after developing. A UV exposed laminated slide showing cross-linked patterns surrounded by uncross-linked resist (a). A developed slide devoid of uncross-linked resist (b).

Developer solution was prepared by dissolving sodium carbonate (Sigma Aldrich, UK) 0.8% w/v in deionised water. The developer solution was poured into a Petri dish which had been placed within an ultrasonic cleaner (Ultra 6000, Maplin UK).

Development of a laminated slide was performed as follows: (1) a laminated slide was put laminate side (face) down into the Petri dish and the ultrasonic cleaner switched on. The slide was left face down for 40–60 s. (2) The laminated slide was then flipped face up and left for 30–50 s. (3) The ultrasonic cleaner was then turned off. The laminated slide was gently rubbed by hand for 30–45 s. (5) The slide was removed from the Petri dish and rinsed thoroughly under a water tap. (6) The slide was visually inspected to determine if further development was required. If further development was required, the process was repeated but with shorter time intervals to prevent over-developing (see workflow diagram in Appendix A.2).

Once fully developed (e.g. Figure 4.3), a slide was cleaned with dishwashing liquid and deionized water, rinsed with water and then dried with nitrogen. The cleaned slide (replication master) was then silanized.

4.2.1.6 Silanization

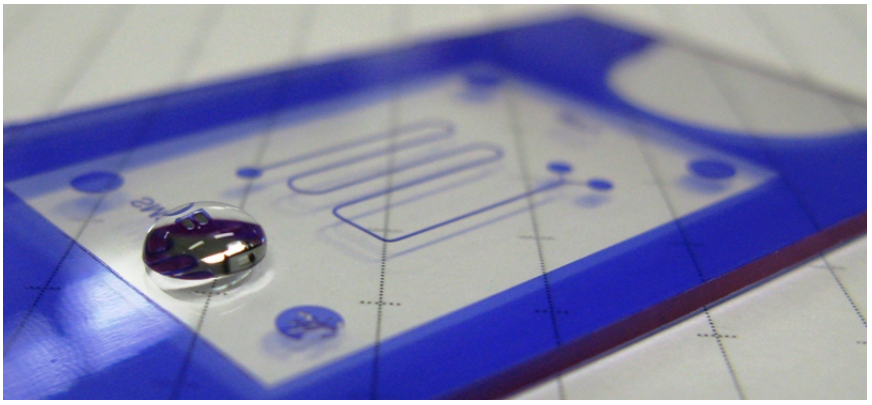

Figure 4.4: A silanized replication master. A drop of water placed takes on a spherical shape indicative of a hydrophobic surface.

Silanization was performed in a vacuum desiccator similar to the method described by Sandison et al. (2007). Briefly a drop of trichloro(1H,1H–2H,2H–perfluorooctyl)silane 97% (Sigma Aldrich, UK) was pipetted on to a coverslip which had been put inside a vacuum desiccator. Replication masters were placed within the desiccator and positioned around the coverslip. A vacuum was applied to the desiccator for 30 minutes. The vacuum pump was turned off and the desiccator left sealed for an additional 30 minutes. Afterwards the desiccator was

vented to atmosphere. Replication masters were removed from the desiccator and then baked at 120 ^{o}C for 20 minutes. From this process the replication masters were rendered hydrophobic (Figure 4.4) exhibiting a contact angle with water of approximately 103^{o} (see appendix A.3). Rendering replication masters hydrophobic was essential to aid the release of cured PDMS from replication masters without damage either to PDMS structures, or to replication master features.

4.2.2 PDMS processing

4.2.2.1 Casting PDMS

PDMS (Dow Corning Sylgard®184) was purchased from Farnell (Leeds, UK). The PDMS was prepared by mixing base polymer with catalyst at the manufacturer's standard ratio of 10:1. The PDMS mixture was then degassed for 30 minutes in a vacuum desiccator. Using the technique described by O'Neill et al. (2006), aluminium foil was folded and shaped around replication masters to contain poured PDMS. PDMS was poured on to replication masters. Air bubbles introduced into the PDMS mixture during pouring, were burst or moved to the periphery of the replication master using a scalpel blade. Persistent bubbles were removed by simply allowing the poured PDMS to stand for several minutes before baking. The poured PDMS was cured by baking for 1 hour on a hot plate set to a temperature of 100 ^{o}C. After curing, the hardened PDMS was separated from the replication master. Fluid access holes were cored through the cured PDMS using a 1 mm biopsy punch.

4.2.2.2 Spin coating PDMS films

PDMS was mixed and prepared as described above. Replication masters were loaded in turn onto a vacuum chuck within a spin coater (Model 4000, Electronic Microsystems Ltd., UK). PDMS was poured onto the replication master. Using spin coater operating parameters modified from (Zhang et al., 2004), the spin coater was programmed to: (1) spin at 500 RPM for 15 s. (2) Ramp the spin speed up to a final spin speed with an acceleration of 20 RPM/s. (3) Maintain the final speed for 60 s before decelerating to a standstill. The PDMS coated master was then removed and placed on a hot plate set to 100 ^{o}C and left to cure for 1 hour.

4.2.2.3 Oxygen plasma bonding

Figure 4.5: Glass and PDMS samples undergoing oxygen plasma exposure.

A Diener Femto RF oxygen plasma system (Henniker Scientific, Cheshire, UK) was used to bond PDMS either to PDMS or to glass microscope slides. The plasma system was operated with RF power set to 50 W, an input oxygen flow rate of between 70 to 80% of 90 sccm/min and exposure time of 30 s, which resulted in a blue-white plasma (see Figure 4.5). After exposure the bonding process was performed by: (1) bringing plasma exposed samples into conformal contact, (2) applying pressure by hand to force out trapped air from between the contacted samples, (3) leaving the samples to stand for 10 minutes and (4) baking the samples for 10 minutes on a hot plate set to 70 ^{o}C. After baking, the bonded layers were left to cool to room temperature before carrying out any further processing.

4.2.3 Fabrication of rounded channel devices

Replication masters for rounded channels were fabricated by first creating a PDMS vacuum mould, which involved: (1) creating a rectangular replication master in dry film resist. (2) Pouring and curing PDMS on top of the rectangular replication master. (3) Spinning a thin 40 μm PDMS film on to a featureless silanized glass slide. (4) Oxygen plasma bonding the bottom of the patterned PDMS to the PDMS film.

Following Figure 4.6, a diaphragm pump was connected to the PDMS vacuum mould. The diaphragm pump (Air Admiral, Cole-Palmer UK) was set to deliver 600 mbar (gauge pressure) of vacuum. Hot glue was dispensed using a hot glue gun (Tec 150, RS Components) on to the PDMS vacuum mould. A clean glass slide was pressed firmly against the dispensed hot glue and left to cool for 10 minutes. The vacuum supply to the PDMS vacuum mould was interrupted and the glue master released from the vacuum mould.

The glue master did not require silanization. PDMS was mixed and degassed as described previously but with a base to curing agent ratio of 5:1. The 5:1 ratio PDMS was poured on to the glue master and cured on a hot plate set to 50 ^{o}C for 5 hours. Afterwards the cured PDMS was released from the glue master where it could then be further processed.

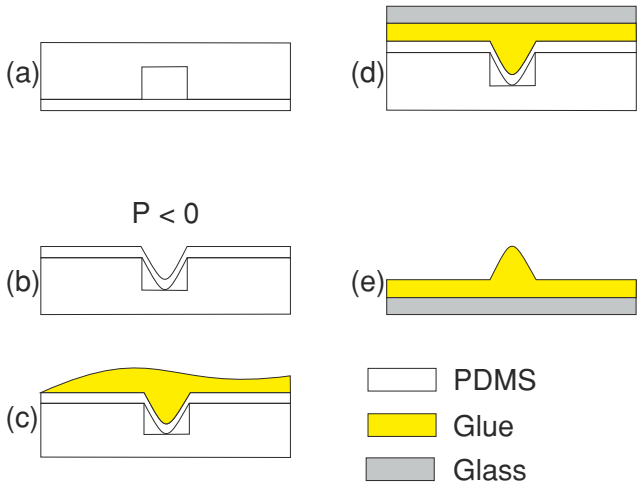

Figure 4.6: The fabrication of replication masters containing rounded features. A vacuum mould is constructed by bonding a patterned PDMS layer to a thin PDMS film (a). Vacuum is applied to the mould causing the membrane to be pulled inwards (b). Hot glue is dispensed on to the vacuum mould (c). A glass microscope slide is pressed firmly on top of the dispensed hot glue (d). After cooling the replication master is released and ready to be used (e).

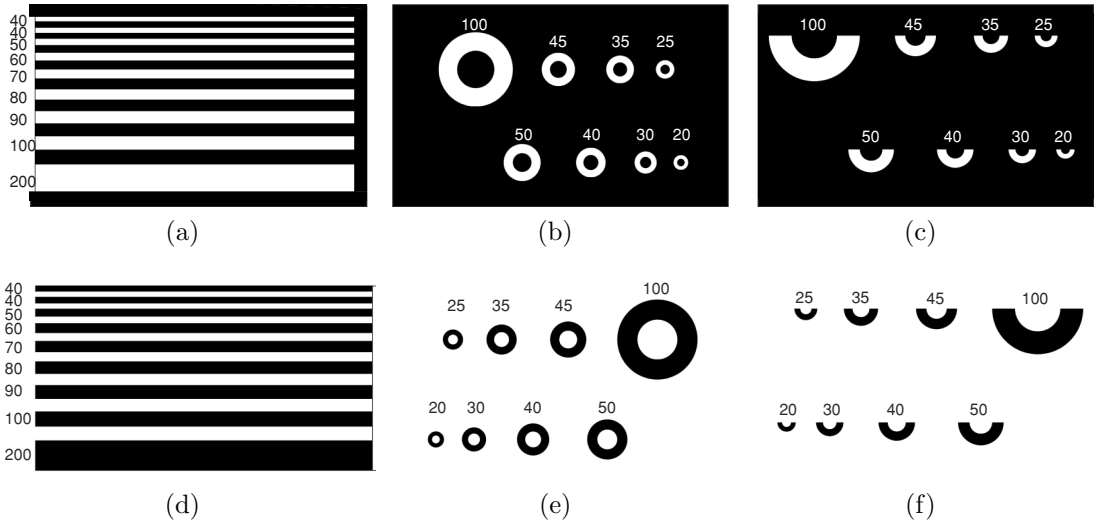

Figure 4.7: Test patterns used to evaluate DFR performance. The patterns were duplicated with both dark (a)-(c) and bright (d)-(f) fields. Line patterns (a) & (d) varied both in thickness and spacing. The numbers to the left of each line indicate their thickness in micrometres. Starting from the top lines in (a) and (d), the spacing between each line increases in 10 μm steps from 40 μm up to 100 μm. Circular (b) & (e) and semi-circular (c) & (f) patterns. The values above each pattern indicate the inner diameter and channel width of each pattern.

4.2.4 Characterisation of the dry film resist

Experiments were conducted to evaluate the performance of the photoresist and to optimise the fabrication process. The patterns shown in Figure 4.7 were replicated in dry film resist laminated on to glass slides. The patterns were designed to evaluate the ability of the DFR to resolve typical channel design elements. The design elements included channels of varying size in close proximity (Figure 4.7a & 4.7d), circular channels (Figure 4.7b & 4.7e) and corners (Figure 4.7c & 4.7f). Developed slides containing the test patterns were inspected under a Nikon LV-UDM optical microscope equipped with a DS-Fi CCD camera.

4.2.5 Cross-section profiling

Cross-sectioned samples were mounted on to a microscope slide. The microscope slide was oriented on its side and held in position on a microscope stage with a document clip. Cross-section profiles were recorded with a Nikon LV-UDM optical microscope equipped with a DS-Fi CCD camera.

4.2.6 Demonstration device: peristaltic pump

The three-valve peristaltic pump design shown in Figure 4.8 was used to test the suitability of dry film resists in the creation of valved devices. The device was constructed by bonding a layer containing a fluidic channel on top of a layer containing valve channels. The valve layer was then irreversibly sealed by bonding with a glass microscope slide. The fluidic channel layer was created by pouring PDMS on to a rounded master, which had been created from dispensing hot glue on to a vacuum mould as described above. A rectangular master patterned with 50 μm tall features was used to obtain the vacuum mould. The layer containing valve channels was created by spin coating PDMS onto a rectangular master patterned with 75 μm high features. The spin coating speed was selected to result in a PDMS film taller than the replication master features. By this method the membrane required between valve and fluidic channels was directly integrated into the valve layer.

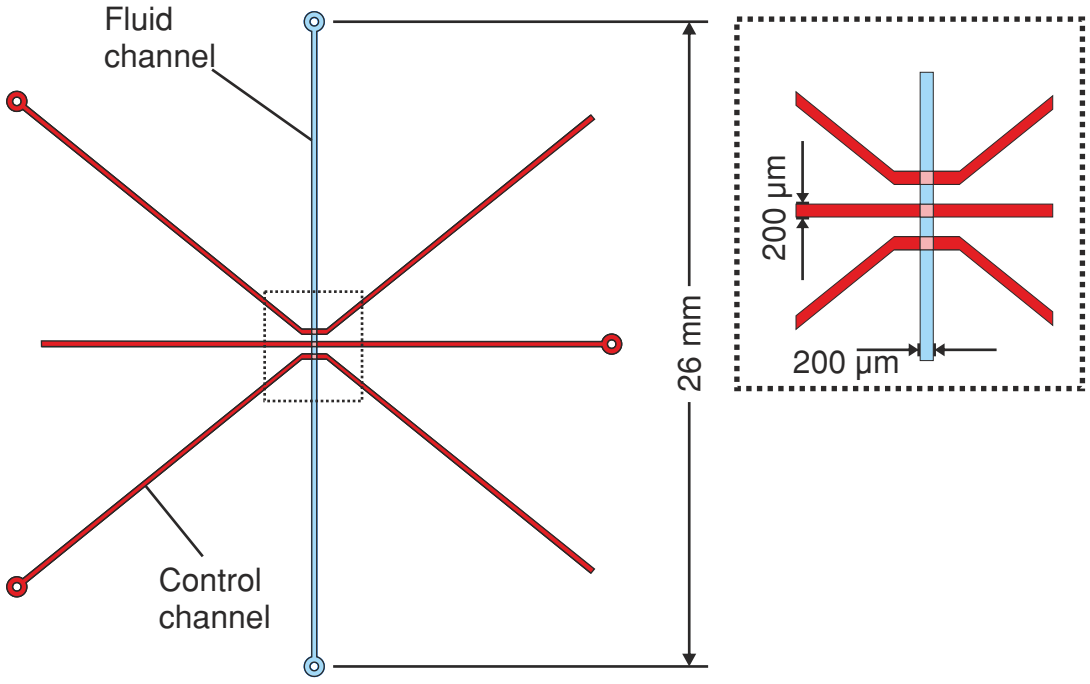

Figure 4.8: A three-valve peristaltic pump. The control channels (red) used in this design are configured as normally-open, push-up valves. The valve channel dimensions are: 200 μm wide by $\times$ 75 μm deep.

4.2.7 Demonstration device: testing

Regulated positive pressure was supplied from an air compressor (Thorlabs PTA511, Thorlabs UK) to the inputs of 3 way normally closed solenoid valves (Clippard Minimatic Mouse Series, The West Group, Hampshire, UK). Tygon® tubing was used to connect the outputs of the solenoid valves to the control channels of the peristaltic pump. The solenoid valves were powered with 6 Vdc from converting the output of a 15 Vdc 5 A rated switched-mode power supply. Switching of the solenoid valves was controlled by a USB interface (Phidget interfacekit 0/16/16, Active Robots UK) and custom software (see Appendix B).

Control channels of the peristaltic pump were filled with an aqueous solution using the channel outgas technique described by Monahan et al. (2001). The resistance of closed on-chip valves to pressurised flow was determined by measuring the pressure delivered to the valve and flow channels. This was achieved by first priming the fluidic channel of a pump with deionised water. Food colourant was then injected into one inlet of the pump, which allowed for visual determination of valve leakage. A valve was closed and the food colourant pressurised. Pressure readings were obtained with pressure transducers (PX40 100 PSI 0 to 4.5 Vdc output, Omega Engineering UK). Measurements were recorded from the pressure transducers using a National Instruments USB DAQ 6008 and Labview software. Pumping experiments were recorded under a stereo zoom microscope (Zeiss Discovery V8) with video captured using a Zeiss Axiocam ICc1 camera and Axiovision software.

4.3 Results and discussion

4.3.1 Resist processing and characterisation

Processing both types of resist took approximately 40 minutes to complete, which is comparable to the time required to process a 50 μm layer of SU-8 (see Table 4.1). It was found that due to the regular 10 minute intervals between processing steps for the DFR, up to four microscope slides measuring up to 75 mm $\times$ 50 mm in size could be processed in 2 minute staggered intervals by one person in under an hour. Developing time varied but generally did not exceed more than 6 minutes. The variation experienced during developing was dependent on the thickness of the resist being developed, with thicker films taking longer.

Table 4.1: Comparison of SU-8 50 and AM 150 Processing Times

SU-8 50 50 μm		AM 150 50 μm	
Spin	30 s	Prebake	10 min (110 ^{o}C)
Soft Bake	3 min (65 ^{o}C)	Laminate	20 s
	6 min (95 ^{o}C)	Cool	10 min
Exposure	17 s	Exposure	10 s
Post-Exposure	1 min (65 ^{o}C)	PEB	10 min (65 ^{o}C)
Bake (PEB)	6 min (95 ^{o}C)	Cool	2 min
Develop	6 min 30 s	Develop	$<$ 6 min
Hard Bake	10 min		
Total	33 min 17 s	Total	38 min 30 s

Vulto et al. (2005) experienced cracking in the laminate of a laminated slide if it was cooled too quickly after a post exposure bake, and the cracking was found to occur independent of substrate. The cracking problem was not experienced here even when placing a slide on an aluminium heat sink. The absence of cracking could be due to the linear thermal expansion coefficients of the laminate and glass slides being similar enough to cause minimal thermal stress during cooling.

The test pattern characterisation results are shown in Figure 4.9. The patterns obtained in the DFR from the dark field mask (Figure 4.9a–4.9e) were capable of being reproduced close to their designed sizes. The dry film was capable of resolving the smallest of the line patterns. The width of the smallest reproduced line pattern was measured to be 41.84 μm. At this width the aspect ratio was calculated to be 1.20:1 for the 50 μm thick resist. The smaller width line patterns

exhibited more pronounced rounding at their ends when compared to the larger width line patterns. As larger lines were found to take longer to develop than smaller lines, the rounding effect is thought to be due to overdeveloping. In the circle patterns (Figure 4.9c) measurements revealed features below 40 μm were significantly larger than their targets, ranging from 11% larger at 35 μm up to 44% larger at 20 μm. Similar results were obtained for the corner patterns (Figure 4.9e); corners below 25 μm were however completely etched away. Rounding was again more pronounced at smaller dimensions.

The bright field mask, which would allow for sunk-relief features to be created, resulted in poorer reproduction of the test patterns when compared to the dark field mask patterns. The smallest relief pattern achieved (Figure 4.9b) was measured to be 36.7 μm, a 10.1% error. The error improved modestly with increased relief size. A 200 μm relief pattern the error was 7.5%. Worse yet were the reproduced circle (Figure 4.9d) and corner relief patterns (Figure 4.9f) with all features measured to be significantly smaller than designed. Increasing the UV exposure time would result in smaller features as more resist would remain after developing. Increasing the development time for a given UV exposure had little effect resulting in features of similar size.

From the results above, the DFR and fabrication process should be suitable for creating the replication masters necessary for integrated valve PDMS devices, particularly as features as small as 40 μm wide by 50 μm can be supported. This is within the range of feature sizes used for valve devices (Studer et al., 2004). Note from these results that 40 μm features could be achieved despite the UV light source used to pattern the DFR not being collimated. Previously it was found that patterns created in dry film resist smaller than 130 μm (Vulto et al., 2005) and 200 μm (Stephan et al., 2007) were not possible without a collimated light source.

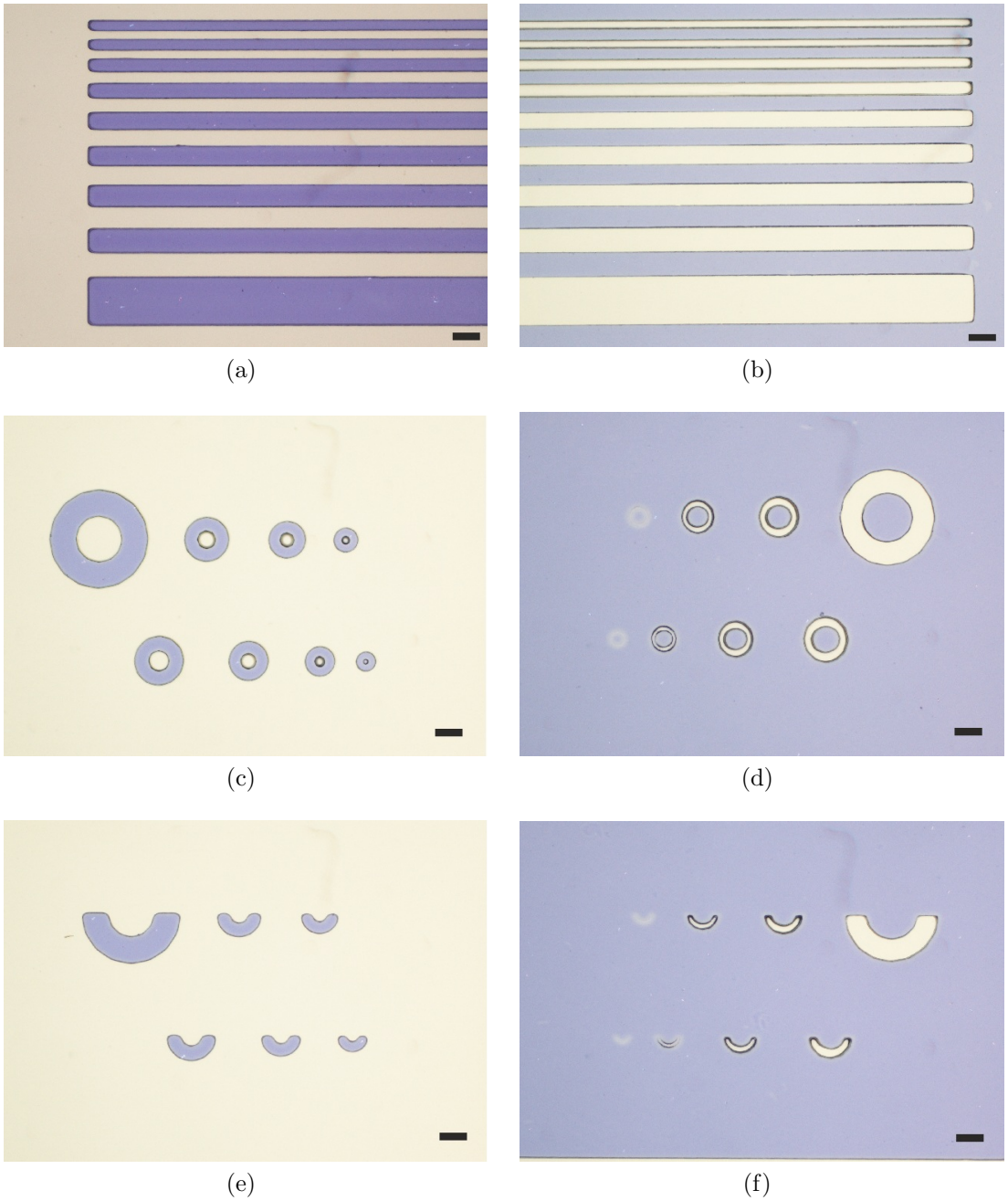

(a) (b) (c) (d) (e) (f)

Figure 4.9: Resulting test patterns in dry film resist. Patterns from dark (a), (c), (e) and bright (b), (d), (f) field masks. Scale bars: 100 μm.

4.3.2 Patterning PDMS

4.3.2.1 Spinning thin films

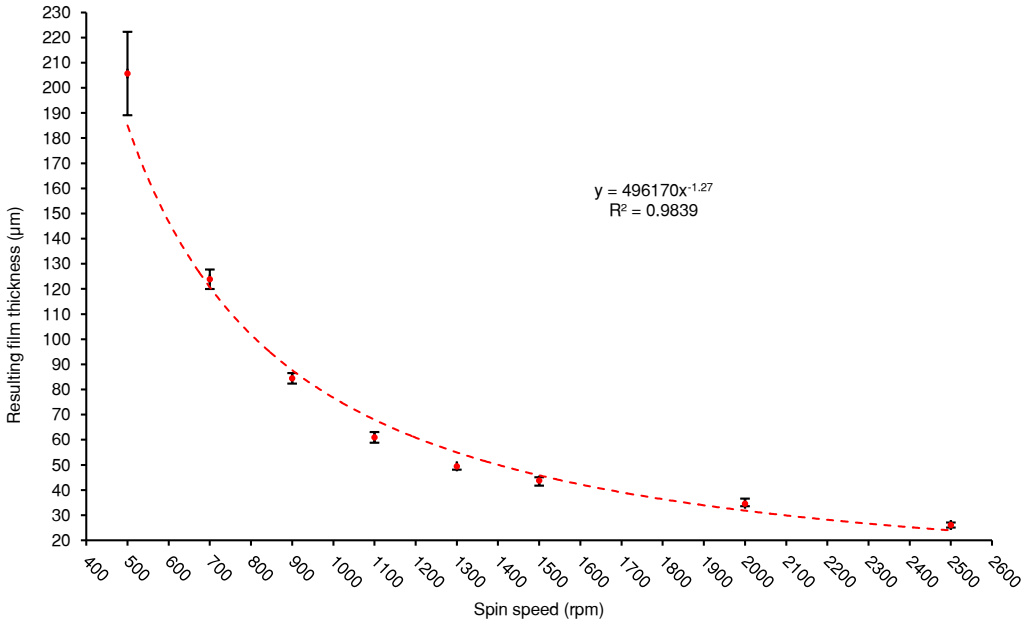

Figure 4.10: PDMS film thickness versus spin coating speed.

Plotted in Figure 4.10 are results obtained from characterising the effect of spin speed on PDMS film thickness. The trend in the data follows a power law as expected from similar results reported in the literature (Zhang et al., 2004).

4.3.2.2 Rectangular channels in PDMS

A PDMS microchannel patterned with a DFR master is shown in Figure 4.11. The width of the channel was measured to be 203.76 μm, slightly less than the designed value of 204 μm. The channel was designed to be 204 μm to accommodate for PDMS shrinkage during curing (Lee and Lee, 2008), however shrinkage was found to be minimal.

PDMS channels patterned with DFR masters were cross-sectioned so that profiles could be measured. In Figure 4.12 it can be seen that the sidewalls of the PDMS channel are near vertical, despite the DFR master having been created without a collimated light source.

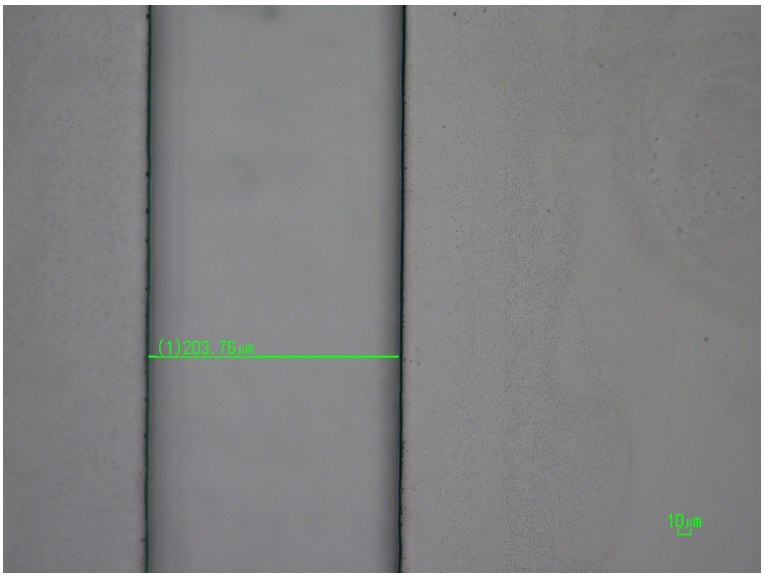

Figure 4.11: An approximate 200 μm wide channel patterned in PDMS using a DFR replication master. Scale bar: 10 μm.

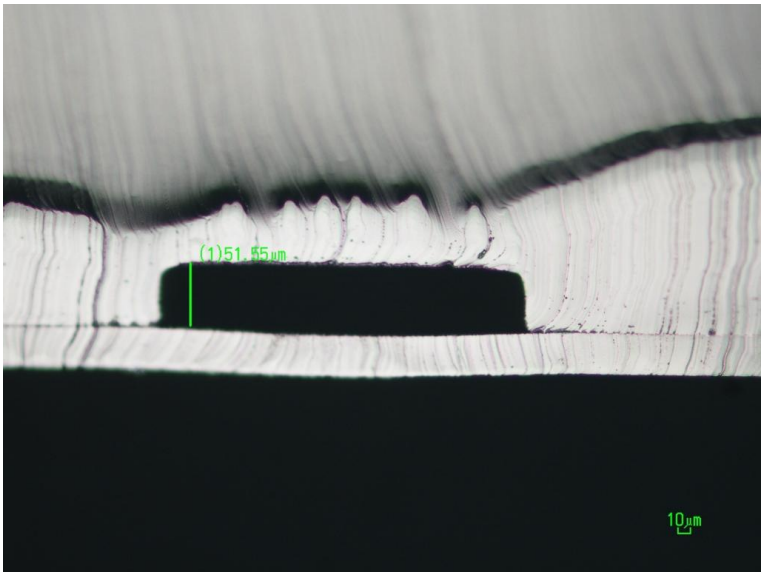

Figure 4.12: Cross-section of a PDMS channel patterned with a DFR replication master. The cross-sectioned channel was bonded against a thin PDMS film to aid assessment of the cross-section profile. Scale bar: 10 μm.

4.3.2.3 Rounded channels

Replication masters could be obtained quickly and simply within 10 minutes by using hot glue and a vacuum mould. No silanization treatment was required, therefore as soon as the hot glue had cooled the rounded master could be used. The hot glue was found to begin melting at temperatures above 55 ^{o}C. Therefore, curing of PDMS on top of a glue replication master had to be limited to a maximum temperature of 50 ^{o}C. The lower cure temperature resulted in both longer cure times and cured PDMS that was noticeably less rigid than PDMS cured at 100 ^{o}C. The softer PDMS would make processing, such as hole coring more difficult. The PDMS mix ratio was modified to increase the amount of catalyst. This ensured a shorter cure time, as well as PDMS that was similar in firmness to PDMS cured at 100 ^{o}C.

A glue master containing a rounded channel is shown imaged from above in Figure 4.13a. The channel width was measured to be 205.25 μm, which is slightly more than the designed channel width of 204 μm. A cross-section profile obtained from PDMS cured on the glue master is shown in Figure 4.13b. The channel height was found to be lower at 30 μm than the height of the channel within the vacuum mould, which was 50 μm. To make up for the difference in height, a vacuum mould containing a deeper channel could be used. So far the simple case of a creating a rounded master with a lone straight channel has been demonstrated. To test the applicability of the method, a design containing several channels that meet at junctions was attempted. The result is shown in Figure 4.14. It can be seen that

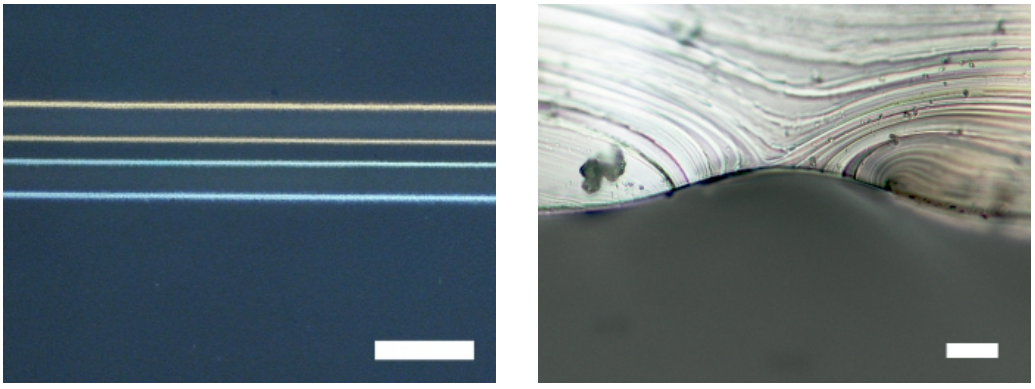

(a) (b)

Figure 4.13: A rounded replication master and the resulting profile in PDMS. The replication master contains only a straight channel (a); scale bar: 200 μm. The resulting cross-section profile of PDMS patterned with the replication master (b); scale bar: 30 μm.

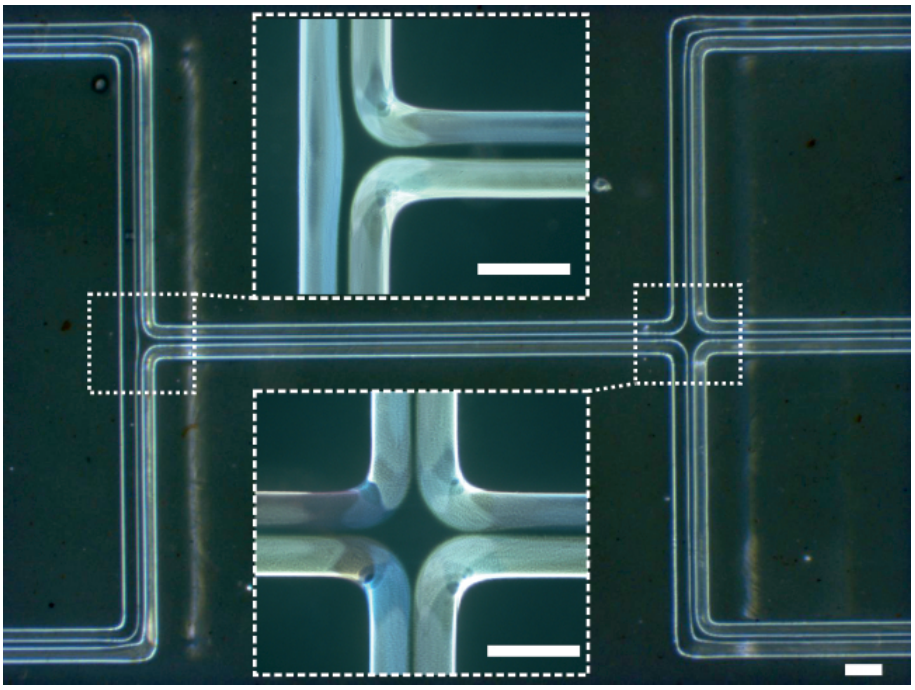

Figure 4.14: A rounded hot glue master containing several microfluidic channels that meet at junctions. The insets show the junction points at greater magnification. Scale bars: 200 μm.

more complex designs can be implemented in rounded masters made with hot glue and a vacuum mould.

4.3.3 Peristaltic pump

Basic characterisation tests were first performed on the experimental set-up to determine limits of operation. Shown in Figure 4.15 are results from solenoid valve actuation tests. The solenoid valves were connected to pressure transducers and programmed to switch with a delay between opening and closing. It appears that switching times lower than 40 ms are not sufficiently long enough to allow near complete pressurisation. This limitation was found to be dependent on the air content of the tubing connected to the solenoid. By partially filling the tubing with water, complete pressurisation was achieved with switching times as short as 15 ms.

Two types of pumps were fabricated, one with a rounded fluidic channel and the other with a rectangular fluidic channel. The resistance of closed on-chip valves to pressurised flow was measured for both types of pump. The pump containing a rectangular fluidic channel was found to perform relatively poorly. The valves in the rectangular channel pump could not stop flow in the fluidic channel despite being driven with 4 bar of pressure. Conversely the valves in the rounded channel pump when pressured with 2 bar of pressure, were found capable of stopping flow driven with pressure in excess of 100 kPa.

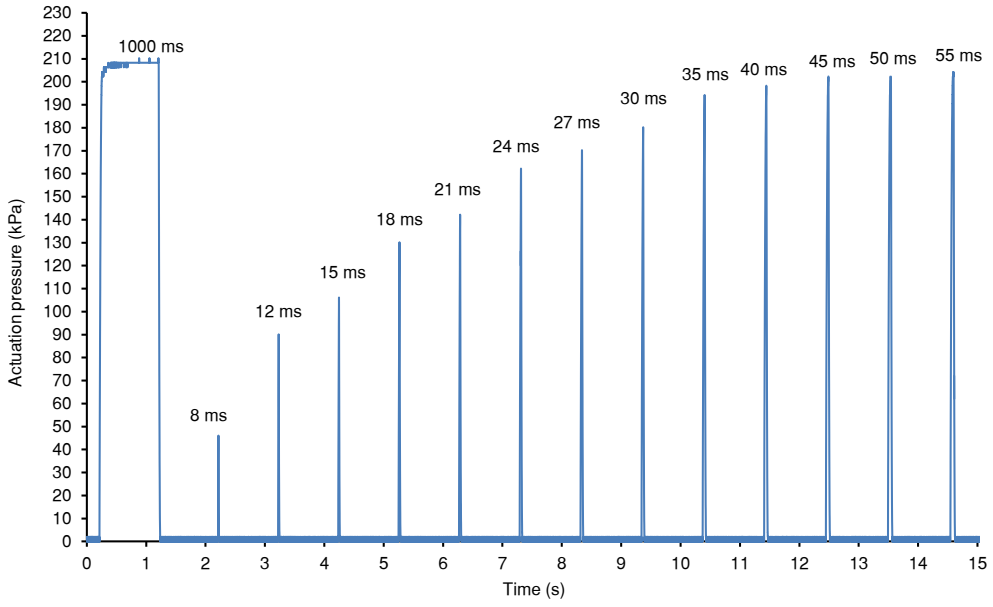

Figure 4.15: Pressure measurements recorded from the outlet of a solenoid with delayed switching between opening and closing. The delay between open and closing of the solenoid is indicated above each peak.

The operation of the pump is shown in Figure 4.16. The valves were driven with 2 bar of pressure and the pump was operated with a 50 ms delay between valve switching. The 50 ms delay translated into a pump cycle taking 300 ms to complete. To estimate the flow rate of the pump, food colourant was injected into the fluidic channel, allowed to settle, and then monitored during pumping. The distance travelled by the front of the food colourant was measured for 30 s of pumping. The food colourant was found to travel at a linear velocity of 632.1 μm/s. This was converted into flow rate by multiplying the linear velocity with the cross-sectional area of the channel. The cross-sectional area of the channel was calculated by treating the cross-section profile as half an ellipse. Assuming a channel height of 30 μm and channel width of 210 μm, the flow rate was calculated to be 93.83 pl min^{-1}. The pump flow rate is quite low when compared to the literature (e.g. (Graf and Bowser, 2008)). Optimisation of the pump design is required, however for the purpose of proof of principle the pump design was adequate. During fabrication of the pump an important issue became apparent. That was how to obtain accurate alignment between the control and fluidic layers when bonding each layer together.

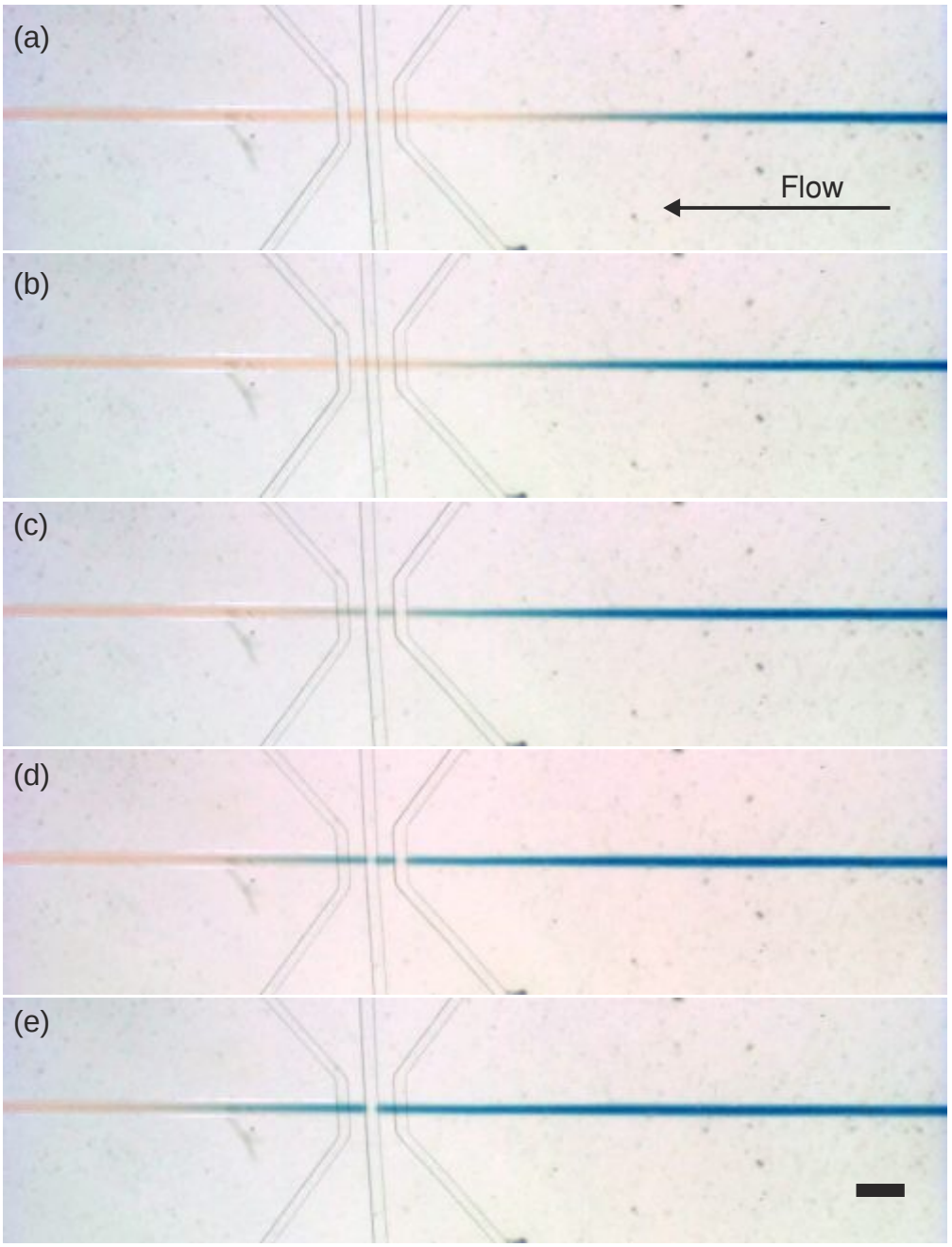

Figure 4.16: Operation of the peristaltic pump. The action of the three integrated valves drives the blue food colourant from right to left (a)–(e). Scale bar: 800 μm.

4.4 Summary

A set of fabrication techniques has been presented that allow for integrated valved devices to be created in a standard chemistry laboratory environment without need for sophisticated equipment. Dry film resists are laminated onto glass slides to obtain replication masters containing features with rectangular profiles. Replication masters containing features with rounded profiles are fabricated by depositing hot glue on to vacuum moulds. This method for creating rounded masters is capable of supporting simple and more complex channel designs. The implementation of a peristaltic pump device by using the fabrication techniques described here, served to demonstrate the suitability of the methods to the creation of integrated valve devices. From this work, barriers to integrated valve technology are now diminished. However an issue that was not fully addressed here was how to obtain good alignment between the device layers when constructing valved devices.

Chapter 5

Water alignment vacuum extraction

5.1 Introduction

The creation of sophisticated microfluidic devices, such as three-dimensional mixers (Lee et al., 2006; Cha et al., 2006) or integrated valve devices (Thorsen et al., 2002; Hong et al., 2004b), typically requires several individual device layers to be irreversibly assembled vertically on top of one another. Each device layer has to be accurately aligned to ensure correct operation of the microfluidic device. Oxygen plasma bonding, which is one of the most commonly used methods for irreversibly sealing PDMS against PDMS or glass, makes the alignment of device layers particularly challenging.

The exposure of glass and PDMS substrates to an oxygen plasma causes their surfaces to become oxidised, resulting in the formation of reactive silanol groups (Si-OH). When two oxidised surfaces containing silanol groups are brought into contact, a condensation reaction takes place between the silanol groups resulting in the formation of covalent siloxane (Si-O-Si) bonds (Duffy et al., 1998). This process is rapid and completes within seconds. Therefore caution has to be exercised when aligning two plasma exposed PDMS layers, as contact between them would result in near instantaneous irreversible bonding.

Several research groups therefore use mechanical jigs to first align plasma exposed PDMS layers before bonding (Chiu et al., 2000; Hofmann et al., 2001; McDonald and Whitesides, 2002; Baek et al., 2005). However there exists a problem in that

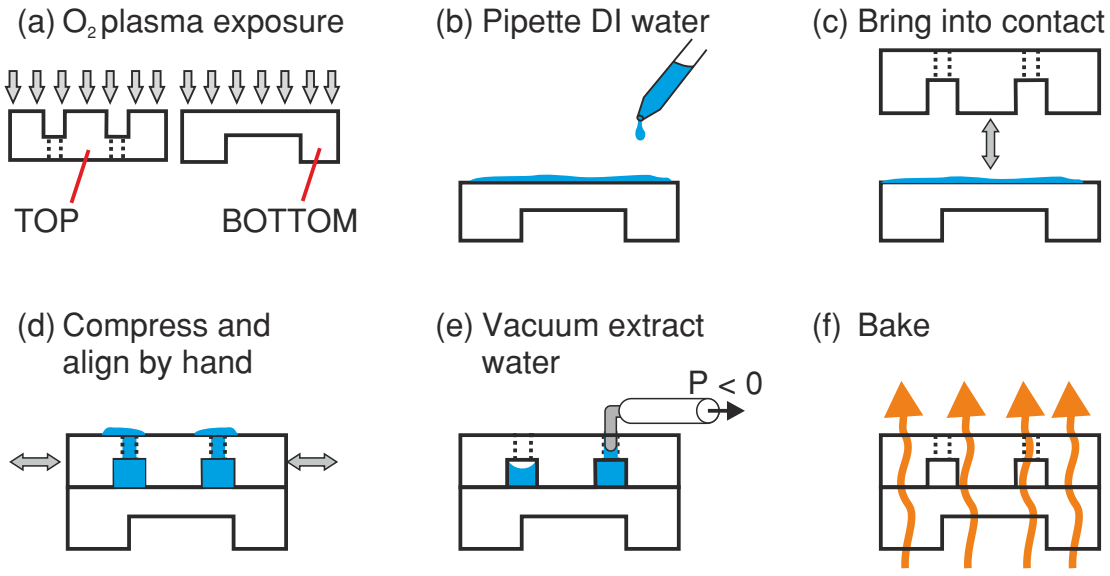

Figure 5.1: The WAVE technique included as part of the oxygen plasma bonding process. Two PDMS device layers TOP and BOTTOM are exposed to oxygen plasma (a). Deionised water is pipetted on to the BOTTOM layer (b) and the TOP layer is then brought into contact with water-covered BOTTOM layer (c). The two layers are compressed against each other and aligned by hand under a microscope (d). Water between the layers is then extracted by applying a vacuum to the inlets and outlets of the TOP layer (e). The two layers are then baked to finalise their bonding (f).

PDMS bonding can only be performed within the first few minutes after oxygen plasma exposure. The surface reactivity necessary for bonding degrades with time. By coating oxidised PDMS with hydrophilic liquids such as water, methanol and trifluoroethanol, the surface reactivity can be prolonged (Anderson et al., 2000).

Methanol can be used in combination with a mechanical alignment jig to address the issues of alignment and reactivity lifetime (Kim et al., 2005). Similarly without a jig, methanol has been used to align oxidised PDMS layers simply by hand (Jo et al., 2000). However methanol swells PDMS (Lee et al., 2003) sufficiently to warrant its exclusion from the alignment process (Moraes et al., 2009). The alternative is to use water, which does not swell PDMS. Water has been used in the alignment of oxidised glass and PDMS, as well as several oxidised PDMS layers (Irimia et al., 2004; Cho et al., 2009; Ding et al., 2011). But the effects of water on the bonding strength of device layers has not yet been fully explored and therefore is not well understood.

This chapter describes results from investigations into the effect of water on

bonding between PDMS and PDMS, and PDMS and glass device layers. Test devices are constructed to represent three device configurations that can be considered typical in microfluidics. The test devices are fabricated by (1) bonding a patterned PDMS layer to glass, (2) bonding a patterned PDMS layer against an equally thick featureless PDMS block, and (3) bonding a patterned PDMS layer against a thin PDMS film. The test devices are assembled both with and without water used as a lubricant. Pressure tests are conducted on the test devices to determine how much pressure can be supported. Analysis of the results from pressure testing are used to establish what effect water has on bonding. Also tested is a new technique introduced here called Water Alignment Vacuum Extraction (WAVE). The WAVE technique (Figure 5.1) can be used to obtain accurate alignment and robust bonding between oxidised microfluidic device layers, without need of mechanical jigs. The WAVE technique is shown to be capable of supporting the alignment of device layers in the construction of valved and three-dimensional mixer microfluidic devices.

5.2 Experimental methods

5.2.1 Device fabrication

PDMS devices were fabricated using the methods described in chapter4. Device layers were either directly bonded together or subjected to an alignment process after exposure to oxygen plasma.

5.2.2 Water alignment

The water assisted alignment procedure used here was based on that described by Cho et al. (2009) Alignment was performed between two device layers at a time; i.e. between an upper and a lower device layer. After exposure to oxygen plasma, a 50 μl drop of deionised water was pipetted onto the surface of a lower device layer. The complementary upper device layer was then brought into contact with the water-covered lower device layer. The upper device layer was then compressed by hand against the lower device layer to force out trapped air. While observing through a stereo zoom microscope (Zeiss Discovery V8) with oblique brightfield illumination, the two device layers were aligned by hand. Once aligned, the device layers were placed on a hot plate at 80 ^{o}C for 10 minutes. Afterwards, approximately 3.2 kPa of pressure was applied to the device layers using a sealed bottle filled with water. The device layers were then baked for an additional 50 minutes.

5.2.3 Water alignment vacuum extraction (WAVE)

Alignment was performed between two device layers using water as a lubricant as described above. Instead of baking the device layers after alignment, a vacuum (-500 mbar) was applied in turn to all fluid access holes. The vacuum apparatus consisted of a diaphragm pump (Air Admiral, Cole-Palmer UK) connected by Tygon® tubing to a 22 gauge (0.8 mm diameter) blunt syringe needle. The vacuum pump was turned off when moving the 22 gauge needle from one fluid access hole to another to prevent accidental separation of the device layers when moving the needle. Within a few minutes of vacuum extraction, fluidic channels would appear dry. At this point the upper device layer was compressed by hand against the lower device layer to force remnants of water from between the device

layers into the fluidic channels where it could be extracted. The device layers were subjected to continued cycles of compression by hand until all water from between the device layers had been extracted. Afterwards the device layers were baked for 30 minutes at 65 ^{o}C on a hot plate. The device layers were then baked for an additional hour on a hot plate set to 100 ^{o}C. After baking, the layers were left to cool to room temperature before being used.

5.2.4 Pressure testing: apparatus and procedure

Following Figure 5.2, pressure testing was performed using an air compressor (Thorlabs PTA511, Thorlabs UK) capable of producing up to 825 kPa of pressure. Blunt syringe needles 1.2 mm in diameter (19 gauge) were inserted into the ends of Tygon® tubing to serve as the interface between pneumatic components and test device inlets (1 mm diameter cored holes). Two pressure transducers (PX40 100 PSI 0 to 4.5 Vdc output, Omega Engineering UK) were set-up to provide measurements at the inlet and outlet of the test devices. This arrangement allowed for pressure losses to be accounted for. Voltage signals from the pressure transducers were captured using a National Instruments USB DAQ 6008 and Labview software. Pressure testing was conducted under a stereo zoom microscope (Zeiss Discovery V8) with images captured at 15 frames per second using a digital camera (Zeiss Axiocam ICc1) and Axiovision software. Pressure testing proceeded by adjusting the regulator on the air compressor from closed, up to a maximum pressure of 689 kPa (transducer limit) within 30 seconds.

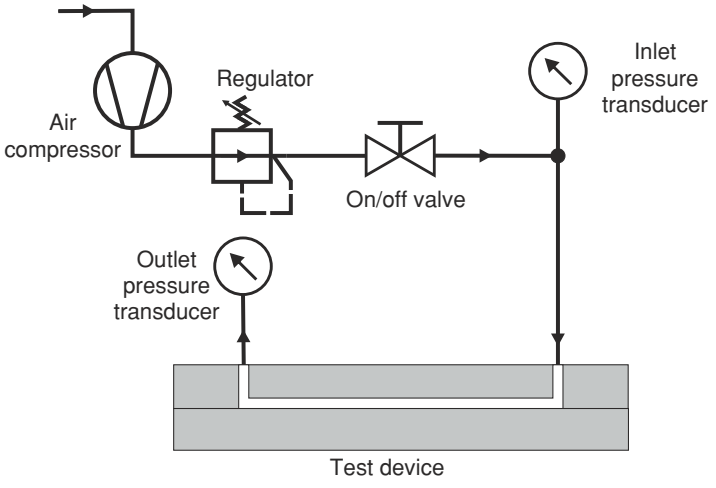

Figure 5.2: Schematic of the pressure test apparatus with connections test device.

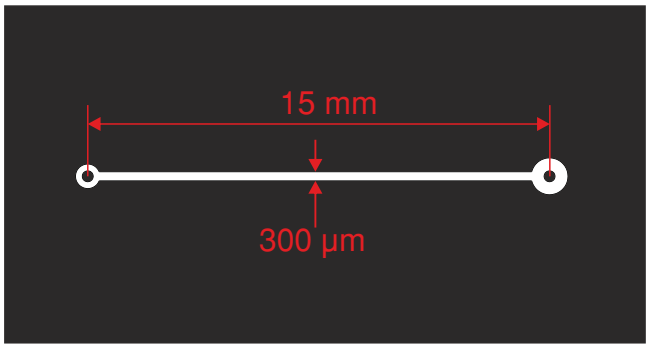

Figure 5.3: Pressure test device design. The channel height is 50 μm.

5.2.5 Pressure testing: test devices

The straight channel design shown in Figure 5.3 was used in testing the effects of water on bonding, as well as WAVE. The test channel device layers were obtained by pouring and baking PDMS on top of a replication master. The pressure test channel layers were bonded against featureless counter layers. The counter layers were chosen to represent three typical bonding scenarios. The bonding scenarios were: (1) sealing of the test channel against an equally thick featureless block of PDMS, i.e. "PDMS-Thick", (2) sealing of the test channel against a 100 μm thin PDMS film, i.e. "PDMS-Thin" and (3) sealing of the test channel against a cleaned glass microscope slide, i.e. "PDMS-Glass". A total of 18 test devices were created: Six controls that were directly bonded without water, six were aligned with water and six were subjected to WAVE. During alignment the devices layers were moved in arbitrary directions for 2 minutes. Test devices sealed with a thin PDMS layer were directly bonded to glass slides to represent the typical construction of a valved microfluidic device.

5.2.6 Demonstration device: F-mixer

The F-mixer (Figure 5.4) was used to test the applicability of the WAVE technique to three-dimensional channel designs. Dry film resist with a thickness of 50 μm was processed as described above to yield the necessary replication masters. PDMS was processed as thick device layers that were then exposed to oxygen plasma and WAVE aligned. To test the functionality of the F-mixer, food dye was driven through the inlets of a finished F-mixer with positive air pressure supplied by a diaphragm pump (Air Admiral, Cole-Palmer UK) capable of producing pressures up to 200 kPa.

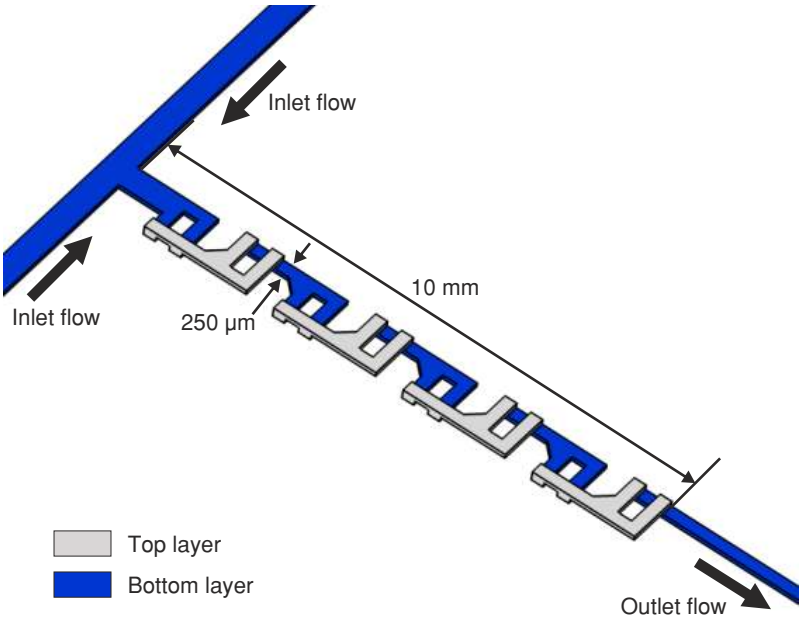

Figure 5.4: Schematic of the F-mixer. The F-mixer originally demonstrated by Kim et al. (2004) consists of a series of isolated features patterned in two separate planes or device layers.

5.2.7 Demonstration device: valved junction

The applicability of the WAVE technique was tested on an integrated valve device. The three-way to two-way junction design shown in Figure 5.5 was used, with valves controlling the fluid path between the inlet and outlet channels. PDMS was processed as described previously. Layers were exposed to oxygen plasma and aligned using WAVE. Control channels of the valve device were filled with aqueous solution using the channel outgas technique described by Monahan et al. (2001). Regulated positive pressure was supplied from an air compressor (Thorlabs PTA511, Thorlabs UK) to the inputs of 3 way normally-closed solenoid valves (Clippard Minimatic Mouse Series, The West Group, Hampshire, UK). Tygon® tubing was used to connect the outputs of the solenoid valves to the control channels of the valve devices. Switching of the solenoid valves was controlled by a USB interface (Phidget interfacekit 0/16/16, Active Robots UK) and custom software (see appendix B), which consequently actuated the on-chip valves of the demonstration device. Three Harvard Apparatus 11+ syringe pumps were used to drive fluid through the fluidic channel inlets of the valved device.

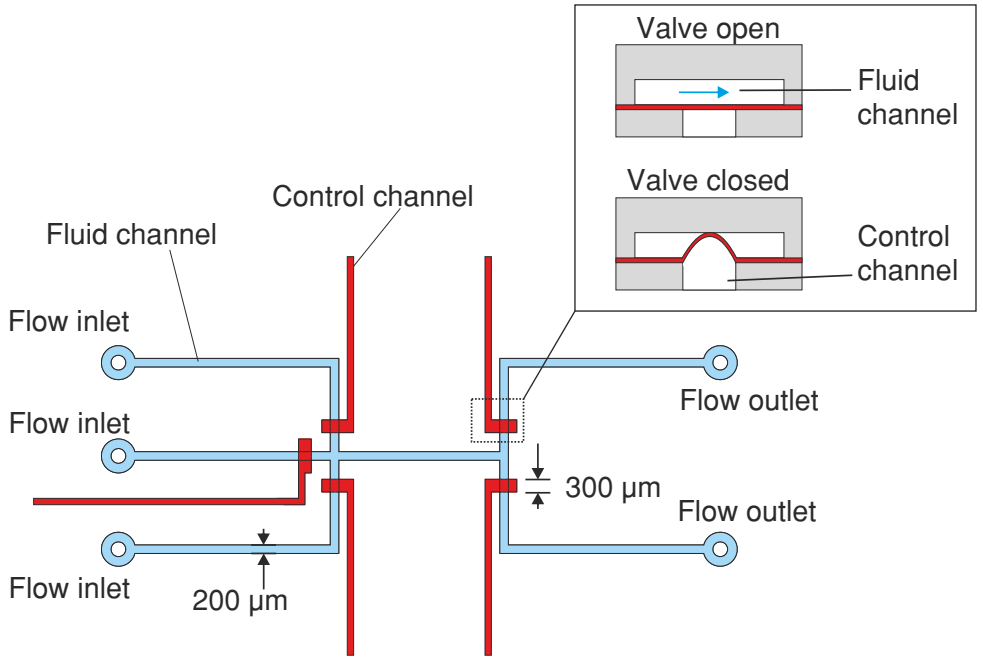

Figure 5.5: Valved junction design. Conceptually the normally-open valve design consists of a thin PDMS membrane sandwiched between two PDMS layers patterned with channels. Fluidic channels are open-ended whereas control channels are dead-ended. The intersection of a fluidic and control channel constitutes a valve. Positive pressure supplied to the control channel deflects the membrane into the fluidic channel thus stopping the flow.

5.3 Results and Discussion

5.3.1 Pressure testing

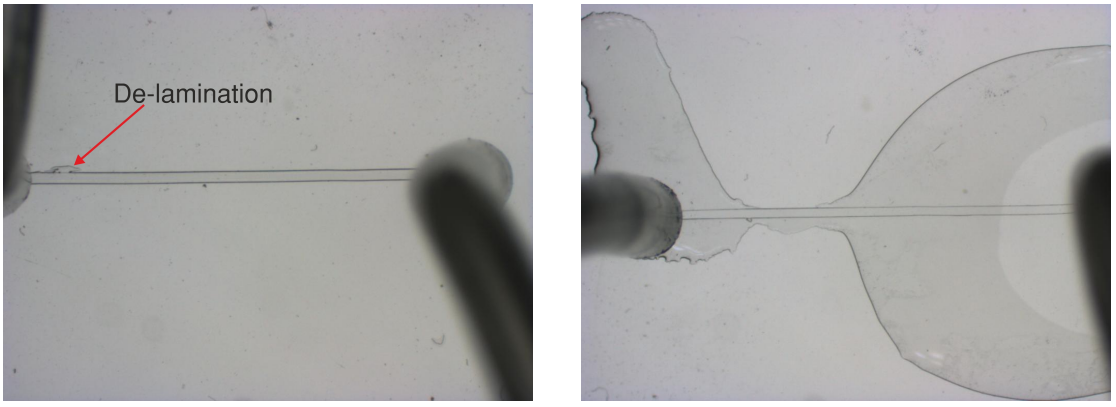

(a) (b)

Figure 5.6: Typical failure modes ranged from minor de-lamination (a) to more extreme failure (b). The channel widths of each test device are 300 μm.

Test devices would fail exhibiting two general modes as shown in Figure 5.6. Results from pressure testing are summarised in Figure 5.7. Control test devices, i.e. those that were directly bonded after plasma exposure, exhibited bond strengths capable of withstanding test pressures in excess of 570 kPa. This was consistent across all three bonding scenarios. The test pressures supported by the control devices are similar to the maximum bond strengths obtained by Bhattacharya et al. 2005 ($\approx$ 510 kPa). The variation between maximum and minimum supported test pressures here appears to be substantially lower than the variation in bond strengths achieved by Eddings and co-workers for directly bonded samples (Eddings et al., 2008).

Test devices that were water aligned but not subjected to WAVE failed at relatively low test pressures. Test devices constructed by sealing channels with a thin PDMS layer were found to be capable of supporting higher test pressures on average at 343$\pm$53 kPa (mean$\pm$standard error; n = 3). Conversely devices sealed with either glass or a thick PDMS layer supported lower test pressures, 168$\pm$51 kPa (mean$\pm$standard error; n = 3) and 176$\pm$23 kPa (mean$\pm$standard error; n = 3). It is believed that the discrepancy between the methods for sealing channels arises from an extra bonding step. Recall from the experimental methods above that channels sealed with thin PDMS layers were directly plasma bonded onto glass.

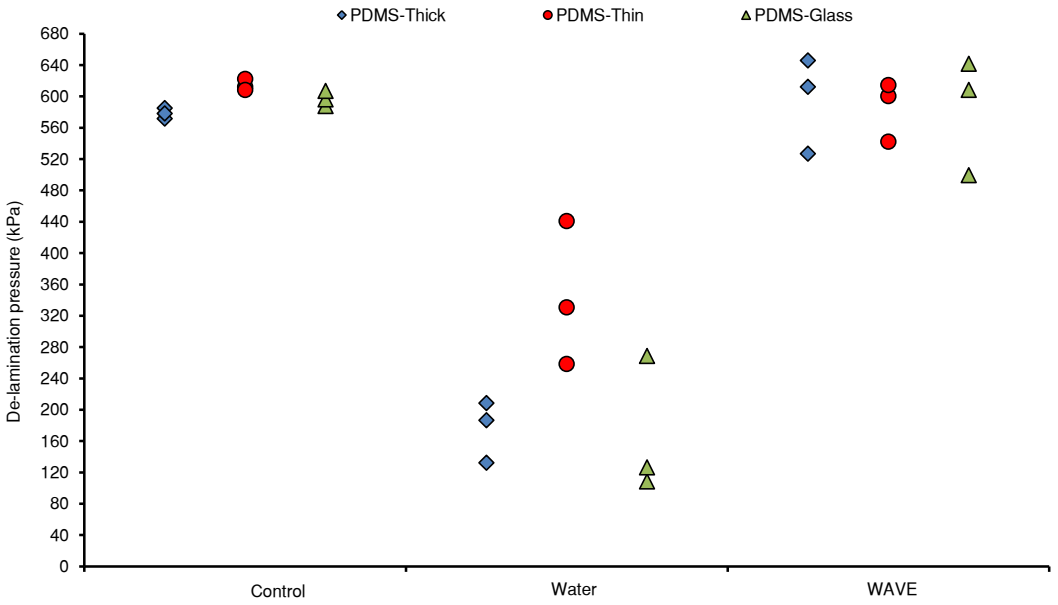

Figure 5.7: Pressure test results. Maximum supported pressures of devices, directly bonded without water (Control), aligned and bonded with water (Water), and aligned and bonded with WAVE.

This was performed to represent the typical construction steps of a valved device. The additional bonding step performed between channels sealed with a thin PDMS film to glass appears to have a more pronounced effect for devices that were water aligned.

Test devices that were subjected to WAVE were found to be capable of supporting test pressures on average, in excess of 580 kPa. Although similar in magnitude to the average supported pressure of control test devices, the variation of supported pressures was higher for devices subjected to WAVE. From these results, it appears that WAVE can be used without incurring the apparently detrimental effect water has on bonding.

5.3.2 Applicability of WAVE to three-dimensional microfluidic designs

Having demonstrated the WAVE method capable of producing devices that can sustain high pressures, the next step was to assess the applicability of WAVE in the fabrication of three-dimensional microfluidic designs.

5.3.2.1 Suitability for valved designs

Microfluidic designs that have integrated microvalves such as demonstrated by the Quake group (Unger et al., 2000) could benefit from the WAVE technique, particularly where alignment is required between hundreds of elements as in (Thorsen et al., 2002). The WAVE technique was tested on a more simple valved junction design, which consists of five valves requiring alignment over flow channels.

The need for potentially expensive equipment to obtain good alignment between the device layers was not necessary when using the WAVE method. Alignment was performed simply by hand. It was found that during alignment, natural evaporation of water from between device layers would aid alignment. This was because the effect of evaporation rendered the PDMS surfaces in contact slightly tacky, and therefore finer adjustments were more easily accomplished. For bonding to be strong between device layers, any water inside channels has to be completely extracted. This can take time, which does slow down the fabrication process. Furthermore the WAVE method requires open ended channels in order to generate enough flow to sufficiently remove water. Normally-closed valve designs cannot be aligned using WAVE. The WAVE technique made the device assembly relatively easy, particularly as the method was found to be far less time sensitive when compared to bonding directly after oxygen plasma exposure.

Presented in Figure 5.8 is a valved junction device aligned and bonded by exposure to oxygen plasma exposure and WAVE. The operation of the valved junction is shown in Figure 5.9. The on-chip valves were driven with approximately 2 bar of pressure. The flow rates for each inlet were set at 20 μl/min. Valved microfluidic devices typically include some tolerance in their designs to account for some misalignment. A more challenging microfluidic design is considered next, where tolerances are more critical than in valved designs.

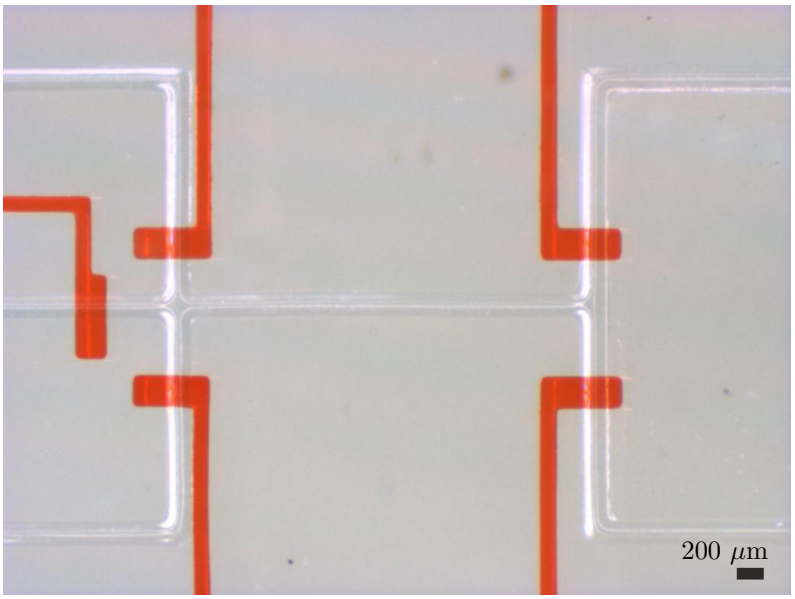

Figure 5.8: A valved junction device created using WAVE. Valve control channels are filled with red food colourant for imaging purposes.

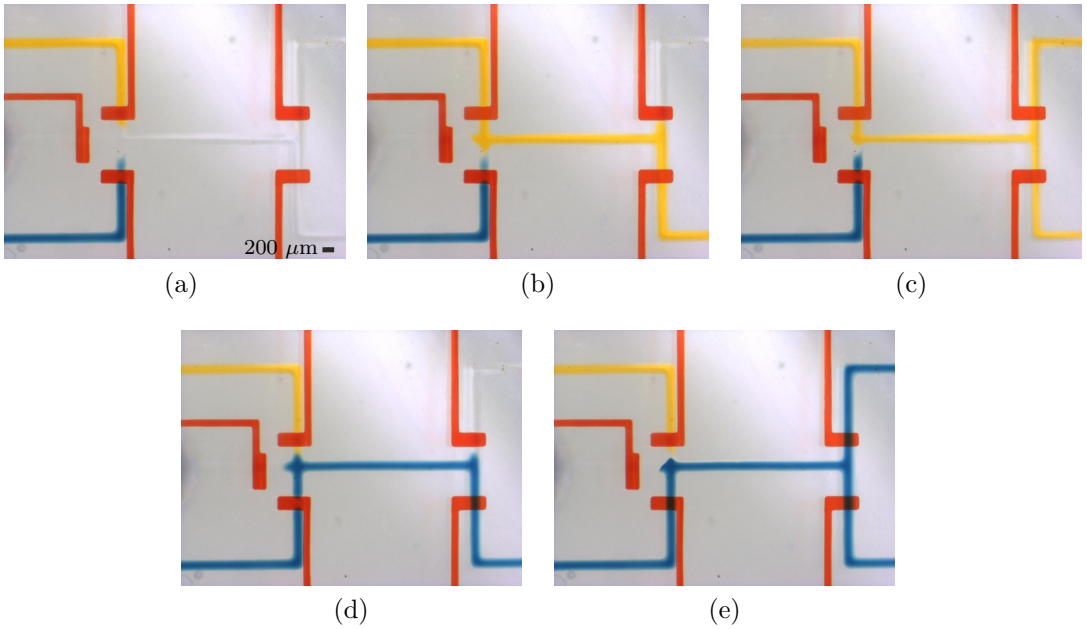

Figure 5.9: Operation of the valved junction. Flow is from left to right controlled by the switching of the on-chip valves (red). The three inlets on the left contain: yellow food colourant, water, and blue food colourant. The junction is cleared by opening the water inlet valve (a). Starting with all valves closed, the yellow inlet and lower outlet valves are opened (b). The upper outlet valve is opened (c). The junction is cleared once more with water. Again starting with all valves closed, the blue inlet and lower outlet valves are opened (d). The upper outlet valve is opened (e).

5.3.2.2 Suitability for channels spanning multiple planes

As seen from above, WAVE can be easily applied to microfluidic designs where channels are all in the same plane. However, in designs where channels are formed in more than one plane, WAVE may be more difficult to conduct as channels may not be continuous at first. The F-mixer (Kim et al., 2004) is one such design that can pose such a challenge. The F-mixer design consists of a series of isolated features patterned in two separate planes or device layers. The two planes, when brought into contact and correctly aligned, form a continuous channel that varies in all three spatial dimensions. Getting the two device layers of F-mixer to form a continuous channel requires finer tolerance during alignment.

The sequence in Figure 5.10 demonstrates the water supported alignment of two F-mixer layers after exposure to oxygen plasma. In Figure 5.11 vacuum extraction was initiated leading to a channel devoid of water. From the finalised device the misalignment was measured to be as low as 8.49 μm (measurement error: $\pm 0.49\mu$m) or 3.4% of the channel width. In Figure 5.12 the operation of the F-mixer is demonstrated, with food colourant being driven through the two inlets of the F-mixer at a pressure of 200 mbar. Despite challenges of F-mixer, the discontinuous elements and need for fine alignment, WAVE was found to remain a highly effective method.

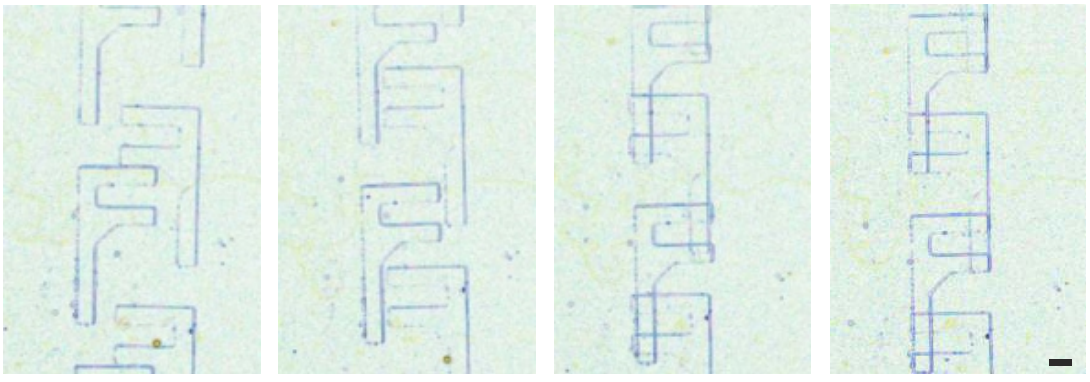

(a) (b) (c) (d)

Figure 5.10: Alignment of top and bottom layers of the F-mixer. These optical micrographs have been post-processed for visual clarity. Starting from (a) the top layer was moved until coarsely aligned over the bottom layer (b) through (c). A series of fine adjustments were then made to achieve the alignment shown in (d). Scale bar: 250 μm.

(a) (b)

Figure 5.11: Water extraction from the aligned layers of the serpentine lamination mixer. A 500 mbar vacuum was applied to the outlet of the serpentine lamination mixer (a). This process was continued until all water was extracted from the microfluidic channel (b).

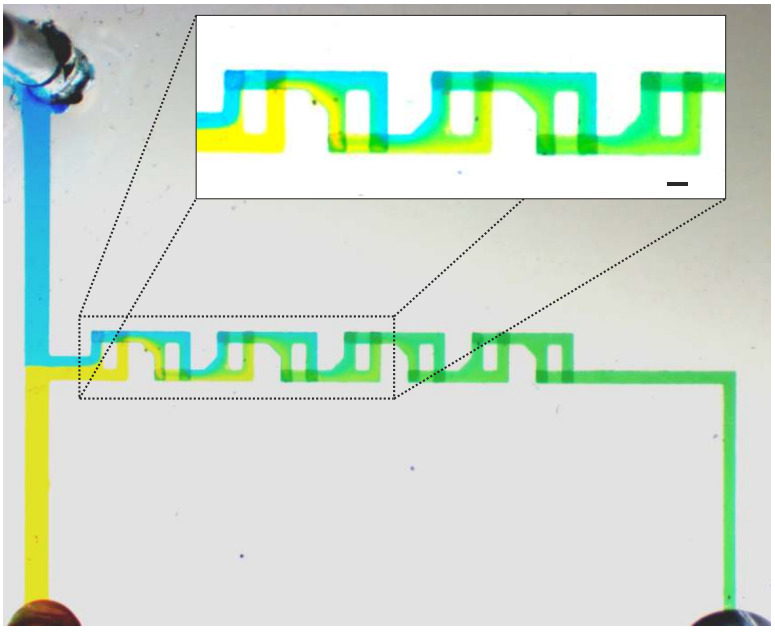

Figure 5.12: Operation of the F-mixer. Blue and yellow food colourant are driven into the F-mixer where they mix and form a green colour solution. Scale bar: 250 μm.

5.4 Summary

An investigation of the effect of water on the bonding strength of oxidised PDMS and glass samples has been conducted. Water was found to have had a detrimental effect on bonding strength. Despite this water can still be used as a lubricant and high bonding strengths achieved, provided all water is extracted from between device layers after alignment. The water alignment vacuum extraction (WAVE) technique is used to do this. The WAVE technique was shown to support the accurate alignment of valved and three-dimensional mixer device layers simply by hand. Complex devices can now be easily assembled by utilising WAVE in conjunction with oxygen plasma treatments.

Chapter 6

Ultraviolet photometer

6.1 Introduction

In order to conduct enzymatic computing studies with a microfluidic autonomous experimentation platform, a means of observing the enzymatic reaction is required. As a starting point for the development of the autonomous experimentation system, the enzyme malate dehydrogenase is of particular interest. Malate dehydrogenase catalyses the reaction of its substrate in the presence of nicotinamide adenine dinucleotide (Englard and Siegel, 1969). Nicotinamide adenine dinucleotide (NAD^+) is a biological molecule that participates in numerous enzyme-catalysed reactions, specifically reduction-oxidation (redox) reactions. Following Figure 6.1, within an enzyme catalysed redox reaction NAD^+ acts as an oxidising agent where it accepts electrons and a proton (H^+) from a substrate molecule. From the oxidation process NAD^+ is converted to a reduced form known as NADH, which is capable of donating electrons and a proton. The oxidised and reduced forms of nicotinamide adenine dinucleotide absorb light differently, particularly in the ultraviolet region between 340 and 360 nm where NADH absorbs relatively strongly compared to NAD^+. As the rate of conversion between NAD^+ and NADH is dependent on the catalytic activity of an enzyme, the difference in light absorption between the two forms can be exploited to monitor the rate of the enzymatic reaction.

Spectrophotometers are used to monitor the concentration of light absorbing molecules such as NADH. While spectrophotometers are capable of measuring over a broad range of optical wavelengths (190-1100 nm is typical), generally they are physically large and are not always easily interfaced with microfluidic

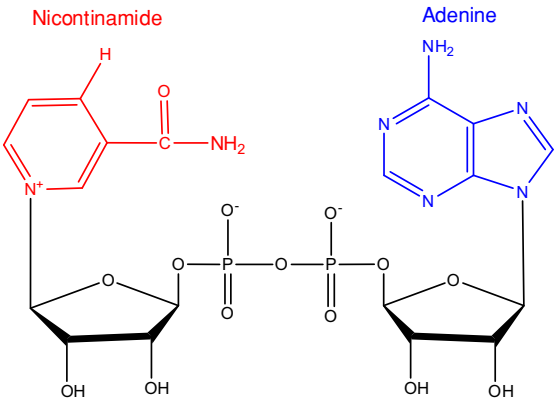

(a)

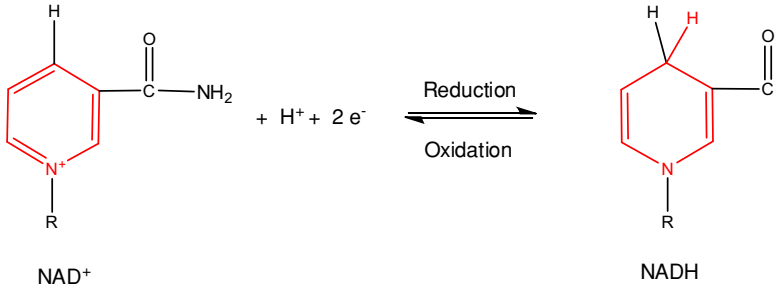

(b)

Figure 6.1: The structure of nicotinamide adenine dinucleotide in oxidised and reduced forms. The oxidised form of nicotinamide adenine dinucleotide NAD^+ (a). NAD^+ accepts a proton and electrons when participating in a redox reaction. The NAD^+ is converted to NADH (b), which is capable of donating its gained electrons and proton.

devices. Smaller fibre optic spectrophotometers do exist, but are expensive and are not available for all light wavelengths. With the increasing availability of low-cost semiconductor optoelectronics in numerous wavelengths, it is possible to build custom spectrophotometers cheaply and more amenable to integration with microfluidic devices. For example, application specific photometer–i.e. limited to one or two wavelengths–systems have been developed to measure both visible (Srinivasan et al., 2004) and UV (260 and 280 nm) (Pan et al., 2010) light in microfluidic devices.

Photometers can be assembled relatively easily from a few off-the-shelf electronic

components by ensuring the light source is unmodulated (Thal and Samide, 2001). However analogue circuits operating at low frequencies (near DC) are inherently vulnerable to noise. Lock-in amplification is one means by which electronic noise can be combated (described in section 6.2). There are several examples of custom lock-in amplification schemes in the literature (e.g. Sonnaillon and Bonetto 2005) some of which are designed to be used for optical measurements (Barragán and Artigas, 2001; Alonso et al., 2003; Sengupta et al., 2005). A low-cost digital lock-in amplifier currently can be assembled from code freely available online (Wenn, 2007) and a dsPIC® digital signal controller. A dsPIC running lock-in amplifier code is originally intended to be used for impedance measurements. For a dsPIC lock-in to be adapted to optical measurements, the necessary analogue circuitry requires development.

This chapter discusses the development of a low-cost, physically compact, UV photometer instrument built using optical semiconductor components and driven by a digital lock-in amplifier. The photometer is designed to enable optical absorbance measurements to be recorded from solutions containing NADH. With reference to the conceptual schematic of the photometer system in Figure 6.2, a 350 nm LED is used as the UV light source. A digital signal controller is configured to drive the UV LED and simultaneously capture measurements from a photodetection circuit. The digital signal controller is programmed to run a lock-in amplification algorithm, thereby providing some degree of noise immunity. The suitability of the UV photometer for measuring NADH is assessed by testing against a commercial spectrophotometer.

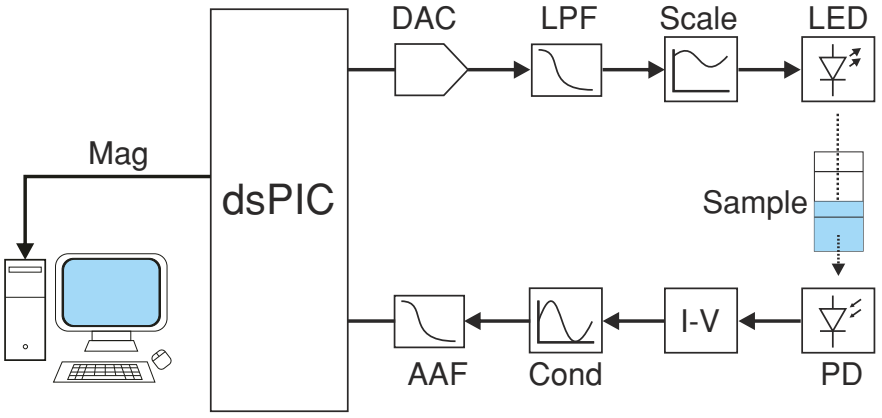

Figure 6.2: Conceptual UV photometer device incorporating a dsPIC-based lock-in amplifier. The dsPIC generates a modulated LED drive signal through a digital-to-analogue converter (DAC). A low-pass filter (LPF) smooths the LED drive signal before it is scaled. The scaled signal is then used to drive the UV LED. The modulated light detected by the photodiode (PD) generates a current that is converted to a voltage using a transimpedance amplifier (I-V). The voltage signal is conditioned before being fed into an anti-alias filter (AAF). The filtered signal is captured by the analogue input on the dsPIC where it is digitised. The magnitude of the signal (Mag) calculated by the lock-in algorithm is communicated to a personal computer.

6.2 Theory

This section discusses basic electronic circuit theory relevant to the work described later in this chapter. Photodiode amplification, noise and bandwidth considerations, and the theory of lock-in amplifiers are covered.

6.2.1 The transimpedance amplifier

Photodiode amplification circuits consist of a photodiode connected to the input of an operational amplifier (op amp) (Graeme, 1996). The photodiode can be configured as either operating in photoconductive or photovoltaic mode as shown in Figure 6.3. In photoconductive mode, a voltage bias is applied to the photodiode that reduces the photodiode's intrinsic capacitance (C_{PD}). This serves to improve the response time of the photodiode but at the expense of increased dark current, which is the current generated by the photodiode in the absence of illumination. The output from the photodiode increases logarithmically with increasing illumination when connected in the photoconductive configuration. In photovoltaic mode there is no bias applied to the photodiode. The response time

of the photodiode is therefore slower, however the dark current is minimised. The output of the photodiode increases linearly with increasing illumination when connected in the photovoltaic configuration. Therefore the photovoltaic mode is more suitable to applications where linear sensitivity to illumination is favoured. Before implementing a photodiode amplifier, the relationship between noise sources present in the circuit, as well the bandwidth and stability of the circuit require consideration.

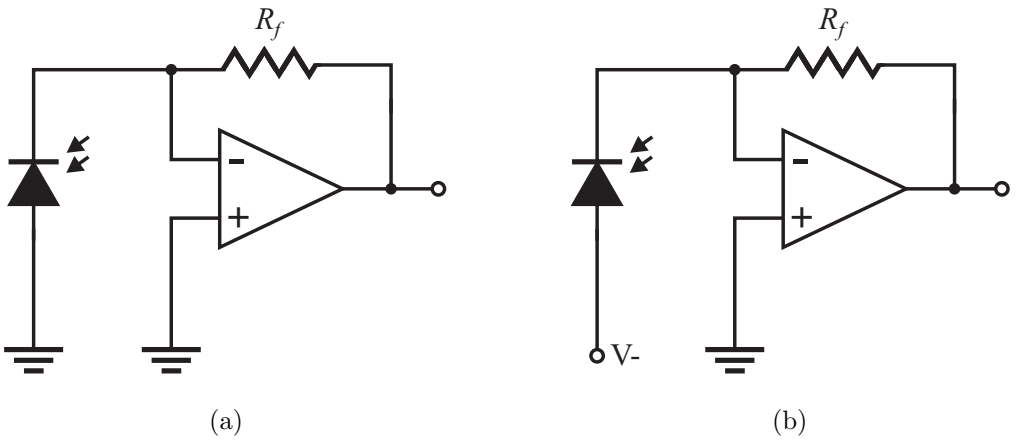

Figure 6.3: Photodiodes connected in two different modes to an op amp configured as a transimpedance amplifier. In (a) the photodiode is connected in photovoltaic mode with no bias. In photoconductive mode (b) a negative voltage bias is applied to the photodiode.

6.2.2 Stability analysis of the amplification circuit

Referring to the transimpedance amplifier model depicted in Figure 6.4 the analysis begins with a description the op amp behaviour. The op amp produces an output voltage (e_o) which is ideally the product of the input current (i_p) from the photodiode and the feedback resistor (R_f). The closed-loop gain (A_{cl}) of the op amp is equivalent to the value of the feedback resistor. However the circuit design does not end with simply selecting a value of R_f for a desired gain. As both the op amp and photodiode exhibit capacitance, C_d and C_{ia} respectively, the effect of the capacitance on bandwidth and stability has to be taken into account. This is done through performing a frequency response analysis of the transimpedance circuit which utilises three equations. The first equation is the transimpedance transfer function $T(s)$ which relates transimpedance gain and bandwidth:

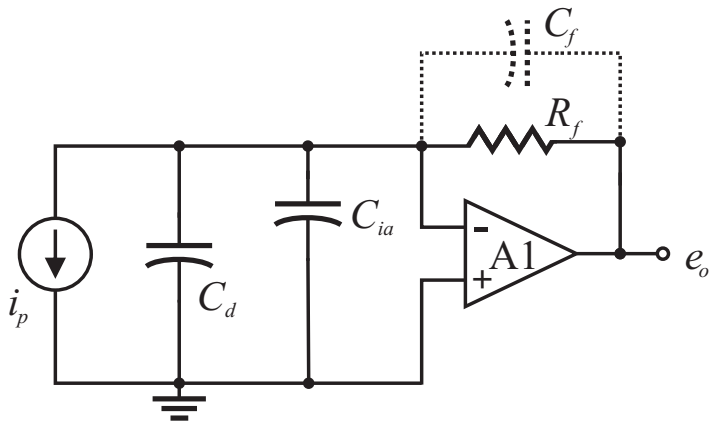

Figure 6.4: Transimpedance amplifier model. The photodiode is modelled as a current source operating in parallel with a capacitor C_d that represents the junction capacitance of the photodiode. The capacitor C_{ia} represents the input capacitance of the op amp A1. The feedback resistor R_f determines the transimpedance gain. The phase compensation capacitor C_f can be excluded depending on the stability requirements of the circuit.

$$T(s) = \frac{e_o}{i_p} \frac{Z_f(s)}{1 + \frac{1}{A_o(s) \cdot \beta(s)}} \tag{6.1}$$

with complex frequency variable $s = \mathbf{j}2\pi f$ and $\mathbf{j}^2{=}{-}1$, $Z_f(s)$ the feedback impedance, $A_o(s)$ the frequency dependent open-loop gain of the op amp and $\beta(s)$ the feedback fraction. Note where $R_f \gg C_f$, $Z_f \simeq R_f$. The second equation required for the frequency response analysis describes the frequency dependent open-loop gain of the op amp:

$$A_o(s) = \frac{A_o}{1 + \frac{s}{\omega_c}} \tag{6.2}$$

where A_o is the DC open-loop gain, and ω_c is the cut-off frequency where the op amp open-loop gain starts rolling off. The third equation describes the relationship between the feedback impedance (Z_f) and the impedance of the circuit presented at the input of the op amp (Z_i). The relationship is described by:

$$\beta = \frac{Z_i}{Z_i + Z_f} \tag{6.3}$$

From Figure 6.4 it can be seen that two scenarios can exist, one where a phase compensation capacitor (C_f) is omitted from the feedback loop and the second

where it is included. This leads to two definitions of β distinguished here as β_{uncomp} and β_{comp}. Starting with C_f omitted, the frequency response of $\beta_{uncomp}(s)$ is:

$$\beta_{uncomp}(s) \;=\; \frac{X_i}{X_i \,+\, Z_f} \;=\; \frac{\frac{1}{s \cdot C_i}}{\frac{1}{s \cdot C_i} \,+\, R_f} \;=\; \frac{1}{s \cdot R_f \cdot C_f \,+\, 1} \tag{6.4}$$

where C_i is the total input capacitance, i.e. $C_d + C_{ia}$. For $\beta_{comp}(s)$:

$$\beta_{comp}(s) \;=\; \frac{X_i}{X_i \,+\, (R_f \parallel X_f)} \;=\; \frac{s \cdot C_f \cdot R_f \,+\, 1}{R_f(C_i \,+\, C_f) \cdot s \,+\, 1} \tag{6.5}$$

With equations 6.1–6.4 a Bode plot can be constructed allowing for visualisation during frequency response analysis. The next step is to consider the stability of the circuit which concerns the noise gain, $\frac{1}{\beta s}$. Particular attention has to be given to the slope of the noise gain where it intersects $A_o(s)$. A near perpendicular intersection indicates gain peaking and instability at the corresponding frequency. To stabilise the circuit, the feedback capacitor C_f is included causing the noise gain to flatten. An appropriate value for C_f can be determined from,

$$C_f \;=\; \sqrt{\frac{C_i}{2\pi R_f f_{GBW}}} \tag{6.6}$$

where f_{GBW} is the gain-bandwidth product of the op amp, i.e. the frequency where $A_o = 1$. This concludes the bandwidth and stability analysis of the transimpedance circuit. Next the noise sources present in the transimpedance amplifier circuit and their analysis are discussed.

6.2.3 Noise analysis of the amplification circuit

Noise added to the photodiode signal through transimpedance amplification is an important factor in determining the performance of the circuit as well as providing a basis for component selection. The analysis begins with the noise model for the transimpedance amplifier is depicted in Figure 6.5. In the noise model there are voltage e_{ne} and current i_{ni} noise sources present at the input to the op amp, and a voltage noise e_nR due to the feedback resistor R_f. Corresponding to these three noise sources are three output noise voltages, E_{ne}, E_{ni} and E_{nR}. Through

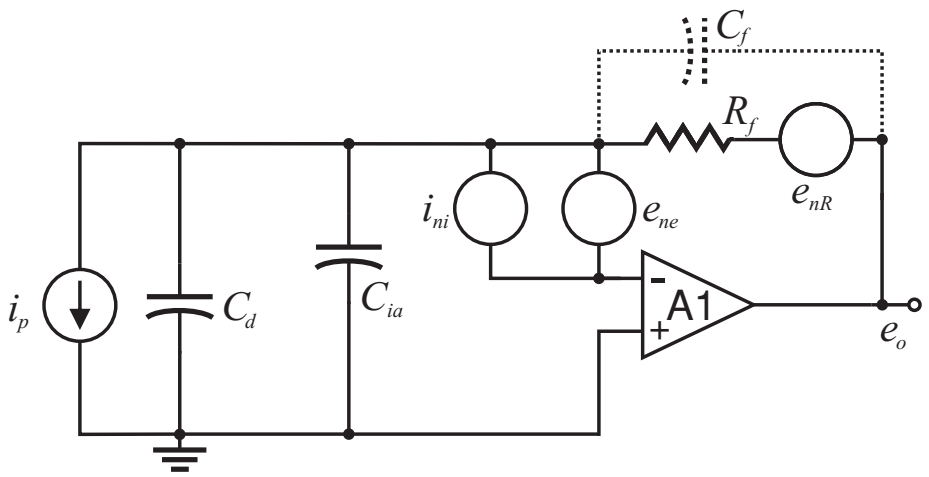

Figure 6.5: The transimpedance amplifier noise model. Voltage e_{ne} and current i_{ni} noise sources are present at the input to the op amp. A voltage noise e_nR due to the feedback resistor R_f is present at the output of the op amp.

root mean square (RMS) summation the total output noise RMS voltage can be calculated as:

$$E_{no(RMS)} = \sqrt{(E_{ne})^2 + (E_{ni})^2 + (E_{nR})^2} \tag{6.7}$$

Starting with the noise due to the feedback resistor:

$$e_{nR(RMS)} = \sqrt{4kTR_f\Delta f} \tag{6.8}$$

operating in the bandwidth Δf with feedback resistor R_f, k the Boltzmann constant (1.38×10^{-23} J/K) and T absolute temperature in Kelvin. This is an example of Johnson or thermal noise, which arises from the thermal agitation of charge carriers within the resistor. Johnson noise is class of white noise as its noise power does not vary with frequency. The thermal voltage noise e_{nR} transfers to the output of the transimpedance amplifier at unity gain, therefore $e_{nR} = E_{nR}$. Reducing thermal noise can be achieved through increasing the value of R_f as the output signal increases directly by R_f, the corresponding noise signal increases by $\sqrt{R_f}$. But increasing the feedback resistor reduces amplifier bandwidth.

The two other noise sources are products of the op amp. The current noise source i_{ni} arises from charge carriers crossing the potential barrier at the input of the op

amp. This type of noise is an example of shot noise and in this case it is related to the input bias current I_{b-} of the op amp by:

$$i_{ni}(RMS) = \sqrt{2qI_{b-}\Delta f} \tag{6.9}$$

at a bandwidth Δf with q the elementary charge (1.6×10^{-19} C). The shot noise is amplified by the gain of the transimpedance amplifier (i.e. $E_{ni} = i_{ni} \times R_f$) and appears as a voltage (E_{ni}) at the output. Shot noise like Johnson noise is white as it too does not vary with frequency. As shot noise is a property of op amp bias current, it can only be minimised through selecting an op amp with a low input bias current.

The input noise voltage e_{ne} of the op amp behaves in a more complicated manner when compared to the other two noise sources. It varies with frequency, exhibiting a $1/f$ relationship ($1/f$ or pink noise) up to a corner frequency where it then minimises and behaves as white noise. The input noise voltage e_{ne} is amplified by a noise gain A_n due to the feedback loop with $A_n = 1/\beta$. As the noise is frequency dependent it has to be integrated over a range of frequencies to obtain its contribution to the output noise E_{ne}:

$$E_{ne}(RMS) = \sqrt{\int_{f_l}^{f_u} (A_n \cdot e_{ne})^2 df} \tag{6.10}$$

with Δf equivalent to $f_u - f_l$. The noise gain varies with frequency which can complicate the integration. To simplify the process, the integration can be performed on split frequency segments of E_{ne}, which are then added to yield the E_{ne} for the full bandwidth. For example on five frequency segments:

$$E_{ne}(RMS) = \sqrt{(E_{ne1})^2 + (E_{ne2})^2 + (E_{ne3})^2 + (E_{ne4})^2 + (E_{ne5})^2} \tag{6.11}$$

Once again as for input noise current, the input noise voltage is op amp dependent.

6.2.4 Lock-in amplification

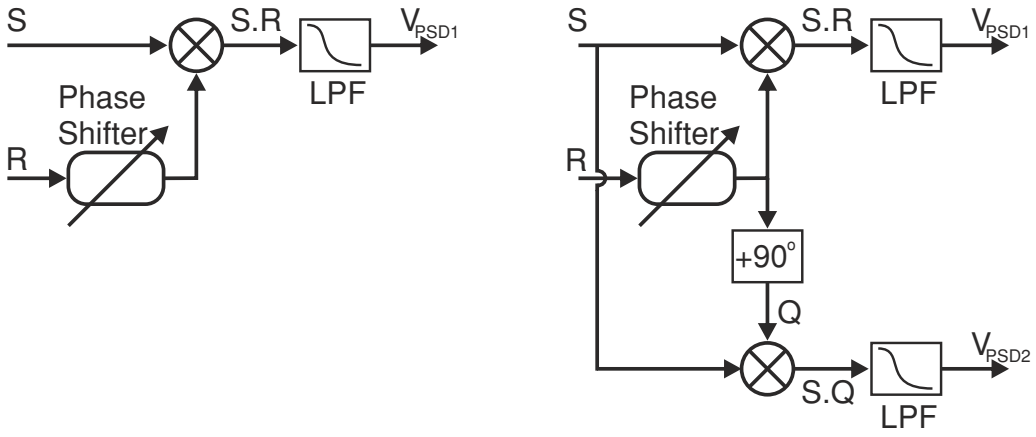

(a) (b)

Figure 6.6: Principle components of a lock-in amplifier. In (a) a single phase sensitive detector (PSD) multiplies the input (S) and reference (R) signals before feeding the product through a low-pass filter (LPF), which in turn produces the output V_{PSD1}. In (b) two PSDs are used. The reference signal is phased shifted by 90^o creating the quadrature signal (Q). In this case two outputs are generated V_{PSD1} and V_{PSD2} respectively which allow for the reduction of phase dependence on the signals.

Lock-in amplifiers are used to detect small signals within a noisy environment. Central to a lock-in amplifier is the phase sensitive detector (PSD), which is a signal mixer followed by a low-pass filter (Figure 6.6). In operation a signal is modulated at a reference frequency, which is then detected and demodulated. Demodulation is performed by multiplying the reference signal by the detected signal and then low-pass filtering the product to obtain a measure of the magnitude of the detected signal. By this approach noise signals at frequencies other than the reference frequency are rejected.

As an example consider a lock-in amplifier containing one PSD. The reference signal is a sine wave with amplitude V_{ref}, angular frequency ω_{ref} and phase θ_{ref}:

$$R(t) \;=\; V_{ref} \cdot \sin(\omega_{ref} \cdot t \;+\; \theta_{ref}) \tag{6.12}$$

similarly the detected signal is:

$$S(t) \;=\; V_{sig} \cdot \sin(\omega_{sig} \cdot t \;+\; \theta_{sig}) \tag{6.13}$$

Multiplying the reference and detected signals yields:

$$S \cdot R = \frac{V_{sig} \cdot V_{ref}}{2} \cdot \cos([\omega_{sig} - \omega_{ref}] \cdot t + \theta_{sig} - \theta_{ref}) - \frac{V_{sig} \cdot V_{ref}}{2} \cdot \cos([\omega_{sig} + \omega_{ref}] \cdot t + \theta_{sig} + \theta_{ref}) \quad (6.14)$$

with $\omega_{sig} = \omega_{ref}$ and after low pass filtering, the output from the PSD reduces to:

$$V_{PSD2} = \frac{V_{sig} \cdot V_{ref}}{2} \cdot \cos(\theta_{sig} - \theta_{ref}) \quad (6.15)$$

It can therefore be seen that the output from the lock-in amplifier containing a single PSD is sensitive to changes in the phase difference between the detected and reference signals. By incorporating a second PSD the phase dependence can be eliminated. This is achieved by taking the reference signal and phase shifting it by 90^o (Figure 6.6b) before multiplying it by the detected signal with a second PSD. The resulting output from the second PSD is:

$$V_{PSD2} = \frac{V_{sig} \cdot V_{ref}}{2} \cdot \sin(\theta_{sig} - \theta_{ref}) \quad (6.16)$$

By taking the in-phase I (i.e. V_{PSD1}) and quadrature Q (i.e. V_{PSD2}) components, the magnitude of the detected signal M independent of phase can be obtained:

$$M = \sqrt{I^2 + Q^2} = \frac{V_{sig} \cdot V_{ref}}{2} \quad (6.17)$$

6.3 Experimental methods

6.3.1 UV LED characterisation

Three different LEDs were selected as candidate light sources for the photometer. A Nitride Semiconductor (NS) 355 nm UV LED was purchased from Roithner Lasertechnik (Vienna, Austria). Two Fox Group (FG) 350 nm UV LEDs were obtained from DComponents (Vermont, USA). Of the two Fox Group LEDs, one was supplied with a ball lens and the other in a standard 5 mm package. A bench-top power supply unit with programmable current limiting capability was used to power the LEDs. The power supply unit (PSU) was set to limit current to 20 mA, which was the typical operating current for the three UV LEDs specified by both manufacturers. The voltage supplied to each LED was increased up to the current limit. The spectral emission and optical power output of the LED were then measured.

A Thorlabs (Cambridgeshire, UK) PM300E dual channel optical power meter equipped with a Thorlabs S120UV broadband (200 nm – 1100 nm) photodiode sensor was used to measure the optical power of a LED. The LED was positioned to be in contact with the photodiode sensor of the optical power meter during measurement. The emission spectra of the LEDs were recorded using an Ocean Optics HR2000+ USB UV-Vis spectrophotometer connected to a personal computer running SpectraSuite software (Ocean Optics, Dunedin, USA).

6.3.2 Circuitry: design and implementation

During the design process, the photometer circuitry was simulated in SIMetrix-SIMPLIS SPICE software (SIMetrix Technologies Ltd, UK). Printed circuit board fabrication and circuit assembly were conducted in-house. The photometer circuitry was implemented as three physically separate units: a main circuit, floating LED, and a satellite photodiode circuit.

The satellite photodiode circuit contained the photodiode, transimpedance amplifier and voltage follower. Signals were transmitted from the photodiode circuit to the main circuit via a shielded coaxial cable. This arrangement of the photodiode circuit ensured the transimpedance amplifier was as close to the photodiode as possible, thereby reducing signal paths and minimising electronic noise. A UVA sensitive gallium nitride photodiode (GUVA-S20ED, sglux SolGel Technologies

GmbH, Germany) was used to detect light from the LED. A low input bias current (3 fA) operational amplifier (LMP7721, National Semiconductor) was configured as the transimpedance amplifier. The input bias current rating of the op amp is sufficiently lower than the dark current of the photodiode (1 nA) to ensure measurements are limited by shot noise from the photodiode rather than shot noise from the op amp. The floating LED unit consisted of just the LED mounted on a PCB. This allowed for the LED to be mounted to the cuvette holder described below. The main circuit unit contained all other analogue circuitry necessary to drive the LED, and condition detected signals from the photodiode.

In operation, the photometer circuitry was powered with 9 volts from a simple AC to DC regulated power supply (Maplin, UK). The circuitry was monitored with an oscilloscope (Tektronix DPO4034, Tektronix UK Ltd. Bracknell UK). Manual adjustments could be made to the amplification and DC offset of signals within the circuit through rotating potentiometers.

6.3.3 Circuitry: lock-in amplifier

An Explorer 16 evaluation board was purchased from Microchip Ltd. (Wokingham, UK). The dsPIC33FJ256GP710 supplied with the Explorer 16 board was used to run the lock-in amplifier code. The lock-in code (AN1115) was downloaded from the Microchip website. Modifications were made to the lock-in code that enabled measured values to be displayed on a liquid crystal display present on the evaluation board. The lock-in code was compiled in the MPLAB development environment and programmed on to the dsPIC using a PICkit 2 USB microcontroller programmer. Outputs from the lock-in amplifier were communicated to a personal computer (PC) via a RS232 serial connection. The outputs from the lock-in amplifier were captured with custom software running on the PC (see appendix B). The custom software was written in the Visual C# programming language. The cost of the components used in the LED drive and photodetection circuits, including optoelectronics and dsPIC, was less than £75.

6.3.4 Quantifying NADH: set-up

A cuvette holder jig was fabricated by cutting out pieces of 5 mm thick acrylic with an Epilog mini 18 30 W CO_2 laser (EMCO Education Ltd., Havant UK). The cut pieces of acrylic were bonded together with super glue. The LED and

photodiode circuit were attached to the acrylic jig with mechanical fasteners. A 10 mm cuvette could then be securely positioned between the LED and photodiode circuit during measurements. The set-up is shown in Figure 6.7.

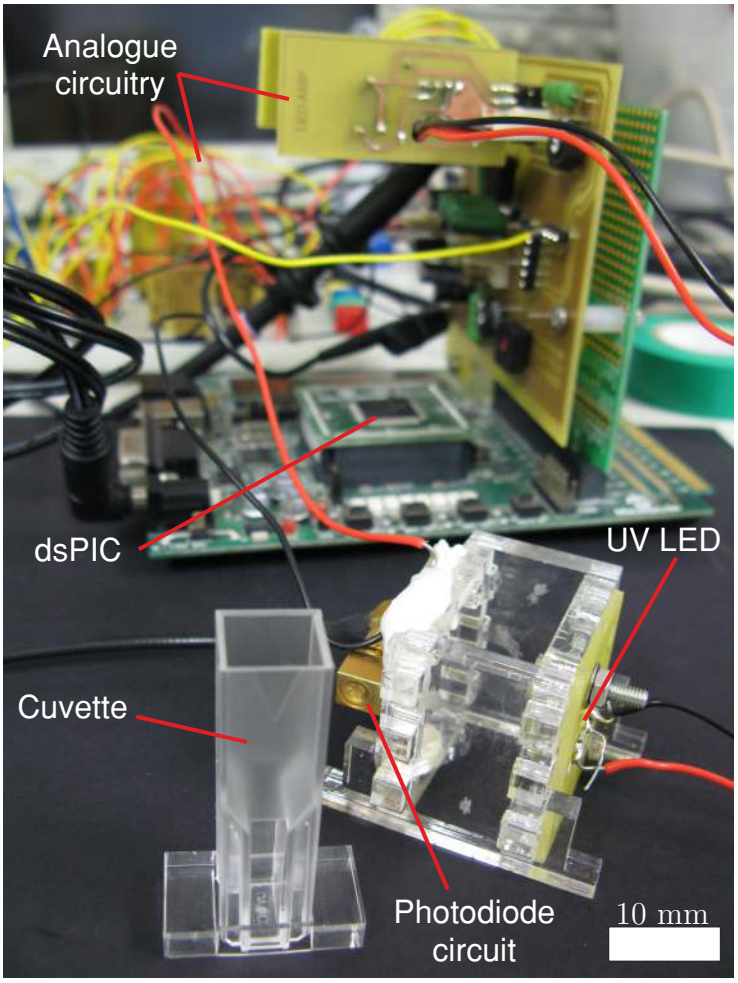

Figure 6.7: A photograph of the UV photometer set-up. A 10 mm path length cuvette is positioned in front of the acrylic jig. Attached to the jig are the UV LED and photodiode circuit.

6.3.5 Quantifying NADH: procedure

Tris(hydroxymethyl)aminomethane (Tris) buffer (1 M pH 9.0), and β-NADH reduced dipotassium salt were purchased from Sigma Aldrich (Dorset, UK). The UV photometer was tested against a Thermo Scientific Biomate 3 UV-VIS spectrophotometer. Aqueous solutions of NADH of varying concentration were used to test both instruments. A 0.01 M pH 9.0 Tris buffer was prepared fresh. Following the manufacturer's guidelines, a concentrated stock solution of 5 mM NADH in 0.01 M ph 9.0 Tris buffer was prepared fresh. Dilute NADH samples were created by serial dilution with the Tris buffer. Samples were pipetted into 2 ml volume, 10 mm path length, cuvettes. Prior to measuring samples containing NADH, both instruments were intentionally blanked with nothing in their cuvette holders. Eight cuvettes containing only buffer solution were measured with both instruments, thus allowing for the limit of detection of each instrument to be calculated. Samples containing NADH were then measured with the UV photometer and spectrophotometer instruments.

6.4 Results and discussion

6.4.1 UV LED characterisation

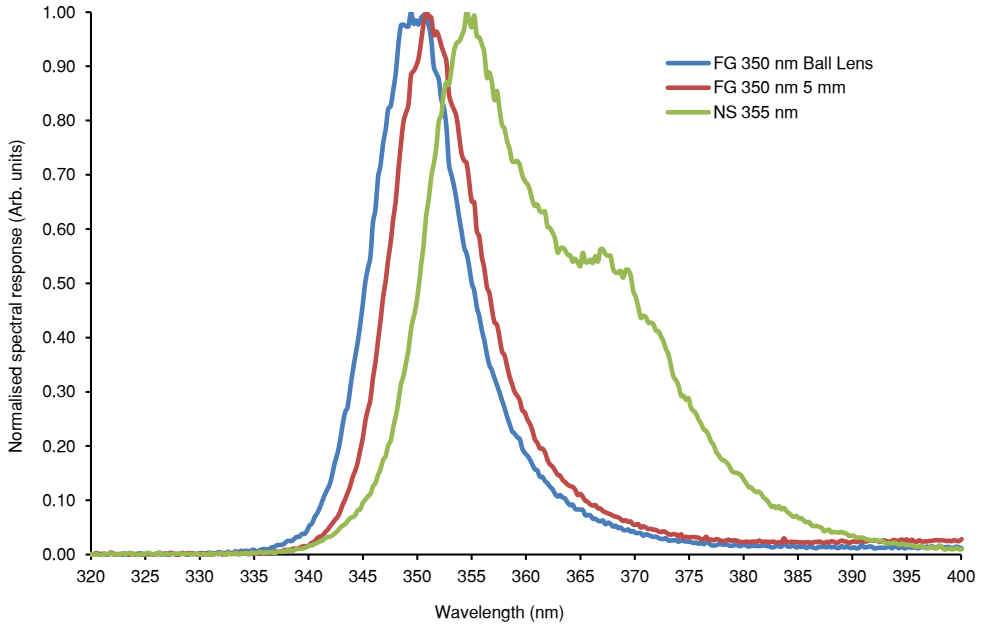

Figure 6.8: Comparison of the spectral responses of the optoelectronic components. Each response is normalised with respect to the maximum response of an individual component.

In Figure 6.8, the emission spectra of the candidate LEDs are plotted against one another. It can be seen that the 355 nm rated LED emits light over a wider range of wavelengths than the two 350 nm LEDs. The wider emission band makes the 355 nm particularly unsuitable for photometric measurements where ideally monochromatic light is required. The two 350 nm LEDs exhibit similar widths in their emission bands. The ball lens LED emits at slightly lower wavelengths when compared to the 5 mm 350 nm LED. The range of emissions within 10% of the peak spectral response is distributed between 348 and 351 nm for the ball lens LED. Similarly for the 5 mm LED the range of emissions within 10% of the peak spectral response is distributed between 349 and 352 nm.

The results from peak optical power output measurements for each LED are summarised in Table 6.1. Despite limiting the supply current to each LED as per manufacturers' specifications, measurements of the forward voltages and optical power outputs of each LED were found to differ from those reported by each manufacturer.

Table 6.1: Comparison of recorded and reported performance characteristics.

Type	Forward Voltage (V)		Optical Power (μW)	
	Rated	Measured	Rated	Measured
FG 350 nm ball lens	5.0	3.98	100	56.1
FG 350 nm 5 mm	4.5	4.31	350	225
NS 355 nm 5 mm	4.2	3.43	1200	501

FG – Fox Group, NS – Nitride Semiconductor

From these data the required gain of the photodetection circuitry was estimated. The distribution of the optical power over the emission spectra of a LED was calculated by: (1) integrating its emission spectra to obtain a dimensionless total response value (S_t), (2) multiplying the total response value (S_t) by the measured optical power (P_o), (3) integrating across 1 nm ranges of the emission spectra to obtain discrete response values ($S(\lambda)$), and (4) calculating the ratio of the discrete response values ($S(\lambda)$) to the total response value (S_t) multiplied by the measured optical power (P_o). Integration was performed by using the trapezium rule over the intervals (λ, λ+0.96 nm). The calculation of power distribution is summarised by the equation:

$$P(\lambda) \;=\; \frac{S(\lambda)}{S_t} \;\times\; P_o \tag{6.18}$$

and from which the plot in Figure 6.9 was obtained for the ball lens LED. The total current output (I_p) from the UV photodiode was calculated for the range 337 to 363 nm giving a theoretical value of 6.67 μA. The power measurements reported above had been made with the LED in contact with the optical power meter. Given that distance is required between photodiode and LED to accommodate a 10 mm cuvette, the total current output was divided by 100 to yield a theoretical current of 66.7 nA. The value of 100 is based on the assumptions that light intensity decreases over distance following an inverse square law, that 10 mm represents a 10 fold increase in distance, and minimal divergence of the light emitted from the LED. Therefore the estimated transimpedance gain (R) for the photodetection circuit assuming V = I_pR where V is 5 volts, is approximately 75×10^6. Following Figure 6.10 a gain of 75×10^6 should not lead to instability within the transimpedance amplifier (see section 6.2.2 for further details).

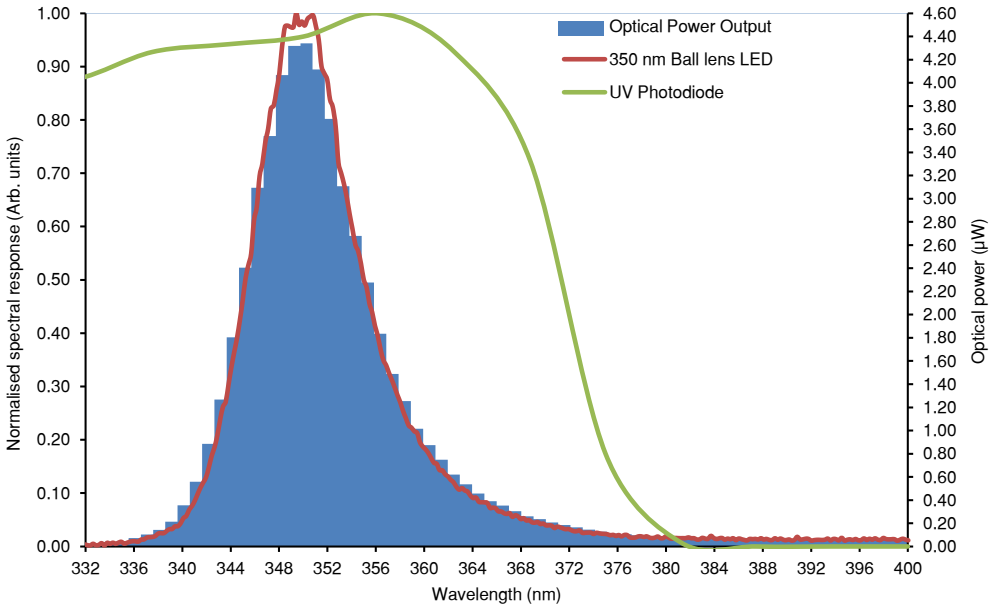

Figure 6.9: Optical power distribution for the ball lens LED. Included in the plot is the normalised spectral response of the UV photodiode, obtained from the manufacturer's datasheet.

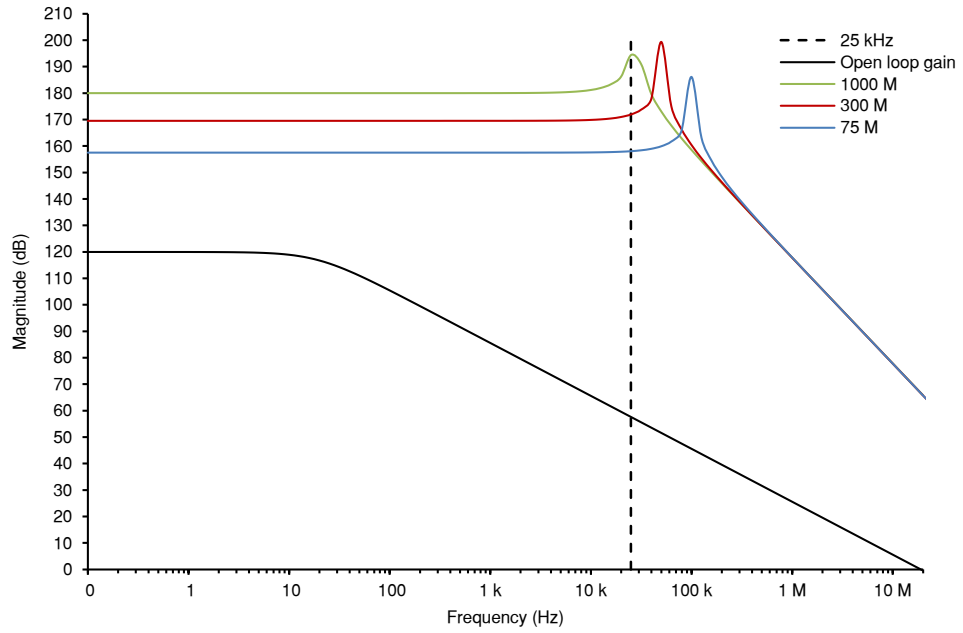

Figure 6.10: Transimpedance gain versus frequency. The frequency of interest is 25 kHz. Gain peaking that can lead to instability can be seen to shift to lower frequencies as gain is increased from 75×10^6 to 1000×10^6. The open loop gain of the op amp is included for reference.

6.4.2 Circuit implementation: UV LED drive circuitry

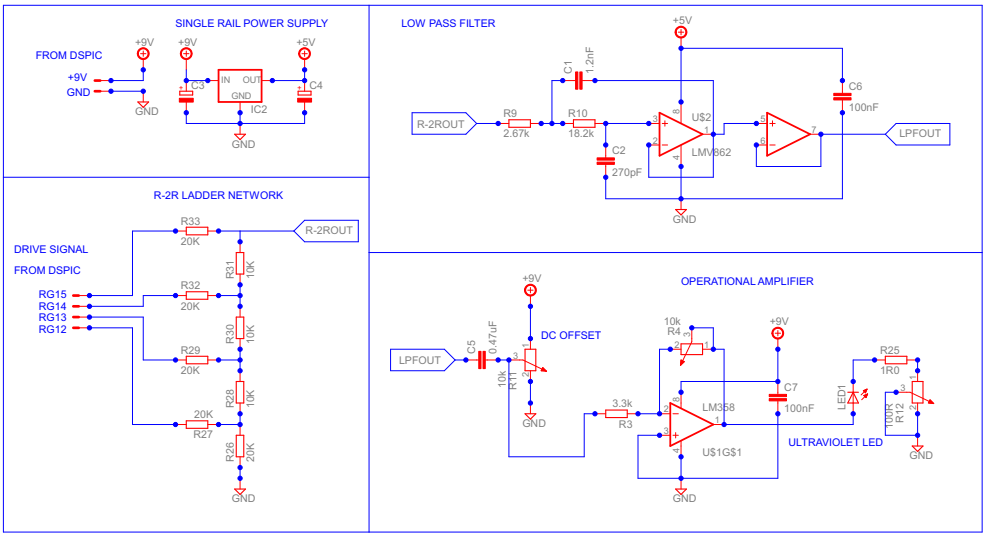

Figure 6.11: Circuitry required to drive the ultraviolet LED.

The circuitry developed to drive the ultraviolet LED is shown in Figure 6.11. The drive circuit consists of a R-2R ladder network that acts as a digital-to-analogue converter. Pulse-width modulated signals generated by the dsPIC are summed by the R-2R ladder yielding the noisy 25 kHz LED drive signal in Figure 6.12a. The noisy signal is fed into a low pass Butterworth filter (LPF) designed to have a corner frequency of 40 kHz. The Butterworth filter configuration was selected to ensure a flat frequency response in the passband. The output of the low pass filter is shown in Figure 6.12b. A DC offset is applied to the filtered signal before being fed into an operational amplifier. The operational amplifier drives the ball lens UV LED with the offset signal (see Figure 6.12c). The 350 nm ball lens LED exhibits less light divergence and resulted in a stronger response from the transimpedance amplifier when compared to the 5 mm LED.

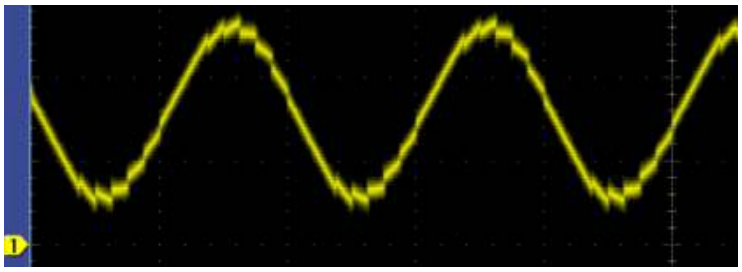

(a)

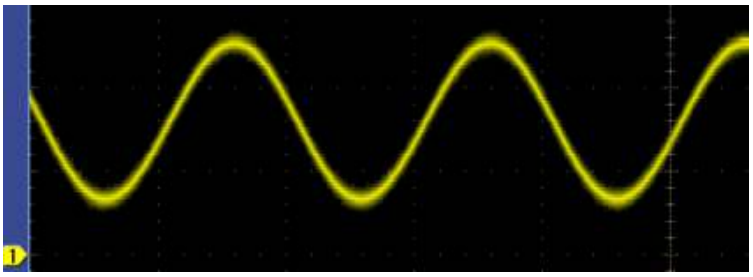

(b)

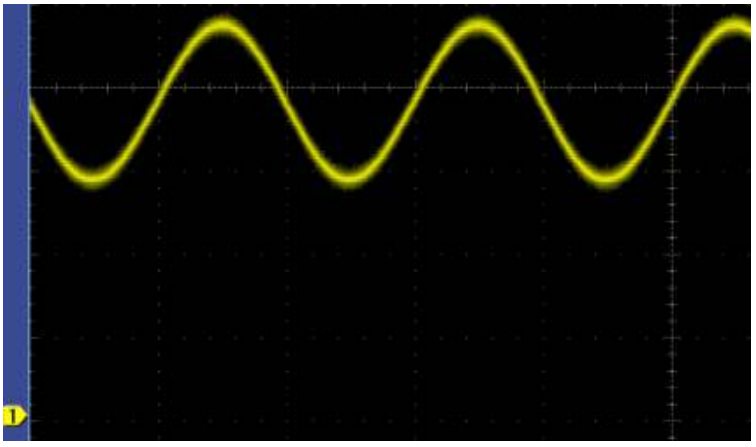

(c)

Figure 6.12: Voltage waveforms captured from LED drive circuit. A 2 V_{pp} waveform was measured at the output of the R-2R ladder network (a). The waveform measured at the output of the low pass filter was 2 V_{pp} (b). The waveform used to drive the UV LED was measured as 2 V_{pp} with a DC offset of 3.8 V (c). The yellow arrow at the bottom left of each image indicates the DC bias.

6.4.3 Circuit implementation: photodetection circuitry

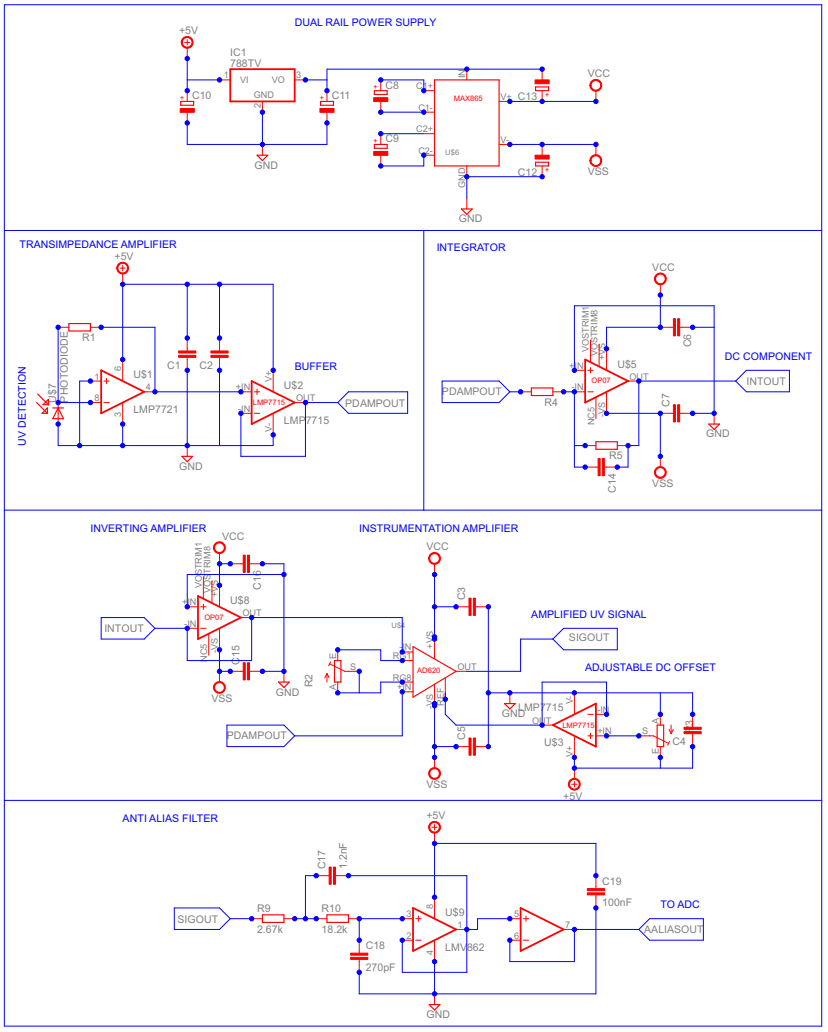

Figure 6.13: Circuitry required to detect modulated UV light.

The circuitry developed to detect UV light is shown in Figure 6.13. A photodiode is connected in photovoltaic mode to a transimpedance amplifier giving a linear response to increasing illumination. The transimpedance gain is 150×10^6, double that which was previously estimated. A higher gain requirement in implementing the circuit was expected. The output from the transimpedance amplifier is buffered with a voltage follower. The waveform at the output of the voltage follower is shown in Figure 6.14a, and is approximately half the amplitude of the waveform driving the LED. The output from the voltage follower is split in two feeding an integrator, and an instrumentation amplifier. The integrator circuit extracts the DC component of the signal, which is then inverted. The inverted DC component is fed into the instrumentation amplifier where it is added to the original detected signal. By this approach, DC offsets are automatically subtracted from detected

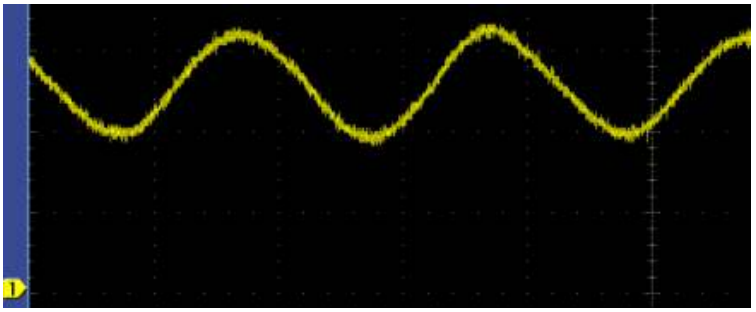

(a)

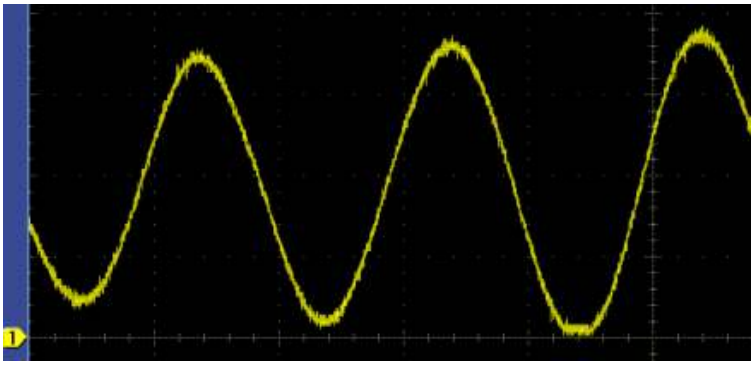

(b)

Figure 6.14: Voltage waveforms captured from the photodetection circuitry. A 1.1 V_{pp} waveform with a DC offset of 2 V was measured at the output of the transimpedance amplifier (a). After conditioning, a 3.5 V_{pp} waveform with a 0.2 V DC offset was measured at the input to the dsPIC analogue-to-digital converter (b). The yellow arrow at the bottom left of each image indicates the DC bias.

signals. The instrumentation amplifier is used to both amplify, and apply a user specified DC offset to the detected signal. The output from the instrumentation amplifier passes through an anti-aliasing filter yielding the waveform shown in Figure 6.14b, which then feeds into the analogue-to-digital converter of the dsPIC.

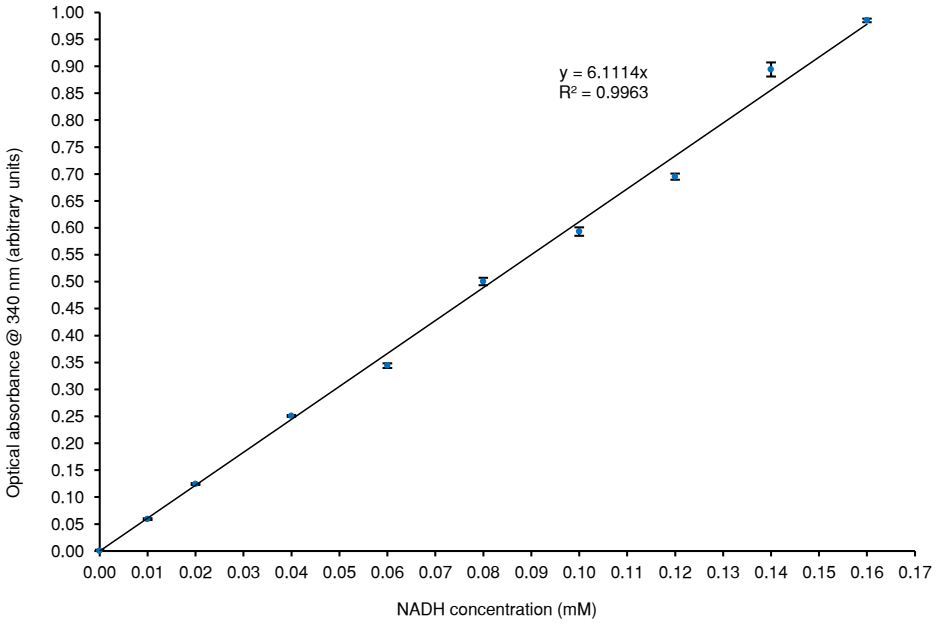

(a)

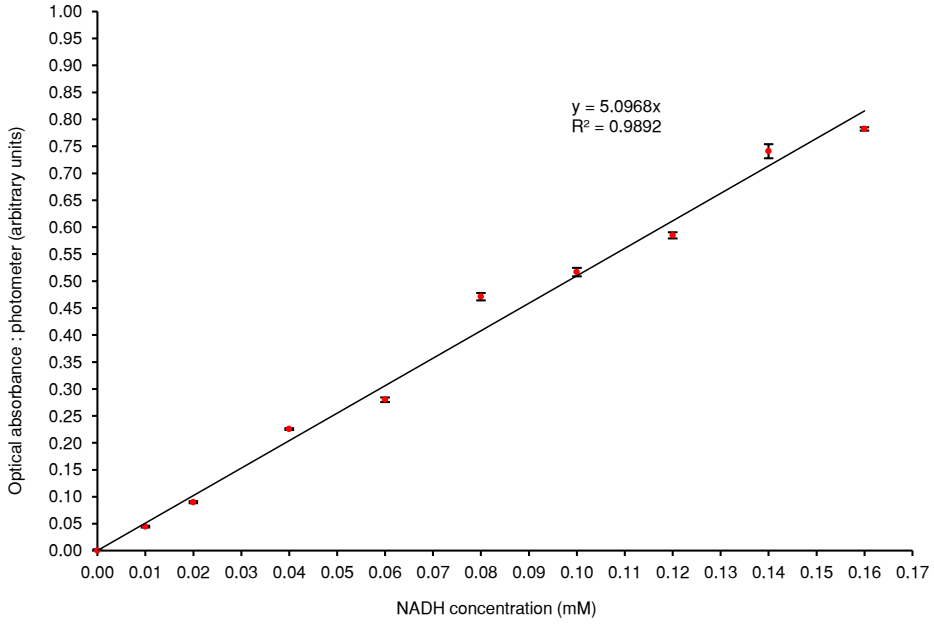

(b)

Figure 6.15: Optical absorbance measurements obtained from solutions containing different concentrations of NADH. Measurements obtained with a commercial spectrophotometer are shown in (a). Measurements obtained with the photometer system described here are shown in (b). Error bars indicate standard error (n = 3).

6.4.4 Relative performance test: quantifying NADH

Shown in Figure 6.15 are optical absorbance measurements recorded from solutions containing different concentrations of NADH using a commercial spectrophotometer and the photometer system described above. With the commercial spectrophotometer set to record optical absorbance at 340 nm the results in Figure 6.15a were obtained. A linear slope was fitted to the spectrophotometer results, indicating a Beer-Lambert relationship. The molar extinction coefficient (ε) was calculated to be 6111.4 M^{-1} cm^{-1}, which is close to that reported for NADH in the literature (Siegel et al., 1959). Likewise for the photometer, a linear slope could be fitted to the results also indicating a Beer-Lambert relationship. The molar extinction coefficient in this case was calculated to be 5096.8 M^{-1} cm^{-1}, which is close to that calculated for 355 nm from measurements made by the spectrophotometer on the same samples (Table 6.2).

Table 6.2: Molar extinction coefficients (ε) and limits of detection (LOD) calculated from measurements obtained from the spectrophotometer at different wavelengths (λ).

λ [nm]	ε [M^{-1} cm^{-1}]	LOD [μM]
350	5601.7	3.95
351	5521.6	3.93
352	5417.7	4.12
353	5317.8	4.06
354	5209.5	4.16
355	5070.2	4.28

The limit of detection (LOD) for both instruments was computed from:

$$LOD = \frac{3SD_{blank}}{\varepsilon} \tag{6.19}$$

where SD_{blank} is the standard deviation of the blank measurements, i.e. cuvettes filled with just buffer solution. Accordingly the photometer LOD was calculated to be 3.53 μM (from 8 blank measurements), lower than that calculated for the spectrophotometer between 350 and 355 nm. The correlation between the photometer measurements and spectrophotometer measurements at 355 nm is plotted in Figure 6.16. A linear relationship can be identified between measurements from the two instruments with the correlation coefficient calculated

to be 0.996. A possible explanation for the difference between device measurements may be the polychromatic nature of the light source in the photometer system.

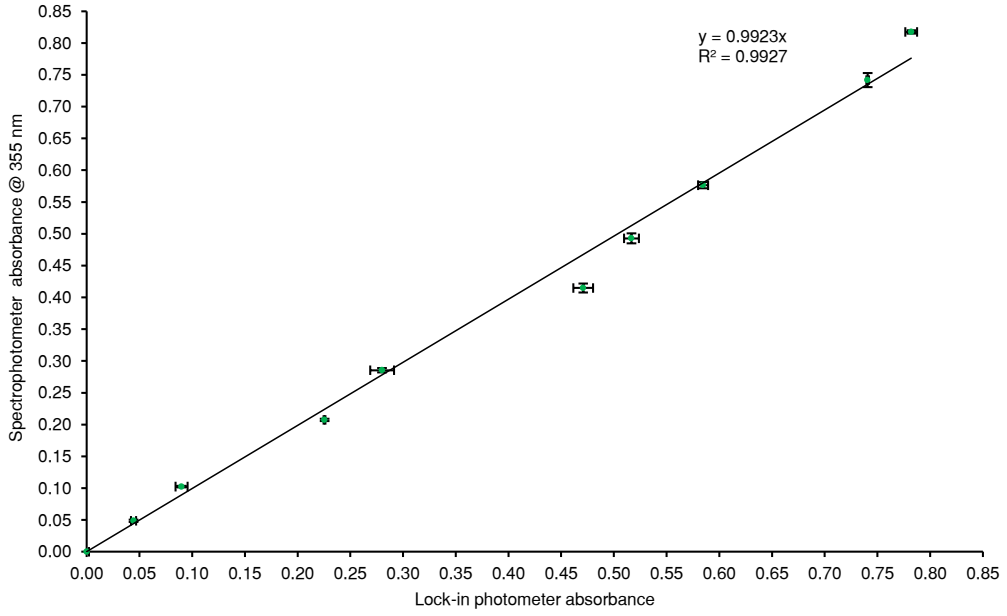

Figure 6.16: Correlation plot used to assess the agreement between instruments. Error bars indicate standard error (n = 3).

6.5 Summary

A low-cost, physically compact UV photometer system built using optical semiconductor components has been presented. The UV photometer system was tested against a commercially available spectrophotomter by conducting photometric experiments. The photometric experiments involved the measurement of the degree of light absorbance by dilute solutions containing NADH. In comparing the data obtained from both instruments, a strong correlation was found between both instruments at a wavelength of 355 nm. Therefore the spectrophotomter can be substituted by the UV photometer system when measuring the absorbance of 355 nm light by NADH.

Chapter 7

Droplet microfluidics for autonomous experimentation

7.1 Introduction

Despite attractive features of microfluidic technology such as lower reagent consumption and automatability, issues still exist that are particularly detrimental to enzymatic computing studies. Ideally, complex chemical mixtures would be considered to explore enzyme interactions. However producing a complex chemical mixture would require many chemical inputs, multiple arbitrarily defined dilutions and their mixing. In microfluidics, even achieving several discrete dilutions necessitates a high number of associated microfluidic channels, pumps and valves (e.g. Yun et al. 2011). Microfluidic designs that contain high valve densities are not only challenging to implement, fixed dilution networks such as those reported by Walker et al. (2007); Kim et al. (2008); Hattori et al. (2009) impose a limit on the complexity of chemical mixtures that can be produced on-chip. The droplet-based approach to microfluidics and specifically where integrated valves are used, may provide a solution to these issues.

Droplet microfluidic devices have been shown easily capable of producing on-demand, aqueous droplets of varying size with only one integrated valve required per aqueous input stream (Zeng et al., 2009). However, fusing two or more droplets together to create a mixture has been more difficult than generation. There are several approaches to fusing droplets, which include using chemically modified surfaces (Fidalgo et al., 2007), electric fields (Ahn et al., 2006a), or physical traps (Niu et al., 2008). Valves have been integrated with physical traps to fuse

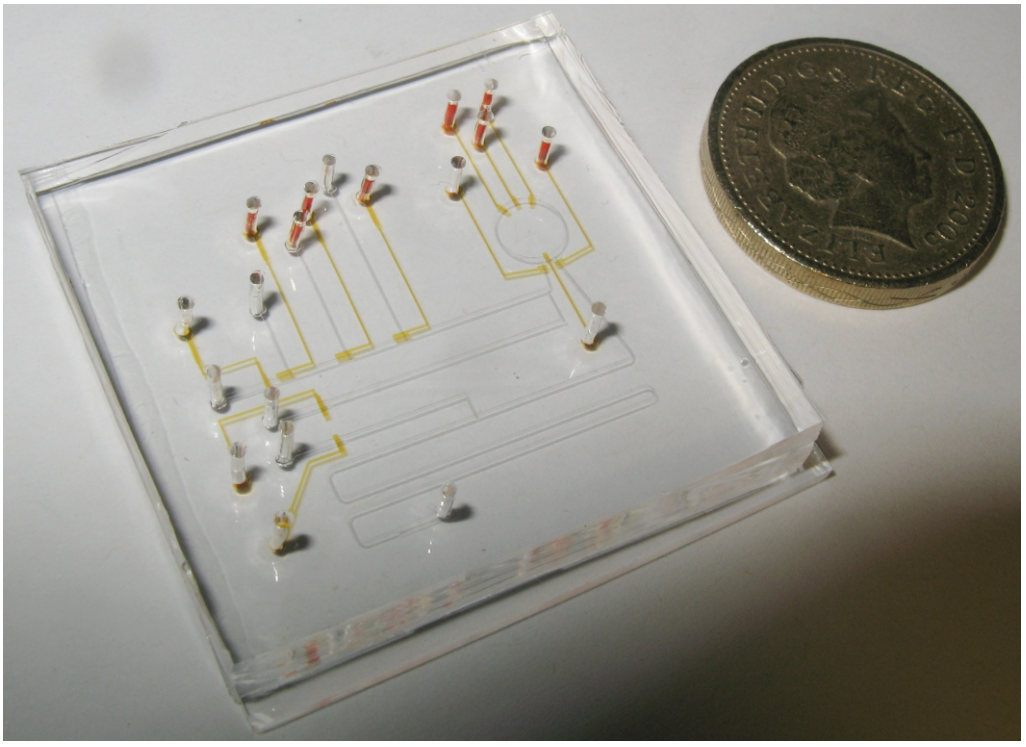

Figure 7.1: Photograph of a three-input automated droplet microfluidic device designed for autonomous experimentation. The device contains integrated valves (filled with yellow food colouring) that give the device dilution and mixing functionality. Next to the device is a 1 GBP coin to provide a sense of scale.

droplets (Lin and Su, 2008). More recently it has been shown that by stopping the oil stream with a valve, a droplet can be moved from one aqueous inlet to another, allowing for direct injection of an aqueous stream into the droplet (Guo et al., 2011). A potential disadvantage of directly injecting into droplets, is that the approach runs the risk of triggering premature reactions.

Associated with droplet microfluidic devices are a number of ancillary equipment pieces. Generally a syringe pump is required for each inlet stream to a droplet microfluidic device, directly impacting on the requirement for multiple chemical inputs for enzymatic computing studies. Not only are syringe pumps physically bulky, they are also expensive.

This chapter discusses an automated droplet microfluidic device designed to be used as part of an autonomous experimentation system for enzymatic computing studies. The microfluidic device (Figure 7.1) is designed to operate on aqueous droplets (reaction vessels) formed by injecting aqueous streams into an oil phase (oleic acid) via T-junctions. Control over the size of a generated droplet from an

aqueous stream only requires a two pneumatically controlled on-chip valves, one at the T-junction and one to interrupt the oil stream. By this approach single droplets can be created ranging in size from approximately 120 μm, in diameter to in excess of 10 mm in length. Therefore dilutions continuous in range can now be easily achieved. Also presented is a novel approach to mixing and fusing multiple droplets separated by oil in one step, which involves the manipulation of a third immiscible phase. The detection volume in this device is four orders of magnitude smaller than a standard 2 ml cuvette, thereby addressing the need to maximise available resources. A major advantage of the approach presented here is the requirement for minimal ancillary equipment. Only one pump is required to generate flow within the device regardless of the number of chemical inputs. Therefore the restriction to a small number of chemical inputs can now be addressed.

7.2 Device design

Before designing the device, a model was created to evaluate the effects of device dimensions on flow characteristics.

7.2.1 Modelling

Given the physical constants of the oil phase (Oleic acid, $\eta = 27.64$ mPa.s, $\rho = 895$ kg/m^3, $\gamma_{PDMS} = 15.6$ mN/m), the device design was modelled starting with the analytical solution to fluidic resistance:

$$R = \frac{12\eta L}{wh^3}\left[1 - \frac{h}{w}\left(\frac{192}{\pi^5}\sum_{n=1,3,5}^{\infty}\frac{1}{n^5}\tanh\left(\frac{n\pi w}{2h}\right)\right)\right]^{-1} \tag{7.1}$$

Assuming a predefined channel height and width, 50 μm and 200 μm, fluidic resistance was calculated for a unit length (i.e. 1 mm). Subsequently the volumetric flow rate was calculated by using the HagenPoiseuille equation (see chapter 3) for driving pressures ranging between 10 and 50 kPa (limitations of the equipment). Converting the volumetric flow rate to velocity, the Reynolds (Re) and Capillary (Ca) numbers were derived for the unit length. The length was increased to give enable a sufficient range of flow velocities to be obtained for the given driving pressures. Based on previous experiments, 116 mm was found to be an optimal length, which gave a theoretical flow velocity range of 0.65 mm/s to 3.24 mm/s. The corresponding Re and Ca values ranged from, 0.0017–0.0057 and 0.0011–0.0084 respectively, therefore suggesting linear predictable flows. Moreover with Ca < 0.01 the flow should favour direct injection of aqueous streams into previously generated droplets (Song et al., 2006), as well being capable of supporting long droplets without their breakup (Liau et al., 2005).

7.2.2 Design

From the model, the microfluidic device design shown in Figure 7.2 was created. The device features three aqueous inlet channels forming T-junctions with a main channel. All inlet channels have isolation valves. The aqueous inputs are designed to be used one at a time. The length of each aqueous input channel differs to match the hydraulic resistance between each inlet and outlet ports. To generate

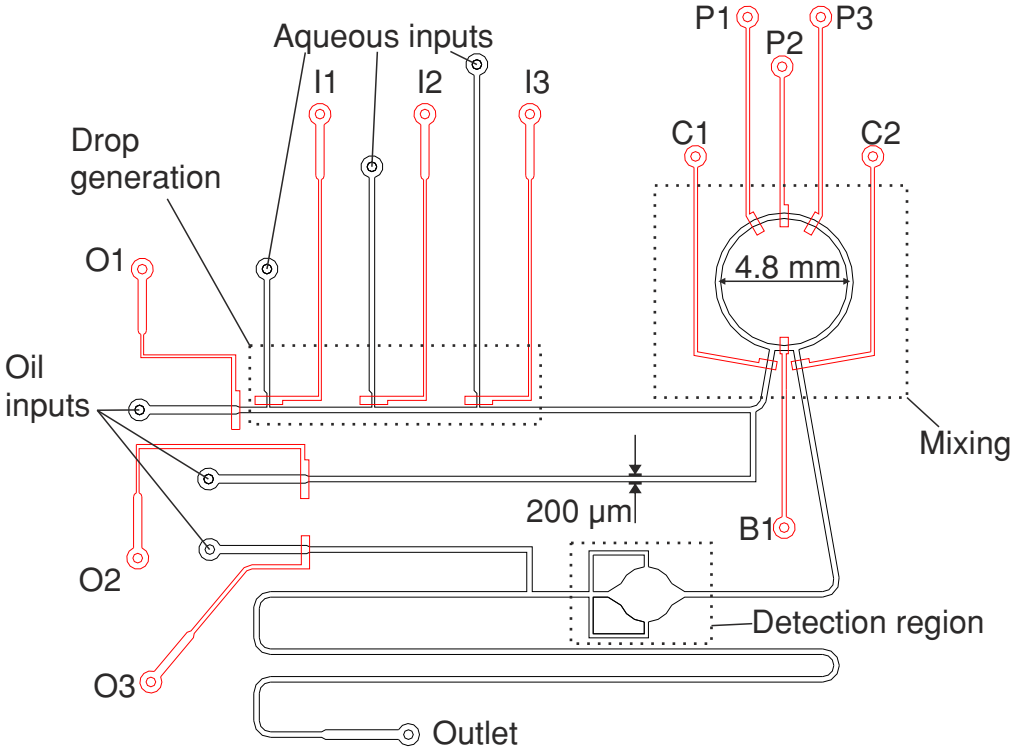

Figure 7.2: Droplet microfluidic device designed for autonomous experimentation. The design contains 12 integrated valves (red). The three oil inputs can be shut off using valves O1, O2, and O3. Aqueous inputs are shut off from the main flow channel by valves I1, I2 and I3. Valves C1 and C2 isolate the rotary mixer from the main channel. Valve B1 is a bypass valve. Valves P1, P2 and P3 act as a peristaltic pump that drive fluids around the ring of the rotary mixer. Droplets are generated and flow left to right. Mixing and fusion is performed in a single step within the rotary mixer. An expansion chamber serves as a measurement region.

droplets, first valves O1, O2 and O3 are closed. An aqueous inlet valve is opened and after a predefined delay closed. The delay between valve open and closure determines the length of the drop. After generating a drop O1 is opened to allow the drop to be transported downstream to the rotary mixer.

The rotary mixer design is used to fuse droplets and mix their contents. From the design there are two possible flow paths between rotary mixer inlet and outlet. The shorter of the two paths contains a single bypass valve B1 that allows for switching of the flow path between the shorter and longer distances. When generating droplets the bypass valve B1 is first kept open. After generating a droplet the bypass valve B1 is then closed. Droplets are then loaded into the longer path of the rotary mixer where they are stored while other droplets are generated. Multiple droplets are stored in the longer flow path of the rotary mixer. Mixing and fusion

are conducted in one step. The isolation valves C1 and C2 of the rotary mixer are closed. The bypass valve B1 is opened. The three pump valves P1, P2 and P3 are actuated sequentially with the pattern: 001, 011, 010, 110, 100, 101 repeatedly for a predefined number of cycles. The pumping action drives the fusion and mixing of the droplets. Once fused and mixed, the new longer droplet is released from the rotary mixer by opening the isolation valves C1 and C2.

After fusion and mixing drops are transported to the measurement region. As the measurement region becomes completely filled with a drop, the valves O1 and O2 close, while valve O3 opens. This is to prevent the drop from leaving the measurement region. When all measurements are recorded, valves O1 and O2 are opened while valve O3 is closed. The drop is then transported out of the measurement region and downstream to waste.

7.3 Experimental methods

7.3.1 Device fabrication

Replication masters were fabricated by patterning dry film resist laminated on to glass slides, using the methods described in chapter 4. The microfluidic device design utilised on-chip valves, which required two functional layers: a fluidic layer containing 50 μm high features and a valve layer containing 75 μm high features. The fluidic layer was made by casting a thick layer of PDMS over the fluidic replication master. The valve layer was fabricated by spinning a thin film of PDMS over the valve replication master. After curing, holes were cored through the fluidic layer using a 1 mm biopsy punch. The fluidic and valve layers were then aligned and bonded together after oxygen plasma exposure. The WAVE technique (chapter 5) was used to obtain alignment between the layers. The bonded PDMS layers were then baked for 4 hours at 100 ^oC to recover surface hydrophobicity (see contact angles in appendix D.1). After baking, a 1 mm biopsy punch was used to core holes through both layers thus providing access to the valve channels. Finally the valve layer was sealed by bonding to a cleaned glass microscope slide after oxygen plasma exposure.

7.3.2 Device set-up and operation

7.3.2.1 Macroscopic equipment

Two pressure systems were required for operation of the microfluidic device. Following Figure 7.3, a vacuum system was used to generate flow in the fluidic channels, while a compressed air system was used to drive on-chip valves. The vacuum system consisted of a vacuum pump (Air Admiral, Cole-Palmer UK) connected to a sealed waste collection bottle with an inlet and an outlet port. The outlet from the waste collection bottle was connected to a needle valve, pressure gauge and Tygon® tubing. The Tygon® tubing was used to connect the vacuum system to a microfluidic device. By adjusting the needle valve, the vacuum could be varied between 0 and -550 mbar gauge pressure. The compressed air system was the same as that used in chapter 5 to drive the valves of the valved junction device.

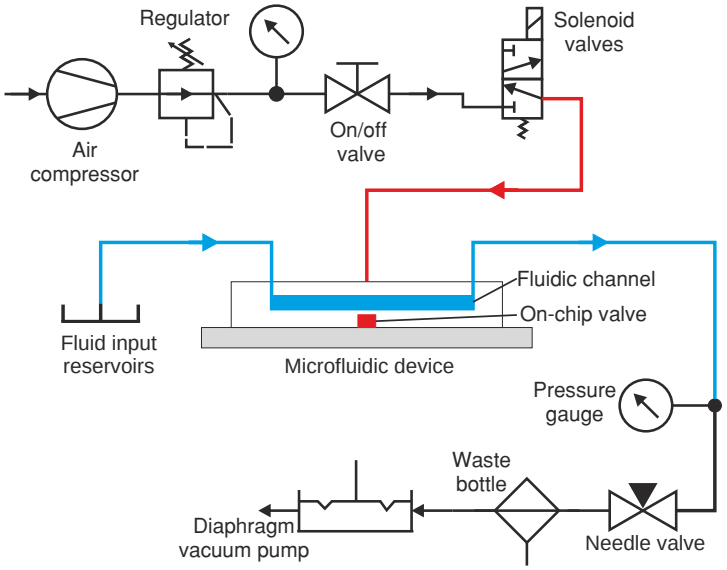

Figure 7.3: Schematic of the macroscopic equipment necessary for device operation. On-chip valves are driven by positive air pressure supplied by the air compressor. Only a single vacuum pump is used to generate flow within the fluidic channels of the device.

7.3.2.2 Device preparation

On-chip valve control channels were filled with deionised water. The control channels were filled by first dispensing a drop of water over each control channel inlet hole. A vacuum was applied to each control inlet using a syringe equipped with a blunt needle. The syringe was then removed from an inlet causing the drop of water to be sucked into the control channel. A water filled syringe was then used to drive additional water into a partially filled control channel. Pressure was maintained on the water filled syringe until all air had been driven from the control channel. Once filled, a control channel was then connected to a solenoid valve using Tygon® tubing.

For each inlet (oil and aqueous) a small 10 μl pipette tip was used as a fluid reservoir. Before operation, the fluidic channels of a device were primed. First all aqueous input channels were isolated from the main flow channel by closing the relevant on-chip valves. Technical grade oleic acid mixed 2% w/w with Span 80 was used as the main flow fluid (oil phase). The oleic acid was dispensed into the three main channel fluid reservoirs. Vacuum was applied to the outlet of the microfluidic device for 2 minutes causing the main channel to fill with oleic acid. The main flow reservoirs were then isolated by closing their on-chip valves. Each aqueous inlet was then primed in turn by opening their valves. Finally, the

aqueous inlets were once more isolated and the oleic acid stream was flowed for an additional 2 minutes. Afterwards the device was ready for operation.

7.3.3 Device characterisation

7.3.3.1 Droplet generation

Droplet generation experiments were recorded under a stereo zoom microscope (Zeiss Discovery V8) with still images captured using a Zeiss Axiocam ICc1 camera and Axiovision software. The oil stream flow rate was adjusted by altering the vacuum delivered to the device between 0 and -550 mbar. After setting a negative pressure, a 10 s delay was adhered to, allowing for flow stabilisation prior to generating a droplet. Basic droplet generation experiments were conducted to determine an optimal vacuum setting. Droplet generation experiments were driven by scripts read by the custom control software (e.g. appendix D.5.1). Images of generated droplets were captured and measurements of a droplet size performed in Axiovision software.

7.3.3.2 Fusion and mixing

Mixing and fusion experiments were recorded under a stereo zoom microscope (Zeiss Discovery V8) with video captured at 15 frames per second using a Zeiss Axiocam ICc1 camera and Axiovision software. Individual frames were analysed using ImageJ software. Food colourant was used throughout fusion and mixing characterisation. The efficacy of the mixer was characterised by comparing the image intensity profiles of captured images. Specifically, mixed droplets were compared to a control solution. The control solution was created by premixing blue and yellow food colourant in a 1:1 v/v ratio. Control solution was flowed into the rotary mixer and images captured. Afterwards two equal sized droplets, one containing blue colourant and the other yellow colourant, were in turn generated and transported into the rotary mixer. The fusion and mixing of the two droplets were then explored as the rotary mixer operation parameters (i.e. number of iterations, speed) were adjusted.

7.4 Results and discussion

7.4.1 Droplet generation

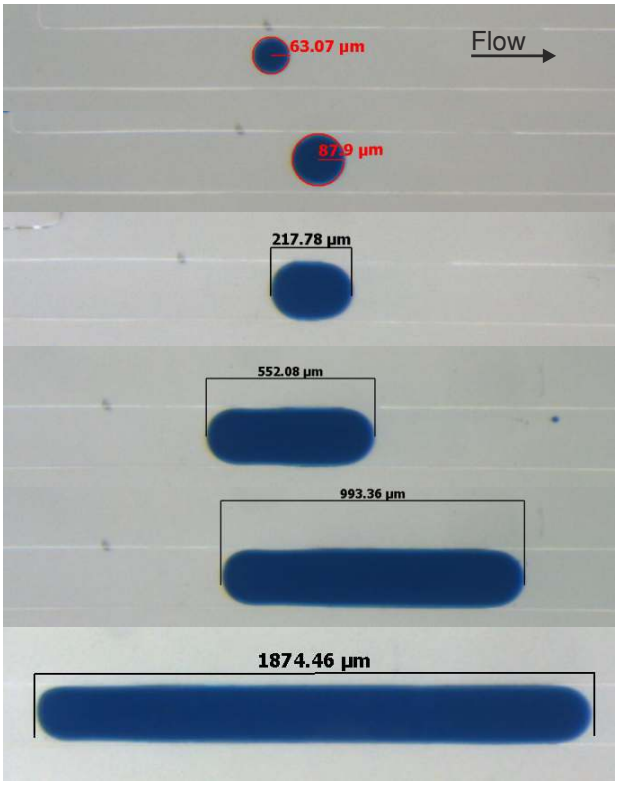

Figure 7.4: Drop sizes resulting from the opening and closing of an aqueous inlet valve. Starting from the top the inlet valve was kept open for, (a) 32 ms, (b) 64 ms, (c) 128 ms, (d) 256 ms, (e) 512 ms and (f) 1024 ms before closing. The channel width is 200 μm.

The vacuum pump connected to the microfluidic device was set to deliver -350 mbar of vacuum. On-chip valves were driven with 3 bar of pressure. Due to the rectangular profile of the fluidic channels, vacuum pressures greater than -350 mbar would result in leakage of aqueous streams beyond their inlet valves. Vacuum pressures lower than -350 mbar resulted in a slower travelling oil stream, which also increased the size of drops at shorter inlet valve actuation times.

Droplet generation from each aqueous inlet was characterised in turn. During droplet generation all oil stream inlets were closed. This allowed for extremely long droplets equal to the channel length of the microfluidic device to be generated. Conversely without closing all oil stream inlets during droplet generation, the longest drop lengths that could be generated from each aqueous input were measured to be, 522.7 μm (Input 1), 861.25 μm (Input 2) and 906.39 μm (Input

3). During generation, droplet lengths were defined by the delay between opening and closing an aqueous inlet valve. The delay between opening and closing of an aqueous inlet valve was varied from 32 to 1024 ms. Actuation times less than 32 ms did not reliably produce droplets for all 3 aqueous inlets, either no droplets were generated or several small droplets would form. This is believed to be an inherent limitation of the on-chip valves. Shown in Figure 7.4 are droplets of different size generated from aqueous Input 3.

Two types of droplet of characteristic length were generated from each input. Generated droplets were either smaller than the channel width, or large enough to be in contact with the channel walls. Therefore the volume of generated droplets was estimated using two equations. For droplets smaller than the channel width, their volume (V_s) was estimated by assuming a cylindrical shape:

$$V_s \approx 1000\pi r^2 h \tag{7.2}$$

where r is the measured radius of the droplet and h the height of the channel, 50 μm. For droplets large enough to be in contact with the sidewalls, their two-dimensional shape was assumed to consist of a rectangle bounded by two semicircles. Thus the volume of a large droplet was estimated by adding the volumes for a cylinder of radius 100 μm and a rectangular prism:

$$V_l \approx 1000\left(wh(l-w) + \frac{1}{4}\pi h w^2\right) \tag{7.3}$$

where w is the width of the channel 200 μm, l the measured length of the droplet. Plotted in Figure 7.5 are the estimated volumes of droplets generated at each aqueous inlet for a predefined valve actuation time. Droplet volumes as small as 0.88 nl and as large as 19.23 nl could be generated from aqueous input 1, a 21 fold range. Droplet volumes as small as 0.72 nl and as large as 24.37 nl could be generated from aqueous input 2, a 33 fold range. Droplet volumes as small as 0.63 nl and as large as 19.36 nl could be generated from aqueous input 3, a 30 fold range. In theory the actual range of drop sizes that could be achieved by this device is limited to approximately 75 fold, based on the assumption that a single drop no larger than 10 mm (the measurement region length) would be used.

The relationship between generated droplet volumes (V) and valve actuation times (t) for each inlet were found to follow, $V = ct^n$, where c and n are constants (see Table 7.1). Despite designing the aqueous inlet lengths to have equal fluidic

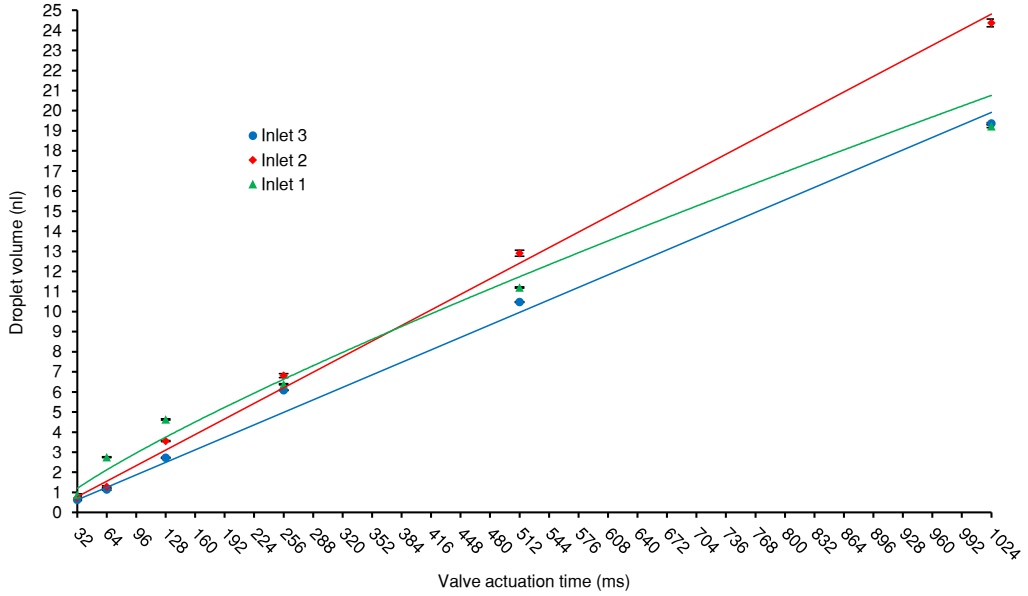

Figure 7.5: Droplet volumes resulting from predefined valve actuation times.

resistances, it is surprising to see that the three inlets exhibit different relationships between generated drop size and valve actuation time. Especially aqueous inlet 1, where its relationship follows a power law compared to inlets 2 and 3 that exhibit linear relationships. It is believed that the amount of oil displaced by the aqueous stream is responsible for the discrepancy between the inlets. Essentially there is more oil to move before aqueous inlet 1 is drawn into the main channel when compared to the other two inlets. It is postulated that in changing the device design to ensure that the amount of oil to be displaced is equal for all three inputs, the behaviour of each inlet should be more alike.

Table 7.1: Constants c and n, used in describing the relationship between drop volume and valve actuation time

	c	n	R^2
Inlet 1	0.069	0.8234	0.9627
Inlet 2	0.0242	1	0.9973
Inlet 3	0.0195	1	0.9928

7.4.2 Fusion and mixing

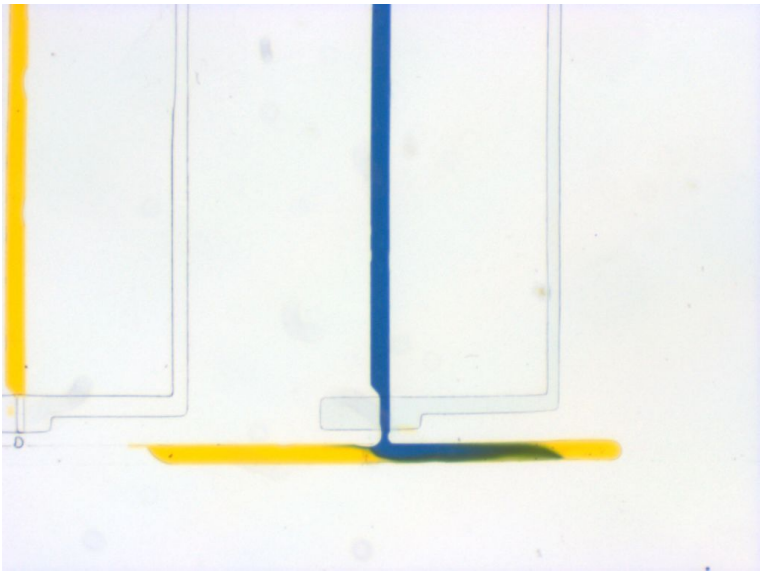

Figure 7.6: Fusion of an aqueous inlet stream with a droplet. A droplet containing yellow food colourant is generated at the first aqueous inlet and halted at the junction with the second aqueous inlet. The valve to the second aqueous inlet is opened causing blue food colourant to be injected into the droplet. The channel width is 200 μm.

The device design is capable of stopping the oil stream with an on-chip valve, similar to Guo et al. (2011). A generated droplet can therefore be moved from one aqueous inlet to another, allowing for direct injection of an aqueous stream into the droplet. There are two problems with this approach to fusion. First it is difficult to determine the amount of fluid being injected into the droplet, as the interface between droplet and aqueous stream is less clearly defined as can be seen in Figure 7.6. It is possible to keep sufficient distance between a droplet and aqueous inlet so as to ensure a second droplet is generated without touching the first droplet. But by this manner of droplet generation, fusion between two droplets cannot be guaranteed particularly when droplets are of equal size, or when the second droplet is larger. This is due to larger droplets travelling more quickly downstream than smaller droplets.

The second problem with this approach to fusion, is that reactions may occur prematurely. For example, if three streams are to be fused, by the time the first and second streams are fused a reaction may have started before reaching the third stream. The approach taken here was to keep all droplets separate and fuse them in a single step. This is achieved by first loading and storing each generated droplet in the loop of the rotary mixer, and then operating the rotary mixer. The

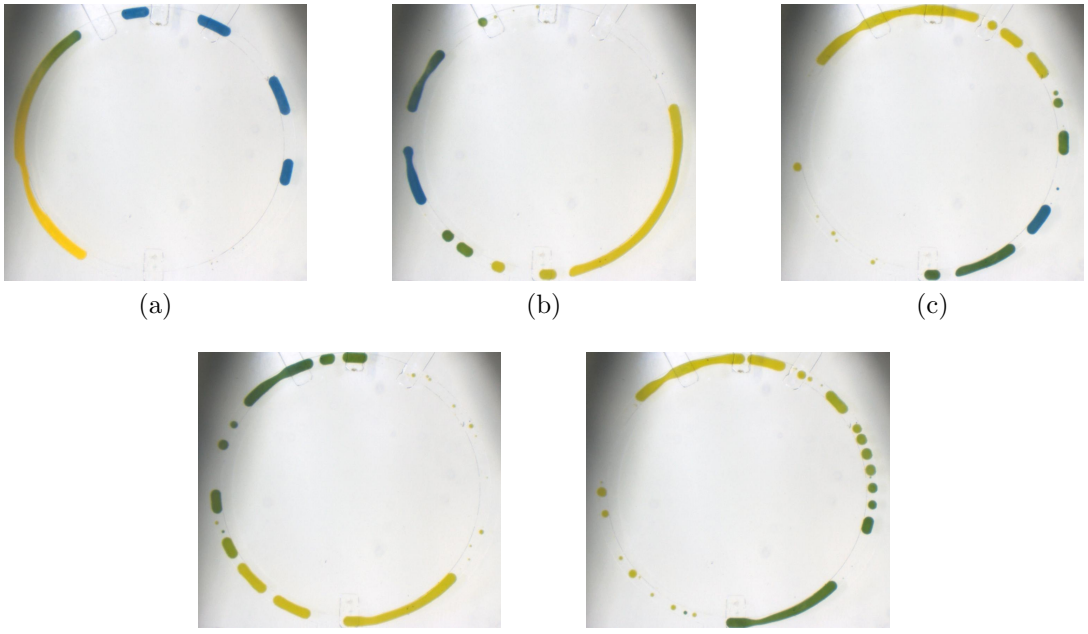

Figure 7.7: Unsuccessful mixing within a rotary mixer. Five droplets are initially loaded into the rotary mixer (a). The rotary mixer is operated to stir its contents clockwise starting at (b) and ending several cycles later at (e). Droplets are not only resistant to fusing, the valves used in operation of the rotary mixer cause breakup of the droplets. The channel width of the rotary mixer is 200 μm.

storage functionality of the rotary mixer is achieved through actuating the bypass valve between its inlet and outlet.

Mixing within small droplets is achieved rapidly when simply traversing downstream within the device. Long droplets however do not mix so readily. Previous attempts by the author to mix long droplets used bumpy serpentine mixer designs (see appendix D.3) but with little success. The rotary mixer also proved to be at first unsuccessful as can be seen from Figure 7.7. However, it was found that by purposefully injecting air into the mixer, along with the oil stream and aqueous droplets, mixing could be significantly improved as shown in Figure 7.8.

The rotary mixer was characterised by first measuring the speed at which a sample travelled around the loop. Air was initially introduced into the rotary mixer before filling with a long droplet and a small amount of oil. The long droplet and oil occupied approximately half of the rotary mixer. The peristaltic pump on the rotary mixer was actuated with different valve timings and the motion of the droplet observed. The number of peristaltic pump cycles to achieve one revolution of the droplet about the ring was noted for each valve timing. The highest

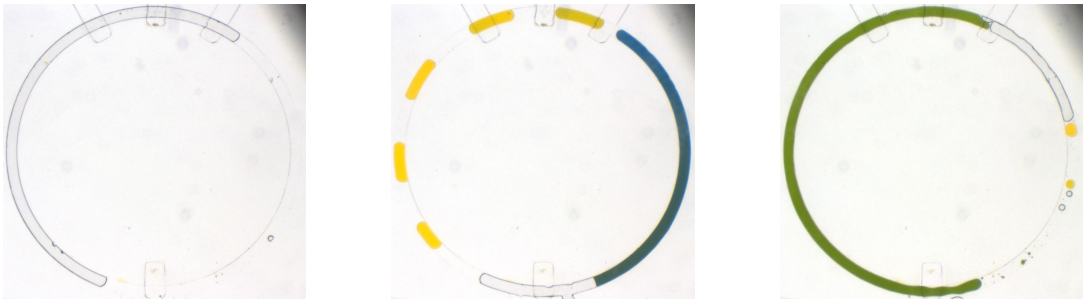

(a) (b) (c)

Figure 7.8: Mixing and fusion of droplets within a rotary mixer. Air is first injected into the rotary mixer (a). Six droplets are loaded into the loop of the mixer (b). After several cycles of mixing, a large fused and mixed droplet is obtained (c).

frequency of drop rotation about the ring was 0.33 Hz ($\approx$ 5 mm/s), which was achieved by delaying the switching of the peristaltic pump valves by 20 ms. Both shorter and longer switching times between valve actuations resulted in slower rotations about the ring.

Figure 7.9 shows the intensity profiles measured from images taken of the green control solution, yellow food colourant, and solution of yellow and blue food colourant mixed within the rotary mixer. From a sequence of images captured during mixing, intensity values were computed to give an estimate of the degree of mixing M_n:

$$M_n \approx \frac{2}{100}\left[Y_v - \left(100 - \left(\frac{(I_o - I)}{I_o}\right) \times 100\right)\right] \tag{7.4}$$

where Y_v is the intensity of the yellow food colourant, I_o the intensity of the control solution (1:1 v/v blue and yellow food colourant) and I the intensity of the solution undergoing mixing. The degree of mixing is normalised with respect to the yellow food colourant peak intensity value. The degree of mixing is plotted against mixing time in Figure 7.10. The relationship between the degree of mixing and mixing time is approximately logarithmic. The apparent delay in mixing is due two reasons, first droplets have to fuse before mixing, and second measurements are recorded at the end of a yellow droplet rather than where it meets a blue droplet. Near complete mixing of two approximately equal sized droplets is achieved within 25 seconds.

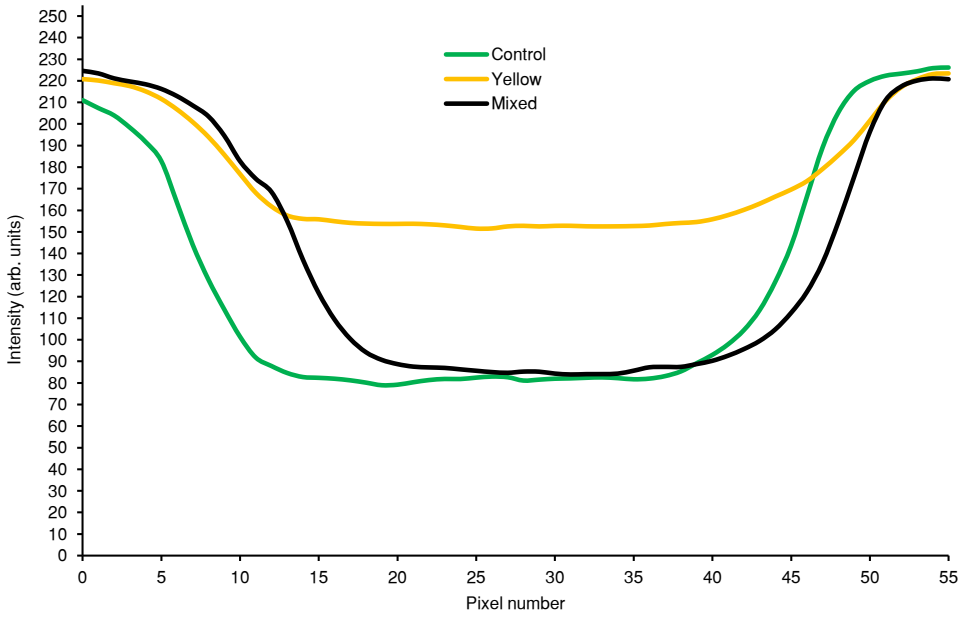

Figure 7.9: Intensity plots across part of the rotary mixer. The plots are obtained from measuring across the channel width. Shown are plots for the control solution, unmixed yellow solution and yellow-blue mixed solution.

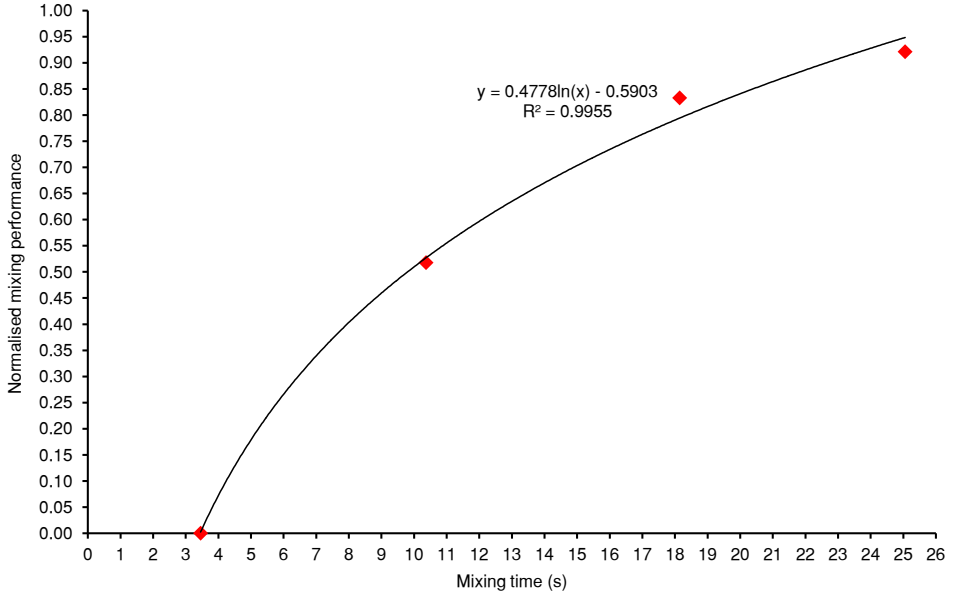

Figure 7.10: Normalised mixing performance versus mixing time. Zero indicates no mixing while one indicates complete mixing. Complete mixing between two large equal-sized droplets is achieved within 25 seconds.

The speed of rotation of the droplet about the ring increases 1.3× from initially 1.66 mm/s to 2.18 mm/s during mixing. The type of mixing exhibited in this case appears to be Taylor dispersion-mediated (Squires and Quake, 2005). With a food colourant diffusion coefficient (D) of approximately 200 $\mu m^2/s$ (Wei et al., 2010), the Péclet number (see chapter 3) is calculated from:

$$Pe = \frac{Uh}{D} \tag{7.5}$$

with U equal to 2.18 mm/s and h equal to 50 μm. The Péclet number is found to be 545, which is below the lower limit for convective stirring calculated from $2\pi R/h$. For malate dehydrogenase (D of 64.5 $\mu m^2/s$) Pe would exceed 940 (i.e. $2\pi R/h$), and therefore more rapid mixing due to convective stirring could be expected.

7.4.3 Measurement region

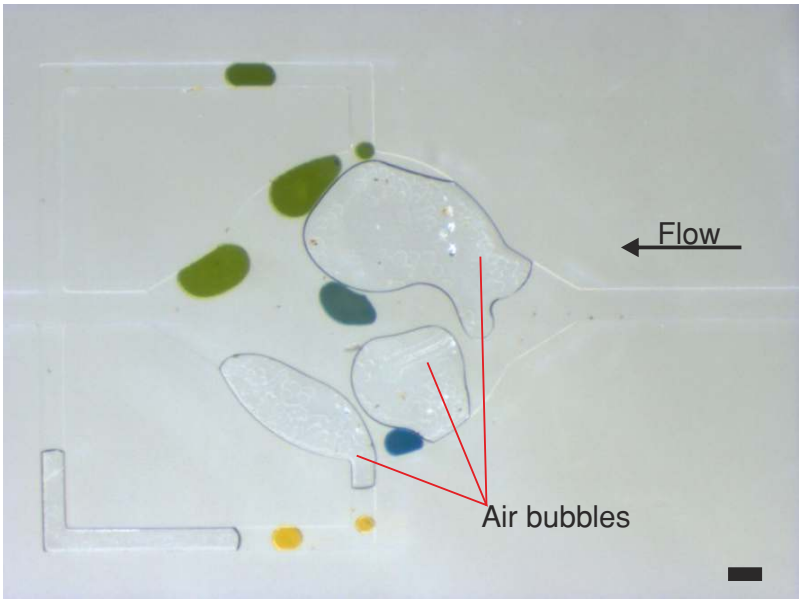

Figure 7.11: An expansion channel acting as a measurement region. Air bubbles can be seen to partially obstruct the expansion channel. Scale bar: 200 μm

An expansion channel design modified from a previous design (see Appendix D.4) is used as a measurement region. The expansion channel has a 1 mm radius and a detection volume of 157 nl. Above and below the expansion channel are side channels, which are included to ensure droplets entering the expansion are centred. The expansion channel design proved to be unsuccessful. As demonstrated in Figure 7.11, air bubbles would partially block the expansion channel and resist flowing downstream. Two sources have been identified from which the air bubbles originate. The first source is from operating the rotary mixer. The second source is due to the air permeability of PDMS. With the oil flow driven under vacuum, air is pulled from the bulk PDMS into the expansion channel region. When a simple straight channel was used instead of an expansion channel, air did not become trapped.

7.5 Summary

An automated droplet microfluidic device has been presented for automonous experimentation. A key feature of the device design is its minimal requirements for ancillary equipment. A single vacuum pump is all that is required to drive multiple streams. The device greatly reduces the volume of resources that would typically be used in macroscale laboratory equipment. The device was characterised and shown capable of producing droplets out of a single inlet ranging in volume from 0.63 nl to in excess of 25 nl. Also demonstrated was an approach whereby droplets could be stored while other droplets were generated. Droplets could be stored separated by oil to prevent premature reactions taking place. A novel approach to fuse and mix the droplets in one sequence was developed where air was purposefully preloaded into a rotary mixer. A consequence of actively using air, was that a detection chamber design based around an expansion channel would become partially obstructed by air bubbles.

Chapter 8

Conclusions and prospects

The work documented in this thesis investigated the development of microfluidic technology for autonomous experimentation. Specifically the aims of the work were to demonstrate a system that, supported scalability in its design, was capable of automating processes, and was built from technology readily accessible to other researchers. As a starting point the system was intended to perform automated enzymatic assays. This required diluting, mixing, and measurement functionalities to be included in the system design.

To meet the aim of producing technology readily accessible to other researchers, a set of fabrication techniques was developed (chapter 4) that allow for computer controlled microfluidic devices to be created in a standard chemistry laboratory environment without need for sophisticated equipment. The implementation of a peristaltic pump device by using the fabrication techniques demonstrated the suitability of the methods for the creation of automated devices. Despite barriers to microfluidic integrated valve technology being diminished, the fabrication techniques of chapter 4 did not address the issues of alignment during the construction of devices from multiple layers.

The alignment between oxidised device layers in the construction of integrated valve microfluidic devices has been problematic in the field of microfluidics for many years. Despite the many potential solutions in the literature (see examples described by Eddings et al. 2008), not one has found to be sufficiently reliable to become a recognised standard. Where water is used as a lubricant to aid alignment during bonding (Cho et al., 2009; Ding et al., 2011), no consideration had been given to whether or not water had a detrimental effect on bonding. An investigation of the effect of water on the bonding strength of oxidised PDMS

and glass samples was conducted (chapter 5). The presence of water was found to reduce the strength of bonding between oxidised layers. A new technique known as water alignment vacuum extraction (WAVE) was developed and introduced. The WAVE technique allowed for water to be used as a lubricant to facilitate alignment and obtain high bonding strengths between device layers. The WAVE technique was shown to support the accurate alignment of valved and three-dimensional mixer device layers simply by hand. Complex devices capable of withstanding high pressures can now be easily assembled by utilising WAVE in conjunction with oxygen plasma treatments.

To meet the measurement requirement in the system design, a low-cost physically compact ultra-violet photometer system built using optical semiconductor components was developed (chapter 6). The UV photometer system was tested against a commercially available spectrophotometer by measuring dilute solutions of nicotinamide adenine dinucleotide (NADH). A strong correlation was found between measurements from both instruments at a wavelength of 355 nm. The data indicated good agreement between the two instruments. The UV photometer system therefore allows for enzymatic assays involving NADH to be monitored. In the context of the autonomous experimentation system, the UV photometer provides the machine learning algorithms the necessary capability to observe experiments in order to drive the automated hardware.

An automated droplet microfluidic device was designed for autonomous experimentation with enzymes (chapter 7). To fully survey the potential computational characteristics of enzymes, a complex chemical environment is required which in turn necessitates numerous chemical inputs. The current trend in microfluidics sees designs (e.g. Tice et al. 2003) that do not easily accommodate numerous chemical inputs without requiring the same number of often expensive and bulky ancillary equipment pieces. The design presented in this work can easily support multiple chemical input streams, while only requiring a single vacuum pump to provide flow. The same microfluidic device was designed to enable the production of aqueous droplets of different size that could be varied continuously. This was achieved by utilising an actuation scheme that employs two separate valves in turn for droplet production. This allowed for droplets or slugs to be produced independent of oil flow thus removing the upper limit to slug size typical in droplet microfluidics. The scheme described in this thesis allows for droplets as small as half the channel width and as long as the length of the device main channel to be generated, therefore providing a wide continuous range for creating dilutions. This is an improvement over devices in the literature which largely use fixed networks of

microfluidic channels to obtain discrete dilutions (Walker et al., 2007; Kim et al., 2008; Hattori et al., 2009).

Also demonstrated in this work is a novel means by which multiple droplets can be fused and mixed in one step. The microfluidic design in this work utilises a circular channel mixer similar to the rotary mixer described by Chou et al. (2001), except that whereas Chou et. al. had used the rotary mixer for single-phase aqueous solutions, here it is used to fuse and mix aqueous droplets suspended in oil. The mixer consists of inlet and outlet channels in close proximity, separated by an active bypass valve. With the bypass valve closed droplets are stored within the mixer and when the bypass valve is opened, the flow proceeds between inlet and outlet without disturbing the stored droplets. To fuse and mix the droplets the circular mixer is first isolated from the main channel of the device, flow is then generated by an integrated peristaltic pump. At first the mixing scheme was found to perform poorly with droplets resisting fusion and the peristaltic pump causing droplet breakup. However by introducing a third phase (air) to the fluid system, fusion was far more reliable, droplet breakup was eliminated, and complete mixing possible within 25 seconds for a 15 mm long slug. The advantages of the approach include, the prevention of reactions taking place prematurely, and the ability to fuse and mix multiple droplets in one step. The scheme of using a circular mixer together with purposeful injection of air to fuse and mix aqueous slugs in oil is novel and the results from the scheme are to be published. Droplet microfluidic technology has not only allowed for a device capable of automatically performing diluting and mixing functions, it has also opened up potential scalability to utilise many different chemicals in experiments. Furthermore the use of droplet microfluidic technology has allowed sample volumes to be reduced by almost four orders of magnitude when compared to standard 1.5 ml cuvettes used in enzymatic assays.

In conclusion from this work, the previous limits of the experimental apparatus component of autonomous experimentation systems, specifically for chemical and biological studies, have now been overcome. There are however still some technical challenges remaining that this work has not been able to fully address. Ideally a control feedback mechanism would be implemented to allow for finer control of fluids on-chip. A machine vision approach may be a possible means to achieve this. The integration of optical measurement components into the microfluidic device is still a problem that requires some attention, but a good starting point would be to look at the work on dye-doping and out-of-plane detection channels described in appendix F. Despite the open challenges, the work described in this thesis in combination with novel machine learning algorithms (Lovell, 2011) makes for the

exciting and realistic prospect that autonomous experimentation could soon be used as a standard method to drive scientific discovery in the chemistry or biology laboratory. This is in turn could rapidly advance research into cures for diseases, the creation of new materials, and exploitation of biological systems as powerful computers.

8.1 Publications resulting from work reported in this thesis

Jones, G., Lovell, C., Gunn, S., Morgan, H., & Zauner, K.-P. (2012) Enabling the Discovery of Computational Characteristics of Enzyme Dynamics. In: *IEEE WCCI CEC 2012*, pp. 1806–1813

Jones, G., Lovell, C., Morgan, H., & Zauner, K.-P. (2011) Organising Chemical Reaction Networks in Space and Time with Microfluidics. *International Journal of Nanotechnology and Molecular Computation (IJNMC)*, pp. 35–56 IGI Publishing. ISSN: 1941-6318

Lovell, C., Jones, G., Gunn, S. & Zauner, K.-P. (2010) An Artificial Experimenter for Enzymatic Response Characterisation. In: Pfahringer, B., Holmes, G., & Hoffmann, A. (Eds.) *13th International Conference on Discovery Science*, pp. 42-56, Springer-Verlag. ISBN: 978-3-642-16183-4

Jones, G., Lovell, C., Morgan, H., & Zauner, K.-P. (2010) Characterising Enzymes for Information Processing: Microfluidics for Autonomous Experimentation (abstract). In: Calude, C., Hagiya, M., Morita, K., Rozenberg, G. & Timmis, J. (Eds.) *9th International Conference on Unconventional Computation*, pp. 191, Springer Berlin / Heidelberg. ISBN 978-3-642-13522-4

Lovell, C., Jones, G., Gunn, S. & Zauner, K.-P. (2010) Autonomous Experimentation: Active Learning for Enzyme Response Characterisation. In: *Workshop on Active Learning and Experimental Design*, 16th May 2010, Sardinia, Italy.

Lovell, C. J., Jones, G. & Zauner, K.-P. Autonomous Experimentation: Coupling Machine Learning with Computer Controlled Microfluidics (abstract). *ELRIG Robotics Workshop, ELRIG Drug Discovery 2009* (Liverpool, UK, 2009).

Jones, G. J. & Zauner, K.-P. New Apparatus for Characterising Molecular Computing Substrates (poster). *3rd Microsoft Research Summer School 2008* (Cambridge, UK, 2008, and *SemiBiotic Systems Conference* (Malta, 2008).

Appendix A

Accessible prototyping of integrated valve microfluidic devices

A.1 UV exposure intensity data

Table A.1: UV light intensity versus distance with and without IR filter. Unpublished data courtesy of (Aghdaei, 2010)

Distance from Lamp (mm)	Intensity with IR Filter (mW/cm^2)	Intensity without IR Filter (mW/cm^2)
70	2.7	11.4
125	2.2	6.4
185	1.2	4.9

A.2 DFR processing workflow

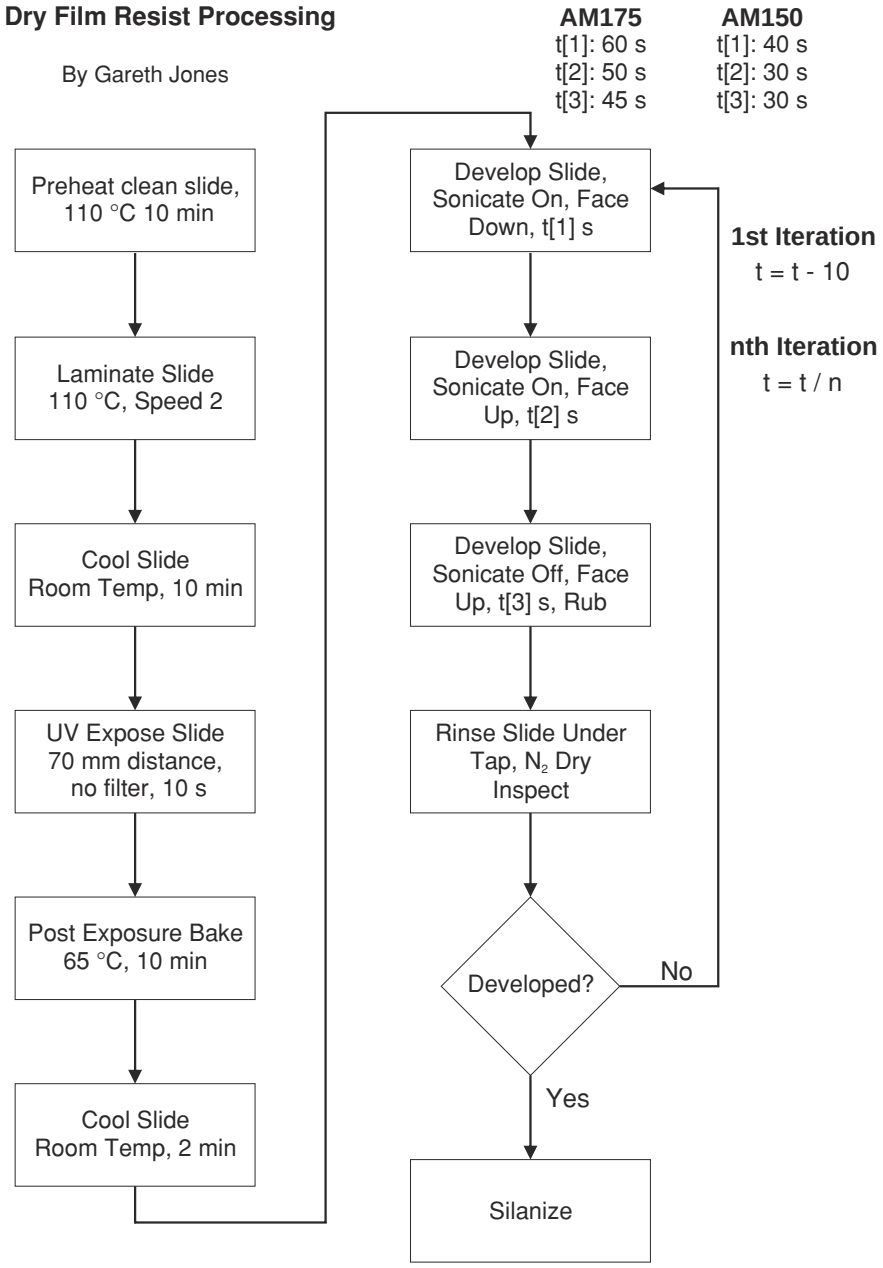

A.3 Silanized replication master contact angle

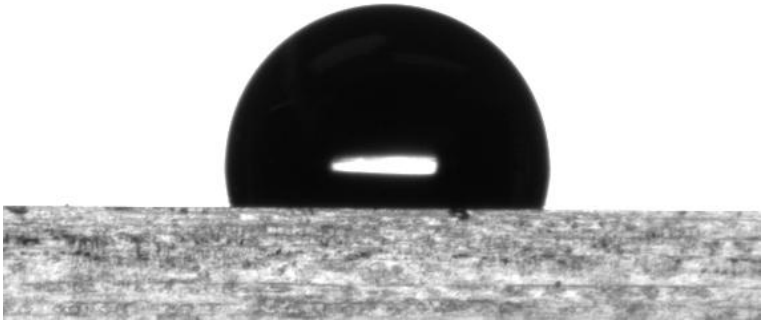

Figure A.1: A drop of water on a silanized replication master. A contact angle of approximately 103^o was recorded.

A.4 PDMS base weight and resulting thickness

Table A.2: PDMS Prepared Weight and Resulting Layer Thickness

Replication Master Dimensions (width × length [mm])	Elastomer Base Weight [grams]	Layer Thickness [mm]
25 x 75	5	2.06
25 x 75	10	4.22
25 x 75	15	6.94
35 x 75	5	1.21
35 x 75	10	2.64
35 x 75	15	4.5
50 x 75	10	2.02
50 x 75	15	3.22

Table A.3: Manufacturer's suggested curing times for PDMS, obtained from (Corning, 2009)

Temperature (^{o}C)	Time (mins)
150	10
125	20
100	45
Room	48Hrs

Table A.4: Commonly-used Solvents and the amount of swelling caused in PDMS, data from (Lee et al., 2003)

Solvent	Swelling (%)
Acetone	6
Methanol	2
Toluene	31
1-propanol	9

A.5 PDMS cure times and temperature

A.6 PDMS–Solvent compatibility

A.7 Solenoid test script

```
valve 8 on
wait 1000
valve 8 off
wait 1000
valve 8 on
wait 8
valve 8 off
wait 1000
valve 8 on
wait 12
valve 8 off
wait 1000
valve 8 on
wait 15
```

```
valve 8 off
wait 1000
valve 8 on
wait 18
valve 8 off
wait 1000
valve 8 on
wait 21
valve 8 off
wait 1000
valve 8 on
wait 24
valve 8 off
wait 1000
valve 8 on
wait 27
valve 8 off
wait 1000
valve 8 on
wait 30
valve 8 off
wait 1000
valve 8 on
wait 35
valve 8 off
wait 1000
valve 8 on
wait 40
valve 8 off
wait 1000
valve 8 on
wait 45
valve 8 off
wait 1000
valve 8 on
wait 50
valve 8 off
wait 1000
```

```
valve 8 on
wait 55
valve 8 off
wait 1000
valve 8 on
wait 60
valve 8 off
wait 1000
valve 8 on
wait 65
valve 8 off
wait 1000
valve 8 on
wait 70
valve 8 off
wait 1000
valve 8 on
wait 75
valve 8 off
wait 1000
END
```

Appendix B

Control software

B.1 Optical measurement

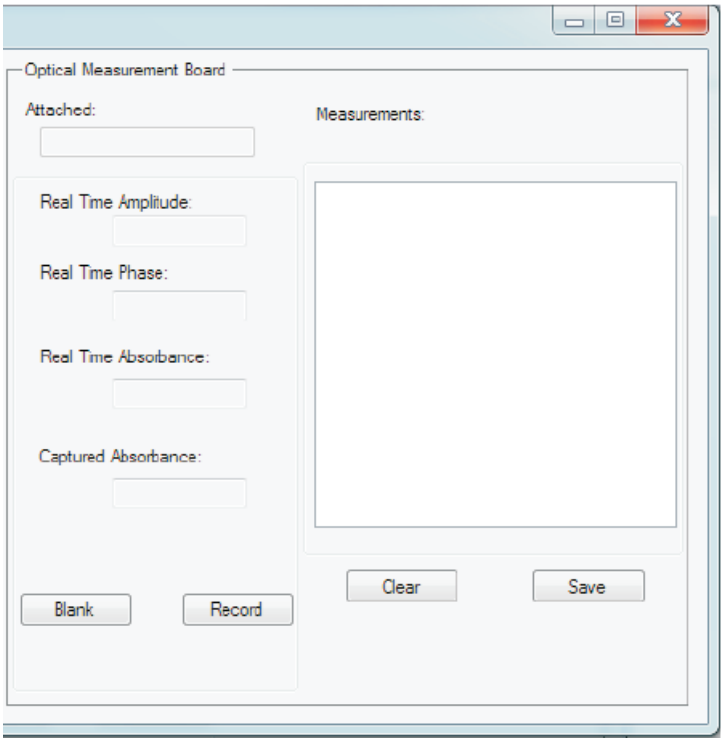

Figure B.1: Optical measurement component of the GUI.

B.2 Valve control and scripting

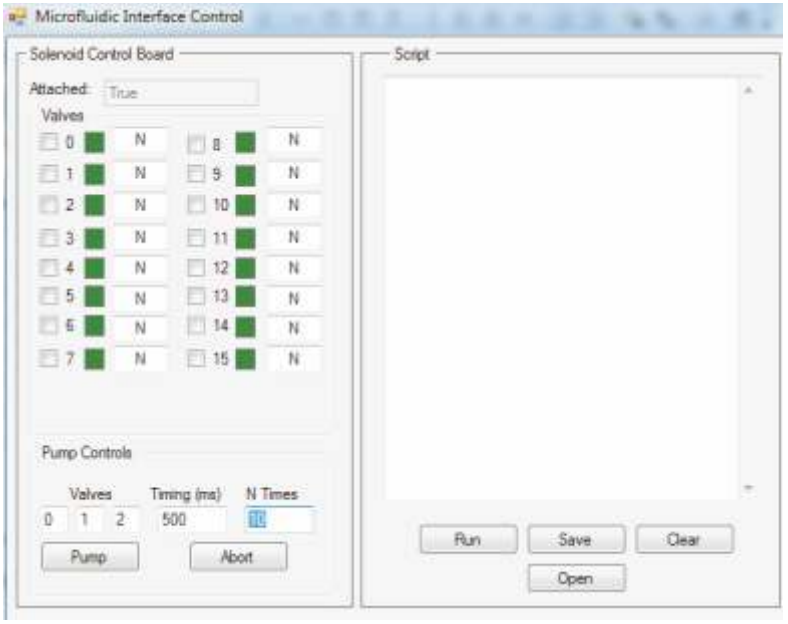

Figure B.2: GUI developed to allow both manual and automated control of on-chip valves

B.3 Code listing

```
using System;
using System.Collections.Generic;
using System.ComponentModel;
using System.Data;
using System.Drawing;
using System.Linq;
using System.Text;
using System.Windows.Forms;
using Phidgets;
using Phidgets.Events;
using System.IO.Ports;
using System.Threading;
using System.Numeric;
using System.Diagnostics;


namespace DeviceInterface
{
    public partial class Interface : Form
    {
        static BackgroundWorker bw;
        static BackgroundWorker bwComms;
        static BackgroundWorker[] ValveWorkers;

        private static InterfaceKit ifkit;                        //create new ifkit object
        private static CheckBox[] ValvesCheck = new CheckBox[16]; //create 16 Checkbox objects
        private static Panel[] ValvesPanel = new Panel[16];       //create 16 Panel objects
        private static TextBox[] valveSelect = new TextBox[3];
        private static SerialPort serialPort = new SerialPort();
        private static TextBox CommsPhase = new TextBox();
        private static TextBox CommsAmp = new TextBox();
        private static TextBox CaptAbs = new TextBox();
        private static TextBox RTAbs = new TextBox();
        private static TextBox[] valveTime = new TextBox[16];
        private static ListBox Target = new ListBox();

        #region Global Variables
        //Define some global variables
        public static class GlobVars
        {   public static int NoWorkers;
            public static int PumpTime1;
            public static int[] pumpValves = new int[3];
            public static string ReadRS;
            public static bool FormClosingFlag;
            public static double BlankRead;
            public static double AbsRead;
            public static bool CameraStarted = false;
            public static int[] ValveTiming  = new int[16];
            public static int PumpNTimes;
        }
        #endregion
        public Interface()
        {
            InitializeComponent();
        }
        private void Form1_Load(object sender, EventArgs e)
        {
            GlobVars.PumpNTimes = 10;
            GlobVars.NoWorkers = 16;
            GlobVars.BlankRead = 1;
            GlobVars.PumpTime1 = 500;
            GlobVars.pumpValves[0] = 0;
            GlobVars.pumpValves[1] = 1;
            GlobVars.pumpValves[2] = 2;
            GlobVars.FormClosingFlag = false;
            pumpTime.Text = GlobVars.PumpTime1.ToString();
            MakeValveControl();   //Assigns Checkboxes and Panels in form to objects created above
            CommsPhase = (TextBox)groupBox1.Controls["textBox3"];
            CommsAmp = (TextBox)groupBox1.Controls["textBox2"];
            RTAbs = (TextBox)groupBox1.Controls["textBox4"];
            CaptAbs = (TextBox)groupBox1.Controls["textBox1"];
            //build the background worker object and assign hooks
            bw = new BackgroundWorker();
            bwComms = new BackgroundWorker();
```

```
    bwComms.WorkerSupportsCancellation = true;
    bw.WorkerSupportsCancellation = true;
    bw.DoWork += bw_DoWork;
    bw.RunWorkerCompleted += bw_RunWorkerCompleted;
    bwComms.DoWork += bwComms_DoWork;
    bwComms.RunWorkerCompleted += bwComms_RunWorkerCompleted;
    SerialStart();

    try
    {
        ifkit = new InterfaceKit();
        ifkit.Attach += new AttachEventHandler(ifkit_Attach);
        ifkit.Detach += new DetachEventHandler(ifkit_Detach);
        ifkit.Error += new ErrorEventHandler(ifkit_Error);
        FormClosing += new FormClosingEventHandler(Form1_FormClosing);
        serialPort.DataReceived += new SerialDataReceivedEventHandler(serialPort_DataReceived);
        //serialPort.Open();

        openCmdLine(ifkit);
    }
    catch (PhidgetException ex)
    {
        bw.CancelAsync();
    }
    catch (Exception ex)
    {
        bwComms.CancelAsync();
    }
}
private void SerialStart()
{
    serialPort.PortName = "COM9";
    serialPort.BaudRate = 115200;
    serialPort.DataBits = 8;
    serialPort.Parity = Parity.None;
    serialPort.StopBits = StopBits.One;
    serialPort.Handshake = Handshake.None;
    //serialPort.ReadTimeout = 500;  no timeout otherwise exception when pic stopped
    try
    {
        serialPort.Open();
    }
    catch (Exception ex)
    {
        return;
    }
}

#region Serial Port Data Received
void serialPort_DataReceived(Object sender, SerialDataReceivedEventArgs e)
{
    if (!bwComms.IsBusy && !GlobVars.FormClosingFlag)
    {
            bwComms.RunWorkerAsync();
        return;
    }
    else if (GlobVars.FormClosingFlag)
    {
        bwComms.CancelAsync();
        serialPort.Close();
        serialPort.DataReceived -= new SerialDataReceivedEventHandler(serialPort_DataReceived);
    }
    return;
}
#endregion


#region Refresh Phidgets Outputs
//clear all outputs
private void refresh()
{
    for (int i = 0; i != 16; i++)
    {
        ifkit.outputs[i] = false;
    }
}
#endregion
```

```
        #region Phidget Handlers
        //ifkit attach handler
        //Display text "attached"
        //Enable manual valve control
        void ifkit_Attach(object sender, AttachEventArgs e)
        {
            InterfaceKit ifkit = (InterfaceKit)sender;
            attachedTxtBox.Text = ifkit.Attached.ToString();
            EnableValveControl();
            refresh();
            //on clicking pumpButton fire the background worker
            pumpButton.Click += new EventHandler(runBw);
            pumpAbortButton.Click += new EventHandler(cancelBw);
        }

        //ifkit detach handler
        void ifkit_Detach(object sender, DetachEventArgs e)
        {
            if (!bw.CancellationPending)
            {
                bw.CancelAsync();
            }
            InterfaceKit ifkit = (InterfaceKit)sender;
            attachedTxtBox.Text = ifkit.Attached.ToString();
            DisableValveControl();
        }
        //ifkit error event handler
        void ifkit_Error(object sender, ErrorEventArgs e)
        {
        }
#endregion


        #region Background Worker Pumping Methods
        //cancel the background worker
        void cancelBw(object sender, EventArgs e)
        {
            bw.CancelAsync();
        }



        //run the background worker
        void runBw(object sender, EventArgs e)
        {
            if (!bw.IsBusy)
            {
                bw.RunWorkerAsync();
            }
        }
        //background worker do work function
         static void bw_DoWork(object sender, DoWorkEventArgs e)
        {
            BackgroundWorker bw = sender as BackgroundWorker;
            int time = GlobVars.PumpTime1;
            int index = GlobVars.pumpValves.Length - 1;
             //While there are no cancellation pending signals, try pumping, fail if phidgets acts up.
             while(!bw.CancellationPending)
            {
                try
                {
                    ValvePumpSequence();
                }
                catch (PhidgetException ex)
                {
                }
            }
             //Need to check if ifkit still attached when cancelling otherwise exception thrown as
             //phidget not available
             if (bw.CancellationPending && ifkit.Attached)
             {
                 ifkit.outputs[GlobVars.pumpValves[index]] = false;
                 ifkit.outputs[GlobVars.pumpValves[index - 1]] = false;
                 ifkit.outputs[GlobVars.pumpValves[index - 2]] = false;
                 ValvesPanel[GlobVars.pumpValves[index - 2]].BackColor = Color.Green;
                 ValvesPanel[GlobVars.pumpValves[index - 1]].BackColor = Color.Green;
                 ValvesPanel[GlobVars.pumpValves[index]].BackColor = Color.Green;
                 e.Cancel = true;
```

```
        return;
    }
    else
    {
        e.Cancel = true;
        return;
    }
}
//background worker on complete function
static void bw_RunWorkerCompleted(object sender, RunWorkerCompletedEventArgs e)
{
}
#endregion


#region Background Worker Comms Methods
static void bwComms_DoWork(object sender, DoWorkEventArgs e)
{
    string temp;
    double working;
    double final;

   BackgroundWorker bwComms = sender as BackgroundWorker;
   CommsPhase.Invoke(new Action(delegate { CommsPhase.Text = serialPort.ReadTo(",").Substring(0,7); }));
   CommsAmp.Invoke(new Action(delegate { CommsAmp.Text = serialPort.ReadTo(",").Substring(10,8); }));
   temp = serialPort.ReadTo(",").Substring(10, 8);

    if (double.TryParse(temp, out working) == false)
    {
        working = 1;
    }
    final = (Math.Log10(working / GlobVars.BlankRead));
    if (final != 0)
    {

        RTAbs.Invoke(new Action(delegate { RTAbs.Text = final.ToString().Substring(0,6); }));
    }
    else if (final == 0)
    {
       RTAbs.Invoke(new Action(delegate { RTAbs.Text = final.ToString(); }));
    }
}



static void bwComms_RunWorkerCompleted(object sender, RunWorkerCompletedEventArgs e)
{

}
#endregion

#region Pump Sequence Method
//drives the pump sequence
static void ValvePumpSequence()
{
    int t = GlobVars.PumpTime1;
    int i = GlobVars.pumpValves.Length - 1;

    //disables manual user input when pumping
    for (int j = 0; j != 3; j++)
    {
        int s = GlobVars.pumpValves[j];
        ValvesCheck[s].Invoke(new Action(delegate { ValvesCheck[s].Enabled = false; }));
        ValvesCheck[s].Invoke(new Action(delegate { ValvesCheck[s].Checked = false; }));
    }

        for (int r = 0; r < GlobVars.PumpNTimes; r++)
        {
            ifkit.outputs[GlobVars.pumpValves[i]] = true;               //101
            ifkit.outputs[GlobVars.pumpValves[i - 2]] = true;
            ValvesPanel[GlobVars.pumpValves[i - 2]].BackColor = Color.Red;
            ValvesPanel[GlobVars.pumpValves[i]].BackColor = Color.Red;
            Thread.Sleep(t);
            ifkit.outputs[GlobVars.pumpValves[i]] = false;               //100
            ValvesPanel[GlobVars.pumpValves[i]].BackColor = Color.Green;
            Thread.Sleep(t);
            ifkit.outputs[GlobVars.pumpValves[i - 1]] = true;                  //110
            ValvesPanel[GlobVars.pumpValves[i - 1]].BackColor = Color.Red;
```

```
            Thread.Sleep(t);
            ifkit.outputs[GlobVars.pumpValves[i - 2]] = false;                //010
            ValvesPanel[GlobVars.pumpValves[i - 2]].BackColor = Color.Green;
            Thread.Sleep(t);
            ifkit.outputs[GlobVars.pumpValves[i]] = true;                  //011
            ValvesPanel[GlobVars.pumpValves[i]].BackColor = Color.Red;
            Thread.Sleep(t);
            ifkit.outputs[GlobVars.pumpValves[i - 1]] = false;                //001
            ValvesPanel[GlobVars.pumpValves[i - 1]].BackColor = Color.Green;
            Thread.Sleep(t);
         }
        for (int j = 0; j != 3; j++)
        {
            int s = GlobVars.pumpValves[j];
            ValvesCheck[s].Invoke(new Action(delegate { ValvesCheck[s].Enabled = true; }));
        }
    bw.CancelAsync();
}
#endregion
#region Check Box Valve Control Method

//Links the check changed state of the check boxes to the changing of the panels representing
//the outputs of the phidget.
private void checkBox_CheckedChanged(object sender, EventArgs e)
{
   CheckBox outputChk = (CheckBox)sender;
    int outputIndex = int.Parse((string)outputChk.Tag);
    //Checks to see if valves have been assigned to pumps and disallows their manual actuation.
  //  if ((outputIndex == GlobVars.pumpValves[0]) || (outputIndex == GlobVars.pumpValves[1]) || (outputIndex == GlobVars.pumpValves[2]))
   // {
     //   return;
    //}

    //With the current checkbox, if the time is NaN, allow manual switching
    if (int.TryParse(valveTime[outputIndex].Text, out GlobVars.ValveTiming[outputIndex]) == false)
    {
        ifkit.outputs[outputIndex] = outputChk.Checked;
        if (ValvesPanel[outputIndex].BackColor != Color.Red)
        {
            ValvesPanel[outputIndex].BackColor = Color.Red;
        }
        else if (ValvesPanel[outputIndex].BackColor != Color.Green)
        {
            ValvesPanel[outputIndex].BackColor = Color.Green;
        }
    }
    //If there is a number, fire up the background worker
    else if (int.TryParse(valveTime[outputIndex].Text, out GlobVars.ValveTiming[outputIndex]) == true)
    {
        if (!ValveWorkers[outputIndex].IsBusy)
        {
            ValveWorkers[outputIndex].RunWorkerAsync(outputIndex);
        }
    }
}
#endregion

#region Disable Valve Control
//Stops user manually actuating valves when phidgets unplugged
private void DisableValveControl()
{
    pumpButton.Enabled = false;
    pumpTime.Enabled = false;
    pumpAbortButton.Enabled = false;
 for (int i = 0; i != 16; i++)
    {
      ValvesCheck[i].Enabled = false;
      ValvesPanel[i].BackColor = Color.Gray;
      valveTime[i].Enabled = false;
    }
 for (int i = 0; i < 3; i++)
 {
     valveSelect[i].Enabled = false;
 }

}
#endregion
```

```
#region Enable Valve Control
//Allows user to actuate valves when phidgets connected
private void EnableValveControl()
{
    for (int i = 0; i < 16; i++)
    {
      ValvesCheck[i].Enabled = true;
      ValvesPanel[i].BackColor = Color.Green;
      valveTime[i].Enabled = true;
    }
   for (int i = 0; i < 3; i++)
    {
      valveSelect[i].Enabled = true;
    }
    pumpAbortButton.Enabled = true;
    pumpButton.Enabled = true;
    pumpTime.Enabled = true;
}
#endregion


#region Build Checkboxes to Manually Control Valves
//Assigns checkboxes to ValveCheck objects of which there are 16
//Same for panels 5-20 hence +5
private void MakeValveControl()
{
    pumpAbortButton.Enabled = false;
    pumpButton.Enabled = false;
    pumpTime.Enabled = false;
    for (int i = 0; i < 3; i++)
    {
        valveSelect[i] = (TextBox)pumpGroupBox.Controls["valveSelect" + i.ToString()];
        valveSelect[i].Enabled = false;
        valveSelect[i].Text = GlobVars.pumpValves[i].ToString();
    }


    ValveWorkers = new BackgroundWorker[16];
    for (int i = 0; i < 16; i++)
    {
        ValvesCheck[i] = (CheckBox)groupBoxValves.Controls["checkBox" + (i + 1).ToString()];
        ValvesPanel[i] = (Panel)groupBoxValves.Controls["panel" + (i + 5).ToString()];
        ValvesCheck[i].Enabled = false;
        ValvesPanel[i].Enabled = false;
        ValvesCheck[i].CheckedChanged += new EventHandler(checkBox_CheckedChanged);
        valveTime[i] = (TextBox)groupBoxValves.Controls["valveTime" + i.ToString()];
        valveTime[i].Text = "N";
        valveTime[i].Enabled = false;
        //valveTime[i].TextChanged += new EventHandler(valveTime_Changed);
        //GlobVars.IsNumeric[i] = false;
        ValveWorkers[i] = new BackgroundWorker();
        ValveWorkers[i].WorkerSupportsCancellation = true;
        ValveWorkers[i].DoWork += new DoWorkEventHandler(Valve_DoWork);
    }
}
#endregion

#region Valve Do Work for Timed Valves
void Valve_DoWork(object sender, DoWorkEventArgs e)
{
    BackgroundWorker ValveWorker = sender as BackgroundWorker;
    int i = (int) e.Argument;
    while (!ValveWorker.CancellationPending)
    {
        try
        {
            ValvesCheck[i].Invoke(new Action(delegate { ValvesCheck[i].Enabled = false; }));
            ValvesCheck[i].Invoke(new Action(delegate { ValvesCheck[i].Checked = false; }));
            ValvesPanel[i].Invoke(new Action(delegate { ValvesPanel[i].BackColor = Color.Red; }));
            ifkit.outputs[i] = true;
            Thread.Sleep(GlobVars.ValveTiming[i]);
            ifkit.outputs[i] = false;
            ValveWorker.CancelAsync();
            ValvesCheck[i].Invoke(new Action(delegate { ValvesCheck[i].Enabled = true; }));
            ValvesPanel[i].Invoke(new Action(delegate { ValvesPanel[i].BackColor = Color.Green; }));
        }
        catch
        {
```

```
            ValveWorker.CancelAsync();
        }
    }
}
#endregion

#region Form Closing

private void Form1_FormClosing(object sender, FormClosingEventArgs e)
{
    GlobVars.FormClosingFlag = true;
    //kill the bw if still running
    for (int i = 0; i > 16; i++)
    {
        if (!ValveWorkers[i].CancellationPending)
        {
            ValveWorkers[i].CancelAsync();
        }

    }

    if (!bw.CancellationPending || !bwComms.CancellationPending)
    {
        bw.CancelAsync();
        bwComms.CancelAsync();
    }

    if (ifkit.Attached)
    {
        refresh();
    }
    ifkit.Attach -= new AttachEventHandler(ifkit_Attach);
    ifkit.Detach -= new DetachEventHandler(ifkit_Detach);
    ifkit.Error -= new ErrorEventHandler(ifkit_Error);
    bw.DoWork -= bw_DoWork;
    bw.RunWorkerCompleted -= bw_RunWorkerCompleted;
    pumpButton.Click -= new EventHandler(runBw);
    pumpAbortButton.Click -= new EventHandler(cancelBw);

    for (int i = 0; i > 16; i++)
    {
        ValvesCheck[i].CheckedChanged -= new EventHandler(checkBox_CheckedChanged);
        ValveWorkers[i].DoWork -= new DoWorkEventHandler(Valve_DoWork);
    }
    Application.DoEvents();
    ifkit.close();
}

#endregion

//Parses command line arguments and calls the appropriate open
#region Command line open functions
private void openCmdLine(Phidget p)
{
    openCmdLine(p, null);
}
  private void openCmdLine(Phidget p, String pass)
{
    int serial = -1;
    int port = 5001;
    String host = null;
    bool remote = false, remoteIP = false;
    string[] args = Environment.GetCommandLineArgs();
    String appName = args[0];
    try
    { //Parse the flags
        for (int i = 1; i < args.Length; i++)
        {
            if (args[i].StartsWith("-"))
                switch (args[i].Remove(0, 1).ToLower())
                {
                    case "n":
                        serial = int.Parse(args[++i]);
                        break;
                    case "r":
                        remote = true;
                        break;
                    case "s":
```

```
                        remote = true;
                        host = args[++i];
                        break;
                    case "p":
                        pass = args[++i];
                        break;
                    case "i":
                        remoteIP = true;
                        host = args[++i];
                        if (host.Contains(":"))
                        {
                            host = host.Split(':')[0];
                            port = int.Parse(host.Split(':')[1]);
                        }
                        break;
                    default:
                        goto usage;
                }
            else
                goto usage;
        }
        if (remoteIP)
            p.open(serial, host, port, pass);
        else if (remote)
            p.open(serial, host, pass);
        else
            p.open(serial);
        return; //success
    }
    catch { }
usage:
    StringBuilder sb = new StringBuilder();
    sb.AppendLine("Invalid Command line arguments." + Environment.NewLine);
    sb.AppendLine("Usage: " + appName + " [Flags...]");
    sb.AppendLine("Flags:\t-n   serialNumber\tSerial Number, omit for any serial");
    sb.AppendLine("\t-r\t\tOpen remotely");
    sb.AppendLine("\t-s   serverID\tServer ID, omit for any server");
    sb.AppendLine("\t-i   ipAddress:port\tIp Address and Port. Port is optional, defaults to 5001");
    sb.AppendLine("\t-p   password\tPassword, omit for no password" + Environment.NewLine);
    sb.AppendLine("Examples: ");
    sb.AppendLine(appName + " -n 50098");
    sb.AppendLine(appName + " -r");
    sb.AppendLine(appName + " -s myphidgetserver");
    sb.AppendLine(appName + " -n 45670 -i 127.0.0.1:5001 -p paswrd");
    MessageBox.Show(sb.ToString(), "Argument Error", MessageBoxButtons.OK, MessageBoxIcon.Error);
    Application.Exit();
}
#endregion

#region Manual Pump Settings
  private void PumpNTimesInput_TextChanged(object sender, EventArgs e)
  {
      if (int.TryParse(PumpNTimesInput.Text, out GlobVars.PumpNTimes) == false)
      {
          GlobVars.PumpNTimes = 1;
      }
  }

    //Capture manually inputted pump time and save to GlobVars.PumpTime1
  private void pumpTime_TextChanged(object sender, EventArgs e)
  {
      if (int.TryParse(pumpTime.Text, out GlobVars.PumpTime1) == false)
      {
          GlobVars.PumpTime1 = 500;
      }
  }

    //TODO: handle all valve selects under 1 function as per check boxes
    // Capture assignment of valves to pumps, update GlobVars.pumpValves[] accordingly
private void valveSelect0_TextChanged(object sender, EventArgs e)
{
    if (int.TryParse(valveSelect0.Text, out GlobVars.pumpValves[0]) == false)
    {
        GlobVars.pumpValves[0] = 0;
    }

}
```

```
 private void valveSelect1_TextChanged(object sender, EventArgs e)
 {
     if (int.TryParse(valveSelect1.Text, out GlobVars.pumpValves[1]) == false)
     {
         GlobVars.pumpValves[1] = 0;
     }
 }

 private void valveSelect2_TextChanged(object sender, EventArgs e)
 {
     if (int.TryParse(valveSelect2.Text, out GlobVars.pumpValves[2]) == false)
     {
         GlobVars.pumpValves[2] = 0;
     }
 }

   #endregion


#region Spectrophotometer Reading Controls
 //Capture Absorbance
 private void button2_Click(object sender, EventArgs e)
 {
     Capture_Absorbance();
 }

 private void Capture_Absorbance()
 {
     double temp;
     double actual;
     if (double.TryParse(CommsAmp.Text, out GlobVars.AbsRead) == false)
     {
         GlobVars.AbsRead = 1;
     }
     actual = GlobVars.AbsRead;
     temp = (-1 * Math.Log10(GlobVars.AbsRead / GlobVars.BlankRead));


     if (temp != 0)
     {

         textBox1.Text = temp.ToString().Substring(0, 6);
         listBox2.Items.Add(textBox7.Text.ToString() + "\t" + temp.ToString().Substring(0, 6)
          + "\t" + actual.ToString() + "\t" + DateTime.Now.ToString());
     }
     else if (temp == 0)
     {
         textBox1.Text = temp.ToString();
         listBox2.Items.Add(textBox7.Text.ToString() + "\t" + temp.ToString() +
         "\t" + actual.ToString() + "\t" + DateTime.Now.ToString());
     }
     listBox2.SelectedIndex = listBox2.Items.Count - 1; // makes listbox autoscroll with inputs
     return;
 }


 //Capture Blank Value
 private void button1_Click(object sender, EventArgs e)
 {
     Capture_Blank();
 }

 private void Capture_Blank()
 {
     if (double.TryParse(CommsAmp.Text, out GlobVars.BlankRead) == false)
     {
         GlobVars.BlankRead = 1;
     }
     listBox2.Items.Add("Blanked\t" + GlobVars.BlankRead.ToString() + "\t" + DateTime.Now.ToString());
     listBox2.SelectedIndex = listBox2.Items.Count - 1; // makes listbox autoscroll with inputs
     return;
 }

 //Save file dialog
 private void button3_Click(object sender, EventArgs e)
 {
     string S = "listBox2";
     SaveFile(S);
```

```
}

//Clear listbox of all recorded values
private void button8_Click(object sender, EventArgs e)
{
    listBox2.Items.Clear();
}
#endregion

#region Save File Dialog
private void SaveFile(string S)
{
    Target = (ListBox)groupBox2.Controls[S];
    SaveFileDialog saveFileDialog2 = new SaveFileDialog();
    saveFileDialog2.DefaultExt = "txt";
    saveFileDialog2.AddExtension = true;
    saveFileDialog2.Filter = "Text File (*.txt)|*.txt|All Files (*.*)|*.*";
    if (saveFileDialog2.ShowDialog() == DialogResult.OK)
    {
        System.IO.StreamWriter sw = new System.IO.StreamWriter(saveFileDialog2.FileName);
        foreach (object item in Target.Items)
            sw.WriteLine(item.ToString());
        sw.Close();
    };
    saveFileDialog2.Dispose();
}
#endregion



#region Call Webcam
private void button9_Click(object sender, EventArgs e)
{
    if (!GlobVars.CameraStarted)
    {
        try
        {
            Process.Start("TestAviCap32.exe");
            GlobVars.CameraStarted = true;
        }
        catch
        {
            return;
        }

    }
    return;
}
#endregion


#region Scripting Control
private void button5_Click(object sender, EventArgs e)
{
    SaveFileDialog saveFileDialog2 = new SaveFileDialog();

    saveFileDialog2.DefaultExt = "txt";
    saveFileDialog2.AddExtension = true;
    saveFileDialog2.Filter = "Text File (*.txt)|*.txt|All Files (*.*)|*.*";

    if (saveFileDialog2.ShowDialog() == DialogResult.OK)
    {
        System.IO.StreamWriter sw = new System.IO.StreamWriter(saveFileDialog2.FileName);
        //Use StreamWriter class.
        //Use writeline methode to write the text and
        //in para.. put your text, i have used  textBox1's text
        sw.Write(textBox6.Text);
        sw.WriteLine("\r\n" + "END" + "\r\n" + DateTime.Now);

        //always close your stream
        sw.Close();
    };
    saveFileDialog2.Dispose();
}

private void button6_Click(object sender, EventArgs e)
{
    textBox6.Clear();
```

```
}

//opens files
private void button7_Click(object sender, EventArgs e)
{
    OpenFileDialog OpenFileDialog1 = new OpenFileDialog();
    OpenFileDialog1.DefaultExt = "txt";
    OpenFileDialog1.AddExtension = true;
    OpenFileDialog1.Filter = "Text File (*.txt)|*.txt|All Files (*.*)|*.*";
    if (OpenFileDialog1.ShowDialog() == DialogResult.OK)
    {
        System.IO.StreamReader tr = new System.IO.StreamReader(OpenFileDialog1.FileName);
        textBox6.Text = tr.ReadToEnd();

        //always close your stream
        tr.Close();
    };
    OpenFileDialog1.Dispose();
}

//Run Program
private void button4_Click(object sender, EventArgs e)
{

    int index = textBox6.Lines.Length;
    string[] readlines = textBox6.Text.ToString().Split(new char[] {'\n'});
    DisableValveControl();
    pumpAbortButton.Enabled = true;
    string[] decimated;
    string ReadSwitch;
    char[] delimiters = new char[] { '\t' };
    int j;

    //Read through inputs and decide
        for (int i = 0; i < index; i++)
        {
            ReadSwitch = readlines[i].ToUpper();
            decimated = ReadSwitch.Split(delimiters, StringSplitOptions.RemoveEmptyEntries);
            try
            {
                decimated[0] = decimated[0].TrimEnd(new char[] { '\r', '\n' });
                if (decimated[0] == "VALVE")
                {
                    int.TryParse(decimated[1], out j);
                    ActuateValve(j, decimated[2]);
                }

                if (decimated[0] == "AVALVE")
                {
                    int h;
                    int.TryParse(decimated[1], out j);
                    int.TryParse(decimated[2], out h);
                    GlobVars.ValveTiming[j] = h;
                    ValveWorkers[j].RunWorkerAsync(j);

                }

                if (decimated[0] == "WAIT")
                {
                    int.TryParse(decimated[1], out j);
                    Thread.Sleep(j);
                }
                else if (decimated[0] == "END")
                {
                    EnableValveControl();
                }
                else if (decimated[0] == "CLEAR")
                {
                    refresh();
                }
                else if (decimated[0] == "BLANK")
                {
                    Capture_Blank();
                }
                else if (decimated[0] == "MEAS")
                {
                    Capture_Absorbance();
                }
```

```
                else if (decimated[0] == "SPUMP")
                {
                    int h = 0;
                    int k = 1;
                    int l = 2;
                    int m = 500;
                    int n = 10;

                    if (decimated.Length > 5)
                    {
                        int.TryParse(decimated[1], out h);
                        int.TryParse(decimated[2], out k);
                        int.TryParse(decimated[3], out l);
                        int.TryParse(decimated[4], out m);
                        int.TryParse(decimated[5], out n);
                    }
                    GlobVars.pumpValves[0] = h;
                    GlobVars.pumpValves[1] = k;
                    GlobVars.pumpValves[2] = l;
                    GlobVars.PumpTime1 = m;
                    GlobVars.PumpNTimes = n;
                    ValvePumpSequence();
                }

                else if (decimated[0] == "APUMP")
                {
                    int h = 0;
                    int k = 1;
                    int l = 2;
                    int m = 500;
                    int n = 10;

                    if (decimated.Length > 5)
                    {
                        int.TryParse(decimated[1], out h);
                        int.TryParse(decimated[2], out k);
                        int.TryParse(decimated[3], out l);
                        int.TryParse(decimated[4], out m);
                        int.TryParse(decimated[5], out n);
                    }
                    GlobVars.pumpValves[0] = h;
                    GlobVars.pumpValves[1] = k;
                    GlobVars.pumpValves[2] = l;
                    GlobVars.PumpTime1 = m;
                    GlobVars.PumpNTimes = n;
                    bw.RunWorkerAsync();
                }
            }

            catch (IndexOutOfRangeException)
            {
                textBox6.Text += "END";
                EnableValveControl();
            }
        }
}


    private void ActuateValve(int j, string decimated)
    {
        string state = decimated;
        int k = j;
        bool OutputState = true;
        state = state.TrimEnd(new char[] {'\r' , '\n'});

        if (state == "ON")
        {
            OutputState = true;
            ifkit.outputs[k] = OutputState;
        }
        else if (state == "OFF")
        {
            OutputState = false;
            ifkit.outputs[k] = OutputState;
        }
    return;
    }
#endregion
```

```
        private void pumpAbortButton_Click(object sender, EventArgs e)
        {
            GlobVars.PumpNTimes = 0;
        }

        private void checkBox17_CheckedChanged(object sender, EventArgs e)
        {
            for (int z = 10000; z != 0; z--)
            {
                ifkit.outputs[0] = true;
                delay(1250000);
                ifkit.outputs[0] = false;
                delay(1250000);
            }
        }

        private void delay(int z)       //5000000 == 20ms
        {                               //1250000 == 5ms
            while (z != 0)
            {
                z--;
            }
            return;
        }

        private void button1_Click_1(object sender, EventArgs e)
        {
            SerialStart();
        }

        private void button2_Click_1(object sender, EventArgs e)
        {
            serialPort.Close();
        }

        //Rewrite output
        /*textBox6.Clear();
        for (int i = 0; i != index; i++)
        {
            textBox6.Text += readlines[i].ToString() + "\r\t" + (i+1).ToString() +"\r\n";

        }*/
    }
}
```

Appendix C

Ultraviolet photometer

C.1 Data

Op amp (LMP7721) specs:
A_o, 120 dB
GBW, 17 MHz
E_{ni} at 0.1 Hz, 400 nV/$\sqrt{Hz}$
E_{ni} at 1 kHz, 6.5 nV/$\sqrt{Hz}$
i_{ni}, 0.01 pA/$\sqrt{Hz}$
C_{ia}, 15 pF

Circuit specs: R_f, 150 M
C_{PD}, 24 pF
BW, 25000 Hz

Trans amp calcs:
$e_{nR} = \sqrt{4 \times 298.15K \times 1.38 \times 10^{-21} \times 150 \times 10^6 \times 25 \times 10^3} = 2.48$ mV
$e_{ni} = 10 \times 10^{-15} \times 150 \times 10^6 = 1.5\mu$V
$e_{ne} = 7.76$ mV
$e_no = 8.14$ mV

Appendix D

Droplet microfluidics for autonomous experimentation

D.1 Contact angles

Contact angle measurements were recorded with a Kruss DSA 30 Drop shape analysis system (Hamburg, Germany) connected to a PC running Drop shape analysis software.

D.1.1 PDMS–Water

(a) (b) (c)

Figure D.1: PDMS–Water contact angles. A water drop on the surface of PDMS prior to oxygen plasma exposure yields a contact angle of approximately 107^o (a). A water drop on the surface of PDMS minutes after oxygen plasma exposure yields a contact angle of approximately 15^o (b). A water drop on the surface of oxygen plasma exposed PDMS after 4 hours of baking at 100 ^{o}C yields a contact angle of approximately 102^o (c).

D.1.2 PDMS–Oleic Acid

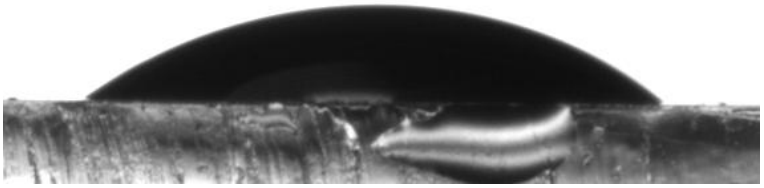

Figure D.2: A drop of oleic acid on a PDMS surface. A contact angle of approximately 40^o was recorded.

D.2 Fusion designs

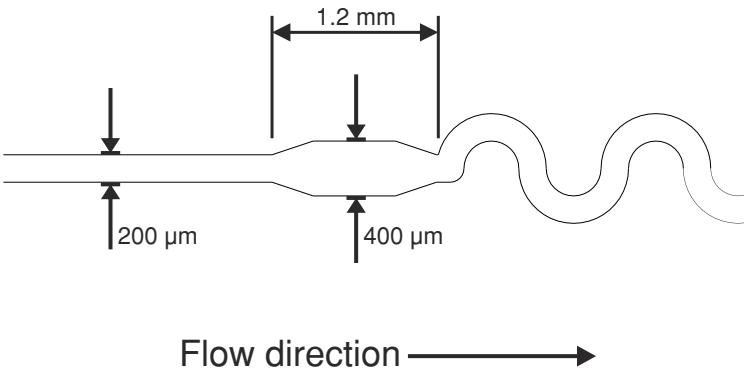

Figure D.3: Simple expansion chamber design to facilitate droplet fusion. Droplets entering the chamber had a tendency to collide without fusing.

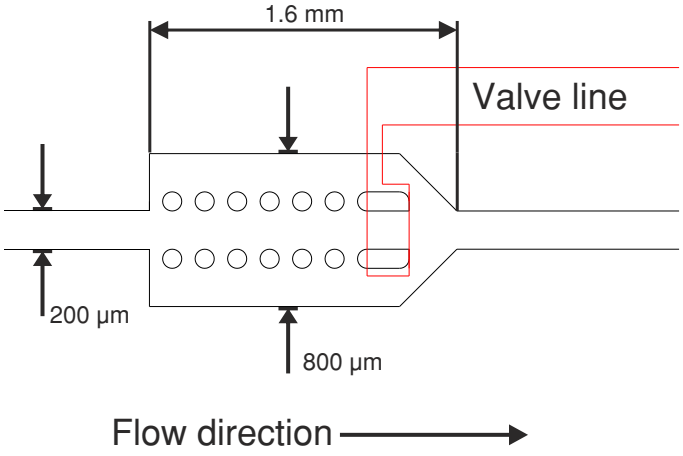

Figure D.4: Valved drop trap design to facilitate droplet fusion. In operation the valve partially blocked the upper channel.

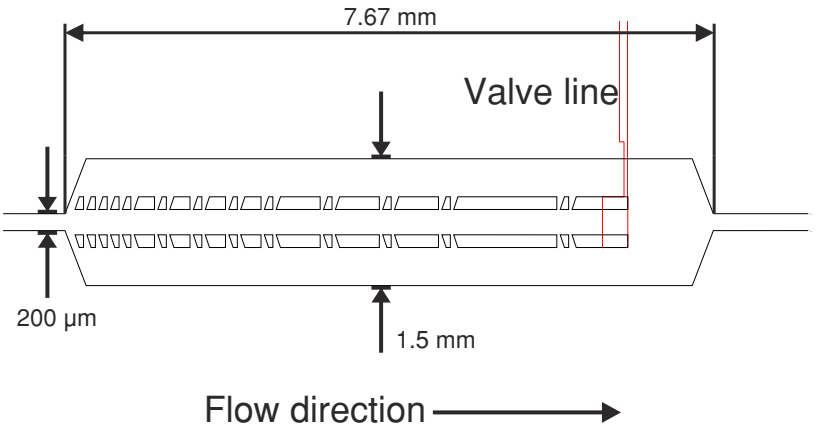

Figure D.5: A larger valved drop trap design to facilitate droplet fusion. The pillars are designed to minimise shear stress imposed at the sides of droplets when in the trapping area. Drops would still shear and air would be pulled into the oil stream from the PDMS bulk (see below).

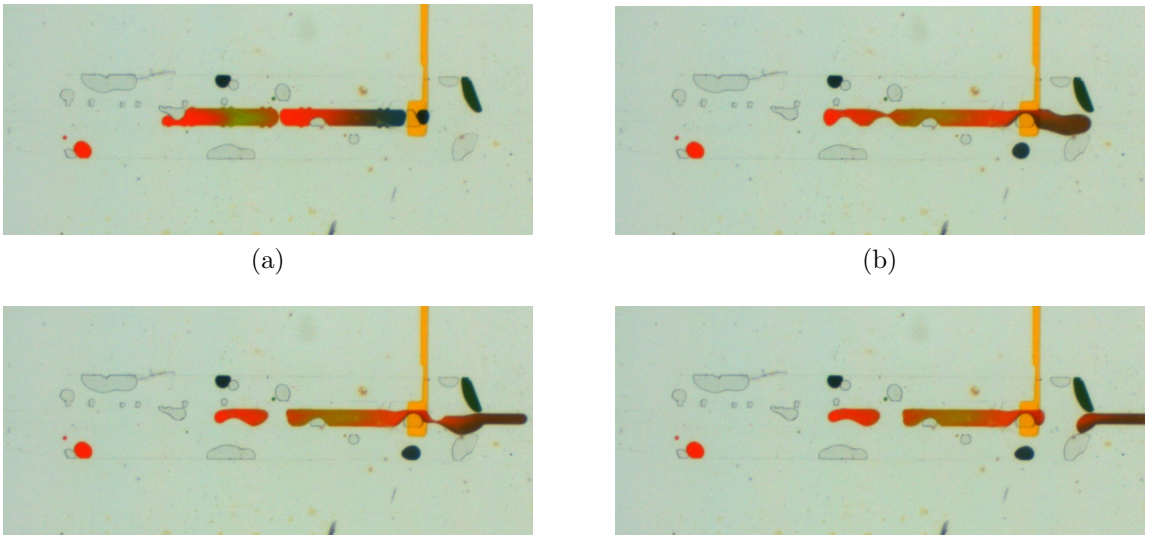

(a) (b)

(c) (d)

Figure D.6: Optical micrographs of the drop trap in operation. Flow is left to right. With the valve closed (yellow) two slugs of different composition are trapped between the comb-like structures of the drop trap (a). The valve is then opened (b), the slugs decompress and partially fuse but do not leave the trap cleanly (c). Part of the fused slug is left behind in the trap.

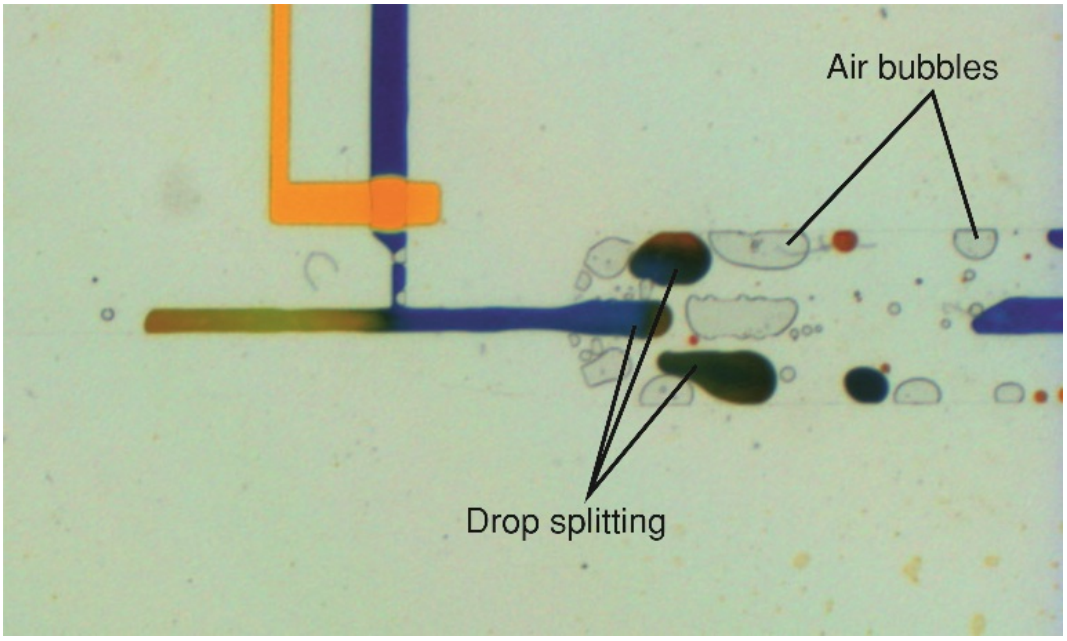

Figure D.7: Unwanted drop separation and air bubbles present in the drop trap. Flow is left to right.

D.3 Mixer designs

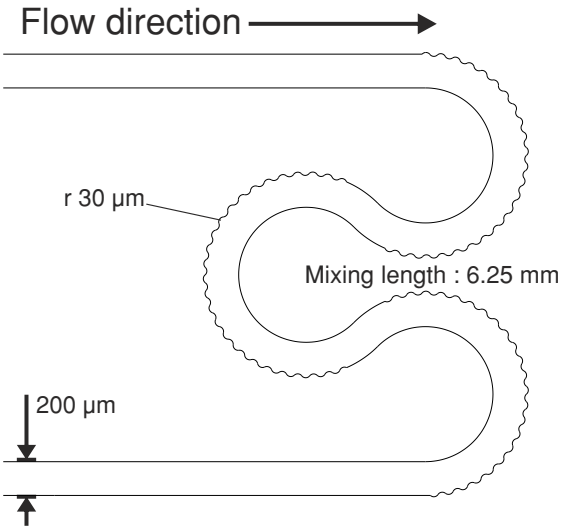

Figure D.8: A serpentine bumpy mixer to aid mixing within droplets. This mixer design was not very effective at mixing, particularly larger droplets. Each bump has a radius of 30 μm.

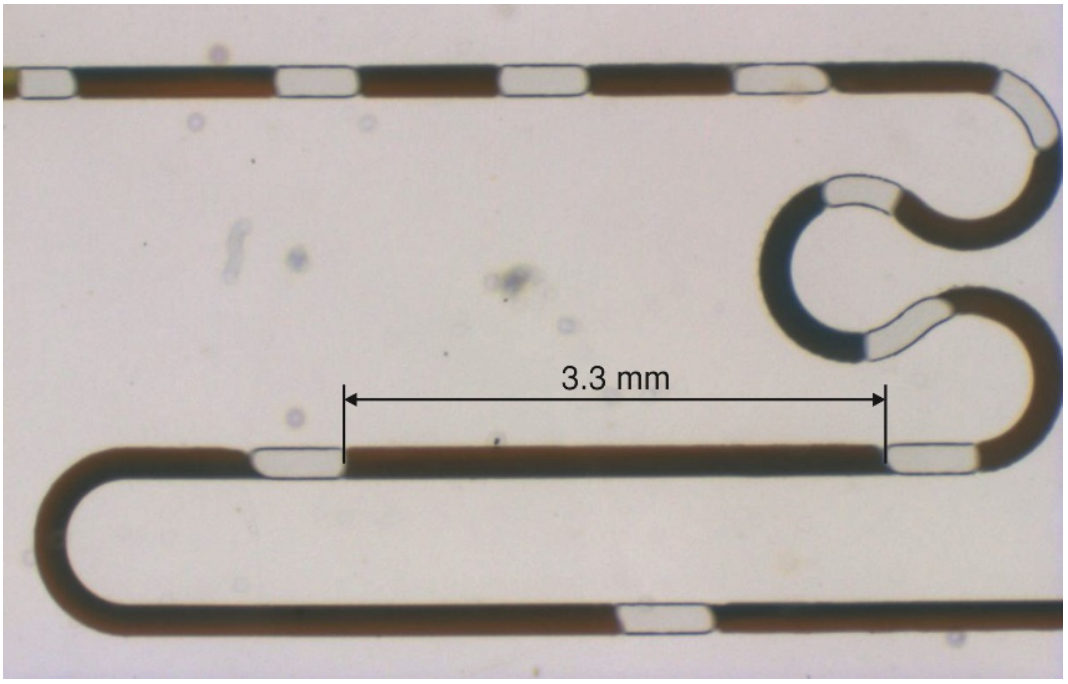

Figure D.9: Optical micrographs of the bumpy serpentine mixer in operation. Long drops or slugs despite being shorter than the mixing path length would mix poorly. The poor mixing was evident in the 3.3 mm long drop where two distinct halves can be identified. From the top flow is left to right.

D.4 Detection channel designs

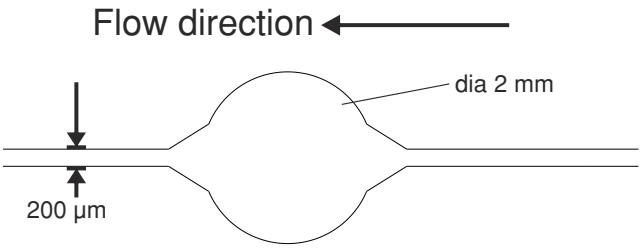

Figure D.10: An expansion chamber where droplet contents can be interrogated with UV light. Droplets entering this chamber would exhibit strange dynamics and would often get stuck in one half of the chamber.

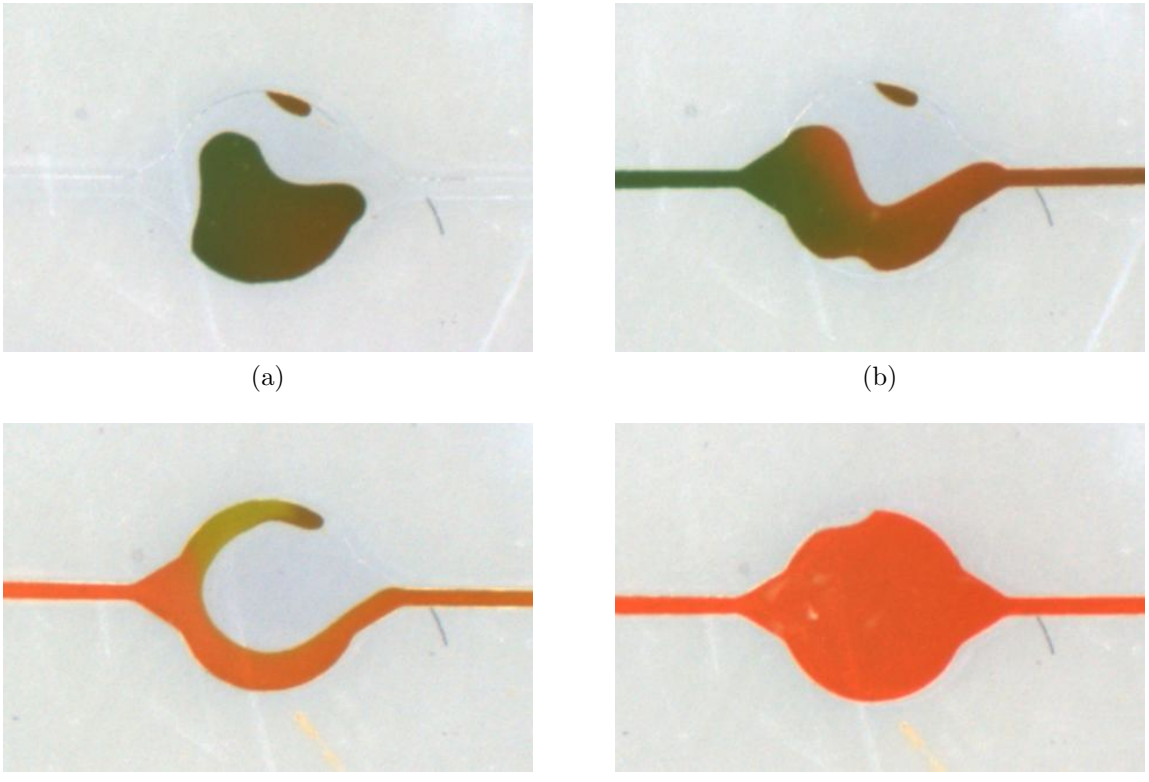

(a) (b)

(c) (d)

Figure D.11: Optical micrographs of the detection expansion channel in operation. Aqueous solutions would attach to the wall of the expansion chamber (a). Increased main flow rate (b)–(c) did not prevent sticking. Even flowing just the aqueous phase, the expansion chamber would not fill completely (d). Flow is left to right.

D.5 Scripts

D.5.1 Droplet generation

```
valve 7 on
wait 500
valve 8 on
wait 370
valve 10 off
wait 64
valve 8 off
valve 10 on
valve 7 off
end
```

Appendix E

Electrohydraulic interface

Current approaches to interfacing and controlling on-chip valves predominantly use moderately expensive pneumatic actuators (Urbanski et al., 2006) but in some instances Braille displays are used (Gu et al., 2004; Futai et al., 2006; Gu et al., 2007). While the cost per actuator of the Braille display approach is lower than that of the pneumatic, it lacks the freedom of pneumatic actuation in allowing for arbitrary placement of the actuators. The approach presented here addressed both issues.

Shown here is a new type of electrohydraulic interface enabling low-cost computer control over valved microfluidic chips. The interface scheme is illustrated in Figure E.1 and uses low-cost (<£9 each) linear action solenoids operating on a sealed microfluidic control channel. The interface scheme has been tested on a prototype valved microfluidic device.

E.1 Design

To give the solenoids flexibility of placement, they are mounted on handmade L-shaped aluminium brackets with height adjustment slots. Neodymium magnets are glued to the base of the brackets allowing for solenoid positioning around a microfluidic chip placed on a sheet of galvanised steel (see Figure E.2c). The magnets allow for the position of the solenoids to be fixed and moved as necessary.

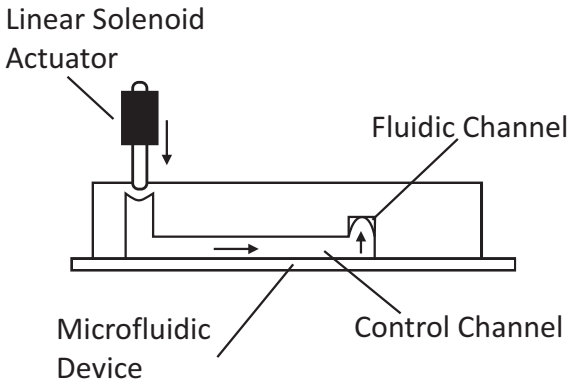

Figure E.1: Electrohydraulic interface. A linear motion solenoid applies pressure on to a sealed hydraulic control channel. The force is transmitted by the hydraulic fluid and deflects the membrane closing the valve.

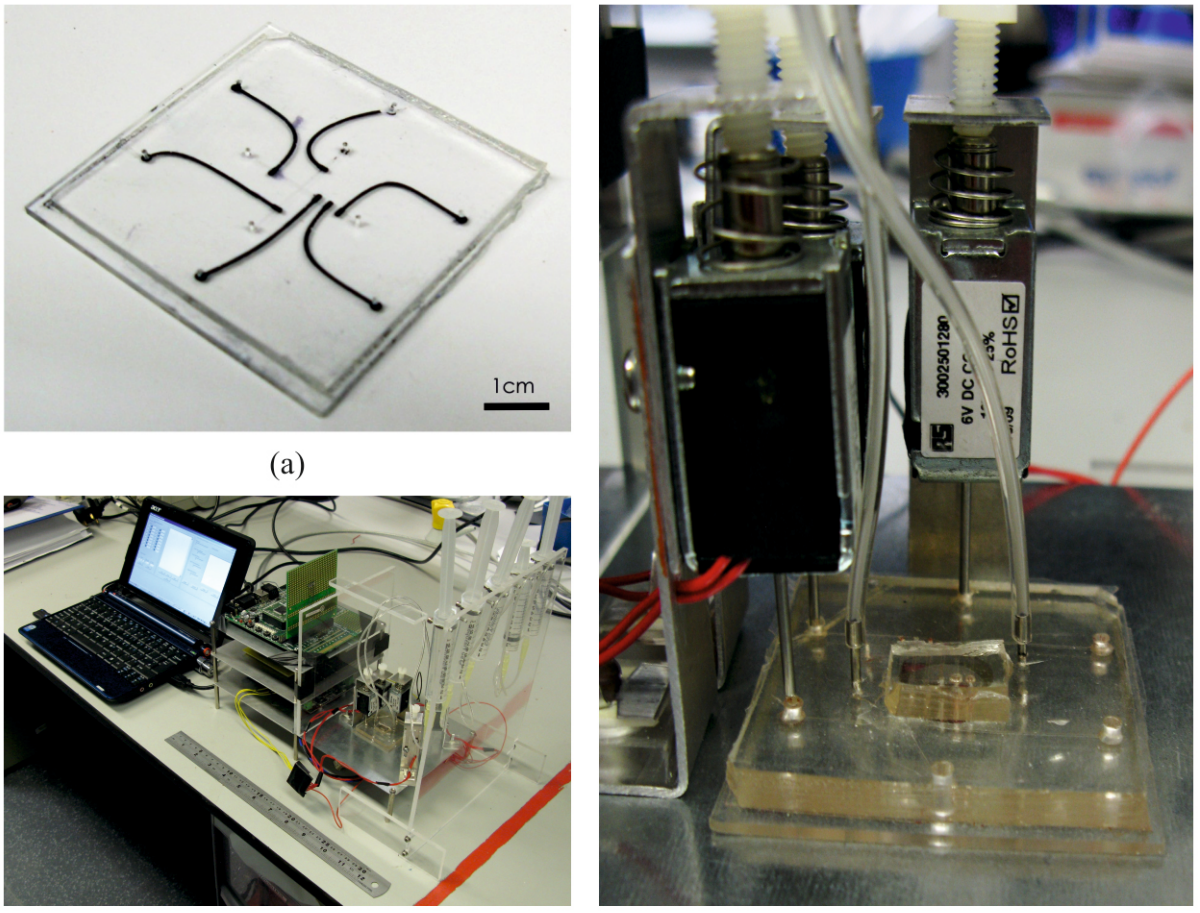

(a) (b) (c)

Figure E.2: Aspects of the prototype automated experimentation system. In (a) is an early prototype valved device with control channels filled with black ink for visibility. Shown in (b) is the overall automated experimentation system hardware and control software. In (c) we see a close-up of the solenoid actuators positioned around a prototype microfluidic device.

E.2 Experimental methods

E.2.1 Electrohydraulic interface: mounts

Solenoid mounts (Figure E.3) were designed using Autodesk Inventor software (Autodesk, USA). These were fabricated from the cutting and forming of 1.2 mm thick sheet aluminium. The aluminium mounts were drilled and tapped from above to accommodate a M6 nylon screw. Acrylic was cut into 18 mm (w) x 18 mm (l) x 5 mm (h) pieces. These were drilled to accommodate a single 10 mm (dia) x 3 mm (h) Neodymium disc magnet (RS695-0172, RS Components Ltd., Corby UK). The acrylic magnet holders were bonded on to the solenoid mounts with superglue. Complete solenoid mount assemblies were placed on 1 mm thick galvanised steel sheet and positioned around microfluidic devices accordingly.

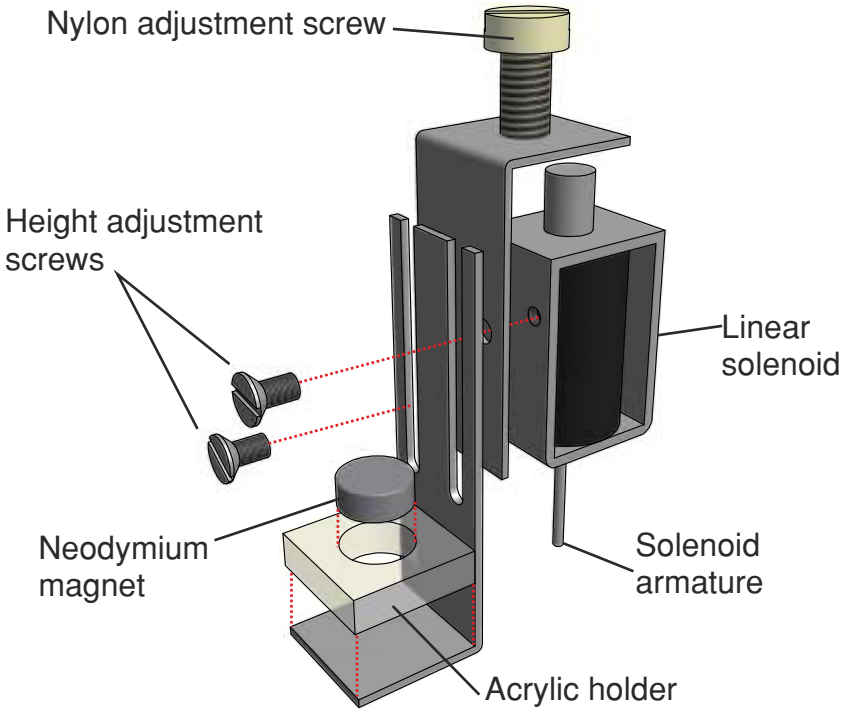

Figure E.3: CAD generated solenoid mount assembly. The nylon adjustment screw mechanically displaces the stroke of solenoid armature. This allows for the solenoid to be adjusted such that it operates within its characteristic linear region. The solenoid can be positioned at varying heights above a microfluidic device using the height adjustment screws. The Neodymium magnet affixes the solenoid mount assembly to a galvanised steel base. The magnet allows for arbitrary positioning of the solenoid.

E.2.2 Electrohydraulic interface: circuitry

Monostable solenoid actuators (RS250–1280, 6 Vdc 0.5 A) were purchased from RS Components Ltd., Corby UK. Following Figure E.4 the solenoids were connected between a 15 Vdc 5 A switched-mode power supply and a low-cost USB PC I/O board (PhidgetInterfaceKit 0/16/16, Active Robots, Somerset UK). Up to ten solenoids could be controlled with this set-up.

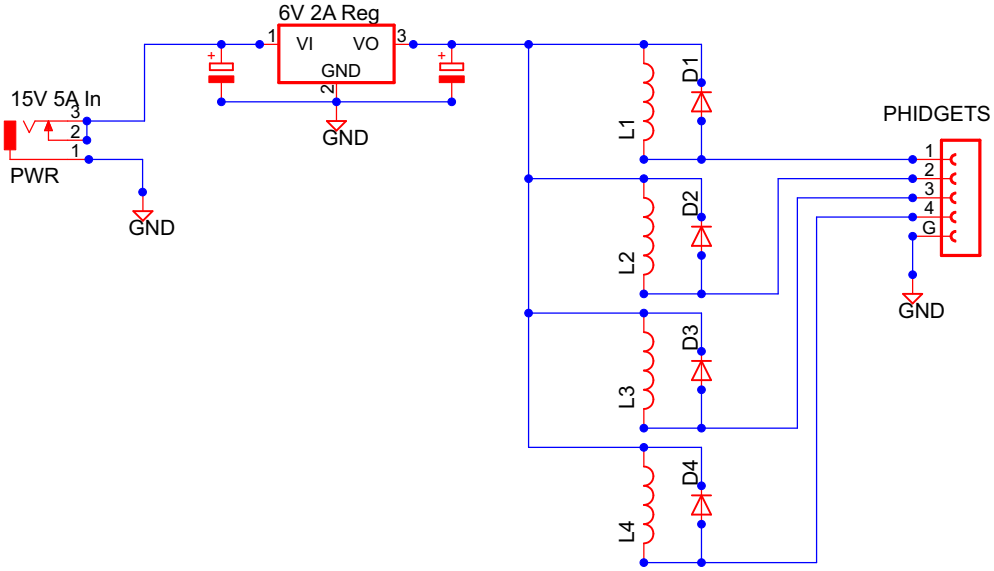

Figure E.4: Electrohydraulic interface circuitry. Protection diodes were included in the design to dissipate energy spikes arising from solenoid actuation.

E.2.3 Electrohydraulic interface: control software

Solenoids were controlled by custom software written in the C# programming language. A graphical user interface provided simple control over the solenoids. More complex operations were possible by using scripted text commands. The software was designed so that each solenoid actuation routine was assigned to a software thread. This allowed both independent and simultaneous switching of the solenoids. Solenoids could be grouped together in software to be actuated sequentially in a finite loop. The switching time of each solenoid and loop duration were user-defined. Solenoids grouped together in an actuation loop were used to drive peristaltic pumps.

E.3 Results

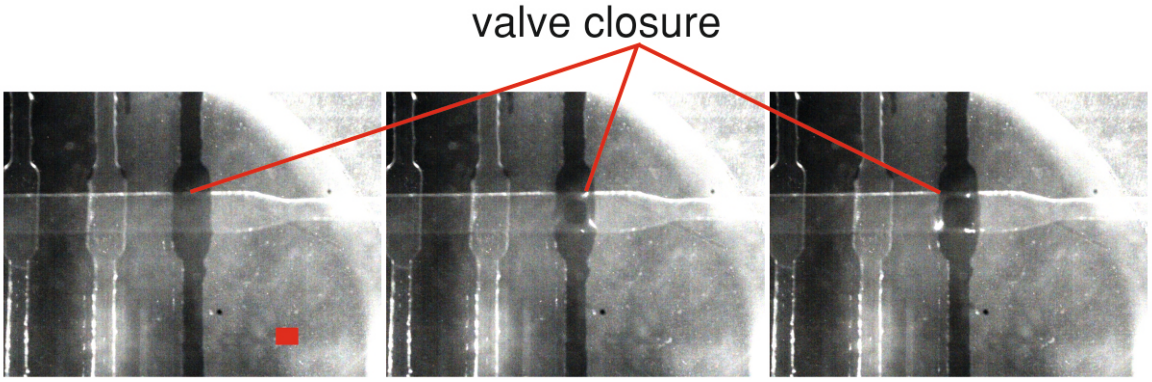

Figure E.5: Photographic sequence showing on-chip valve actuation with force applied by a linear motion solenoid. The control line is seen in black intersecting the transparent fluidic channel. The voltage applied to the solenoid was varied between 0 V and 6 V. In (a), at 0 V the valve was completely open. From (b) to (c) the valve progressively closed with increasing voltage recognisable by the dark area and distortion around it appearing in the centre of the valve. The scale bar represents 400 μm.

Appendix F

Optical interfacing

F.1 Dye-Doped PDMS preparation

PDMS can be doped with dyes allowing for optical filtering. Described here is PDMS doped with a dye, Sudan II (Sigma Aldrich, Dorset, UK) that filters light below 560 nm. PDMS was prepared as described in chapter 4, without degassing and with the weighing boat substituted for a glass petri dish. Using the method described by Bliss et al. (2007) Sudan II was prepared. Briefly, for n grams of PDMS base and catalyst, m milligrams of Sudan II (where $m = 1.2 \times n$) was weighed out in a glass petri dish, $m/20$ mL of toluene was dispensed into the same petri dish and the contents stirred with a metal spatula dissolving the dye. The dissolved dye was then poured into the petri dish containing the prepared PDMS. The dye was then stirred into the PDMS using a metal spatula until a uniform mixture was achieved. The PDMS-dye mixture was then degassed for 30 minutes in a vacuum dessicator, after which it was ready to be poured and cured. A convection oven set to a temperature of 100 ^{o}C was used to cure poured PDMS-dye mixture for a 1 hour duration. Samples from both Sudan II dye-doped and unmodified PDMS have been characterised optically using a UV-VIS spectrophotometer (Perkin Elmer Lambda 650). An empty cuvette served as a blank, the transmission spectra from the two types of PDMS are shown in Figure F.1, which are in good agreement with those reported by Hofmann et al. (2006). Physically the dye-doped PDMS differs in feel from the unmodified PDMS by feeling softer.

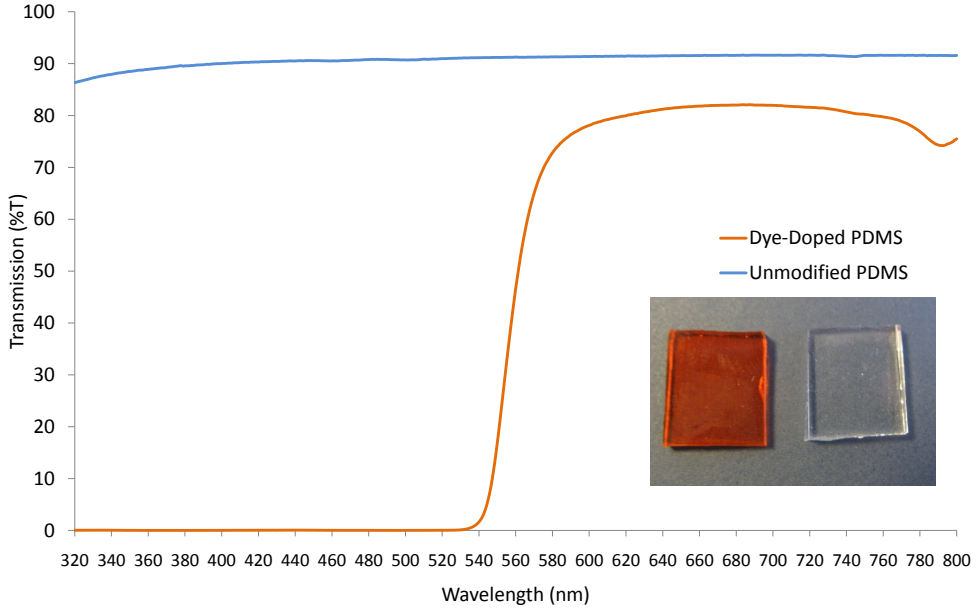

Figure F.1: Transmission spectra of modified and dye-doped PDMS. Photograph of PDMS samples are shown in the inset, left is dye-doped and right is unmodified PDMS.

F.2 Out-of-plane detection channel

By bonding a measurement channel on top of a device, optoelectronic components can be positioned easily around the detection channel. Preventing stray light is an issue. The idea here was to use dye dope the detection channel block to filter out the stray light. An air channel is included in the design (left of fluidic channel in Figure F.2) with a small wall separating the fluidic channel from air. With a dye doped detection channel block, at the air/fluidic channel wall the filter will be least effective therefore allowing light through. The bulk block should filter out stray light. By this approach it is thought that optical fibres will not be necessary.

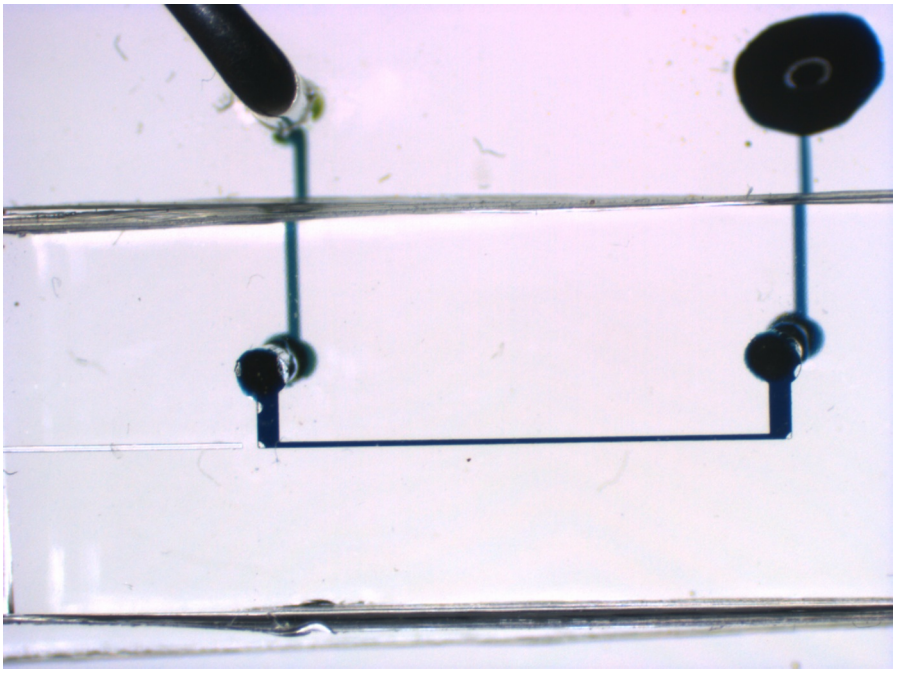

Figure F.2: Out of plane detection channel. Optoelectronic components are not easily interfaced with microfluidic devices. Often optical fibres are used but there are issues such as coupling efficiency to be considered. Here an alternate approach was attempted. Using the WAVE method to assembling PDMS layers, two channels were bonded together to form a single square detection channel with edges of 100 μm in length. The detection channel length is 1 cm long. The channel is designed to be bonded on top of a microfluidic device. Here fluid can be seen to travel from a test device, up through the detection channel and down through an oulet.

References

A. R. Abate, M. B. Romanowsky, J. J. Agresti, and D. A. Weitz. Valve-based flow focusing for drop formation. *Applied Physics Letters*, 94:023503–1–3, 2009.

P. Abgrall, S. Charlot, R. Fulcrand, L. Paul, A. Boukabache, and A.-M. Gué. Low-stress fabrication of 3d polymer free standing structures using lamination of photosensitive films. *Microsystem Technologies*, 14:1205–1214, 2008.

S. Aghdaei. Personal communication, 2010.

J. J. Agresti, E. Antipov, A. R. Abate, K. Ahn, A. C. Rowat, J.-C. Baret, M. Marquez, A. M. Klibanov, A. D. Griffiths, and D. A. Weitz. Ultrahigh-throughput screening in drop-based microfluidics for directed evolution. *PNAS*, 107:4004–4009, 2010.

K. Ahn, J Agresti, H. Chong, M. Marquez, and D. A. Weitz. Electrocoalescence of drops synchronised by size-dependent flow in microfluidic channels. *Applied Physics Letters*, 88:264105–1–3, 2006a.

K. Ahn, C. Kerbage, T. P. Hunt, R. M. Westervelt, D. R. Link, and D. A. Weitz. Dielectrophoretic manipulation of drops for high-speed microfluidic sorting devices. *Applied Physics Letters*, 88:024104–1–3, 2006b.

R. Alonso, F. Villuendas, J. Borja, L. A. Barragán, and I. Salinas. Low-cost, digital lock-in module with external reference for coating glass transmission/reflection spectrophotometer. *Measurement Science and Technology*, 14:551–557, 2003.

J. R. Anderson, D. T. Chiu, R. J. Jackman, O. Cherniavskaya, J. C. McDonald, H. Wu, S. J. Whitesides, and G. M. Whitesides. Fabrication of topologically complex three-dimensional microfluidic systems in pdms by rapid prototyping. *Analytical Chemistry*, 72:3158–3164, 2000.

S. L. Anna, N. Bontoux, and H. A. Stone. Formation of dispersions using "flow focusing" in microchannels. *Applied Physics Letters*, 82(3):364–366, January 20th 2003.

R. Aveyard and D. A. Haydon. Thermodynamic properties of aliphatic hydrocarbon/water interfaces. *Transactions of the Faraday Society*, 61:2255–2261, 1965.

J. Y. Baek, J. Y. Park, J. I. Ju, T. S. Lee, and S. H. Lee. A pneumatically controllable flexible and polymeric microfluidic valve fabricated via in situ development. *Journal of Micromechanics and Microengineering*, 15:1015–1020, 2005.

R. Baron, O. Lioubashevski, E. Katz, T. Niazov, and I. Willner. Elementary arithmetic operations by enzymes : A model for metabolic pathway based computing. *Angew. Chem. Int. Ed.*, 45:1572–1576, 2006a.

R. Baron, O. Lioubashevski, E. Katz, T. Niazov, and I. Willner. Logic gates and elementary computing by enzymes. *J. Phys. Chem. A*, 110:8548–8553, 2006b.

R. Baron, O. Lioubashevski, E. Katz, T. Niazov, and I. Willner. Two coupled enzymes perform in parallel the 'and' and 'inhiband' logic gate operations:. *Organic and Biomolecular Chemistry*, 4:989–991, 2006c.

C. N. Baroud, F. Gallaire, and R. Dangla. Dynamics of microfluidic droplets. *Lab on a Chip*, 10:2032–2045, 2010.

L. A. Barragán and J. I. Artigas. A modular, low-cost, digital signal processor-based lock-in card for measuring optical attentuation. *Review of Scientific Instruments*, 72(1):247–251, January 2001.

H. Becker and Claudia Gärtner. Polymer microfabrication technologies for microfluidic systems. *Analytical and Bioanalytical Chemistry*, 390:89–111, 2008.

H. Becker and U. Heim. Hot embossing as a method for the fabrication of high aspect ratio structures. *Sensors and Actuators A: Physical*, 83:130–135, 2000.

D. J. Beebe, G. A. Mensing, and G. M. Walker. Physics and applications of microfluidics in biology. *Annual Review of Biomedical Engineering*, 4:261–286, 2002.

J. M. Berg, J. L. Tymoczko, and L. Stryer. *Biochemistry*. W. H. Freeman and Company, 2002.

S. Bhattacharya, A. Datta, J. M. Berg, and S. Gangopadhyay. Studies on surface wettability of poly(dimethyl)siloxane (PDMS) and glass under oxygen-plasma treatment and correlation with bond strength. *Journal of Microelectromechanical Systems*, 14(3):590–597, June 2005.

B. P. Binks and J. H. Clint. Solid wettability from surface energy components: Relevance to pickering emulsions. *Langmuir*, 18:1270–1273, 2002.

C. L. Bliss, J. N. McMullin, and C. J. Backhouse. Rapid fabrication of a microfluidic device with integrated optical waveguides for dna fragment analysis. *Lab on a Chip*, 7:1280–1287, 2007.

N. Bremond, A. R. Thiam, and J. Bibette. Decompressing emulsion droplets favours coalescence. *Physical Review Letters*, 100:024501–1–4, 2008.

M. R. Bringer, C. J. Gerdts, H. Song, J. D. Tice, and R. F. Ismagilov. Microfluidic systems for chemical kinetics that rely on chaotic mixing in droplets. *Philisophical Transactions of the Royal Society of London A*, 362:1087–1104, 2004.

M. A. Burns, B. N. Johnson, S. N. Brahmasandra, K. Handique, J. R. Webster, M. Krishnan, T. S. Sammarco, P. M. Man, D. Jones, D. Heldsinger, C. H. Mastrangelo, and D. T. Burke. An integrated nanoliter DNA analysis device. *Science*, 282:484–487, October 16th 1998.

J. Cha, J. Kim, S.-K. Ryu, J. Park, Y. Jeong, S. Park, S. Park, H. C. Kim, and K. Chun. A highly efficient 3D micromixer using soft PDMS bonding. *Journal of Micromechanics and Microengineering*, 16:1778–1782, 2006.

M. K. Chaudhury and G. M. Whitesides. Direct measurement of interfacial interactions between semispherical lenses and flat sheets of poly(dimethylsiloxane) and their chemical derivatives. *Langmuir*, 7:1013–1025, 1991.

D. T. Chiu, N. L. Jeon, S. Huang, R. S. Kane, C. J. Wargo, I. S. Choi, D. E. Ingber, and G. M. Whitesides. Patterned deposition of cells and proteins onto surfaces by using three-dimensional microfluidic systems. *PNAS*, 97(6):2408–2413, March 14 2000.

D. T. Chiu, R. M. Lorenz, and G. D. M. Jeffries. Droplets for ultrasmall-volume analysis. *Anal. Chem.*, 81:5111–5118, 2009.

Y. Cho, H. S. Kim, A. B. Frazier, Z. G. Chen, D. M. Shin, and A. Han. Whole-cell impedance analysis for highly and poorly metastatic cancer cells. *Journal of Microelectromechanical Systems*, 18(4):808–817, 2009.

H.-P. Chou, M. A. Unger, and S. R. Quake. A microfabricated rotary pump. *Biomedical Microdevices*, 3(4):323–330, 2001.

Dow Corning. Sylgard 184 silicone elastomer kit, 2009. http://www.dowcorning.com, [Online; accessed 20th August 2009].

C. Cramer, P. Fischer, and E. J. Windhab. Drop formation in a co-flowing ambient fluid. *Chemical Engineering Science*, 59:3045–3058, 2004.

M. de Menech, P. Garstecki, F. Jousse, and H. A. Stone. Transition from squeezing to dripping in a microfluidic T-shaped junction. *Journal of Fluid Mechanics*, 595:141–161, 2008.

Y. Ding, L. Hong, B. Nie, K. S. Lam, and T. Pan. Capillary-driven automatic packaging. *Lab on a Chip*, 11:1464–1469, 2011.

H. Du and J. S. Lindsey. An approach for parallel and adaptive screening of discrete compounds followed by reaction optimization using an automated chemistry workstation. *Chemometrics and Intelligent Laboratory Systems*, 62:159–170, 2002.

D. C. Duffy, J. C. McDonald, O. J. A. Schueller, and G. M. Whitesides. Rapid prototyping of microfluidic systems in poly(dimethylsiloxane). *Analytical Chemistry*, 70(23):4974–4984, 1998.

M. A. Eddings, M. A. Johnson, and B. K. Gale. Determining the optimal PDMS–PDMS bonding technique for microfluidic devices. *Journal of Micromechanics and Microengineering*, 18:1–4, 2008.

S. Englard and L. Siegel. Mitochondrial l-malate dehydrogenase of beef heart. In J. M. Lowenstein, editor, *Citric Acid Cycle*, volume XIII of *Methods in Enzymology*. Academic Press, New York, 1969.

L. M. Fidalgo, C. Abell, and W. T. S. Huck. Surface-induced droplet fusion in microfluidic devices. *Lab on a Chip*, 7:984–986, 2007.

A. Folch and M. Toner. Cellular micropatterns on biocompatible materials. *Biotechnol. Prog.*, 14:388–392, 1998.

T. Fujii. PDMS–based microfluidic devices for biomedical applications. *Microelectronic Engineering*, 61–62:907–914, 2002.

N. Futai, W. Gu, J. W. Song, and S. Takayama. Handheld recirculation system and customized media for microfluidic cell culture. *Lab on a Chip*, 6:149–154, 2006.

O. Geschke, H. Klank, and P. Tellemann. *Microsystem Engineering of Lab-on-a-Chip Devices*. Wiley-VCH Verlag GmbH & Co., Weinheim, Germany, 2004.

J. S. Go and S. Shoji. A disposable, dead volume-free and leak-free in-place PDMS microvalve. *Sensors and Actuators A*, 114:438–444, 2004.

J. Graeme. *Photodiode Amplifiers: op amp solutions*. McGraw-Hill, New York, USA, 1996.

N. J. Graf and M. T. Bowser. A soft-polymer piezoelectric bimorph cantilever-actuated peristaltic micropump. *Lab on a Chip*, 8:1664–1670, 2008.

W. H. Grover, R. H. C. Ivester, E. C. Jensen, and R. A. Mathies. Development and multiplexed control of latching pneumatic valves using microfluidic logical structures. *Lab on a Chip*, 6:623–631, 2006.

W. Gu, H. Chen, Y.-C. Tung, J.-C. Meiners, and S. Takayama. Multiplexed hydraulic valve actuation using ioninc filled soft channels and braille displays. *Applied Physics Letters*, 90:033505–1–033505–3, 2007.

W. Gu, X. Zhu, N. Futai, B. S. Cho, and S. Takayama. Computerized microfluidic cell culture using elastomeric channels and braille displays. *PNAS*, 101:15861–15866, 2004.

Z.-X. Guo, Q. Zeng, M. Zhang, L.-Y. Hong, Y.-F. Zhao, W. Liu, S.-S. Guo, and X.-Z. Zhao. Valve-based microfluidic droplet micromixer and mercury (ii) ion detection. *Sensors and Actuators A: Physical*, 172:546–551, 2011.

S. Haeberle and R. Zengerle. Microfluidic platforms for lab-on-a-chip applications. *Lab on a Chip*, 7:1094–1110, 2007.

K. Handique and M. A. Burns. Mathematical modeling of drop mixing in a slit-type microchannel. *Journal of Micromechanics and Microengineering*, 11:548–554, 2001.

N. R. Harris, M. Hill, S. Beeby, Y. Shen, N. M. White, J. J. Hawkes, and W. T. Coakley. A silicon microfluidic ultasonic separator. *Sensors and Actuators B*, 95:425–434, 2003.

K. Hattori, S. Sugiura, and T. Kanamori. Generation of arbitrary monotonic concentration profiles by a serial dilution microfluidic network composed of microchannels with a high fluidic-resistance ratio. *Lab on a Chip*, 9:1763–1772, 2009.

K. Haubert, T. Drier, and D. Beebe. PDMS bonding by means of a portable, low-cost corona system. *Lab on a Chip*, 6:1548–1549, 2006.

O. Hofmann, P. Niedermann, and A. Manz. Modular approach to fabrication of three-dimensional microchannel systems in PDMS–application to sheath flow microchips. *Lab on a Chip*, 1:108–114, 2001.

O. Hofmann, X. Wang, A. Cornwell, S. Beecher, A. Raja, D. D. C. Bradley, A. J. deMello, and J. C. deMello. Monolithically integrated dye-doped pdms long-pass filters for disposable on-chip fluorescence detection. *Lab on a Chip*, 6:981–987, 2006.

C.-C. Hong, J.-W. Choi, and C. H. Ahn. A novel in-plane passive microfluidic mixer with modified Tesla structures. *Lab on a Chip*, 4:109–113, 2004a.

J. W. Hong, V. Studer, G. Hang, W. F. Anderson, and S. R. Quake. A nanoliter-scale nucleic acid processor with parallel architecture. *Nature Biotechnology*, 22 (4):435–439, April 2004b.

K. Hosokawa, T. Fujii, and I. Endo. Handling of picoliter liquid samples in a poly(dimethylsiloxane)-based microfluidic device. *Analytical Chemistry*, 71: 4781–4785, 1999.

K. Hosokawa and R. Maeda. A pneumatically-actuated three-way microvalve fabricated with polydimethylsiloxane using the membrane transfer technique. *Journal of Micromechanics and Microengineering*, 10:415–420, 2000.

A. Huebner, S. Sharma, M. Srisa-Art, F. Hollfelder, J. B. Edel, and A. J. deMello. Microdroplets: A sea of applications? *Lab on a Chip*, 8:1244–1254, 2008.

L.-H. Hung, K. M. Choi, W.-Y. Tseng, Y.-C. Tan, K. J. Shea, and A. P. Lee. Alternating droplet generation and controlled dynamic droplet fusion in microfluidic device for CdS nanoparticle synthesis. *Lab on a Chip*, 6:174–178, 2006.

D. Irimia, R. G. Tompkins, and M. Toner. Single-cell chemical lysis in picoliter-scale closed volumes using a microfabricated device. *Analytical Chemistry*, 76: 6137–6143, 2004.

H. H. Jaffé and M. Orchin. *Theory and Applications of Ultraviolet Spectroscopy*. John Wiley and Sons, Inc., New York, USA, 1962.

S. Jambovane, E. C. Duin, S.-K. Kim, and J. W. Hong. Determination of kinetic parameters, k_m and k_{cat}, with a single experiment on a chip. *Analytical Chemistry*, 81(9):3239–3245, 2009.

N. L. Jeon, S. K. W. Dertinger, D. T. Chiu, I. S. Choi, A. D. Stroock, and G. M. Whitesides. Generation of solution and surface gradients using microfluidic systems. *Langmuir*, 16:8311–8316, 2000.

K.-H. Jeong, J. Kim, and L. P. Lee. Biologically inspired artificial compound eyes. *Science*, 312:557–561, 2006.

Z. Jiao, N.-T. Nguyen, and X. Huang. Thermocapillary actuation of a water droplet encapsulated in an oil plug. *Journal of Micromechanics and Microengineering*, 17:1843–1852, 2007.

B.-H. Jo, L. M. Van Lerberghe, K. M. Motsegood, and D. J. Beebe. Three-dimensional micro-channel fabrication in polydimethylsiloxane (PDMS) elastomer. *Journal of Microelectromechanical Systems*, 9(1):79–81, March 2000.

G. Jones, C. Lovell, S. Gunn, H. Morgan, and K.-P. Zauner. Enabling the discovery of computational characteristics of enzyme dynamics. In *Evolutionary Computation (CEC), 2012 IEEE Congress on*, pages 1–8, June 2012.

G. Jones, C. Lovell, H. Morgan, and K.-P. Zauner. Characterising enzymes for information processing: Microfluidics for autonomous experimentation. In C. Calude, M. Hagiya, K. Morita, G. Rozenberg, and J. Timmis, editors, *9th International Conference on Unconventional Computation*, page 191, Tokyo, Japan, 2010.

G. Jones, C. Lovell, H. Morgan, and K.-P. Zauner. Organising chemical reaction networks in space and time with microfluidics. *International Journal of Nanotechnology and Molecular Computation (IJNMC)*, 3(1):35–56, 2011.

E. Kang, D. H. Lee, C.-B. Kim, S. J. Yoo, and S.-H. Lee. A hemispherical microfluidic channel for the trapping and passive dissipation of microbubbles. *Journal of Micromechanics and Microengineering*, 20:1–9, 2010.

C. Kim, K. Lee, J. H. Kim, K. S. Shin, K.-J. Lee, T. S. Kim, and J. Y. Kang. A serial dilution microfluidic device using a ladder network generating logarithmic or linear concentrations. *Lab on a Chip*, 8:473–479, 2008.

D. S. Kim, S. H. Lee, C. H. Ahn, J. Y. Lee, and T. H. Kwon. Disposable integrated microfluidic biochip for blood typing by plastic microinjection moulding. *Lab on a Chip*, 6:794–802, 2006a.

D. S. Kim, S. H. Lee, T. H. Kwon, and C. H. Ahn. A serpentine laminating micromixer combining splitting/recombination and advection. *Lab on a Chip*, 5:739–747, 2004.

J. Y. Kim, J. Y. Baek, K. A. Lee, and S. H. Lee. Automatic aligning and bonding system of PDMS layer for the fabrication of 3D microfluidic channels. *Sensors and Actuators A*, 119:593–598, 2005.

L. Kim, M. D. Vahey, H.-Y. Lee, and J. Voldman. Microfluidic arrays for logarithmically perfused embryonic stem cell culture. *Lab on a Chip*, 6:394–406, 2006b.

R. D. King, K. E. Whelan, F. M. Jones, P. G. K. Reiser, C. H. Bryant, S. H. Muggleton, Douglas B. Kell, and Stephen G. Oliver. Functional genomic hypothesis generation and experimentation by a robot scientist. *Nature*, 427: 247–252, 2004.

H. Kinoshita, S. Kaneda, T. Fujii, and M. Oshima. Three-dimensional measurement and visualization of internal flow of a moving droplet using confocal micro-PIV. *Lab on a Chip*, 7:338–346, 2007.

H. Klank, J. O. Kutter, and O. Geschke. CO_2-laser micromachining and back-end processing for rapid production of PMMA-based microfluidic systems. *Lab on a Chip*, 2:242–246, 2002.

K. T. Kotz, K. A. Noble, and G. W. Faris. Optical microfluidics. *Applied Physics Letters*, 85:2658–2660, 2004.

G. T. Kovacs. *Micromachined Transducers Sourcebook*. McGraw-Hill Science, 1998.

E. T. Lagally, P. C. Simpson, and R. A. Mathies. Monolithic integrated microfluidic DNA amplification and capillary electrophoresis analysis system. *Sensors and Actuators B*, 63:138–146, 2000.

P. Langley. The computational support of scientic discovery. *International Journal of Human-Computer Studies*, 53(3):393–410, 2000.

P. Langley, H. A. Simon, G. L. Bradshaw, and J. M. Zytkow. *Scientific Discovery: Computational Explorations of the Creative Processes*. The MIT Press, Cambridge, MA, 1987.

J. N. Lee, C. Park, and G. M. Whitesides. Solvent compatibility of poly(dimethylsiloxane)–based microfluidic devices. *Analytical Chemistry*, 75 (23):6544–6554, 2003.

S. W. Lee, D. S. Kim, S. S. Lee, and T. H. Kwon. A split and recombination micromixer fabricated in a PDMS three-dimensional structure. *Journal of Micromechanics and Microengineering*, 16:1067–1072, 2006.

S. W. Lee and S. S. Lee. Shrinkage ratio of PDMS and its alignment method for the wafer level process. *Microsystem Technologies*, 14:205–208, 2008.

W. Lee, L. M. Walker, and S. L. Anna. Role of geometry and fluid properties in droplet and thread formation processes in planar flow focusing. *Physics of Fluids*, 21:032103–1–14, 2009.

T. Lemke, J. Kloeker, G. Biancuzzi, T. Huesgen, F. Goldschmidtboeing, and P. Woias. Fabrication of normally-closed microvalve utilizing lithographically defined silicone micro o-rings. *Journal of Micromechanics and Microengineering*, 21:025011–1–11, 2011.

A. Liau, R. Karnik, A. Majumdar, and J. H. Doudna Cate. Mixing crowded biological solutions in milliseconds. *Analytical Chemistry*, 77(23):7618–7625, 2005.

B.-C. Lin and Y.-C. Su. On-demand liquid-in-liquid droplet metering and fusion utilizing pneumatically actuated membrane valves. *Journal of Micromechanics and Microengineering*, 18:1–10, 2008.

C.-H. Lin, G.-B. Lee, Y.-H. Lin, and G.-L. Chang. A fast prototyping process for fabrication of microfluidic systems on soda-lime glass. *J. Micromech. Microeng.*, 11:726–732, 2001.

D. R. Link, S. L. Anna, D. A. Weitz, and H. A. Stone. Geometrically mediated breakup of drops in microfluidic devices. *Physical Review Letters*, 92(5):054503–1–054503–4, February 6th 2004.

D. R. Link, E. Grasland-Mongrain, A. Duri, F. Sarrazin, Z. Cheng, G. Cristobal, M. Marquez, and D. A. Weitz. Electric control of droplets in microfluidic devices. *Angewandte Chemie*, 45:2556–2560, 2006.

H. Lorenz, L. Paratte, R. Luthier, N. F. de Rooij, and P. Renaud. Low-cost technology for multilayer electroplated parts using laminated dry film resist. *Sensors and Actuators A*, 53:364–368, 1996.

R. M. Lorenz, J. S. Edgar, G. D. M. Jeffries, Y. Zhao, D. McGloin, and D. T. Chiu. Vortex-trap-induced fusion of femtoliter-volume aqueous drops. *Analytical Chemistry*, 79:224–228, 2007.

M. W. Losey, R. J. Jackman, S. L. Firebaugh, M. A. Schmidt, and K. F. Jensen. Design and fabrication of microfluidic devices for multiphase mixing and reaction. *Journal of Microelectromechanical Systems*, 11:709–717, 2002.

C. Lovell, G. Jones, S. Gunn, and K.-P. Zauner. An artificial experimenter for enzymatic response characterisation. *13th International Conference on Discovery Science*, pages 42–56, November 2010.

C. Lovell, G. Jones, S. Gunn, and K.-P. Zauner. Autonomous experimentation: Active learning for enzyme response characterisation. In *JMLR: Workshop and Conference Proceedings*, volume 16, pages 141–155, May 2011.

C. J. Lovell. *An Artificial Experimenter for Automated Response Characterisation*. PhD thesis, University of Southampton, 2011.

Y. Ma, X. Cao, X. Feng, Y. Ma, and H. Zou. Fabrication of super-hydrophobic film from PMMA with intrinsic water contact angle below 90^o. *Polymer*, 48(26): 7455–7460, 2007.

F. Malloggi, H. Gu, A. G. Banpurkar, S. A. Vanapalli, and F. Mugele. Electrowetting –a versatile tool for controlling microdrop generation. *The European Physical Journal E*, 26:91–96, 2008.

J. S. Marcus, W. French Anderson, and S. R. Quake. Microfluidic single-cell mRNA isolation and analysis. *Analytical Chemistry*, 78:3084–3089, 2006.

N. Matsumaru, F. Centler, K.-P. Zauner, and P. Dittrich. Self-adaptive scouting autonomous experimentation for systems biology. In G. R. Raidl, S. Cagnoni, J. Branke, D. Corne, R. Drechsler, Y. Jin, C. G. Johnson, P. Machado, E. Marchiori, F. Rothlauf, G. D. Smith, and G. Squillero, editors, *Lecture Notes in Computer Science*, volume 3005, chapter Lecture Notes in Artificial Intelligence, pages 52–62. Springer, Berlin, 2004.

N. Matsumaru, S. Colombano, and K.-P. Zauner. Scouting enzyme behavior. In D. B. Fogel, M. A. El-Sharkawi, X. Yao, G. Greenwood, H. Iba, P. Marrow, and

M. Shackleton, editors, *2002 World Congress on Computational Intelligence, May 12-17*, pages CEC 19–24, Honolulu, Hawaii, 2002. IEEE, Piscataway, NJ.

J. C. McDonald and G. M. Whitesides. Poly(dimethylsiloxane) as a material for fabricating microfluidic devices. *Accounts of Chemical Research*, 35(7):491–499, 2002.

J. Monahan, A. A. Gewirth, and R. G. Nuzzo. A method for filling complex polymeric microfluidic devices and arrays. *Analytical Chemistry*, 73:3193–3197, 2001.

C. Moraes, Y. Sun, and C. A. Simmons. Solving the shrinkage-induced PDMS alignment registration issue in multilayer soft lithography. *Journal of Micromechanics and Microengineering*, 19:1–6, 2009.

N. Nashida, W. Satoh, J. Fukuda, and H. Suzuki. Electrochemical immunoassay on a microfluidic device with sequential injection and flushing functions. *Biosensors and Bioelectronics*, 22:3167–3173, 2007.

D. L. Nelson and M. M. Cox. *Lehninger Principles of Biochemistry*. W. H. Freeman and Company, New York, USA, 4th edition, 2005.

T. Niazov, R. Baron, E. Katz, O Lioubashevski, and I. Willner. Concatenated logic gates using four coupled biocatalysts operating in series. *Proceedings of the National Academy of Sciences*, 103(46):17160–17163, 2006.

T. Nisisako, S. Okushima, and T. Torii. Controlled formulation of monodisperse double emulsions in multiple-phase microfluidic system. *Soft Matter*, 1:23–27, 2005.

X. Niu, S. Gulati, J. B. Edel, and A. J. deMello. Pillar-induced droplet merging in microfluidic circuits. *Lab on a Chip*, 8:1837–1841, 2008.

K. W. Oh and C. H. Ahn. A review of microvalves. *Journal of Micromechanics and Microengineering*, 16:R13–R39, 2006.

E. Ohmae, C. Murakami, K. Gekko, and C. Kato. Pressure effects on enzyme function. *Japan Science Society of Biological Macromolecules*, 7:23–29, 2007.

A. O'Neill, J. Soo Hoo, and G. Walker. Chips & tips: Rapid curing of PDMS for microfluidic applications. *Lab on a Chip*, 2006.

J. M. Ottino and S. Wiggins. Introduction: mixing in microfluidics. *Philisophical Transactions of the Royal Society of London A*, 362:923–935, 2004.

T. Palmer. *Understanding Enzymes.* Ellis Horwood Limited, Chichester, England, 1981.

J.-Z. Pan, B. Yao, and Q. Fang. Hand-held photometer based on liquid-core waveguide absorption detection for nanoliter-scale samples. *Analytical Chemistry*, 82:3394–3398, 2010.

D. L. Pavia, G. M. Lampman, and G. S. Kriz. *Introduction to Spectroscopy.* Thomson Learning, Inc., London, England, 3rd edition, 2001.

J. C. Plouvier, L. A. Corkan, and J. S. Lindsey. Experiment planner for strategic experimentation with an automated chemistry workstation. *Chemometrics and Intelligent Laboratory Systems*, 17:75–94, 1992.

M. G. Pollack, A. D. Shenderov, and R. B. Fair. Electrowetting-based actuation of droplets for integrated microfluidics. *Lab on a Chip*, 2:96–101, 2002.

C. Priest, S. Herminghaus, and R. Seemann. Controlled electrocoalescence in microfluidics: Targeting a single lamella. *Applied Physics Letters*, 89:134101–1–3, 2006.

G. Reiter, R. Khanna, and A. Sharma. Enhanced instability in thin liquid films by improved compatibility. *Physical Review Letters*, 85:1432–1435, 2000.

B. Samel, M. Kamruzzaman Chowdhury, and G. Stemme. The fabrication of microfluidic structures by means of full–wafer adhesive bonding using a poly(dimethysiloxane) catalyst. *Journal of Micromechanics and Microengineering*, 17:1710–1714, 2007.

M. E. Sandison and H. Morgan. Rapid fabrication of polymer microfluidic systems for the production of artificial lipid bilayers. *J. Micromech. Microeng.*, 15:S139–S149, 2005.

M. E. Sandison, M. Zagnoni, M. Abu-Hantash, and H. Morgan. Micromachined glass apertures for artificial lipid bilayer formation in a microfluidic system. *Journal of Micromechanics and Microengineering*, 17:S189–S196, 2007.

F. Sarrazin, L. Prat, N. Di Miceli, G. Cristobal, D. R. Link, and D. A. Weitz. Mixing characterization inside microdroplets engineered on a microcoalescer. *Chemical Engineering Science*, 62:1042–1048, 2007.

S. Satyanarayana, R. N. Karnik, and A. Majumdar. Stamp-and-stick room temperature bonding technique for microdevices. *Journal of Microelectromechanical Systems*, 14(2):392–399, April 2005.

S. K. Sengupta, J. M. Farnham, and J. E. Whitten. A simple low-cost lock-in amplifier for the laboratory. *Journal of Chemical Education*, 82(9):1399–1401, September 2005.

I. Shestopalov, J. D. Tice, and R. F. Ismagilov. Multi-step synthesis of nanoparticles performed on millisecond time scale in a microfluidic droplet-based system. *Lab on a Chip*, 4:316–321, 2004.

J. M. Siegel, G. A. Montgomery, and R. M. Bock. Ultraviolet absorption spectra of DPN and analogs of DPN. *Archives of Biochemistry and Biophysics*, 82: 288–299, 1959.

H. Song, M. R. Bringer, J. D. Tice, C. J. Gerdts, and R. F. Ismagilov. Experimental test of scaling by mixing by chaotic advection in droplets moving through microfluidic channels. *Applied Physics Letters*, 83:4664–4666, 2003a.

H. Song, D. L. Chen, and R. F. Ismagilov. Reactions in droplets in microfluidic channels. *Angewandte Chemie Int. Ed.*, 45:7336–7356, 2006.

H. Song and R. F. Ismagilov. Millisecond kinetics on a microfluidic chip using nanoliters of reagents. *Journal of the American Chemical Society*, 125:14613–14619, 2003.

H. Song, J. D. Tice, and R. F. Ismagilov. A microfluidic system for controlling reaction networks in time. *Angewandte Chemie*, 115:792–796, 2003b.

M. O. Sonnaillon and F. J. Bonetto. A low-cost, high-performance, digital signal processor-based lock-in amplifier capable of measuring multiple frequency sweeps simultaneously. *Review of Scientific Instruments*, 76:024703–1–024703–7, 2005.

T. M. Squires and S. R. Quake. Microfluidics: fluid physics at the nanoliter scale. *Reviews of Modern Physics*, 77:977–1026, 2005.

V. Srinivasan, V. K. Pamula, and R. B. Fair. Droplet-based microfluidic lab-on-a-chip for glucose detection. *Analytica Chimica Acta*, 507:145–150, 2004.

K. Stephan, P. Pittet, L. Renaud, P. Kleimann, P. Morin, N Ouaini, and R. Ferrigno. Fast prototyping using a dry film photoresist: microfabrication of soft-lithography masters for microfluidic structures. *Journal of Micromechanics and Microengineering*, 17:N64–N74, 2007.

L. Stevens. Buffers and the determination of protein concentrations. In E. L. V. Harris and S. Angal, editors, *Protein purification methods: a practical approach*, pages 317–335. Oxford University Press, New York, 1989.

M. Stjernström and J. Roeraade. Method for fabrication of microfluidic systems in glass. *Journal of Micromechanics and Microengineering*, 8:33–38, 1998.

H. A. Stone, A. D. Stroock, and A. Ajdari. Engineering flows in small devices: Microfluidics toward a lab-on-a-chip. *Annual Reviews in Fluid Mechanics*, 36: 381–411, 2004.

A. D. Stroock, S. K. W. Dertinger, A. Ajdari, I. Mezić, H. A. Stone, and G. M. Whitesides. Chaotic mixer for microchannels. *Science*, 295:647–651, January 25 2002.

V. Studer, G. Hang, A. Pandolfi, M. Ortiz, W. F. Anderson, and S. R. Quake. Scaling properties of a low-actuation pressure microfluidic valve. *Journal of Applied Physics*, 95(1):393–398, 2004.

Y.-C. Tan, J. S. Fisher, A. I. Lee, V. Cristini, and A. P. Lee. Design of microfluidic channel geometries for the control of droplet volume, chemical concentration, and sorting. *Lab on a Chip*, 4:292–298, 2004.

Y.-C. Tan, Y. L. Ho, and A. P. Lee. Droplet coalescence by geometrically mediated flow in microfluidic channels. *Microfluid Nanofluid*, 3:495–499, 2007.

S.-Y. Teh, R. Lin, L.-H. Hung, and A. P. Lee. Droplet microfluidics. *Lab on a Chip*, 8:198–220, 2008.

M. A. Thal and M. J. Samide. Applied electronics: Construction of a simple spectrophotometer. *Journal of Chemical Education*, 78(11):1510–1512, November 2001.

A. B. Theberge, F. Courtois, Y. Schaerli, M. Fischlechner, C. Abell, F. Hollfelder, and W. T. S. Huck. Microdroplets in microfluidics: An evolving platform for discoveries in chemistry and biology. *Angew. Chem. Int. Ed.*, 49:5846–5868, 2010.

R. S. W. Thomas, P. D. Mitchell, R. O. C. Oreffo, and H. Morgan. Trapping single human osteoblast-like cells from a heterogeneous population using a dielectrophoretic microfluidic device. *Biomicrofluidics*, 4:022806–1–9, 2010.

T. Thorsen, S. J. Maerkl, and S. R. Quake. Microfluidic large-scale integration. *Science*, 298:580–584, 2002.

T. Thorsen, R. W. Roberts, F. H. Arnold, and S. R. Quake. Dynamic pattern formation in a vesicle-generating microfluidic device. *Physical Review Letters*, 86(18):4163–4166, April 30th 2001.

J. D. Tice, H. Song, A. D. Lyon, and R. F. Ismagilov. Formation of droplets and mixing in multiphase microfluidics at low values of the Reynolds and the Capillary numbers. *Langmuir*, 19:9127–9133, 2003.

K. F. Tipton. *Enzyme Assays*, chapter 1, pages 1–44. Practical Approach. Oxford University Press, Oxford, England, 2nd edition, 2002.

Y.-C. Tsai, H.-P. Jen, K.-W. Lin, and Y.-Z. Hsieh. Fabrication of microfluidic devices using dry film photoresist for microchip capillary electrophoresis. *Journal of Chromatography A*, 1111:267–271, 2006.

P. B. Umbanhowar, V. Prasad, and D. A. Weitz. Monodisperse emulsion generation via drop break off in a coflowing stream. *Langmuir*, 16:347–351, 2000.

M. A. Unger, H.-P. Chou, T. Thorsen, A. Scherer, and S. R. Quake. Monolithic microfabricated valves and pumps by multilayer soft lithography. *Science*, 288: 113–116, April 7th 2000.

J. P. Urbanski, W. Thies, C. Rhodes, S. Amarasinghe, and T. Thorsen. Digital microfluidics using soft lithography. *Lab on a Chip*, 6:96–104, 2006.

A. S. Utada, A. Fernandez-Nieves, H. A. Stone, and D. A. Weitz. Dripping to jetting transitions in coflowing liquid streams. *Physical Review Letters*, 99: 094502–1–4, 2007.

D. van Noort and B.-T. Zhang. PDMS valves in DNA computers. *Biomedical Applications of Micro- and Nanoengineering II*, 5651(1):214–220, 2005.

P. Vulto, N. Glade, L. Altomare, J. Bablet, L. Den Tin, G. Medoro, I. Chartier, N. Manaresi, M. Tartagni, and R. Guerrieri. Microfluidic channel fabrication in dry film resist for production and prototyping of hybrid chips. *Lab on a Chip*, 5:158–162, 2005.

G. M. Walker, N. Monteiro-Riviere, J. Rouse, and A. T. O'Neill. A linear dilution microfluidic device for cytotoxicity assays. *Lab on a Chip*, 7:226–232, 2007.

Y.-C. Wang, M. H. Choi, and J. Han. Two-dimensional protein separation with advanced sample and buffer isolation using microfluidic valves. *Analytical Chemistry*, 76:4426–4431, 2004.

C. Wei, T. Yang, E. Ouellet, and E. T. Lagally. Using inexpensive jell-o chips for hands-on microfluidics education. *Analytical Chemistry*, 82:5408–5414, 2010.

D. B. Weibel, M. Kruithof, S. Potenta, S. K. Sia, A. Lee, and G. M. Whitesides. Torque-actuated valves for microfluidics. *Analytical Chemistry*, 77(15):4726–4733, August 1st 2005.

D. Wenn. *AN1115: Implementing Digital Lock-In Amplifiers Using the dsPIC DSC*. Microchip, 2007.

K. E. Whelan and R. D. King. Intelligent software for laboratory automation. *Trends in Biotechnology*, 22(9):440–445, September 2004.

G. M. Whitesides. The origins and future of microfluidics. *Nature*, 442:368–373, July 27th 2006.

H Willaime, V. Barbier, L. Kloul, S. Maine, and P. Tabeling. Arnold tongues in a microfluidic drop emitter. *Phys. Rev. Lett.*, 96(5):054501, Feb 2006.

J. Y. Yun, S. Jambovane, S.-K. Kim, S.-H. Cho, E. C. Duin, and J. W. Hong. Log-scale dose response of inhibitors on a chip. *Analytical Chemistry*, 83:6148–6153, 2011.

N. A. Md Yunus and N. G. Green. Fabrication of microfluidic device channel using a photopolymer for colloidal particle separation. *Microsystem Technologies*, 16: 2099–2107, 2010.

M. Zagnoni, C. N. Baroud, and J. M. Cooper. Electrically initiated upstream coalescence cascade of droplets in a microfluidic flow. *Physical Review E*, 80: 046303, 2009.

K.-P. Zauner and M. Conrad. Enzymatic computing. *Biotechnology Progress*, 17 (3):553–559, 2001.

S. Zeng, B. Li, X. Su, J. Qin, and B. Lin. Microvalve-actuated precise control of individual droplets in microfluidic devices. *Lab on a Chip*, 9:1340–1343, 2009.

W.-Y. Zhang, G. S. Ferguson, and S. Tatic-Lucic. Elastomer-supported cold welding for room temperature wafer-level bonding. In *Technical Digest of 17th IEEE International Conference on Micro Electro Mechanical Systems (MEMS 2004)*, pages 741–744, Maastricht, The Netherlands, January 25–29 2004.

B. Zheng, L . S. Roach, and R. F. Ismagilov. Screening of protein crystallization conditions on a microfluidic chip using nanoliter-size droplets. *Journal of the American Chemical Society*, 125(37):11170–11171, 2003.